UNIVERSITÀ DI PARMA

UNIVERSITÀ DEGLI STUDI DI PARMA

DOTTORATO DI RICERCA IN

"SCIENZA E TECNOLOGIA DEI MATERIALI"

CICLO XXXVI

Structural investigation of nanocrystalline reticular materials through 3D electron diffraction

Coordinatore:

Prof. Enrico Dalcanale

Tutore:

Dr. Mauro Gemmi

Prof. Enrico Dalcanale

Dottorando: Danilo Marchetti

Anni Accademici 2020/2021-2022/2023

Contents

1 Abstract

The research presented in the following thesis focuses on the synthesis and characterisation of novel nanocrystalline reticular materials. Various organic and metal-organic, porous 2D and 3D crystalline compounds are reported and discussed, including Metal-Organic Frameworks (MOFs), comprising metal ions or clusters held together by organic linkers, and Supramolecular Organic Frameworks (SOFs), which derive from the self-assembly of organic tectons through non-covalent interactions. These materials have been obtained employing a variety of synthetic methods, ranging from solvothermal to mechanochemical synthesis. The crucial role of 3D electron diffraction (3D ED) analysis in the structural investigation of the reported compounds is demonstrated throughout each chapter. Diverse data collection protocols and instrumental setups dedicated to this emerging crystallographic technique are herein reported, as well as the use of a novel electron diffractometer.

In particular, Chapter 4 gives a significative example of the 3D ED potential by introducing a novel approach for the structural investigation of mechanochemically-synthesized reticular materials. Chapter 5 elucidates the dynamic behaviour of SOFs based on the rigid organic tecton tetra-4-(4-pyridyl)phenylmethane (**TPPM**). Chapter 6 describes how **TPPM** and paddle-wheel complexes of Copper(II) can be combined to yield a series of highly interpenetrated MOFs that exhibit diamond-like networks. The functionalisation of these networks by the introduction of fluorinated secondary building units (SBUs) is also discussed, along with the effect this can have on the properties of the materials. Lastly, Chapter 7 discusses the synthesis and characterization of 2D and 3D bismuth-based reticular materials. This part of the work has been carried out at Stockholm University, under the supervision of Prof. Andrew Kentaro Inge.

2 3D Electron Diffraction

In the last decade, the structural analysis of nanocrystalline materials has experienced a significant expansion. The development of protocols for acquiring 3D Electron Diffraction (3D ED) data combined with novel highly sensitive detectors are the primary reasons for the evolution of this scientific field. [1] This method of collecting data is based on the acquisition of single-crystal diffraction patterns by rotating the goniometer axis like in a φ-scan of a single-crystal X-ray diffractometer. The data quality enables the atomic structure determination of materials that would normally fail in a single-crystal X-ray diffraction study, due to the reduced dimensions of their crystals. The 3D ED technique has been applied to a wide range of materials, including zeolites, [2] Metal-Organic Frameworks (MOFs), [3] supramolecular organic frameworks (SOF), [4] active pharmaceutical ingredients (APIs), [5,6] and proteins. [7]

This chapter consists of a brief introduction to the 3D Electron Diffraction technique, in which its basic principles and methods will be explained and discussed.

2.1 Fundamental Concepts in Crystallography

The determination of the atomic coordinates in a crystal is the focus of crystal structure analysis. Crystallographic techniques are based on the diffraction phenomena caused by the interaction between matter and a coherent wave characterized by a wavelength comparable to interatomic distances (X-rays, accelerated electrons, thermal or cold neutrons).

2.1.1 Geometric Theory of Diffraction

Crystalline solids are characterized by a long-range order which extends to the molecular scale. This implies the presence of translational symmetry that allows their description through a lattice function. This function can be described using a *unit cell*, which comprises the smallest set of vectors capable of describing the entire lattice. It results in a parallelogram with a defined size and composed by integer linear combinations of the three lattice vectors $\boldsymbol{a}$, $\boldsymbol{b}$ and $\boldsymbol{c}$ (Figure 2.1). The resulting crystal lattice consists of a grid system in which every node R presents the same environment, and it is characterized by the following relation:

$$R_{u,v,w} = u\boldsymbol{a} + v\boldsymbol{b} + w\boldsymbol{c} \tag{2.1}$$

where u, v and w are integers.

The length of the three vectors is reported as a, b and c, while the angles between them as α, β and γ (where α is opposing $\boldsymbol{a}$, and so on). As a consequence, any position in the crystal can be described as follows:

$$\mathrm{r} = (\mathrm{u} + \mathrm{x}) \cdot \mathbf{a} + (\mathrm{v} + \mathrm{y}) \cdot \mathbf{b} + (\mathrm{w} + \mathrm{z}) \cdot \mathbf{c} \tag{2.2}$$

where u, v and w are integers and x, y and z are *fractional coordinates* within the unit cell.

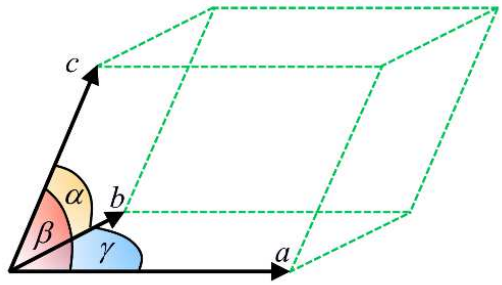

Figure 2.1: Unit cell representation with its related notation.

In 1912, the discovery of the diffraction of X-rays from crystals by Max von Laue demonstrated the periodic nature of crystals. Later, father and son Bragg derived the most iconic equation in crystallography, Bragg's *Law*, in which the diffraction from a crystal is treated as a reflection from lattice planes:

$$2d \cdot sin\,\theta = n\lambda \tag{2.3}$$

where d corresponds to the interplanar distances, λ to the radiation wavelength and θ to the scattering angle. For X-ray and neutron $\lambda \approx 1$ Å while $\lambda \approx 10^{-2}$ Å for the accelerated electrons inside a TEM. [8]

Since then, X-ray diffraction analysis has allowed the crystal structure determination of several thousands of compounds, spanning from inorganic to organic single molecules and biological macromolecules. Meanwhile, electron diffraction and, subsequently, neutron diffraction techniques emerged as valuable methods in the structural investigation of crystalline solids. Although all the above-mentioned methods for structural analysis can be described with the same geometric diffraction theory developed for X-ray, they present peculiar features which defined their application fields. [9]

Equation 2.3 is based on an interpretation of the diffraction phenomena in direct space, in which scattering elements are considered lying along specific planes. The Miller index notation is then used to describe the resulting crystallographic planes, using a sequence of three integers (*hkl*) to identify a family of planes. From this law it is clear the inversely proportional

relationship between sin(θ) and the interplanar spacing (d) in the crystal lattice. It follows that compressed diffraction patterns will be related to crystal structures with large unit cell parameters.

$$sin\theta = \frac{n\lambda}{2}\frac{1}{d} \tag{2.4}$$

A direct relation between sin(θ) and $1/d$ can be introduced, to facilitate the interpretation of diffraction patterns, leading to the construction of the *reciprocal lattice*. In analogy to the real space, also in the reciprocal space a unit cell is defined by three basis vectors **a***, **b*** and **c***. If we generalize the direct and reciprocal vectors as $\mathbf{a}_i$ and $\mathbf{a}^*_i$, the relationship between them results to be:

$$\boldsymbol{a}_i \cdot \boldsymbol{a}_j^* = \delta_{ij} \tag{2.5}$$

Equation 2.5 denotes that reciprocal space vectors are orthogonal to direct planes, so every **a*** can be identified by a set of direct lattice planes (Bragg planes). In analogy to the grid system described for a direct lattice, reciprocal lattice nodes R^*_{hkl} can be defined using the *Miller indices*.

$$R^*_{hkl} = h\boldsymbol{a}^* + k\boldsymbol{b}^* + l\boldsymbol{c}^* \tag{2.6}$$

Moreover, the Laue equation can be introduced to give a more rigorous explanation of the diffraction phenomena. Let us consider an incident wave vector **k** and a resulting scattered wave vector **k'**, that, since we are considering elastic scattering, are both characterized by the same length (1\λ). The diffraction conditions result fulfilled when the following Laue condition is satisfied:

$$R \cdot (k - k') = R \cdot s = u \tag{2.7}$$

where R is defined in Equation 2.1 and u is an integer number.

From the relationship between direct and reciprocal space, to obtain a diffraction event, the scattering vector should correspond to a reciprocal lattice vector. It follows that the positions of measured intensities are directly correlated to reciprocal space nodes and hence a 3D reciprocal space reconstruction can be derived from the collected diffraction patterns.

An important geometric construct, particularly useful for the visualization of the diffraction conditions, is the *Ewald sphere*. Since we are considering only elastic scattering, each scattered electron can be represented by a **k'** vector of equal length (same energy, same wavelength), which will then sit on the surface of the defined sphere. The reflection occurs when, by rotating the reciprocal lattice around its origin, one of its nodes lies on the sphere surface. This also implies the correspondence between the scattering vector **s** and a reciprocal vector $\mathbf{R}^*_{hkl}$.

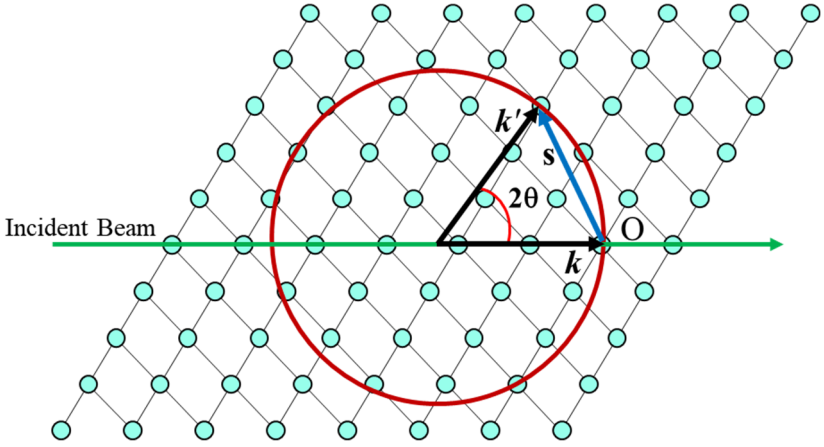

Figure 2.2: Representation of the Ewald sphere on a 2D lattice. The radius of the sphere corresponds to the inverse of the incident beam wavelength (1/λ). The Bragg condition is satisfied once a reciprocal node intersects the surface of the sphere, leading to a scattered beam **k'** at an angle 2θ to the incident beam **k**.

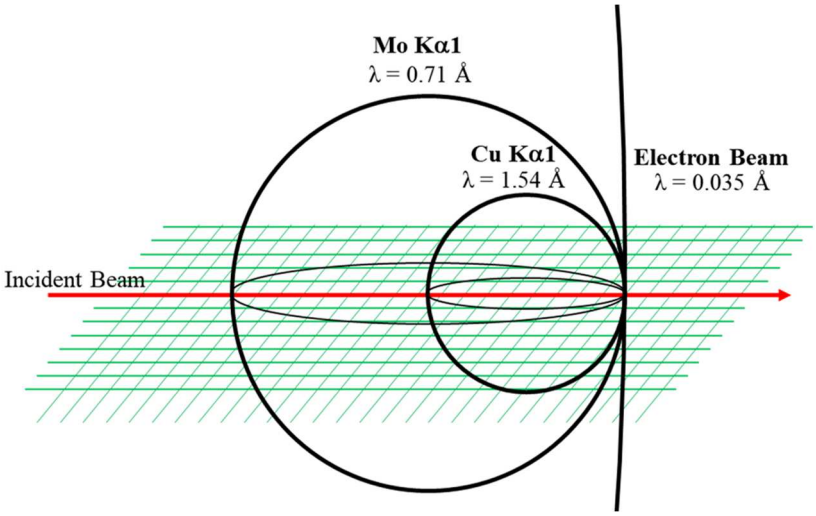

Figure 2.3: Comparison between the Ewald spheres of two common X-ray sources (Cu and Mo) with the one related to an electron beam (120 kV of acceleration).

2.1.2 Diffraction Amplitude

A crucial parameter for crystal structure solution from diffraction analysis is the amplitude of the collected signals. In a *kinematical approach*, from a geometrical point of view, X-ray, neutron and electrons appear identical, differing only in terms of wavelength (λ) and, consequently, scattering angle (θ). Contrary to X-rays, the wave-like nature of electrons and neutrons requires a quantum mechanical description. The main differences among these three methods arise from their different interaction with matter, resulting in the measurement of different physical quantities. Indeed, X-rays are scattered only by the atomic electron shells, being sensitive to the distribution of the crystal's electron density. Electrons are scattered by the electrostatic potential generated by electron clouds and nuclei. Instead, neutrons scattering is related to the delta-function potential of nuclear forces (Figure 2.4). These differences in interaction strength also have consequences on the overall amplitude of the scattered beam. In general, the amplitude rate between X-rays, electrons and neutrons is $1:10^{3}:10^{-2}$, placing limits on the crystal size of the analysed

samples.[9] For brevity's sake, further discussions will be focused on X-rays and electron diffraction only.

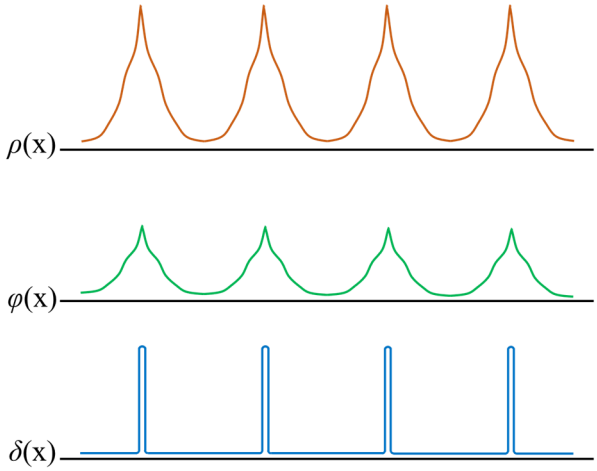

Figure 2.4: Representation of electron density $\rho(x)$, atomic electrostatic potential $\varphi(x)$ and nuclear scattering function $\delta(x)$, in a 1D crystal lattice. [9]

The periodical nature of crystalline solids allows the description of any physical quantity responsible for scattering (S(r)) through Fourier series, in which their components are called *structure factors* and can be calculated as a Fourier transform.

$$\mathfrak{F}[S(r)] = \int_{-\infty}^{\infty} S(r) exp(-2\pi v r)\, dr \tag{2.8}$$

Once the Fourier transform is explicitly calculated, the structure factor of a crystal can be described as follows:

$$F(hkl) = \sum_{j=1}^{N} f_j(hkl) \cdot exp\left[2\pi i\left(hx_j + ky_j + lz_j\right)\right] \tag{2.9}$$

where (hkl) defines a position in the reciprocal lattice, (xyz) the real space position of atom j and $f_j(hkl)$ the atomic scattering factor of the jth atom. Thus, Equation 2.9 can be written in a more concise way:

$$F(\boldsymbol{s}) = \sum_{j=1}^{N} f_j(\boldsymbol{s}) \cdot exp\left[2\pi i\left(\boldsymbol{s} \cdot \boldsymbol{r_j}\right)\right] \tag{2.10}$$

where $\mathbf{s}$ is a reciprocal space vector and $\boldsymbol{r_j}$ is the position of jth atom.

In a diffraction experiment, the scattering quantity S(r) is either the electron density or the electrostatic potential, for X-ray and electrons, respectively. Both can be derived from the atoms contained in the unit cell, in terms of their types and positions: [10]

$$\rho(\boldsymbol{r}) = \sum_{j=1}^{N} \rho_j(\boldsymbol{r} - \boldsymbol{r_j}) \tag{2.11}$$

$$\varphi(\boldsymbol{r}) = \sum_{j=1}^{N} \varphi_j(\boldsymbol{r} - \boldsymbol{r_j}) \tag{2.12}$$

where $\rho_j(\mathbf{r}\text{-}\mathbf{r}_j)$ and $\varphi_j(\mathbf{r}\text{-}\mathbf{r}_j)$ are the contribution by the j^{th} atom to the electron density and the electrostatic potential, respectively, while N is the number of atoms in the unit cell.

However, the above inversion formulas cannot be performed simply starting from the collected diffraction intensities. $F(\mathbf{s})$ is a complex number and contains an amplitude and a phase:

$$F(s) = |F(s)|exp[i\phi(s)] \tag{2.13}$$

During a diffraction experiment the collected signals correspond to the structure factor squared modulus, while the phase information is missing.

$$I(s) = |F(s)|^2 \tag{2.14}$$

This is known as the *phase problem* in crystallography and several different approaches have been developed to overcome it. The structural models reported in the present thesis have been directly solved from diffraction data using *ab-initio* methods. [11–13]

2.2 The 3D Electron Diffraction Technique

In the past two decades, the Electron Diffraction (ED) technique has come back into the limelight thanks to various studies illustrating the employment of data acquired in a transmission electron microscope (TEM) to obtain the crystal structures of diverse nanocrystalline samples. [14–17]

The old-fashioned ED data collection consists in acquiring diffraction patterns while orienting the crystal along well recognizable crystallographic axes (*zone-axes*). [10] This method of data collection is not compatible with classical crystallographic routines and has, for many years, restricted the ED to a time-consuming and specialised technique. The main limitations are the exiguous number of recorded reflections and the presence of strong dynamical effects (multiple scattering phenomena) enhanced by recoding the pattern in zone-axis. [1]

In 2007, Kolb and co-workers suggested an alternative approach of collecting ED data (3D ED). The method consists in acquiring ED patterns *off-zone*, by systematically tilting the sample around a non-crystallographic axis in fixed angular steps. Essentially, this procedure emulated the data acquisition process on a mono-axial diffractometer equipped with an area detector. [18–21] The 3D reconstruction of the reciprocal space could then be achieved by combining the collected patterns considering their angular relationship (Figure 2.5). Enhanced data acquisition procedures and more sensitive detectors allowed the development of dedicated protocols for characterizing the structure of nearly all types of crystalline samples. [2–6,22–24]

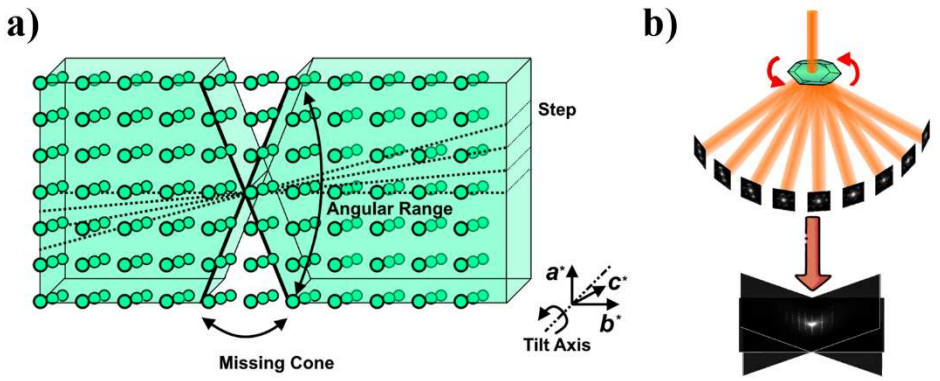

Figure 2.5: Schematic representation of a 3D ED data collection. (a) Example of the reciprocal space sampling during a 3D ED experiment. (b) Schematisation of the workflow process for a 3D ED analysis. [18]

On first approximation, the recorded intensities can be treated with the same routines as in single crystal X-ray diffraction (SC-XRD), due to the improved integration of the observed reflections and a significant reduction in dynamical effects. [11–13] Remarkably, the stronger interaction of electrons with matter allows detectable diffraction signals from crystals that are several orders of magnitude smaller than SC-XRD. In fact, crystals that are usually considered microcrystalline powders for X-ray diffraction analysis, can be analysed as single crystals in 3D ED. The typical crystal size for a sample suitable for electron diffraction analysis is around 10 to 10^{-4} µm (Figure 2.6). [1] Another method for analysing crystals in the same size range is powder X-ray diffraction (PXRD), which, however, has other limitations, such as the loss of dimensionality with all the information compressed into one dimension only (Figure 2.6-d); the challenging phenomenon of peak overlapping, enhanced by peak broadening or by the presence of polyphasic mixtures. In cases like these, the 3D ED technique can provide single-crystal diffraction data, overcoming the problems associated with PXRD data. [1]

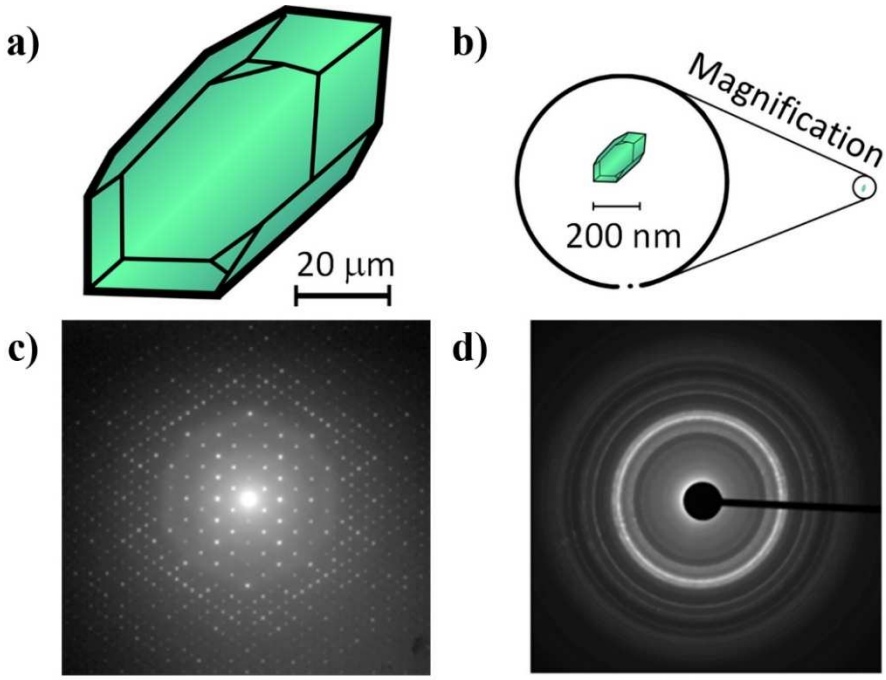

Figure 2.6: Size comparison between a single crystal suitable for SC-XRD analysis (a) and 3D ED (b). The latter can be characterized either with X-ray powder diffraction or as single crystal by 3D ED. (c) and (d) represent two generic diffraction patterns related to a single-crystal and to powder diffraction, respectively.

A 3D ED analysis is typically conducted in transmission electron microscopes. Recently, dedicated instruments tailored for this purpose have been also developed and commercialized. [25,26] Inside these instruments, the generated parallel electron beam can be properly focused, through electromagnetic lenses, in order to record images or diffraction patterns (Figure 2.7). The crystal can be rotated throughout the goniometer axis during the 3D ED data collection. However, the angular range is limited by the presence of the objective lenses. Generally, the total tilt range results constrained around 120° (±60°), thus always leaving a portion of the reciprocal space unsampled (missing cone). This experimental limitation in the reciprocal space coverage can be mitigated by merging diffraction data from various crystals. [1]

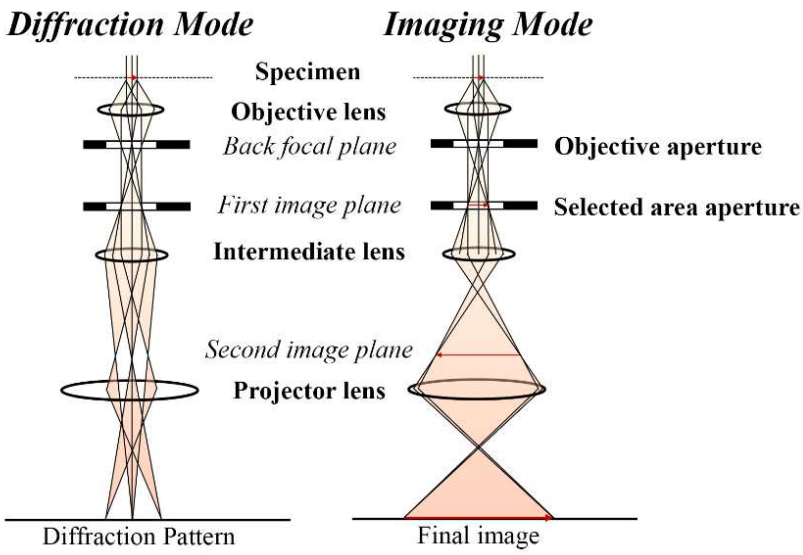

Figure 2.7: Path-ray diagrams for a TEM operating with a parallel beam in Diffraction (left) of Imaging mode (right).

Electron diffraction analysis can be conducted in a normal TEM operating with a selected area (selected area electron diffraction - SAED) or in nanodiffraction mode (NED). The latter is facilitated if the instrument supports the scanning transmission electron microscopy (STEM) mode (Figure 2.8). The SAED consists in acquiring diffraction data with a wide parallel electron beam and filtering out the diffracted intensities from other crystals through a selected area aperture located in the image plane (the smallest SAED aperture select area is around 100 nm). Instead, in nanodiffraction mode the instrument presents a parallel nanometric beam (typically larger than 50 nm). [18] The small-sized beam can be localized on a specific crystal region. In this experimental set up, since the illuminated area is very small, a different imaging method is required. The microscope, in most of the cases, works in STEM mode, in which the same beam used for diffraction is scanned on the area of interest and the electrons scattered at high angle are picked up by an auxiliary dedicated detector called high angle annular dark field detector (HAADF detector). This becomes useful for crystal

centring and also in specific data collections, in which diffraction patterns are collected tracking the position of the crystal image through the HAADF detector. [27,28]

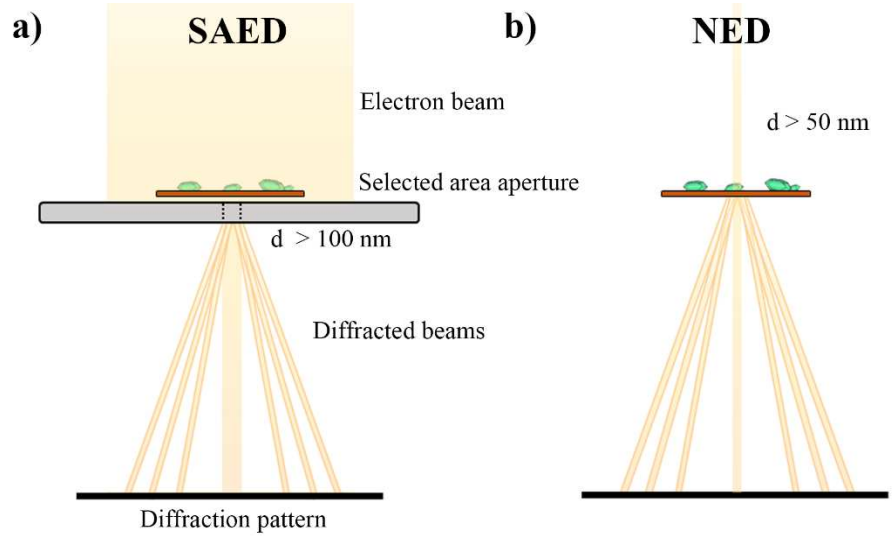

Figure 2.8: Schematic representation of SAED (a) and NED (b) analyses.

A 3D ED experiment can be carried out in several different ways. The first and simplest one consists in the acquisition of diffraction patterns after *stepwise* tilting of the crystals in fixed angular steps (Figure 2.9). The stepwise data collection leads to reliable information on unit cell parameters. However, the collected intensity suffers of imprecise integration since the missing wedge between each pattern orientation is not sampled. The integration process was subsequently improved by introducing protocols with better reciprocal space sampling, such as precession electron diffraction tomography (PEDT) and continuous rotation electron diffraction (cRED). [18,20,21,29,30]

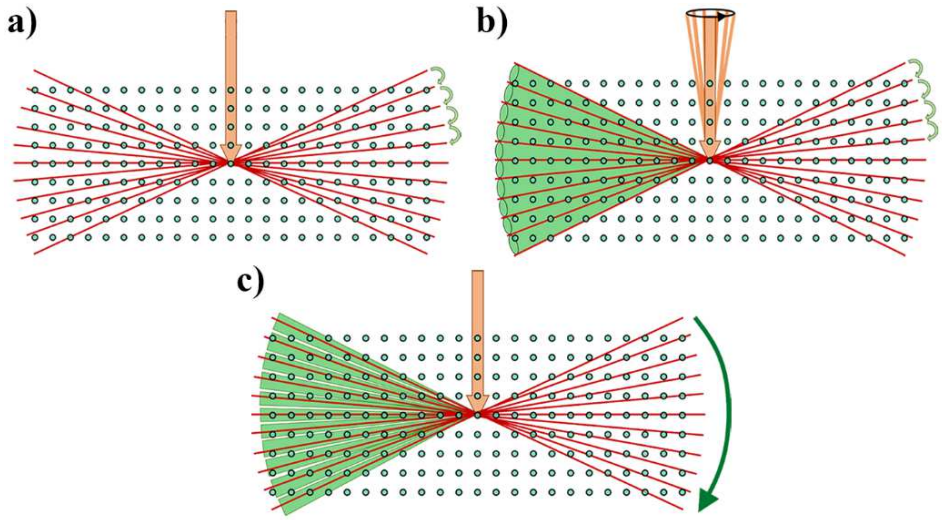

Figure 2.9: Schematic representation of the most common data collection protocols in 3D ED: stepwise (a), PEDT (b), and cRED. The image view is oriented along the goniometer tilt axis. The electron beam is represented in orange, while the angular steps are shown as red lines. The reciprocal space volume, covered during the sample tilt, is represented as a green area. [1]

Data collected following 3D ED protocols display well-sampled intensities and minimized dynamical scattering effects. This is achieved by collecting reflection out from low-index axis and allows to carry out the data analysis through standard routines developed for X-ray crystallography. [11–13]

In the data reduction process either conventional X-ray software (XDS, [31] DIALS, [32] Apex4, [33] CrysAlisPro [34]) or software specific for 3D ED technique (PETS2, [35] ADT3D [21]) can be employed. The first step of the data reduction consists in the unit cell determination and in the indexing of all observed reflections. Furthermore, at this stage, it is possible to produce the reciprocal space reconstruction and its sections. These are important tools that can be used to retrieve information on the symmetry of the system under analysis. However, the symmetry identification can be a challenging step due to the presence of non-negligible dynamical effects.

Indeed, the phenomenon of multiple scattering has several consequences on the diffraction patterns, such as the violation of the extinction rules and Friedel's law (Figure 2.10).

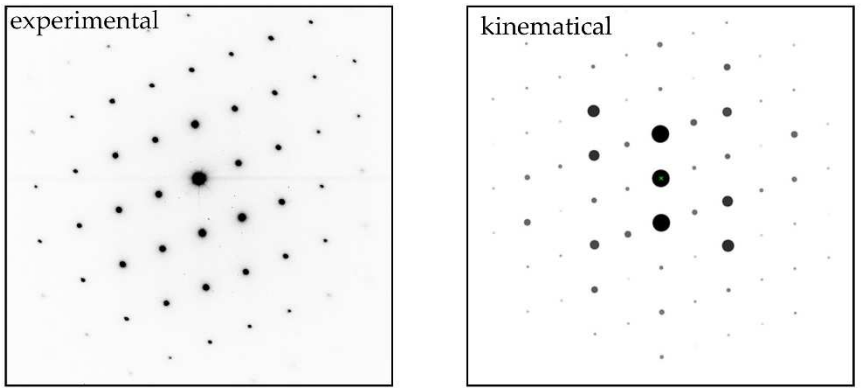

Figure 2.10: Diffraction patterns from a Calcite ($CaCO_3$) crystal oriented along the [100] direction (*left*) and its calculated diffraction pattern (*right*, calculation performed through JEM software). [36] The reported diffraction patterns are oriented along a zone-axis to maximise the dynamical scattering effects.

At this stage, the reflection file obtained from the data reduction process, although still dynamical, can be successfully used in the structure solution as the X-ray data. It can therefore be employed as input for the structure solution process using conventional X-ray software (SHELX, [13] SIR, [12] Superflip [11]).

The minimisation of the dynamical scattering allows a kinematical treatment of the data, which considers the diffracted intensity proportional to the squared modulus of the structure factor. It follows that the refinement can be carried out with the conventional tools for SC-XRD data (e.g. SHEXL [37], Olex2 [38]); the only difference is that the electron scattering factors should be included. However, *dynamical scattering* is a not-negligible component in electron scattering, due to the magnitude of the interaction with matter. Indeed, kinematically refined crystal structures are usually affected by high

figures of merit and reduced sensitivity to atomic displacement parameters, fractional atomic occupancy, and hydrogen atom positions. [1]

In order to handle ED data considering the proper electron scattering theory, Palatinus and coworkers developed an alternative refinement method known as *dynamical refinement.* [39,40] In this refinement, the reflection intensities are considered using a Bloch formalism and the crystal structure is refined together with the sample thickness. [41] This dedicated approach enables a more accurate determination of atomic occupancies, [40,42] positions of light atoms [42–44] and atomic displacement parameters. [45] Refining the structure considering the always present dynamical scattering effects increases the agreement between the calculated and experimental model, leading to a reduction of residual values by a factor 2-3. [40] Moreover, another advantage consists in the possibility to identify the absolute configuration of non-centrosymmetric crystal structures. [6,40,46] The dynamical refinement is a powerful and consistent approach for 3D ED data analysis. On the other side, it is a computationally demanding process that cannot be applied to systems with a large number of independent atoms (e.g. macromolecules).

Bibliography:

[1] M. Gemmi, E. Mugnaioli, T.E. Gorelik, U. Kolb, L. Palatinus, P. Boullay, S. Hovmöller, J.P. Abrahams, "3D Electron Diffraction: The Nanocrystallography Revolution", *ACS Cent. Sci.* 5 (2019) 1315–1329. https://doi.org/10.1021/acscentsci.9b00394.

[2] E. Mugnaioli, A.E. Lanza, G. Bortolozzi, L. Righi, M. Merlini, V. Cappello, L. Marini, A. Athanassiou, M. Gemmi, "Electron Diffraction on Flash-Frozen Cowlesite Reveals the Structure of the First Two-Dimensional Natural Zeolite", *ACS Cent. Sci.* 6 (2020) 1578–1586. https://doi.org/10.1021/acscentsci.9b01100.

[3] Z. Huang, T. Willhammar, X. Zou, "Three-dimensional electron diffraction for porous crystalline materials: structural determination and beyond", *Chem. Sci.* 12 (2021) 1206–1219. https://doi.org/10.1039/D0SC05731B.

[4] P. Cui, E. Svensson Grape, P.R. Spackman, Y. Wu, R. Clowes, G.M. Day, A.K. Inge, M.A. Little, A.I. Cooper, "An Expandable Hydrogen-Bonded Organic Framework Characterized by Three-Dimensional Electron Diffraction", *J. Am. Chem. Soc.* 142 (2020) 12743–12750. https://doi.org/10.1021/jacs.0c04885.

[5] I. Andrusenko, V. Hamilton, E. Mugnaioli, A. Lanza, C. Hall, J. Potticary, S.R. Hall, M. Gemmi, "The Crystal Structure of Orthocetamol Solved by 3D Electron Diffraction", *Angew. Chem. Int. Ed.* 58 (2019) 10919–10922. https://doi.org/10.1002/anie.201904564.

[6] P. Brázda, L. Palatinus, M. Babor, "Electron diffraction determines molecular absolute configuration in a pharmaceutical nanocrystal", *Science* 364 (2019) 667–669. https://doi.org/10.1126/science.aaw2560.

[7] B.L. Nannenga, D. Shi, A.G.W. Leslie, T. Gonen, "High-resolution structure determination by continuous-rotation data collection in MicroED", *Nat. Methods* 11 (2014) 927–930. https://doi.org/10.1038/nmeth.3043.

[8] C. Giacovazzo, M. Catti, G. Ferraris, G. Zanotti, P. Gilli, G. Gilli, M. Milanesio, D. Viterbo, G. Artioli, H.L. Monaco, "Fundamentals of Crystallography", 3rd ed., Oxford University Press, n.d. https://doi.org/10.1093/acprof:oso/9780199573653.001.0001.

[9] B. K. Vainshtein, "Structure Analysis by Electron Diffraction", 1st ed., E. Feigl, J.A. Spink, 1964.

[10] X. Zou, P. Oleynikov, S. Hovmöller, "Electron Crystallography", 1st ed., Oxford University Press.

[11] L. Palatinus, G. Chapuis, "*SUPERFLIP* – a computer program for the solution of crystal structures by charge flipping in arbitrary dimensions", *J. Appl. Crystallogr.* 40 (2007) 786–790. https://doi.org/10.1107/S0021889807029238.

[12] M.C. Burla, R. Caliandro, B. Carrozzini, G.L. Cascarano, C. Cuocci, C. Giacovazzo, M. Mallamo, A. Mazzone, G. Polidori, "Crystal structure determination and refinement *via SIR2014"*, *J. Appl. Crystallogr.* 48 (2015) 306–309. https://doi.org/10.1107/S1600576715001132.

[13] G.M. Sheldrick, "A short history of *SHELX"*, *Acta Crystallogr. A Found. Crystallogr.* 64 (2008) 112–122. https://doi.org/10.1107/S0108767307043930.

[14] D.L. Dorset, H.A. Hauptman, "Direct phase determination for quasi-kinematical electron diffraction intensity data from organic microcrystals", *Ultramicroscopy* 1 (1976) 195–201. https://doi.org/10.1016/0304-3991(76)90034-6.

[15] D.L. Dorset, "Electron crystallography", *Acta Crystallogr. B Struct. Sci.* 52 (1996) 753–769. https://doi.org/10.1107/S0108768196005599.

[16] T.E. Weirich, R. Ramlau, A. Simon, S. Hovmöller, X. Zou, "A crystal structure determined with 0.02 Å accuracy by electron microscopy", *Nature* 382 (1996) 144–146. https://doi.org/10.1038/382144a0.

[17] T.E. Weirich, X. Zou, R. Ramlau, A. Simon, G.L. Cascarano, C. Giacovazzo, S. Hovmöller, "Structures of nanometre-size crystals determined from selected-area electron diffraction data", *Acta Crystallogr. A Found. Crystallogr.* 56 (2000) 29–35. https://doi.org/10.1107/S0108767399009605.

[18] U. Kolb, T. Gorelik, C. Kübel, M.T. Otten, D. Hubert, "Towards automated diffraction tomography: Part I—Data acquisition", *Ultramicroscopy* 107 (2007) 507–513. https://doi.org/10.1016/j.ultramic.2006.10.007.

[19] U. Kolb, T. Gorelik, M.T. Otten, "Towards automated diffraction tomography. Part II—Cell parameter determination", *Ultramicroscopy* 108 (2008) 763–772. https://doi.org/10.1016/j.ultramic.2007.12.002.

[20] E. Mugnaioli, T. Gorelik, U. Kolb, "“Ab initio” structure solution from electron diffraction data obtained by a combination of automated diffraction tomography and precession technique", *Ultramicroscopy* 109 (2009) 758–765. https://doi.org/10.1016/j.ultramic.2009.01.011.

[21] U. Kolb, E. Mugnaioli, T.E. Gorelik, "Automated electron diffraction tomography – a new tool for nano crystal structure analysis", *Cryst. Res. Technol.* 46 (2011) 542–554. https://doi.org/10.1002/crat.201100036.

[22] T. Sun, C.E. Hughes, L. Guo, L. Wei, K.D.M. Harris, Y. Zhang, Y. Ma, "Direct-Space Structure Determination of Covalent Organic Frameworks from 3D Electron Diffraction Data", *Angew. Chem. Int. Ed.* 59 (2020) 22638–22644. https://doi.org/10.1002/anie.202009922.

[23] B.L. Nannenga, D. Shi, J. Hattne, F.E. Reyes, T. Gonen, "Structure of catalase determined by MicroED", *eLife* 3 (2014) e03600. https://doi.org/10.7554/eLife.03600.

[24] A. Lanza, E. Margheritis, E. Mugnaioli, V. Cappello, G. Garau, M. Gemmi, "Nanobeam precession-assisted 3D electron diffraction reveals a new polymorph of hen egg-white lysozyme", *IUCrJ* 6 (2019) 178–188. https://doi.org/10.1107/S2052252518017657.

[25] S. Ito, F.J. White, E. Okunishi, Y. Aoyama, A. Yamano, H. Sato, J.D. Ferrara, M. Jasnowski, M. Meyer, "Structure determination of small molecule compounds by an electron diffractometer for 3D ED/MicroED", *CrystEngComm* 23 (2021) 8622–8630. https://doi.org/10.1039/D1CE01172C.

[26] P. Simoncic, E. Romeijn, E. Hovestreydt, G. Steinfeld, G. Santiso-Quiñones, J. Merkelbach, "Electron crystallography and dedicated electron-diffraction instrumentation", *Acta Crystallogr. E Cryst. Commun.* 79 (2023) 410–422. https://doi.org/10.1107/S2056989023003109.

[27] T. Yang, H. Xu, X. Zou, "Improving data quality for 3D electron diffraction (3DED) by Gatan Image Filter (GIF)", *Microsc. Microanal.* 27 (2021) 198–203. https://doi.org/10.1017/S1431927621001318.

[28] F. Bertocchi, D. Marchetti, S. Doria, M. Di Donato, C. Sissa, M. Gemmi, E. Dalcanale, R. Pinalli, A. Lapini, "Tuning the Optical Properties Through Hydrogen Bond-assisted H-aggregate Formation: The ODIN Case", *Chem. Eur. J.* (2023) e202302619. https://doi.org/10.1002/chem.202302619.

[29] Y. Wang, S. Takki, O. Cheung, H. Xu, W. Wan, L. Öhrström, A.K. Inge, "Elucidation of the elusive structure and formula of the active pharmaceutical ingredient bismuth subgallate by continuous rotation electron diffraction", *Chem. Commun.* 53 (2017) 7018–7021. https://doi.org/10.1039/C7CC03180G.

[30] I. Nederlof, E. Van Genderen, Y.-W. Li, J.P. Abrahams, "A Medipix quantum area detector allows rotation electron diffraction data collection from submicrometre three-dimensional protein crystals", *Acta Crystallogr. D Biol. Crystallogr.* 69 (2013) 1223–1230. https://doi.org/10.1107/S0907444913009700.

[31] M.T.B. Clabbers, E. van Genderen, W. Wan, E.L. Wiegers, T. Gruene, J.P. Abrahams, "Protein structure determination by electron diffraction using a single three-dimensional nanocrystal", *Acta Crystallogr. D Struct. Biol.* 73 (2017) 738–748. https://doi.org/10.1107/S2059798317010348.

[32] M.T.B. Clabbers, T. Gruene, J.M. Parkhurst, J.P. Abrahams, D.G. Waterman, "Electron diffraction data processing with *DIALS"*, *Acta Crystallogr. D Struct. Biol.* 74 (2018) 506–518. https://doi.org/10.1107/S2059798318007726.

[33] Bruker, "APEX4", (2021), Bruker AXS Inc., Madison, Wisconsin, USA.

[34] Rigaku Oxford Diffraction, "CrysAlisPro Software system", (2023), Rigaku Corporation, Wroclaw, Poland.

[35] L. Palatinus, P. Brázda, M. Jelínek, J. Hrdá, G. Steciuk, M. Klementová, "Specifics of the data processing of precession electron diffraction tomography data and their implementation in the program *PETS2.0"*, *Acta Crystallogr. B Struct. Sci. Cryst. Eng. Mater.* 75 (2019) 512–522. https://doi.org/10.1107/S2052520619007534.

[36] P. A. Stadelmann. JEMS - EMS java version, 2004.

[37] G.M. Sheldrick, "Crystal structure refinement with *SHELXL"*, *Acta Crystallogr. C. Struct. Chem.* 71 (2015) 3–8. https://doi.org/10.1107/S2053229614024218.

[38] O.V. Dolomanov, L.J. Bourhis, R.J. Gildea, J.A.K. Howard, H. Puschmann, "*OLEX2*: a complete structure solution, refinement and analysis program", *J. Appl. Crystallogr.* 42 (2009) 339–341. https://doi.org/10.1107/S0021889808042726.

[39] L. Palatinus, V. Petříček, C.A. Corrêa, "Structure refinement using precession electron diffraction tomography and dynamical diffraction: theory and implementation", *Acta Crystallogr. A Found. Adv.* 71 (2015) 235–244. https://doi.org/10.1107/S2053273315001266.

[40] L. Palatinus, C.A. Corrêa, G. Steciuk, D. Jacob, P. Roussel, P. Boullay, M. Klementová, M. Gemmi, J. Kopeček, M.C. Domeneghetti, F. Cámara, V. Petříček, "Structure refinement using precession electron diffraction tomography and dynamical diffraction: tests on experimental data", *Acta Crystallogr. B Struct. Sci. Cryst. Eng. Mater* 71 (2015) 740–751. https://doi.org/10.1107/S2052520615017023.

[41] J.M. Zuo, J.C.H. Spence, "Automated structure factor refinement from convergent-beam patterns", *Ultramicroscopy* 35 (1991) 185–196. https://doi.org/10.1016/0304-3991(91)90071-D.

[42] L. Palatinus, P. Brázda, P. Boullay, O. Perez, M. Klementová, S. Petit, V. Eigner, M. Zaarour, S. Mintova, "Hydrogen positions in single nanocrystals revealed by electron diffraction", *Science* 355 (2017) 166–169. https://doi.org/10.1126/science.aak9652.

[43] J. Hynek, P. Brázda, J. Rohlíček, M.G.S. Londesborough, J. Demel, "Phosphinic Acid Based Linkers: Building Blocks in Metal–Organic Framework Chemistry", *Angew. Chem. Int. Ed.* 57 (2018) 5016–5019. https://doi.org/10.1002/anie.201800884.

[44] E. Mugnaioli, M. Gemmi, "Single-crystal analysis of nanodomains by electron diffraction tomography: mineralogy at the order-disorder borderline", *Z. Kristallogr. Cryst. Mater.* 233 (2018) 163–178. https://doi.org/10.1515/zkri-2017-2130.

[45] D. Marchetti, A. Pedrini, C. Massera, M.D. Faye Diouf, C. Jandl, G. Steinfeld, M. Gemmi, "3D electron diffraction analysis of a novel, mechanochemically synthesized supramolecular organic framework based on tetrakis-4-(4-pyridyl)phenylmethane", *Acta Crystallogr. B Struct. Sci. Cryst. Eng. Mater.* 79 (2023) 432–436. https://doi.org/10.1107/S2052520623007680.

[46] M. Klementová, M. Motlochová, J. Boháček, J. Kupčík, L. Palatinus, E. Pližingrová, L. Szatmáry, J. Šubrt, "Metatitanic Acid Pseudomorphs after Titanyl Sulfates: Nanostructured Sorbents and Precursors for Crystalline Titania with Desired Particle Size and Shape", *Crystal Growth & Design* 17 (2017) 6762–6769. https://doi.org/10.1021/acs.cgd.7b01349.

3 Introduction to Reticular Materials

Reticular chemistry is a field of chemistry dedicated to the synthesis and design of crystalline porous frameworks held together by relatively strong interactions. It is centred on the concept of linking together molecular building blocks with well-defined shapes through robust and directional bonds, resulting in 2D and 3D porous networks. [1] Metal-organic frameworks (MOFs) and covalent organic frameworks (COFs) are two well-known classes of reticular materials, in which their networks are held together by coordinative and covalent bonds, respectively. [2–4] The crystallization of such porous frameworks connected through strong directionals bonds, consists in one of the major challenges of this field. In COFs synthesis, the crystallization of extended lattices is hampered by the lack of reversibility of organic reactions (Figure 3.1). For this reason, the development of COFs experienced a relatively late beginning if compared to MOFs. [4,5]

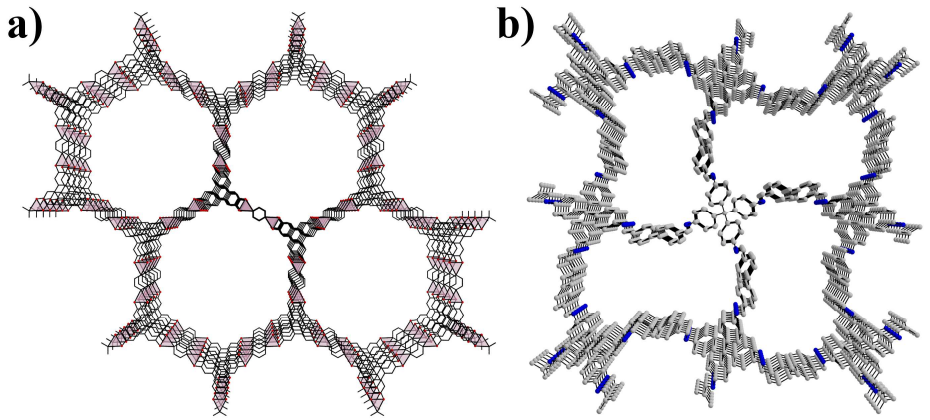

Figure 3.1: Crystal structure expansion of two well-known covalent organic frameworks: (a) COF-5; (b) COF-320. [4,6]

The formation of metal-organic lattices often occurs under a thermodynamic regime, which facilitates the synthesis of highly symmetric and extended architectures. However, it should be noted that the formation of extended frameworks under thermodynamic control favours the formation of dense crystals. [1] The achievement of metal-organic architectures with permanent porosity (Figure 3.2) was reached through the concept of combining shape-persistent organic linkers with inorganic secondary building units (SBUs). [2,3,7]

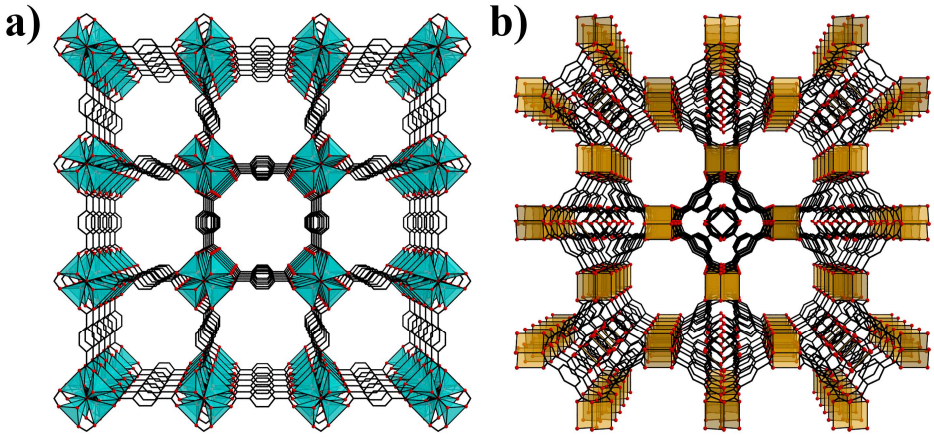

Figure 3.2: Crystal structure expansion of two commonly known metal-organic frameworks: (a) MOF-5; (b) HKUST-1. [8,9]

This has been fundamental in the advancement of reticular materials, which are characterized by extended surface area and tunable chemical and physical properties. In addition, the development of dedicated crystallisation methods, such as slow diffusion, layering, solvothermal and mechanochemical methods, has facilitated progress in this research area. [10–13] In addition, the advancements in the field of reticular materials opened up a wide range of potential applications, from gas storage and separation, to catalysis and sensing. [1,2,14–19] The chemical composition and shape of their building blocks can be varied in many ways, resulting in materials with unique

properties. This has made them the subject of extensive research and industrial applications. [20–22]

This thesis focuses on metal-organic materials with a brief excursion on porous supramolecular organic frameworks. The underlying theme of the discussion is their relatively rapid synthesis and their structural investigation. Most of the materials were obtained as nano- to micro-sized crystals. Therefore, the role of 3D electron diffraction as a single-crystal characterization method to elucidate their crystal structure will be also highlighted.

Bibliography:

[1] R. Freund, S. Canossa, S.M. Cohen, W. Yan, H. Deng, V. Guillerm, M. Eddaoudi, D.G. Madden, D. Fairen-Jimenez, H. Lyu, L.K. Macreadie, Z. Ji, Y. Zhang, B. Wang, F. Haase, C. Wöll, O. Zaremba, J. Andreo, S. Wuttke, C.S. Diercks, "25 Years of Reticular Chemistry", *Angew. Chem. Int. Ed.* 60 (2021) 23946–23974. https://doi.org/10.1002/anie.202101644.

[2] O.M. Yaghi, M. O'Keeffe, N.W. Ockwig, H.K. Chae, M. Eddaoudi, J. Kim, "Reticular synthesis and the design of new materials", *Nature* 423 (2003) 705–714. https://doi.org/10.1038/nature01650.

[3] H. Li, M. Eddaoudi, M. O'Keeffe, O.M. Yaghi, "Design and synthesis of an exceptionally stable and highly porous metal-organic framework", *Nature* 402 (1999) 276–279. https://doi.org/10.1038/46248.

[4] A.P. Côté, A.I. Benin, N.W. Ockwig, M. O'Keeffe, A.J. Matzger, O.M. Yaghi, "Porous, Crystalline, Covalent Organic Frameworks", *Science* 310 (2005) 1166–1170. https://doi.org/10.1126/science.1120411.

[5] C.S. Diercks, O.M. Yaghi, "The atom, the molecule, and the covalent organic framework", *Science* 355 (2017) eaal1585. https://doi.org/10.1126/science.aal1585.

[6] Y.-B. Zhang, J. Su, H. Furukawa, Y. Yun, F. Gándara, A. Duong, X. Zou, O.M. Yaghi, "Single-Crystal Structure of a Covalent Organic Framework", *J. Am. Chem. Soc.* 135 (2013) 16336–16339. https://doi.org/10.1021/ja409033p.

[7] H. Furukawa, K.E. Cordova, M. O'Keeffe, O.M. Yaghi, "The Chemistry and Applications of Metal-Organic Frameworks", *Science* 341 (2013) 1230444. https://doi.org/10.1126/science.1230444.

[8] S. Han, Y. Wei, C. Valente, I. Lagzi, J.J. Gassensmith, A. Coskun, J.F. Stoddart, B.A. Grzybowski, "Chromatography in a Single Metal−Organic Framework (MOF) Crystal", *J. Am. Chem. Soc.* 132 (2010) 16358–16361. https://doi.org/10.1021/ja1074322.

[9] Y. Wu, A. Kobayashi, G.J. Halder, V.K. Peterson, K.W. Chapman, N. Lock, P.D. Southon, C.J. Kepert, "Negative Thermal Expansion in the Metal–Organic Framework Material Cu_3(1,3,5-benzenetricarboxylate)$_2$", *Angew. Chem. Int. Ed.* 47 (2008) 8929–8932. https://doi.org/10.1002/anie.200803925.

[10] S.S.-Y. Chui, S.M.-F. Lo, J.P.H. Charmant, A.G. Orpen, I.D. Williams, "A Chemically Functionalizable Nanoporous Material $[Cu_3(TMA)_2(H_2O)_3]_n$", *Science* 283 (1999) 1148–1150. https://doi.org/10.1126/science.283.5405.1148.

[11] M. Kondo, T. Yoshitomi, H. Matsuzaka, S. Kitagawa, K. Seki, Three-Dimensional Framework with Channeling Cavities for Small Molecules: {[M_2(4, 4′-bpy)$_3$(NO_3)$_4$]·xH_2O}$_n$ (M = Co, Ni, Zn), *Angew. Chem. Int. Ed.* 36 (1997) 1725–1727. https://doi.org/10.1002/anie.199717251.

[12] T.M. Reineke, M. Eddaoudi, M. Fehr, D. Kelley, O.M. Yaghi, "From Condensed Lanthanide Coordination Solids to Microporous Frameworks Having Accessible Metal Sites", *J. Am. Chem. Soc.* 121 (1999) 1651–1657. https://doi.org/10.1021/ja983577d.

[13] S.L. James, C.J. Adams, C. Bolm, D. Braga, P. Collier, T. Friščić, F. Grepioni, K.D.M. Harris, G. Hyett, W. Jones, A. Krebs, J. Mack, L. Maini, A.G. Orpen, I.P. Parkin, W.C. Shearouse, J.W. Steed, D.C. Waddell, "Mechanochemistry: opportunities for new and cleaner synthesis", *Chem. Soc. Rev.* 41 (2012) 413–447. https://doi.org/10.1039/C1CS15171A.

[14] R.B. Getman, Y.-S. Bae, C.E. Wilmer, R.Q. Snurr, "Review and Analysis of Molecular Simulations of Methane, Hydrogen, and Acetylene Storage in Metal–Organic Frameworks", *Chem. Rev.* 112 (2012) 703–723. https://doi.org/10.1021/cr200217c.

[15] K. Sumida, D.L. Rogow, J.A. Mason, T.M. McDonald, E.D. Bloch, Z.R. Herm, T.-H. Bae, J.R. Long, "Carbon Dioxide Capture in Metal–Organic Frameworks", *Chem. Rev.* 112 (2012) 724–781. https://doi.org/10.1021/cr2003272.

[16] M.P. Suh, H.J. Park, T.K. Prasad, D.-W. Lim, "Hydrogen Storage in Metal–Organic Frameworks", *Chem. Rev.* 112 (2012) 782–835. https://doi.org/10.1021/cr200274s.

[17] H. Wu, Q. Gong, D.H. Olson, J. Li, "Commensurate Adsorption of Hydrocarbons and Alcohols in Microporous Metal Organic Frameworks", *Chem. Rev.* 112 (2012) 836–868. https://doi.org/10.1021/cr200216x.

[18] L.E. Kreno, K. Leong, O.K. Farha, M. Allendorf, R.P. Van Duyne, J.T. Hupp, "Metal–Organic Framework Materials as Chemical Sensors", *Chem. Rev.* 112 (2012) 1105–1125. https://doi.org/10.1021/cr200324t.

[19] P. Horcajada, R. Gref, T. Baati, P.K. Allan, G. Maurin, P. Couvreur, G. Férey, R.E. Morris, C. Serre, "Metal–Organic Frameworks in Biomedicine", *Chem. Rev.* 112 (2012) 1232–1268. https://doi.org/10.1021/cr200256v.

[20] H.-C. Zhou, J.R. Long, O.M. Yaghi, "Introduction to Metal–Organic Frameworks", *Chem. Rev.* 112 (2012) 673–674. https://doi.org/10.1021/cr300014x.

[21] U. Mueller, M. Schubert, F. Teich, H. Puetter, K. Schierle-Arndt, J. Pastré, "Metal–organic frameworks—prospective industrial applications", *J. Mater. Chem.* 16 (2006) 626–636. https://doi.org/10.1039/B511962F.

[22] M. Jacoby, "Heading to Market with MOFs: For Metal-Organic Frameworks, lab-scale research is brisk as commercialization begins", *Chem. Eng. News Archive* 86 (2008) 13–16. https://doi.org/10.1021/cen-v086n034.p013.

4 Combined Approach of Mechanochemistry and Electron Crystallography for the discovery of 1D and 2D Coordination Polymers

Mechanochemical synthesis is an attractive preparative method that combines a green approach with versatility, efficiency and rapidity qof reaction. However, it often yields microcrystalline materials whose structural elucidation with conventional single-crystal or powder X-ray diffraction methods is challenging or even impossible. This chapter presents the novel approach of combining mechanochemistry with electron diffraction techniques to elucidate the crystal structure of metal-organic compounds of zinc(II) and copper(II) with 2,6-pyridine dicarboxylic acid and 4,4'-bipyridine. These results have been published in D. Marchetti, F. Guagnini, A.E. Lanza, A. Pedrini, L. Righi, E. Dalcanale, M. Gemmi, and C. Massera. Combined Approach of Mechanochemistry and Electron Crystallography for the Discovery of 1D and 2D Coordination Polymers. Cryst. Growth Des. 2021, 12, 6660–6664.

https://doi.org/10.1021/acs.cgd.1c01058

4.1 Introduction

Mechanochemistry is emerging as a promising environmental-friendly strategy for the preparation of new organic and metal-organic materials in the form of molecular crystals, salts, cocrystals as well as polymeric and framework structures. [1–6] Mechanochemical reactions occur through the absorption of mechanical energy in the solid state. Indeed, this synthetic approach drastically reduces the use of solvents and the amount of excess reagents during the process. Furthermore, it potentially allows to achieve high conversion while minimizing energy consumption and chemical waste (Figure 4.1). [7] Mechanochemical synthesis can also promote the formation of products, polymorphs and topologies that differ from what is obtained with solution methods. [7,8] However, the structural characterization of such new materials is usually complicated by the small crystallite size and multiple twinning induced by the grinding process and the nucleation in almost solvent-free conditions. Conventional single-crystal X-ray diffraction (SC-XRD) on the crude product is therefore not applicable, and powder X-ray diffraction (PXRD) methods are the characterization of choice. Yet, structure solution from PXRD can be extremely challenging, especially in the case of large unit cells, low symmetry, severe peak broadening, low crystallinity and, not least, because of the difficulty of obtaining pure phases. [9]

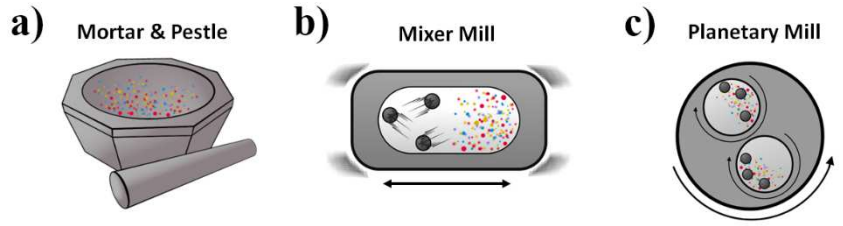

Figure 4.1: Schematic representation of grinding methods in mechanochemical synthesis. (a) Manual grinding conducted using mortar and pestle. (b) and (c) Automatic grinding performed with mixer and planetary mill.

A possible approach to overcome all these drawbacks is to use electron diffraction techniques, which enable the analysis of single nanocrystals, also when mixed phases are present in the sample. [10,11] Electron diffraction has lately experienced a huge development in terms of hardware, software and methodology. The original idea of adopting a data collection strategy similar to single crystal X-ray diffraction with area detectors[12] (usually known as 3D electron diffraction, 3D ED) has completely changed the perspective of electron diffraction as a structure solution technique. The integration of the reciprocal space obtained by collecting the patterns while the sample rotates around the goniometer axis delivers 3D ED intensities that, if treated with the standard kinematical diffraction theory, can be successfully used for structure solution. Nowadays 3D ED can be performed in a variety of ways (Figure 2.9), [13] being successful in the structure determination of a wide class of crystalline materials. [14] The specific development of low dose methods [15] combined with a novel type of very sensitive direct electron detectors [16] has recently allowed the effective application of 3D ED to soft, beam-sensitive nanoporous materials like metal-organic frameworks (MOFs),[17] covalent-organic frameworks (COFs) and supramolecular organic frameworks (SOFs), [18,19] zeolites, [20] active pharmaceutical ingredients (APIs), [21,22] and small molecules. [23–25] With these characteristics, 3D ED is the ideal tool to unlock the full potential of mechanochemistry for materials discovery. Therefore, we have applied this novel combined strategy for the synthesis and characterization of metal-organic compounds, featuring zinc(II) and copper(II) as metal centres and 2,6-pyridine dicarboxylic acid (**H_2PDC**) and 4,4'-bipyridine (**bipy**) as organic ligands. The chosen components have often been employed to synthesize discrete complexes, coordination polymers or metal-organic frameworks, and are therefore ideal benchmark systems. A search using the Cambridge Structural Database (Version 5.42, February 2021) [26] for metal complexes of **PDC^{2-}** yielded 2185 hits, of which 95 include zinc and 319 copper. In most cases, **PDC^{2-}** behaves

as a tridentate, chelating ligand forming discrete complexes, but each of its carboxylate moieties can act as a bidentate bridging group to yield coordination polymers in one and (more rarely) two dimensions (see Scheme 4.1). [27–32]

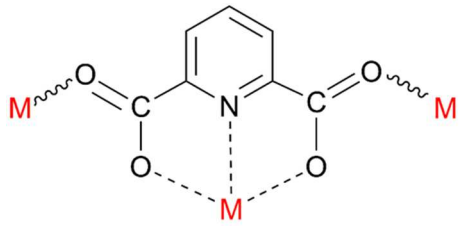

Scheme 4.1: View of the possible coordination modes of PDC^{2-} (chelating and bridging).

Moreover, to obtain structures with increased complexity, carboxylates can be assisted by N-containing auxiliary ligands (such as the **bipy** used in this work) which can act as pillars connecting metal nodes, thus promoting the formation of polymers in two or three dimensions. Indeed, these extended structures (namely coordination polymers and MOFs) are attractive materials whose properties can be tuned by an accurate choice of their inorganic and organic components and that can find application in several fields, like gas adsorption and storage, sensing and catalysis. [33]

4.2 Results and Discussion

4.2.1 Zinc-based pyridine dicarboxylate materials

Initially, **H_2PDC** and zinc nitrate hexahydrate were grounded in a mixer mill, in the presence of absolute ethanol and 33% aqueous ammonia. The product resulted in a colourless microcrystalline solid, whose X-ray powder pattern did not match that of any other existing phase. Since the crude product was moderately soluble in ethanol, an attempt of using the grinded powder as crystallization seed [34] afforded single crystals suitable for X-ray diffraction analysis, which turned out to be the new 1D coordination polymer $\{[Zn(\mathbf{PDC})(H_2O)]0.5H_2O\}_n$ (**1**, Figure 4.2). A comparison between the experimental and calculated PXRD patterns of **1** confirmed that, in this case, the structure obtained from SC-XRD analysis coincides with that of the bulk phase synthesized from the mechanochemical reaction (Figure 4.3).

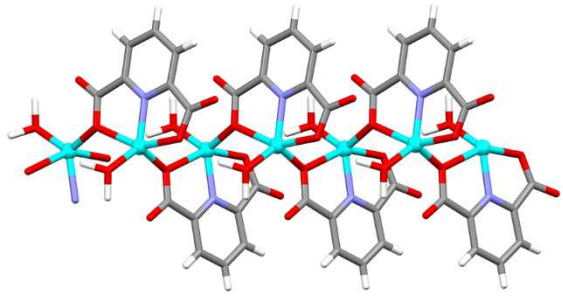

Figure 4.2: Polymeric structure of **1** along the *b*-axis direction. Zn^{2+} cations are represented as cyan spheres. Lattice water molecules have been omitted for clarity.

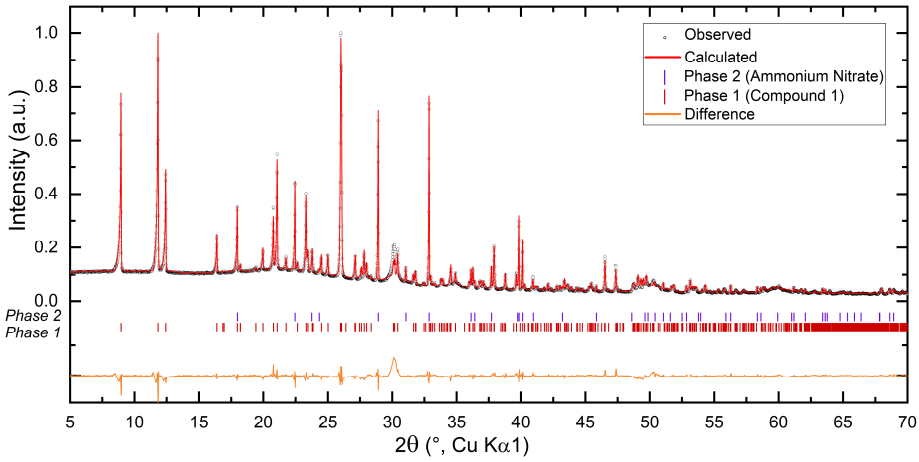

Figure 4.3: Profile fit from Rietveld refinement of **1** (the structural model was obtained by SC-XRD). The reaction crude also contains ammonium nitrate in its crystalline form (ICSD 28069). The shown range is limited to 2θ values of 5–70° for clarity, whereas the Rietveld refinement was carried out in the range 5–94°. The refinement converged to Rwp = 5.32%, RF(obs) = 8.67%, RF2(obs) = 9.11%.

In **1**, the zinc cation shows a trigonal bipyramidal coordination geometry; each metal cation coordinates one deprotonated **PDC^{2-}**, which acts as a tridentate chelating ligand through two oxygen atoms of the carboxylic groups and the pyridinic nitrogen atom, forming two 5-members condensed chelation rings. The fourth coordination position is occupied by one oxygen from an adjacent **PDC^{2-}** ligand, which bridges two zinc centres, thus prompting polymerization along the *b*-axis direction. The coordination sphere is completed by a water molecule. In the crystal structure, the polymeric chains are connected by an H-bonded network, also involving the lattice solvent (see Table S4.3).

To increase the dimensionality of **1**, a mechanochemical synthesis involving **H$_2$PDC**, $Zn(NO_3)_2 \cdot 6H_2O$ and **bipy** as pillar ligand was carried out, yielding again a microcrystalline colourless solid with a distinct XRPD profile. The crude product was insoluble in most common organic solvents, preventing the use of the seeding technique employed to obtain single crystals of **1**.

The nanocrystalline powder was therefore analysed through 3D ED (Figure 4.4, Figure 4.5). Diffraction data were collected in NED mode by the continuous rotation 3D ED protocol, using a parallel electron nano-beam of about 150 nm (see the Supplementary Information section for details). This modality minimizes the electron dose on the sample which could therefore stand the entire diffraction experiment without being amorphized. The collected data were subsequently processed using Pets2 and Jana2006,[35,36] while the structural model was obtained by direct methods and kinematically refined using SHELXL-2014 (see SI Section).[37]

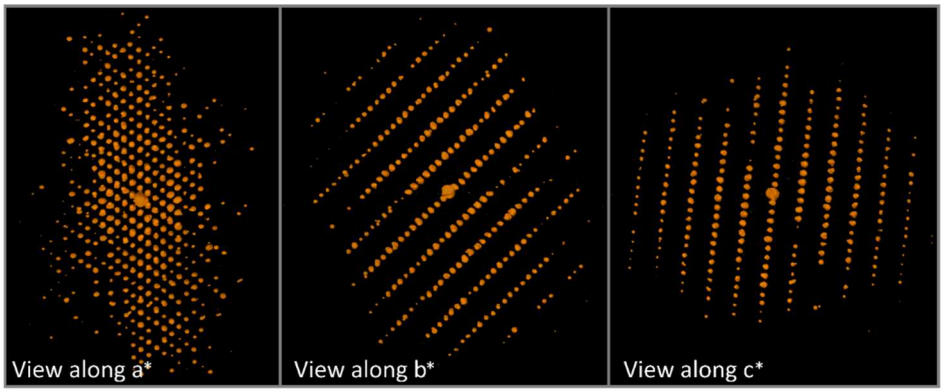

Figure 4.4: 3D reconstruction of the reciprocal lattice, calculated from 3D ED data, of compound **2**.

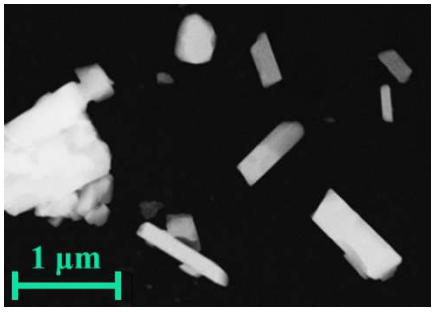

Figure 4.5: STEM-image of the microcrystals of **2** used for the 3D ED data collection.

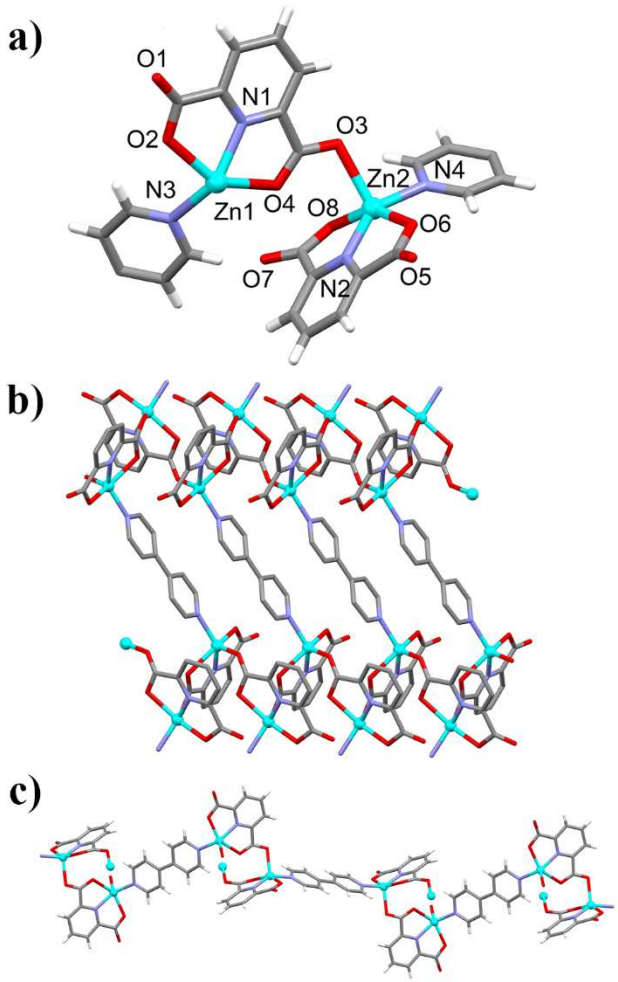

Figure 4.6: (a) Asymmetric unit of **2** with partial labelling scheme; (b) perspective view of two $[Zn_2(\mathbf{PDC})_2]_n$ polymeric chains connected through **bipy** ligands; (c) Detail of the polymeric chain along the unit cell diagonal.

The structure of the new compound consists of a 2D coordination polymer of formula $\{[Zn_2(\mathbf{PDC})_2(\mathbf{bipy})]\}_n$ (**2**) (Figure 4.6). As already observed for **1**, **H_2PDC** is fully deprotonated and acts as a tridentate chelating ligand forming two 5-member condensed rings and occupying three equatorial positions in the distorted squared-base pyramid around the metal centre. The zinc also coordinates an oxygen atom from a bridging carboxylate occupying the apical site of the pyramid, while the fourth equatorial position is occupied by the

nitrogen atom of the ligand **bipy** that substitutes the water molecule present in **1**. The result is that two independent zinc cations (Zn1 and Zn2) are bridged by a carboxylic moiety, thus creating zig-zag $[Zn_2(\mathbf{PDC})_2]_n$ polymeric chains (Figure 4.6b). In addition to this, **bipy** pillars connect $[Zn_2(\mathbf{PDC})_2]_2$ dimers along the unit cell diagonal (Figure 4.6b-c), giving rise to a bi-dimensional structure parallel to the $(0\bar{1}1)$ plane. The stacking of these corrugated planes leaves open channels running parallel to the *a*-axis direction (Figure 4.7a) accounting for ≈ 21% of the unit cell volume (as calculated by the program PLATON [38] with a probe radius of 1.2 A).

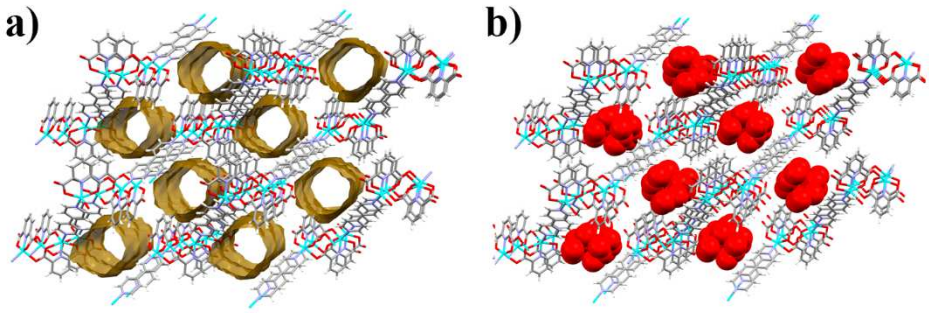

Figure 4.7: Structural model of **2** obtained by 3D ED (a) and Rietveld refinement (b), respectively. Channels are represented as yellow cylinders while water oxygen atom as CPK models.

At ambient conditions, the channels probably contain guest water molecules that could not be detected from 3D ED data, as they are likely removed by the high vacuum in the TEM column (~10^{-10} bar). The discrepancies in low theta intensities, between the calculated and experimental PXRD pattern, confirm the presence of absorbed molecules (Figure 4.8). The Rietveld refinement on PXRD data was the method adopted to assess the atomic coordinates of guest molecules. Such refinement was performed starting from the atomic coordinates obtained by the single-crystal 3D ED model. A Fourier difference map was employed to find the occupied regions and the guests were identified as heavily disordered water molecules, for which

it was not possible to determine a precise occupancy. Moreover, the structural model thus refined comprises the same polymeric backbone obtained by 3D ED analysis (Figure 4.7 and Figure 4.9).

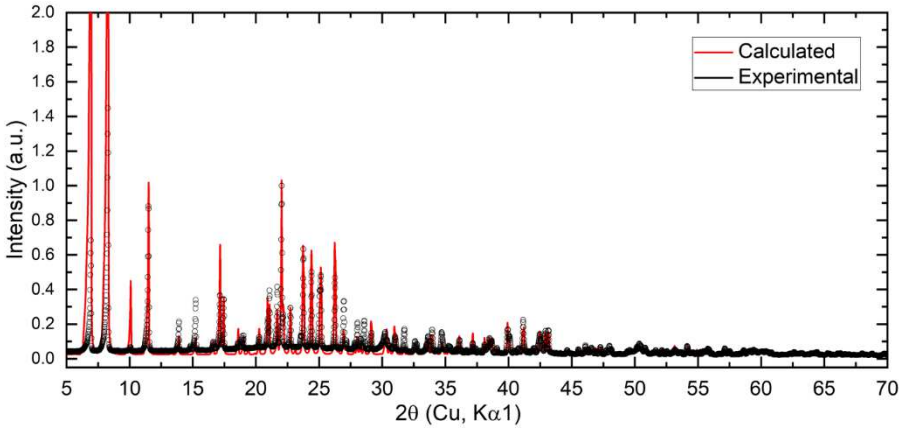

Figure 4.8: Comparison between the PXRD profile calculated from the 3D ED model, in which the solvent is not present, and the experimental pattern collected on the mechanochemical product **2**. The scale factor for the calculated pattern was determined in the range 10-70 deg.

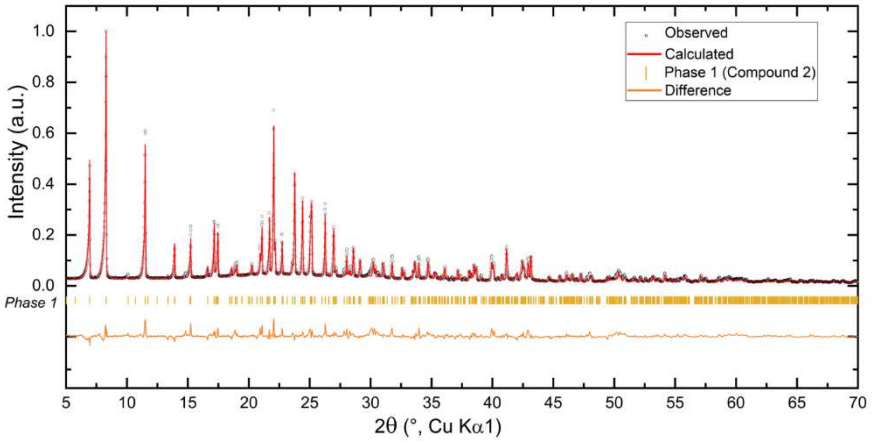

Figure 4.9: Profile fit from Rietveld refinement of **2** conducted starting from the structural model obtained by 3D ED. The shown range is limited to 2θ values of 5–70° for clarity, whereas the Rietveld refinement was carried out in the range 5–94°. The refinement converged to Rwp = 9.51%, RF(obs) = 13.51%, wRF(obs) = 13.26%.

It is interesting to note that even if **1** and **2** present different coordination geometries, the two polymers show a similar concatenation of **PDC**$^{2-}$ ligands. The carboxylic group bridges the metal ions with only one (O2) or both (O3 and O4) oxygen atoms in **1** and **2**, respectively (Figure 4.10).

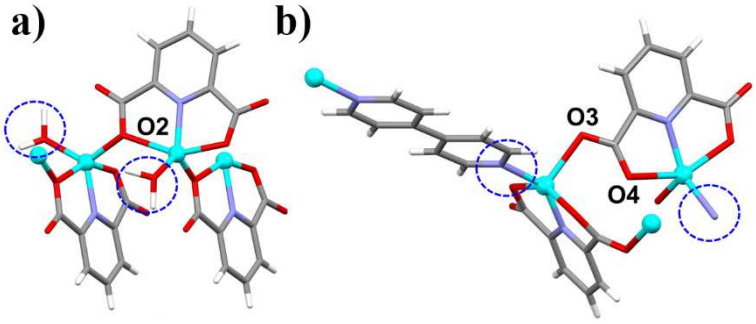

Figure 4.10: Comparison between the coordination sphere of zinc in **1** and **2**. In **1**, the oxygen atom O2 bridges two metal centres, while in **2** both O3 and O4 from the same carboxylic unit connect two different zinc cations. The dotted blue circles highlight the different ligands (water and bipy) in **1** and **2**, respectively.

The biggest difference is that the fifth ligand completing the coordination sphere is a water molecule in **1** and the nitrogen atom of a **bipy** unit in **2**. If the chain comprising Zn^{2+} ions and **PDC**$^{2-}$ ligands is represented as a helix, it is evident how both the water and the **bipy** ligand are protruding from the helix in the same direction (Figure 4.11, Figure S4.2). The presence of **bipy** instead of water increases the dimensionality of the polymeric network from 1D to 2D, creating a potentially porous structure.

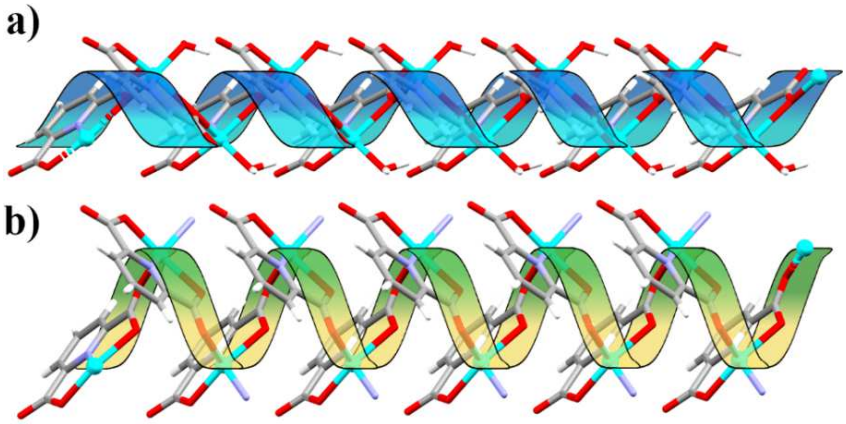

Figure 4.11: Comparison of the polymeric chains formed by zinc(II) and 2,6-pyridinedicarboxylate: $[Zn(\mathbf{PDC})]_n$ in **1** (a, blue helix) and $[Zn_2(\mathbf{PDC})_2]_n$ in **2** (b, green helix). Both the water molecule in **1** and the nitrogen atom belonging to bipyridine in **2** protrude from the helix.

4.2.2 Copper(II)-based pyridine dicarboxylate compounds

The same set of mechanochemical reactions were performed using Cu(II) as metal centre instead of Zn(II). Griding **H_2PDC** and copper nitrate hydrate yielded a blue microcrystalline solid that was identified through PXRD analysis as the mononuclear complex $[Cu(\mathbf{PDC})(H_2O)_2]$ (**3**, Figure 4.12a, Figure 4.13).[39] In contrast to what was observed with zinc, no coordination polymer was obtained, even when different grinding conditions (changing solvent/frequency/time) were employed.

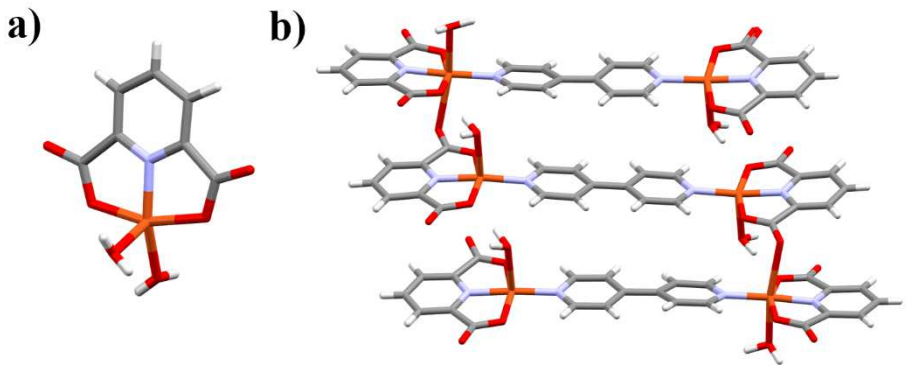

Figure 4.12: Molecular structure of **3** (a) and **4** (b). Lattice water molecules are not shown for clarity.

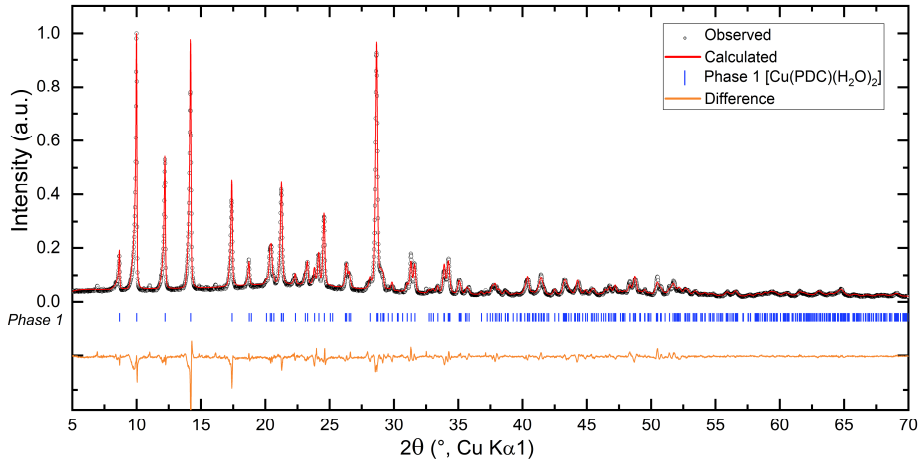

Figure 4.13: Profile fit from Rietveld refinement of **3** conducted starting from the structural model of [Cu(**PDC**)(H_2O)$_2$],(ECAFIX04, CCDC 641317). The shown range is limited to 2θ values of 5–70° for clarity, whereas the Rietveld refinement was carried out in the range 5–94°. The refinement converged to Rwp = 7.79%, RF(obs) = 2.73%, wRF(obs) = 3.34%.

Mixing **H_2PDC**, copper nitrate hydrate and **bipy** in a mixer mill in presence of ammonia and ethanol, yielded a blue microcrystalline solid. The PXRD pattern of the crude product revealed the presence of ammonium nitrate plus an unknown phase. In an attempt to recrystallize the crude product, blue single crystals were grown from ethanol, which turned out to be the hexameric complex [Cu_6(**PDC**)$_6$(**bipy**)$_3$(H_2O)$_6$] (**4**, Figure 4.12b). [40] In this case, bipyridine contributes to producing an oligomer connecting metal-organic nodes formed by copper and **PDC^{2-}** ligands. Interestingly, the calculated PXRD pattern of this complex was different from that of the bulk product synthesized mechanochemically, and further solid-state analysis was therefore needed to elucidate the structure of the unknown phase. While the analysis of the PXRD pattern was hindered by the ammonium nitrate byproduct, 3D ED allowed to collect diffraction datasets selectively from single nanocrystals of the unknown phase. Following the procedure used for compound **2**, nanometric crystals of the crude product (Figure 4.15) were characterized by continuous rotation ED technique (Figure 4.14).

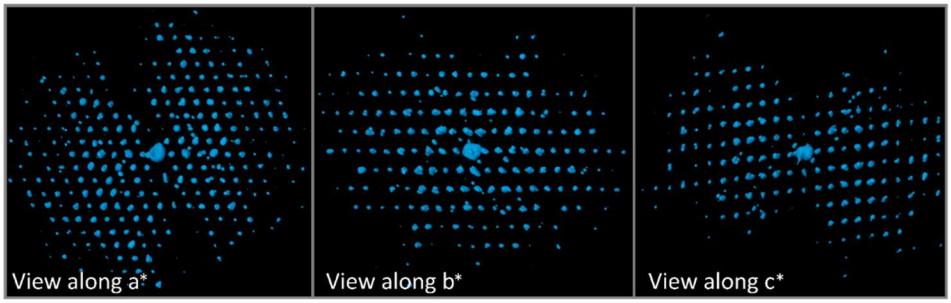

Figure 4.14: 3D reconstruction of the reciprocal lattice, calculated from 3D ED data, of compound **5**.

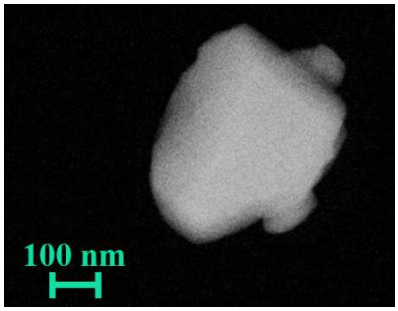

Figure 4.15: STEM-image of the microcrystals of **2** used for the 3D ED data collection.

The structure of this novel compound was then solved *ab-initio* by direct methods in space group *P*-1. The 3D ED model thus obtained was initially refined by a least-squares procedure against 3D ED data and subsequently refined with a Rietveld approach on the XRPD data (Figure 4.17). In this way, the structure of the novel dimeric complex $[Cu_2(\mathbf{HPDC})_2(\mathbf{bipy})(NO_3)_2]\cdot 2H_2O$ (**5**) was elucidated (Figure 4.16).

The dimer is centrosymmetric, and its asymmetric unit consists of a mono-deprotonated **HPDC**$^-$ fragment, (behaving as usual as tridentate ligand), half a **bipy** moiety, one coordinated nitrate anion and one lattice water molecule. The geometry around the metal centre is square pyramidal, with the nitrate occupying the apical position and **bipy** acting as bridge between two $[Cu(\mathbf{HPDC})(NO_3)]\cdot$nodes.

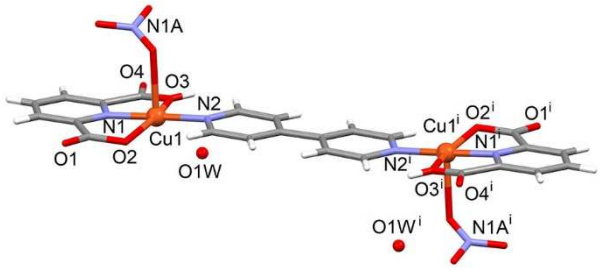

Figure 4.16: Perspective view of **5** with partial labelling scheme. Symmetry code i: -x, 1-y, 2-z.

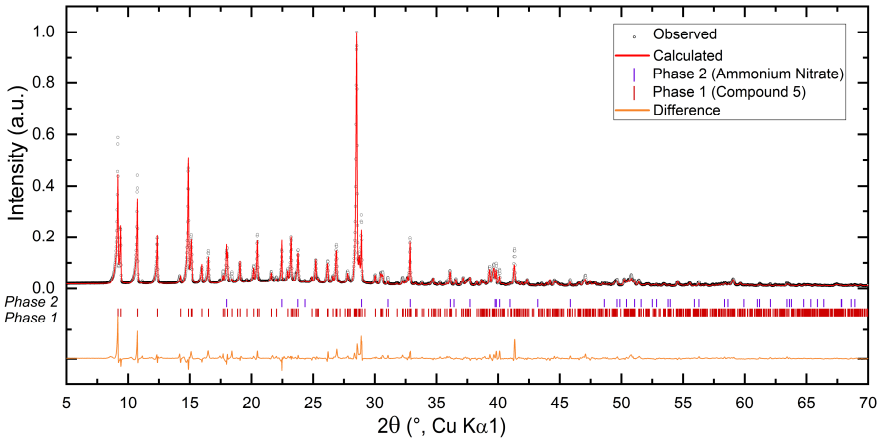

Figure 4.17: Profile fit from Rietveld refinement of **5** starting with the structural model obtained by 3D ED. The reaction crude also contains a crystalline phase of ammonium nitrate (ICSD 28069). The shown range is limited to 2θ values of 5–70° for clarity, whereas the Rietveld refinement was carried out in the range 5–95°. The refinement converged to Rwp = 10.02%, RF(obs) = 12.47%, wRF(obs) = 13.58%.

4.3 Conclusions

In this chapter, was shown how the most recent developments in electron crystallography allow successful structure determination of mechanochemically synthesized metal-organic materials. Under the same reaction conditions, zinc nitrate tend to form coordination polymers, while its copper analogue preferentially yields discrete complexes of different nuclearity. In particular, when zinc was employed, a 1D coordination polymer could be expanded by the incorporation of bipyridine in the mechanochemical synthesis, obtaining a product with higher dimensional topology and a potentially porous structure. In the case of copper, not only mechanochemistry proved to be a fast and efficient alternative to traditional solution methods for the synthesis of a mononuclear complex, but it also enabled the formation of a novel dimeric complex, halting the deprotonation of **H_2PDC** to the first step. Noteworthy, 3D ED analysis was fundamental in elucidating the crystal structure of as-synthesized products, which could not have been determined otherwise. Moreover, the crystal structures from kinematical refinement resulted perfectly suitable for additional refinement against PXRD data. This highlight how the structural information of few nanocrystals could be translated to the bulk product.

4.4 Supplementary information

4.4.1 Synthetic procedures

All commercial reagents and solvents were used as received. 2,6-pyridine dicarboxylic acid, $Zn(NO_3)_2 \cdot 6H_2O$, $CuSO_4 \cdot 5H_2O$, $Cu(NO)_3 \cdot 2.5H_2O$ and $Cu(NO)_3 \cdot 3H_2O$ were purchased from Sigma Aldrich, with the exception of 4,4'-bipyridine that was purchased from TCI Europe. The mechanochemical reactions were conducted with the addition of a small amount of liquid, a synthetic approach called "Liquid Assisted Grinding" (LAG). The amount of liquid added to the reaction mixture and the total mass of the solid fraction are related to the parameter η. [41]

$$\eta = \frac{W(mg)}{V(\mu L)} \tag{4.1}$$

where W corresponds to the reagents total mass and V to the liquid additive volume.

Mechanosynthesis of $\{[Zn(PDC)(H_2O)]0.5H_2O\}_n$, 1

H_2PDC (33.8 mg, 0.20 mmol), $Zn(NO_3)_2 \cdot 6H_2O$ (61.3 mg, 0.21 mmol), absolute ethanol (20 μl) and NH_3 33% (51.4 μL) were placed in a 14 mL zirconia jar with two 7 mm zirconia balls. The mixture was ground using an IST400 mixer mill operating at 30 Hz for 30 min ($\eta = 0.75$). The grinding crude was left in an open container to evaporate the remaining traces of LAG additive.

Mechanosynthesis of $\{[Zn_2(PDC)_2(bipy)]\}_n$, 2

H_2PDC (81.9 mg, 0.49 mmol), 4,4'-bipyridine (37.3 mg, 0.24 mmol), $Zn(NO_3)_2 \cdot 6H_2O$ (137.6 mg, 0.46 mmol), absolute ethanol (65 μl) and NH_3 33% (110 μL) were placed in a 14 mL zirconia jar with two 7 mm zirconia balls. The mixture was ground using an IST400 mixer mill operating at 30 Hz for 30 min ($\eta = 0.68$). The grinding crude was left in an open container to evaporate the remaining traces of LAG additive.

Mechanosynthesis of $[Cu(PDC)(H_2O)_2]$, 3

H_2PDC (40.2 mg, 0.24 mmol), $Cu(NO_3)_2 \cdot 2.5H_2O$ (57.9 mg, 0.25 mmol), absolute ethanol (11.6 µl) and NH_3 33% (58.4 µL) were placed in a 14 mL zirconia jar with two 7 mm zirconia ball. The mixture was ground using an IST400 mixer mill operating at 30 Hz for 30 min ($\eta = 0.725$). The grinding crude was left in an open container to evaporate the remaining traces of LAG additive.

Crystallization of $[Cu_6(PDC)_6(bipy)_3(H_2O)_6] \cdot 6H_2O$, 4.

$[Cu(PDC)(H_2O)_2]$ (~ 3 mg) was placed in a 2 mL glass vial with 1 mL of EtOH abs. The reaction mixture was sonicated for about 2 minutes, in order to suspend the solid, and it was left to slowly evaporate. Small blue single crystals were collected after 15 days.

Mechanosynthesis of $[Cu_2(HPDC)_2(bipy)(NO_3)_2] \cdot 2H_2O$, 5

H_2PDC (33.8 mg, 0.20 mmol), $Cu(NO_3)_2 \cdot 2.5H_2O$ (48.8 mg, 0.21 mmol), 4,4'-bipyridine (16.1 mg, 0.10 mmol), absolute ethanol (21 ml) and NH_3 33% (49 mL) were placed in a 14 mL zirconia jar with two 7 mm zirconia ball. The mixture was ground using an IST400 mixer mill operating at 30 Hz for 30 min ($h = 0.71$). The grinding crude was left in an open container to evaporate the remaining traces of LAG additive.

4.4.2 3D Electron diffraction (3D ED)

Scanning transmission electron microscopy imaging and 3D electron diffraction were carried out on a Zeiss Libra 120 transmission electron microscope, equipped with a LaB_6 source operating at 120 kV (λ=0.0335 Å) and a Timepix single-electron detector by ASI for collecting diffraction in low dose mode. 3D electron diffraction data were collected on single nanocrystals illuminated with a parallel electron beam of 150 nm in diameter. The diffraction patterns where recorded while continuously rotating the crystal around the goniometer axis (continuous rotation mode), obtaining a continuous scan of the reciprocal space up to 120° with an angular integration (performed by the detector) of 0.57° per frame. Due to goniometer instabilities and to the small dimensions of the crystalline grains an entire data collection was composed by some (usually 4) runs of 30-40° each, collected on the same crystal, that were stitched together to maximize the reciprocal space coverage.

Imaging was carried out in STEM mode with a high angular dark field detector (HAADF). The total electron dose was of 2 electron/$Å^2$ for compound **2** and 5.5 electron/$Å^2$ for compound **5**.

The 3D ED data were analysed using the software PETS.[36] Ab-initio structure determination of **2** was performed by standard direct methods (SDM) implemented in the software SHELXT,[42] while **5** was solved by SDM using the SIR2019 package.[43] Data were treated with a fully kinematical approximation, i.e. neglecting dynamical scattering and assuming that I_{hkl} is proportional to $|F_{hkl}|^2$. Least-squares structure refinement was performed with the software SHELXL-2014 [37] interfaced with ShelXle.[44] Crystallographic data for **2** and **5** have been deposited with the Cambridge Crystallographic Data Centre as supplementary publication no. CCDC-2091277 and 2091280.

Table S4.1: Crystallographic data for **2** and **5**.

	2	**5**
Formula	$Zn_2C_{24}H_{34}N_4O_{18}$	$C_{24}H_{20}N_6O_{16}Cu_2$
Formula weight	797.3	775.5
Crystal system	Triclinic	Triclinic
Space group	*P*-1	*P*-1
a/Å	5.2227(1)	7.2743(1)
b/Å	15.8213(3)	10.0186(2)
c/Å	17.9781(4)	10.3652(3)
α/°	78.655(2)	69.932(2)
β/°	81.623(3)	79.590(2)
γ/°	80.529(3)	83.429(2)
V/Å^3	1426.77(5)	696.863
Z	2	1
D_c/g cm^{-3}	1.856	1.848
F(000)	780	392
μ/mm^{-1}	2.926	2.665
$\vartheta_{min,max}$/°	2.5, 47.0	2.5, 47.0
Reflections collected	2597	1241
R [Fo>4σ(Fo)][a], wR_2[a]	0.1351, 0.1326	0.1247, 0.1358

[a] $R_1 = \Sigma||F_o|-|F_c||/\Sigma|F_o|$, $wR_2 = [\Sigma[w(F_o^2\ F_c^2)^2]/\Sigma[w(F_o^2)^2]]^{1/2}$.

4.4.3 Powder X-ray diffraction (PXRD)

The samples were packed in a 0.3 mm borosilicate glass capillary and the high-resolution PXRD patterns were collected in the 2θ range 5–94° using Cu Kα1 radiation (λ=1.5406 Å) on a STOE Stadi P equipped with a Ge(111) Johansson focussing monochromator from STOE & Cie and a Mythen2 1K detector from Dectris. Data were preliminarily processed with WinXPOW (by STOE & Cie).

The Rietveld refinement from powder X-ray diffraction was carried out with Jana2006. [35] The background was described by manually picked and fixed points. Profile parameters were first obtained by LeBail fitting on the diffraction pattern of the sample and then kept fixed. For **1**, the Rietveld refinement was performed for comparison purposes using the refined structural model obtained by SC-XRD (Figure 4.3); the scale factor was the only refined parameter. The refinement converged to Rwp = 5.32%, RF(obs) = 8.67%, RF(obs) = 9.11%. The Rietveld refinement of compound **2** (Figure 4.9) was performed starting from the atomic coordinates obtained by the single-crystal 3D ED model. Since the 3D ED model does not present guest molecules inside the pores, a Fourier difference map was the method adopted to find the occupied regions and the guests were identified as heavily disordered water molecules, for which it was not possible to determine a precise occupancy. The ligand molecules were refined as semi-rigid bodies, in which the torsion angles related to single bonds were freely refined. The refinement converged to Rwp = 9.51%, RF(obs) = 13.51%, wRF(obs) = 13.26%. Rietveld refinement on the phase [Cu(**PDC**)(H_2O)$_2$] (**3**, Figure 4.13) was performed for comparison purposes on the refined model deposited in the CSD (ECAFIX04, CCDC 641317); the unit cell and the scale factor were the only refined parameters. The refinement converged to Rwp = 7.79%, RF(obs) = 2.73%, wRF(obs) = 3.34%. Compound **5** (Figure 4.17) was refined from a biphasic mixture in which the second phase was ammonium nitrate. As in the case of compound

2, the Rietveld refinement of **5** was performed considering the ligand molecules as semi-rigid bodies. Furthermore, for the ammonium nitrate phase, only the unit cell and the profile parameters were refined. The refinement converged to Rwp = 10.02%, RF(obs) = 12.47%, wRF(obs) = 13.58%. Crystal data and experimental details for data collection and structure refinement are reported in Table S1. Crystallographic data for **2** and **5** have been deposited with the Cambridge Crystallographic Data Centre as supplementary publication no. CCDC- 2091276 and 2091279.

4.4.4 Single-crystal X-ray diffraction

The crystal structures of **1** and **4** were determined by X-ray diffraction on single crystals. Crystal data and experimental details for data collection and structure refinement are reported in Table S4.2. Intensity data and cell parameters were recorded at 190(2) K on a Bruker Apex II diffractometer equipped with a CCD area detector, using MoKα radiation (λ = 0.71073 Å) for **1** and on a Bruker D8 Venture PhotonII diffractometer (CuKα radiation λ = 1.54178 Å) for **4**. The raw frame data were processed using SAINT and SADABS to yield the reflection data files. [45,46] The structures were solved by Direct Methods using the SIR2019 program [43] and refined on F_o^2 by full-matrix least-squares procedures, using SHELXL-2018 [37] in the WinGX suite v.2014.1.[47] All non-hydrogen atoms were refined with anisotropic atomic displacements. The aromatic hydrogen atoms were included in the refinement at idealized geometry (C–H 0.93/0.95 Å) and refined "riding" on the corresponding parent atoms with U_{iso}(H) set to 1.2U_{eq}(C). The H atoms of the water molecules were found in the difference Fourier map and refined freely. The weighting schemes used in the last cycle of refinement were $w = 1/[\sigma^2 F_o^2 + (0.0372P)^2 + 4.5618P]$ and $w = 1/[\sigma^2 F_o^2 + (0.0793P)^2 + 2.1833P]$ where $P = (F_o^2 + 2F_c^2)/3$, for **1** and **4**, respectively. Crystallographic data for

1 and **4** have been deposited with the Cambridge Crystallographic Data Centre as supplementary publication no. CCDC- 2091275 and 2091278.

Table S4.2: Crystallographic data for **1** and **4.**

	1	**4**
Formula	$C_7H_6NO_{5.5}Zn$	$C_{72}H_{66}N_{12}O_{36}Cu_6$
Formula weight	257.50	2056.61
Crystal system	Monoclinic	Triclinic
Space group	*C*2/c	*P*-1
a/Å	21.600(6)	10.6460(3)
b/Å	5.658(2)	10.7251(3)
c/Å	15.754(4)	18.6922(4)
α/°	90	84.234(1)
β/°	115.009(4)	86.721(1)
γ/°	90	62.883(1)
V/Å^3	1744.8(9)	1889.89(9)
Z	8	1
D_c/g cm^{-3}	1.960	1.807
F(000)	1032	1044
μ/mm^{-1}	2.816	2.770
$\vartheta_{min,max}$/°	2.081, 28.391	2.38, 72.39
Reflections collected	11498	6286
Independent reflections	2177 (*R*int = 0.0419)	43871 (*R*int = 0.0321)
Observed reflections	1852	1852
Data/restr./param.	2177 / 0 / 144	7225 / 0 / 588
S[a]	1.003	1.001
R [Fo>4σ(Fo)][b], w*R*$_2$[b]	0.0326, 0.0745	0.0392, 0.1117
$\Delta\rho_{min,max}$/e Å^{-3}	0.614, -0.610	1,211, -0.890

[a]Goodness-of-fit S = $[\Sigma w(F_o^2-F_c^2)^2/ (n-p)]1/2$, where n is the number of reflections and p the number of parameters. [b]$R_1 = \Sigma||F_o|-|F_c||/\Sigma|F_o|$, $wR_2 = [\Sigma[w(F_o^2\ F_c^2)^2]/\Sigma[w(F_o^2)^2]]^{1/2}$.

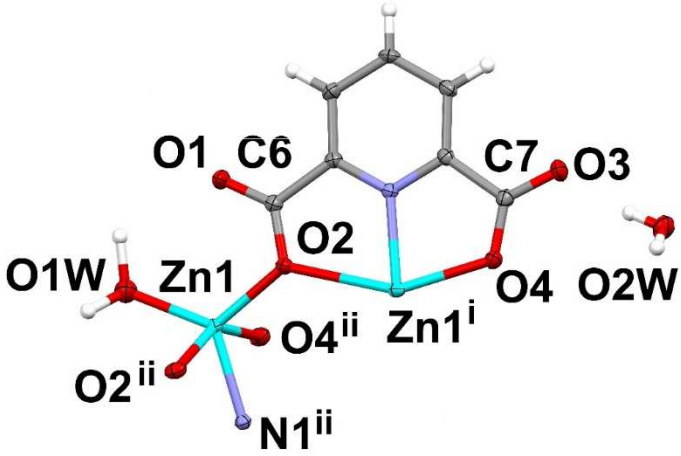

Figure S4.1: Ortep view of **1** with partial labelling scheme. Symmetry code: i = 3/2-x, 1/2+y, 3/2-z; ii = 3/2-x, -1/2+y, 3/2-z.

Table S4.3: Geometrical parameters (Å, °) of the H-bond interactions in **1**.

Donor-H	Donor···Acceptor	H···Acceptor	Donor-H···Acceptor
O2W-H3W 0.785(9)	O2W···O3 2.759(3)	H3W···O3 1.992(9)	O12W-H3W···O3 165.4(9)
O1W-H1W 1.121(9)	O1W···O1iii 3.176(3)	H2W···O1iii 2.148(9)	O1W-H1W···O1iii 150.1(9)
O1W-H2W 1.078(9)	O1W···O4iv 3.017(3)	H2W···O4iv 2.020(9)	O1W-H2W···O4iv 152.5(9)

iii: 3/2-x,-1/2-y,1-z ; iv: 3/2-x, -3/2+y, 3/2-z.

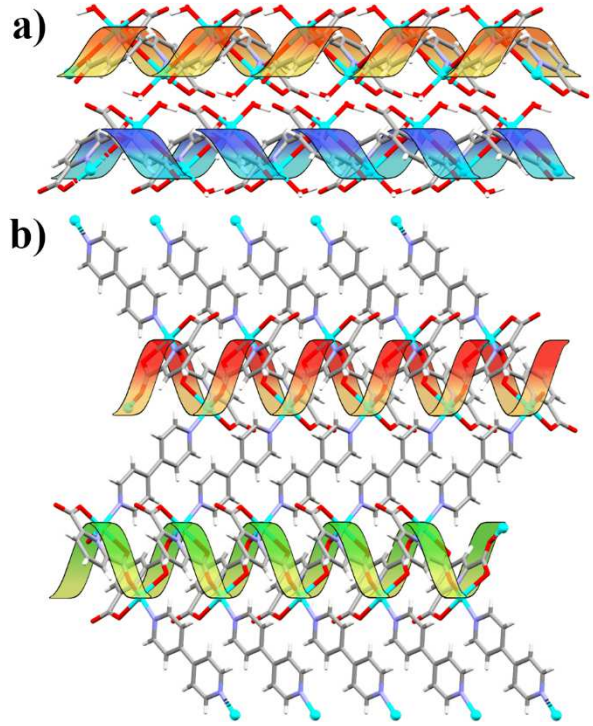

Figure S4.2: Comparison of the interactions between right- and left-handed helices constituted by Zn-**PDC** chains in **1** (a) and **2** (b).

Bibliography:

[1] S.L. James, C.J. Adams, C. Bolm, D. Braga, P. Collier, T. Friščić, F. Grepioni, K.D.M. Harris, G. Hyett, W. Jones, A. Krebs, J. Mack, L. Maini, A.G. Orpen, I.P. Parkin, W.C. Shearouse, J.W. Steed, D.C. Waddell, "Mechanochemistry: opportunities for new and cleaner synthesis", *Chem. Soc. Rev.* 41 (2012) 413–447. https://doi.org/10.1039/C1CS15171A.

[2] L. Takacs, "The historical development of mechanochemistry", *Chem. Soc. Rev.* 42 (2013) 7649. https://doi.org/10.1039/c2cs35442j.

[3] J.L. Howard, Q. Cao, D.L. Browne, "Mechanochemistry as an emerging tool for molecular synthesis: what can it offer?", *Chem. Sci.* 9 (2018) 3080–3094. https://doi.org/10.1039/C7SC05371A.

[4] J. Andersen, J. Mack, "Mechanochemistry and organic synthesis: from mystical to practical", *Green Chem.* 20 (2018) 1435–1443. https://doi.org/10.1039/C7GC03797J.

[5] M. Leonardi, M. Villacampa, J.C. Menéndez, "Multicomponent mechanochemical synthesis", *Chem. Sci.* 9 (2018) 2042–2064. https://doi.org/10.1039/C7SC05370C.

[6] S. Mateti, M. Mathesh, Z. Liu, T. Tao, T. Ramireddy, A.M. Glushenkov, W. Yang, Y.I. Chen, "Mechanochemistry: A force in disguise and conditional effects towards chemical reactions", *Chem. Commun.* 57 (2021) 1080–1092. https://doi.org/10.1039/D0CC06581A.

[7] T. Friščić, C. Mottillo, H.M. Titi, "Mechanochemistry for Synthesis", *Angew. Chem. Int. Ed.* 59 (2020) 1018–1029. https://doi.org/10.1002/anie.201906755.

[8] I.R. Speight, I. Huskić, M. Arhangelskis, H.M. Titi, R.S. Stein, T.P. Hanusa, T. Friščić, "Disappearing Polymorphs in Metal–Organic Framework Chemistry: Unexpected Stabilization of a Layered Polymorph over an Interpenetrated Three-Dimensional Structure in Mercury Imidazolate", *Chem. - Eur. J.* 26 (2020) 1811–1818. https://doi.org/10.1002/chem.201905280.

[9] C. Cappuccino, F. Farinella, D. Braga, L. Maini, "Mechanochemistry, an Easy Technique to Boost the Synthesis of CuI Pyrazine Coordination Polymers", *Crystal Growth & Design*. 19 (2019) 4395–4403. https://doi.org/10.1021/acs.cgd.9b00192.

[10] T. Gruene, J.T.C. Wennmacher, C. Zaubitzer, J.J. Holstein, J. Heidler, A. Fecteau-Lefebvre, S. De Carlo, E. Müller, K.N. Goldie, I. Regeni, T. Li, G. Santiso-Quinones, G. Steinfeld, S. Handschin, E. van Genderen,

J.A. van Bokhoven, G.H. Clever, R. Pantelic, "Rapid Structure Determination of Microcrystalline Molecular Compounds Using Electron Diffraction", *Angew. Chem. Int. Ed.* 57 (2018) 16313–16317. https://doi.org/10.1002/anie.201811318.

[11] M. Ge, Y. Wang, F. Carraro, W. Liang, M. Roostaeinia, S. Siahrostami, D.M. Proserpio, C. Doonan, P. Falcaro, H. Zheng, X. Zou, Z. Huang, "High-Throughput Electron Diffraction Reveals a Hidden Novel Metal–Organic Framework for Electrocatalysis", *Angew. Chem. Int. Ed.* 60 (2021) 11391–11397. https://doi.org/10.1002/anie.202016882.

[12] U. Kolb, T. Gorelik, C. Kübel, M.T. Otten, D. Hubert, "Towards automated diffraction tomography: Part I—Data acquisition", *Ultramicroscopy*. 107 (2007) 507–513. https://doi.org/10.1016/j.ultramic.2006.10.007.

[13] M. Gemmi, A.E. Lanza, 3D electron diffraction techniques, Acta Crystallogr B Struct Sci Cryst Eng Mater. 75 (2019) 495–504. https://doi.org/10.1107/S2052520619007510.

[14] M. Gemmi, E. Mugnaioli, T.E. Gorelik, U. Kolb, L. Palatinus, P. Boullay, S. Hovmöller, J.P. Abrahams, "3D Electron Diffraction: The Nanocrystallography Revolution", *ACS Cent. Sci.* 5 (2019) 1315–1329. https://doi.org/10.1021/acscentsci.9b00394.

[15] A. Lanza, E. Margheritis, E. Mugnaioli, V. Cappello, G. Garau, M. Gemmi, "Nanobeam precession-assisted 3D electron diffraction reveals a new polymorph of hen egg-white lysozyme", *IUCrJ.* 6 (2019) 178–188. https://doi.org/10.1107/S2052252518017657.

[16] I. Nederlof, E. Van Genderen, Y.-W. Li, J.P. Abrahams, "A Medipix quantum area detector allows rotation electron diffraction data collection from submicrometre three-dimensional protein crystals", *Acta Crystallogr. D Biol. Crystallogr.* 69 (2013) 1223–1230. https://doi.org/10.1107/S0907444913009700.

[17] Z. Huang, T. Willhammar, X. Zou, "Three-dimensional electron diffraction for porous crystalline materials: structural determination and beyond", *Chem. Sci.* 12 (2021) 1206–1219. https://doi.org/10.1039/D0SC05731B.

[18] T. Sun, C.E. Hughes, L. Guo, L. Wei, K.D.M. Harris, Y. Zhang, Y. Ma, "Direct-Space Structure Determination of Covalent Organic Frameworks from 3D Electron Diffraction Data", *Angew. Chem. Int. Ed.* 59 (2020) 22638–22644. https://doi.org/10.1002/anie.202009922.

[19] P. Cui, E. Svensson Grape, P.R. Spackman, Y. Wu, R. Clowes, G.M. Day, A.K. Inge, M.A. Little, A.I. Cooper, "An Expandable Hydrogen-Bonded Organic Framework Characterized by Three-Dimensional Electron Diffraction", *J. Am. Chem. Soc.* 142 (2020) 12743–12750. https://doi.org/10.1021/jacs.0c04885.

[20] E. Mugnaioli, A.E. Lanza, G. Bortolozzi, L. Righi, M. Merlini, V. Cappello, L. Marini, A. Athanassiou, M. Gemmi, "Electron Diffraction on Flash-Frozen Cowlesite Reveals the Structure of the First Two-Dimensional Natural Zeolite", *ACS Cent. Sci.* 6 (2020) 1578–1586. https://doi.org/10.1021/acscentsci.9b01100.

[21] I. Andrusenko, V. Hamilton, E. Mugnaioli, A. Lanza, C. Hall, J. Potticary, S.R. Hall, M. Gemmi, "The Crystal Structure of Orthocetamol Solved by 3D Electron Diffraction", *Angew. Chem. Int. Ed.* 58 (2019) 10919–10922. https://doi.org/10.1002/anie.201904564.

[22] P. Brázda, L. Palatinus, M. Babor, "Electron diffraction determines molecular absolute configuration in a pharmaceutical nanocrystal", *Science*. 364 (2019) 667–669. https://doi.org/10.1126/science.aaw2560.

[23] P.P. Das, I. Andrusenko, E. Mugnaioli, J.A. Kaduk, S. Nicolopoulos, M. Gemmi, N.C. Boaz, A.M. Gindhart, T. Blanton, "Crystal Structure of Linagliptin Hemihydrate Hemiethanolate $(C_{25}H_{28}N_8O_2)_2(H_2O)(C_2H_5OH)$ from 3D Electron Diffraction Data, Rietveld Refinement, and Density Functional Theory Optimization", *Crystal Growth & Design*. 21 (2021) 2019–2027. https://doi.org/10.1021/acs.cgd.0c01379.

[24] L.J. Kim, M. Xue, X. Li, Z. Xu, E. Paulson, B. Mercado, H.M. Nelson, S.B. Herzon, "Structure Revision of the Lomaiviticins", *J. Am. Chem. Soc.* 143 (2021) 6578–6585. https://doi.org/10.1021/jacs.1c01729.

[25] C.G. Jones, M.W. Martynowycz, J. Hattne, T.J. Fulton, B.M. Stoltz, J.A. Rodriguez, H.M. Nelson, T. Gonen, "The CryoEM Method MicroED as a Powerful Tool for Small Molecule Structure Determination", *ACS Cent. Sci.* 4 (2018) 1587–1592. https://doi.org/10.1021/acscentsci.8b00760.

[26] C.R. Groom, I.J. Bruno, M.P. Lightfoot, S.C. Ward, "The Cambridge Structural Database", *Acta Crystallogr. B Struct. Sci. Cryst. Eng. Mater.* 72 (2016) 171–179. https://doi.org/10.1107/S2052520616003954.

[27] H.-L. Gao, L. Yi, B. Zhao, X.-Q. Zhao, P. Cheng, D.-Z. Liao, S.-P. Yan, "Synthesis and Characterization of Metal−Organic Frameworks Based on 4-Hydroxypyridine-2,6-dicarboxylic Acid and Pyridine-2,6-dicarboxylic Acid Ligands", *Inorg. Chem.* 45 (2006) 5980–5988. https://doi.org/10.1021/ic060550j.

[28] Y.-Q. Huang, Y. Wan, H.-Y. Chen, Y. Wang, Y. Zhao, X.-F. Xiao, "Construction of metal–organic coordination networks with various metal-linker secondary building units: structures and properties", *New J. Chem.* 40 (2016) 7587–7595. https://doi.org/10.1039/C6NJ01231K.

[29] W.-P. Wu, Y.-Y. Wang, Y.-P. Wu, J.-Q. Liu, X.-R. Zeng, Q.-Z. Shi, S.-M. Peng, "Hydro(solvo)thermal synthesis, structures, luminescence of 2-D zinc(ii) and 1-D copper(ii) complexes constructed from pyridine-2,6-dicarboxylic acid N-oxide and decarboxylation of the ligand", *CrystEngComm.* 9 (2007) 753. https://doi.org/10.1039/b701384a.

[30] L.-L. Wen, D.-B. Dang, C.-Y. Duan, Y.-Z. Li, Z.-F. Tian, Q.-J. Meng, "1D Helix, 2D Brick-Wall and Herringbone, and 3D Interpenetration d^{10} Metal−Organic Framework Structures Assembled from Pyridine-2,6-dicarboxylic Acid *N* -Oxide", *Inorg. Chem.* 44 (2005) 7161–7170. https://doi.org/10.1021/ic0509985.

[31] S. Demir, H.M. Çepni, M. Hołyńska, M. Kavanoz, F. Yilmaz, Y. Zorlu, "Copper(II) complexes with pyridine-2,6-dicarboxylic acid from the oxidation of copper(I) iodide", *J. Coord. Chem.* 70 (2017) 3422–3433. https://doi.org/10.1080/00958972.2017.1393071.

[32] M. Felloni, A.J. Blake, P. Hubberstey, C. Wilson, M. Schröder, "Solvent Control of Supramolecular Architectures Derived from 4,4′-Bipyridyl-Bridged Copper(II) Dipicolinate Complexes", *Crystal Growth & Design.* 9 (2009) 4685–4699. https://doi.org/10.1021/cg900552b.

[33] D. Farrusseng, "Metal-Organic Frameworks: Applications from Catalysis to Gas Storage", 1st ed., Wiley-VCH Verlag GmbH & Co. KGaA, 2011. https://onlinelibrary.wiley.com/doi/book/10.1002/9783527635856.

[34] F. Grepioni, M. Polito, L. Maini, S.L. Giaffreda, D. D'Addario, D. Braga, "Intra-Solid and Inter-Solid Reactions of Molecular Crystals: a Green Route to Crystal Engineering", 1st ed., Springer, Berlin, Heidelberg, 2005. https://doi.org/10.1007/b100996.

[35] V. Petříček, M. Dušek, L. Palatinus, "Crystallographic Computing System JANA2006: General features", *Z. Kristallogr. Cryst. Mater.* 229 (2014) 345–352. https://doi.org/10.1515/zkri-2014-1737.

[36] L. Palatinus, V. Petříček, C.A. Corrêa, "Structure refinement using precession electron diffraction tomography and dynamical diffraction: theory and implementation", *Acta Crystallogr. A Found. Adv.* 71 (2015) 235–244. https://doi.org/10.1107/S2053273315001266.

[37] G.M. Sheldrick, "Crystal structure refinement with *SHELXL"*, *Acta. Crystallogr. C Struct. Chem.* 71 (2015) 3–8. https://doi.org/10.1107/S2053229614024218.

[38] A.L. Spek, "Single-crystal structure validation with the program *PLATON"*, *J. Appl. Crystallogr.* 36 (2003) 7–13. https://doi.org/10.1107/S0021889802022112.

[39] Q. Zang, G.-Q. Zhong, M.-L. Wang, "A copper(II) complex with pyridine-2,6-dicarboxylic acid: Synthesis, characterization, thermal decomposition, bioactivity and interactions with herring sperm DNA", *Polyhedron*. 100 (2015) 223–230. https://doi.org/10.1016/j.poly.2015.08.007.

[40] S.C. Manna, J. Ribas, E. Zangrando, N. Ray Chaudhuri, "Supramolecular networks of dinuclear copper(II): Synthesis, crystal structure and magnetic study", *Inorganica Chim. Acta.* 360 (2007) 2589–2597. https://doi.org/10.1016/j.ica.2006.12.041.

[41] T. Friščić, S.L. Childs, S.A.A. Rizvi, W. Jones, "The role of solvent in mechanochemical and sonochemical cocrystal formation: a solubility-based approach for predicting cocrystallisation outcome", *CrystEngComm*. 11 (2009) 418–426. https://doi.org/10.1039/B815174A.

[42] G.M. Sheldrick, "*SHELXT* – Integrated space-group and crystal-structure determination", *Acta Crystallogr. A Found. Adv.* 71 (2015) 3–8. https://doi.org/10.1107/S2053273314026370.

[43] M.C. Burla, R. Caliandro, B. Carrozzini, G.L. Cascarano, C. Cuocci, C. Giacovazzo, M. Mallamo, A. Mazzone, G. Polidori, "Crystal structure determination and refinement *via SIR2014"*, *J. Appl. Crystallogr.* 48 (2015) 306–309. https://doi.org/10.1107/S1600576715001132.

[44] C.B. Hübschle, G.M. Sheldrick, B. Dittrich, "*ShelXle*: a Qt graphical user interface for *SHELXL"*, *J. Appl. Crystallogr.* 44 (2011) 1281–1284. https://doi.org/10.1107/S0021889811043202.

[45] SADABS Bruker AXS; Madison, Wisconsin, USA, (2004).

[46] G. M. Sheldrick, SADABS v2.03: Area-Detector Absorption Correction., (1999).

[47] L.J. Farrugia, "*WinGX* suite for small-molecule single-crystal crystallography", *J. Appl. Crystallogr.* 32 (1999) 837–838. https://doi.org/10.1107/S0021889899006020.

5 Tetra-4-(4-pyridyl)phenylmethane-based Supramolecular Organic Frameworks

In this chapter, the dynamic behaviour of a Supramolecular Organic Framework (SOF) based on the rigid tetra-4-(4-pyridyl)phenylmethane (**TPPM**) organic tecton will be elucidated. The SOF undergoes a reversible crystal-to-crystal transformation when exposed to vapours of selected organic solvents, moving from a closed structure with isolated small voids to an expanded structure with filled channels extended along the *b-axis*. The observed selectivity is dictated by the fitting of the guest in the expanded SOF, following the degree of packing coefficient.

The following discussion will be divided into two sub-chapters, each based on recently-published material. [1,2] The first comprises the discussion on the SOF dynamicity, with a particular focus on the structural characterization of the crystalline phases involved in the process. Moreover, the effect of solvent uptake on **TPPM** solid-state fluorescence was investigated, evidencing a significant variation in the emission profile only in the presence of chloroform.[1] The second sub-chapter focuses on the mechanochemical synthesis of a new expanded phase of the **TPPM**-based SOF and its structural characterisation through a novel electron diffractometer. [2]

5.1 Selective and Reversible Solvent Uptake in TPPM-based Supramolecular Organic Frameworks

5.1.1 Introduction

In recent years, supramolecular organic frameworks (SOFs) have emerged as an important class of functional porous materials alongside coordination polymers (CPs), metal-organic frameworks (MOFs) and covalent organic frameworks (COFs) for applications such as molecular sensing, gas storage and separation. [3–6] Usually, SOFs are obtained through the self-assembly of organic tectons *via* highly directional hydrogen bonds, [7–21] but examples of materials held together by van der Waals interactions, π···π stacking, halogen bonds and, quite recently, chalcogen bonds have also been reported. [22–28] Compared to other classes of reticular materials based on coordinative or covalent bonds, SOFs lack robustness and tend to loose porosity when guests molecules are removed. [4] On the other side, they have the advantage of coupling flexibility and reversibility with relatively simple synthetic procedures under mild conditions. [11] These considerations become especially important when targeting stimuli-responsive crystalline materials, which respond to external solicitations such as electric, mechanical and thermal ones. [29–32] The design of SOFs showing dynamic properties is a challenging task which involves both the synthesis of suitable building blocks, assembled through crystal engineering, and the mastering of molecular and supramolecular interactions in the solid state. [5,15,24,33–36]

Among the possible building blocks, tetraphenylmethane (**TPM**) derivatives, with their tetrahedral symmetry, represent effective tectons for the formation of 3D architectures (Scheme 5.1). [37,38]

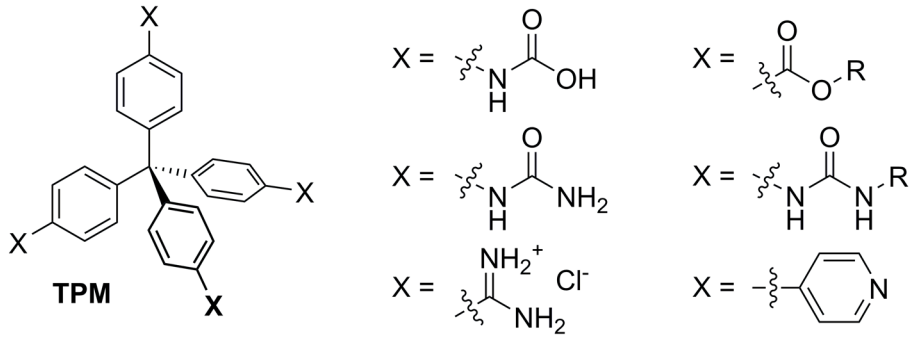

Scheme 5.1: Molecular sketches of tectons based on tetraphenylmethane (**TPM**).[38]

Exploiting their structural rigidity and synthetic versatility, these tectons have been successfully applied to the preparation of SOFs through the formation of highly oriented hydrogen bonding motifs based on 2-pyridone, [39] phenol, [40] boronic acid, [41] urethane [42] and carboxylic acid [43] functional groups. Instead, tetra-4-(4-pyridyl)phenylmethane (**TPPM**, Scheme 5.2), the rigid aromatic tecton obtained by the decoration of **TPM** 4 positions with *p*-substituted pyridyl rings, has been successfully employed for the synthesis of Cu-based porous MOFs, [44–47] but its potential as building block for SOFs is still unexplored.

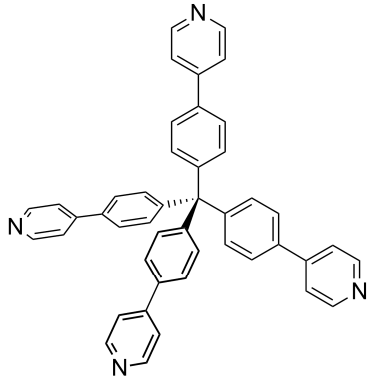

Scheme 5.2: Molecular sketch of tetra-4-(4-pyridyl)phenylmethane (**TPPM**).

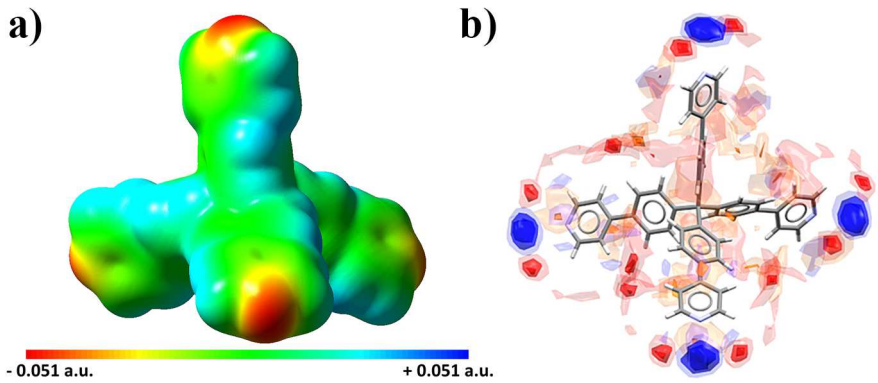

Figure 5.1: Electrostatic potential surface (a) and Full Interaction Map (b) for **TPPM**. The surface has been calculated at the B3LYP/6-311++G(d,p) level of theory using Gaussian09. [48] The colour code from red to blue indicate areas of rich and depleted electron density, respectively. In the Full Interaction Map, the different contour surfaces are used to indicate the likelihood of the molecule to form interactions with H-bond donors (in red), acceptors (in blue) and hydrophobic groups (in orange).

As shown by the electrostatic potential surface and by the Full Interaction Map (Figure 5.1), [49] **TPPM** can act as hydrogen bond acceptor with its four nitrogen atoms, as weak hydrogen bond donor with the C-H moieties and can give rise to π···π and C-H···π interactions due to the presence of aromatic rings.

It is therefore expected that, according to Kitaigorodskii studies on organic crystals, the molecules assemble in the solid state to minimise free space.[50] However, the relative weakness of the supramolecular interactions likely involved in stabilizing the crystal structure of **TPPM** enhances the probability of obtaining a flexible network [51] susceptible of external, stimuli-mediated structural changes. [33]

In this chapter, the dynamic behaviour of **TPPM** will be presented. This molecule, in its crystalline form, can reversibly switch from a non-porous empty to a filled solvated phase and *vice-versa*, when exposed to vapours of organic solvents and heat, respectively (Figure 5.2). Remarkably, this crystal-to-crystal transformation [52–55] is selectively triggered only by a group of solvents, namely chloroform, dichloroethylene, trichloroethylene, benzene and

toluene. Moreover, in the specific case of chloroform uptake, a significant variation of the fluorescence emission profile was observed.

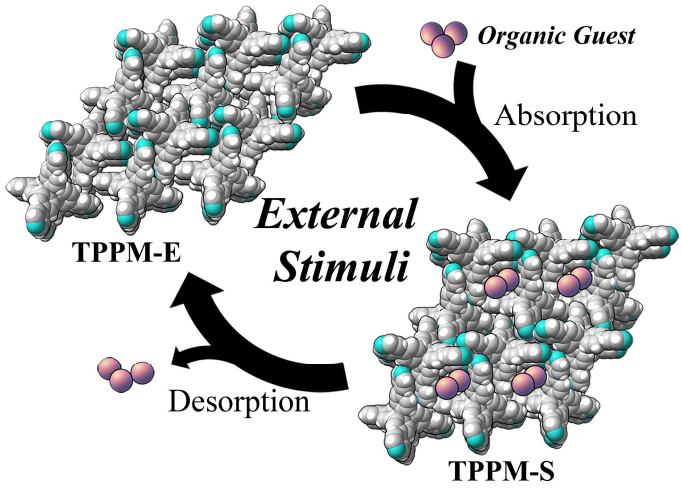

Figure 5.2: Schematic representation of the stimuli-responsive behaviour of **TPPM**-based SOF. **TPPM-E** corresponds to the empty phase while **TPPM-S** to the filled solvated one. [2]

5.1.2 Expanded framework of TPPM-based SOFs

The solid-state behaviour of **TPPM** was studied growing crystals from the slow evaporation of a chloroform solution and analysing them through X-ray diffraction methods. **TPPM** crystallizes as a 1:1 $CHCl_3$ solvate (**TPPM·CHCl₃**) in the space group C2/*c*. The asymmetric unit consists of half a molecule of **TPPM** and half a molecule of the guest, disordered over two equivalent positions by a rotation around the C-H bond (Figure 5.3).

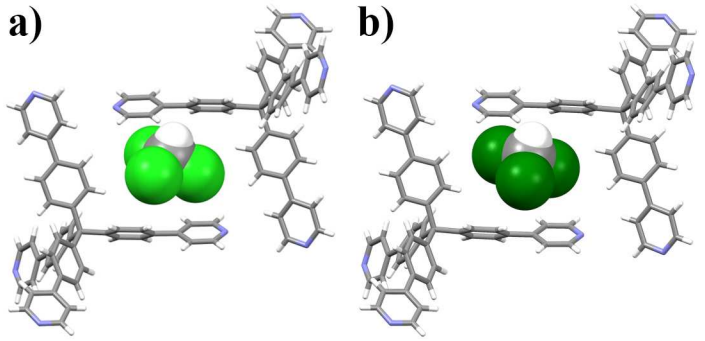

Figure 5.3: Detail of the two possible orientation of $CHCl_3$ molecules embedded in the channels of **TPPM** solvate phase. (a) and (b) are obtained by rotating the $CHCl_3$ around its C-H bond.

The **TPPM** units assemble to give a supramolecular three-dimensional network held together by several C-H···N interactions. In particular, each **TPPM** forms symmetry-related C12B-H12B···N1A, C3-H3A···N1B and C10-H10A···N1B contacts (Figure 5.4).

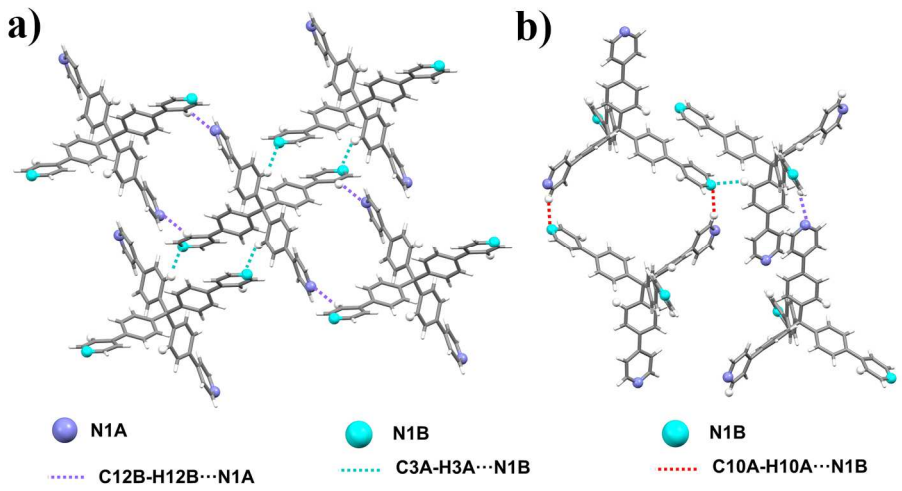

Figure 5.4: View of the relevant C-H···N interactions in **TPPM·CHCl$_3$**. The N and H atoms involved in the interactions have been drawn as spheres while solvent molecules have been omitted for clarity.

This assembly contains channels parallel to the *b* axis direction filled by the disordered solvent molecules (Figure 5.5). Inside the pores, chloroform forms two C-H···C$_{aromatic}$ interaction involving the atoms C5A and C8A of **TPPM** (Figure S5.1).

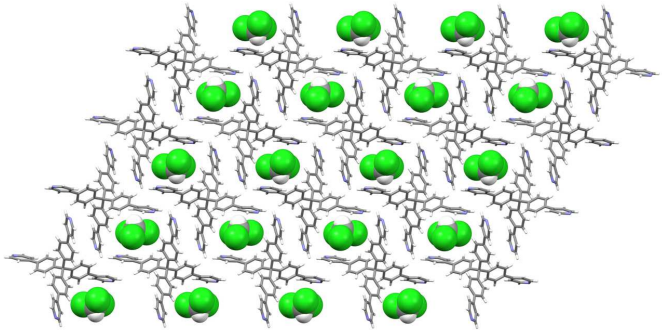

Figure 5.5: View along the *b*-axis direction of the crystal lattice of **TPPM·CHCl$_3$.**

Interestingly, the same supramolecular network also forms when **TPPM** is crystallized from different solvents, as reported in the literature for DMF [44] (CSD [56] refcode IVETEJ) and DMSO [45] (CSD refcode: ZISXAC). In both isomorphous crystals, the solvent molecules occupy the channels in a 1:1 ratio.

This prompted us to further study the robustness and the reproducibility of the SOF, by soaking single crystals of the chloroform solvate (for 2 hours at room temperature) in different media such as ethanol, benzene and acetonitrile, potentially capable of forming hydrogen bonds or π···π stacking interactions with **TPPM**. In all three cases, the crystals retained their transparency and habit; X-ray diffraction analysis confirmed the substitution of chloroform by the bulk solvents, and the formation of the three solvates **TPPM·EtOH**, **TPPM·C_6H_6** and **TPPM·0.5CH_3CN**. All solvates crystallize in the space group C2/*c* with comparable unit cell dimensions; **TPPM·EtOH** and **TPPM·C_6H_6** possess the same supramolecular network described above for **TPPM·$CHCl_3$**, **TPPM·DMF** and **TPPM·DMSO** (Figure 5.6 and Table S5.1).

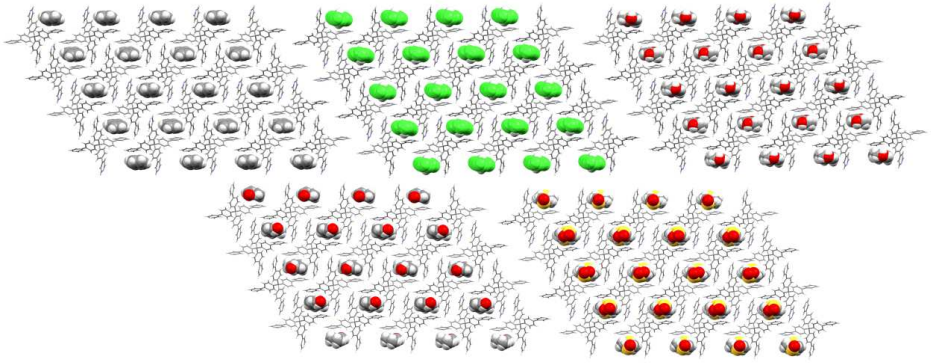

Figure 5.6: Crystal structure of the different solvates of **TPPM** (**TPPM-S**; from left to right, from top to bottom: C_6H_6, $CHCl_3$, EtOH, DMF, DMSO).

The asymmetric unit of **TPPM·EtOH** consists of half a molecule of **TPPM** and half a molecule of the guest, which, due to symmetry, occupies the channels formed by the ligand with two different, symmetry-related orientations (Figure 5.7a-b). Analogously, the asymmetric unit of **TPPM·C_6H_6** consists of half a molecule of **TPPM** and half a molecule of the guest. Figure 5.7c shows benzene sandwiched between two symmetry-related **TPPM** ligands, highlighting the shape complementarity of the guest with the channels formed by the host.

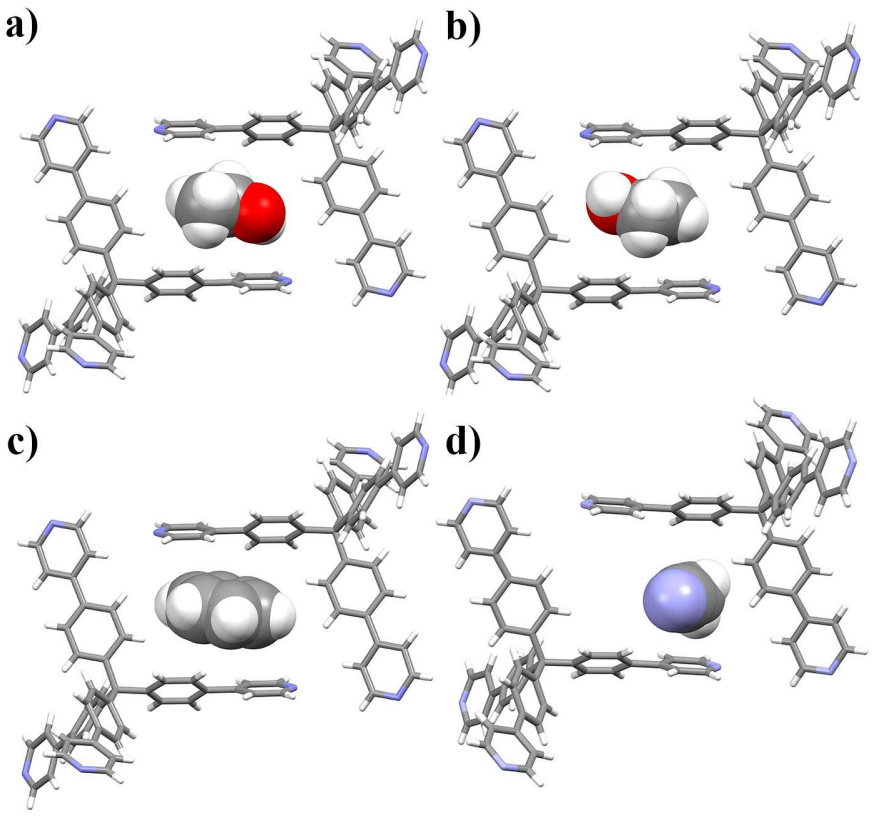

Figure 5.7: (a,b) View of the two symmetry-related orientations of ethanol in the crystal structure of **TPPM·EtOH**. (c) View of benzene sandwiched between two **TPPM** ligands in **TPPM·C_6H_6**. (d) View of acetonitrile inside the channels in **TPPM·0.5CH_3CN**

In the case of **TPPM·0.5CH_3CN**, the asymmetric unit comprises half a molecule of **TPPM** and one fourth of a molecule of acetonitrile. Interestingly, **TPPM** resulted disordered over two positions, one of which is not compatible with the presence of the solvent; this means that in the crystal, both a solvate (Figure 5.7d) and an unsolvate (Figure 5.8b) phase are present. The N1S atom of acetonitrile forms a C-H···N interactions with a pyridine moiety (Figure 5.8a and Figure S5.5). The framework of the solvate phase of **TPPM·0.5CH_3CN** still contains channels along the *b*-axis direction, but it is consolidated by a different set of interactions, comprising also C-

H···π·interactions (Figure 5.8b). The framework of the unsolvated phase, which is quite compact and contains unconnected voids summing up to 6% of the unit cell volume, is also consolidated by C-H···N and C-H···π interactions (Figure 5.8c).

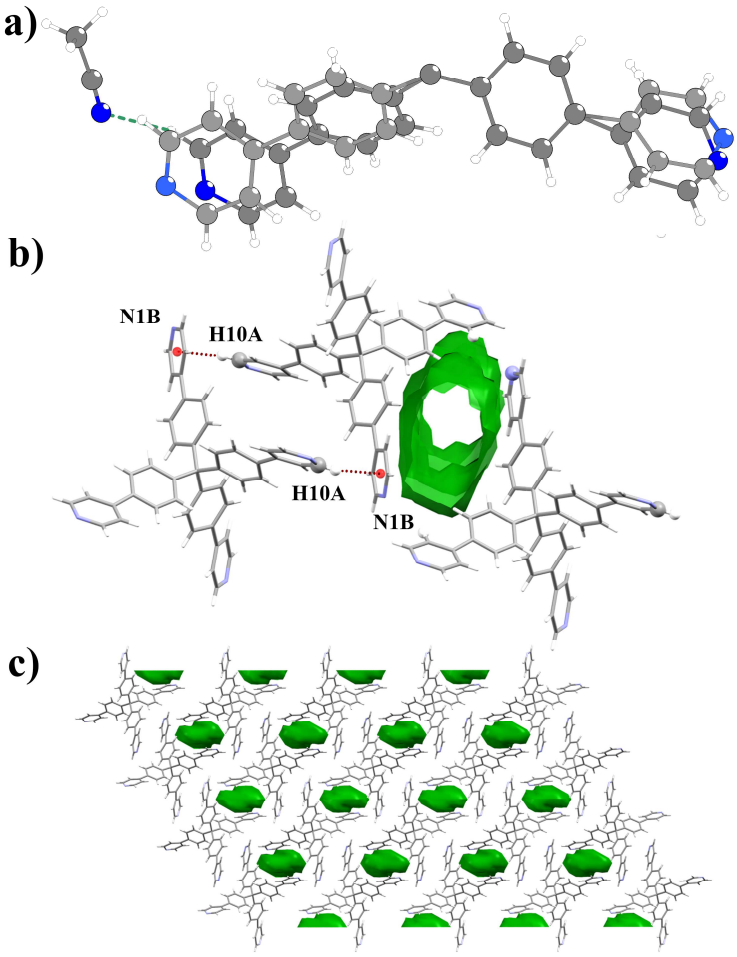

Figure 5.8: (a) View of the asymmetric unit of **TPPM·0.5CH₃CN**. The two different orientations of **TPPM** for filled and empty phase are shown in dark and light tones, respectively. (b) View of the C-H···π interactions in the filled phase of **TPPM·0.5CH₃CN**. The red spheres are the centroids Cg of ring C8B-C12B/N1B. C10A···Cg: 3.403(3) Å; C10A-H10···Cg, 167.8(5)°. The channels containing the solvent (removed for clarity) are in green. (c) View along the *b*-axis direction of the empty phase in **TPPM·0.5CH₃CN**.

Crystals of **TPPM·CHCl$_3$** were also exposed both to water vapours and soaked in distilled water for seven days to assess the stability of the solvate in humid and wet conditions. After these treatments, the X-ray diffraction analysis of the crystals revealed the presence of the unaltered chloroform solvate.

The host-guest interactions for the different solvates were compared by means of a Hirshfeld analysis, performed with CrystalExplorer17.[57] The Hirshfeld surface of **TPPM** is quite similar for **TPPM·EtOH** and **TPPM·C$_6$H$_6$**, indicating that the presence of the guest does not influence much the supramolecular interactions consolidating the framework of the host (Figure 5.9). The Hirshfeld surface of **TPPM·CHCl$_3$** shows an additional bright red spot relative to the C-H···C$_{aromatic}$ interactions shown in Figure S5.1, while the red spots on the Hirshfeld surface of **TPPM·0.5CH$_3$CN** derive from the C-H···π interactions (Figure 5.8a) which are missing in the other solvates. For all the forms, the general trend is a predominance of dispersion forces and of H···H, C···H/H···C and N···H/H···N contacts (see fingerprint plots in Figure S5.6 and Table S5.2).

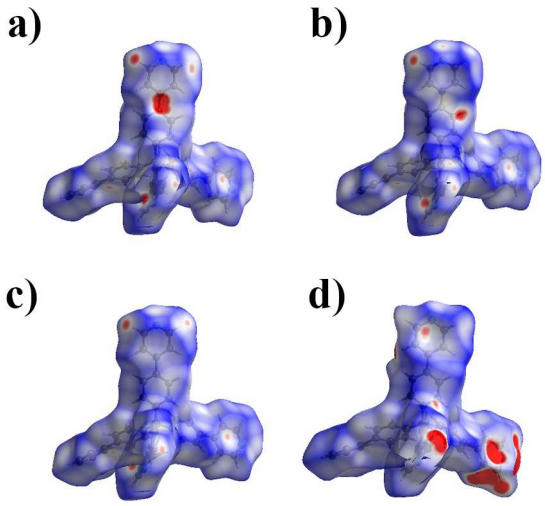

Figure 5.9: Comparison of the Hirshfeld surface for **TPPM** solvate phase of: (a) **TPPM·CHCl$_3$**, (b) **TPPM·EtOH**, (c) **TPPM·C$_6$H$_6$** and (d) **TPPM·0.5CH$_3$CN.**

5.1.3 Contracted Framework for TPPM-based SOFs

This peculiar behaviour prompted us to investigate the possibility to isolate an empty crystal structure of **TPPM** alone. To this purpose, a batch of single crystals of **TPPM·CHCl3** was heated at 100 °C for 2 hours (Figure 5.10).

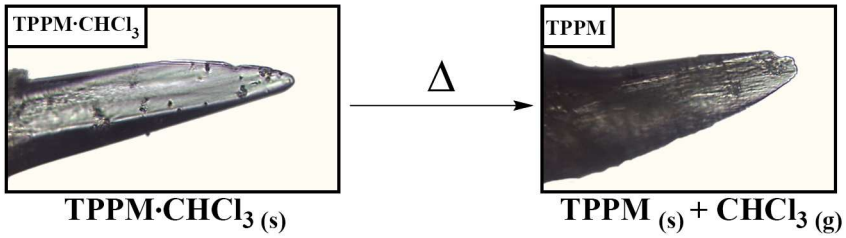

Figure 5.10: Sketch of the temperature induced solvent desorption on **TPPM·CHCl3** single crystal. The figure reports optical microscope images before (*left*) and after (*right*) the treatment

A portion of the thermally treated batch was grinded and analysed through PXRD analysis; the comparison between the diffractograms of the chloroform solvate and the activated form clearly showed the formation of a new phase displaying high micro-crystallinity, probably due to the lack of disordered solvent inside the channels. Remarkably, the remaining single crystals show increased mosaicity and defectivity (Figure 5.10) which hamper the use of single crystal X-ray diffraction and calls for 3D electron diffraction (3D ED),[58–60] which can be successfully employed with nanometric samples possessing small crystalline domains. Although **TPPM** crystals are sensitive to the electron beam, thanks to a special low dose set up in which the electron dose is reduced below 0.05 el $s^{-1}Å^{-2}$ and the diffraction patterns are collected with a Timepix single electron detector,[61] a full 3D ED experiment covering a 120° of reciprocal space can be performed without the amorphization of the crystals or a significant loss of resolution in the diffraction signal. The 3D ED data have been collected in precession electron diffraction mode (PEDT) over a single nanocrystal (Figure 5.11) and allowed the *ab-initio* structure determination of **TPPM** using direct methods.

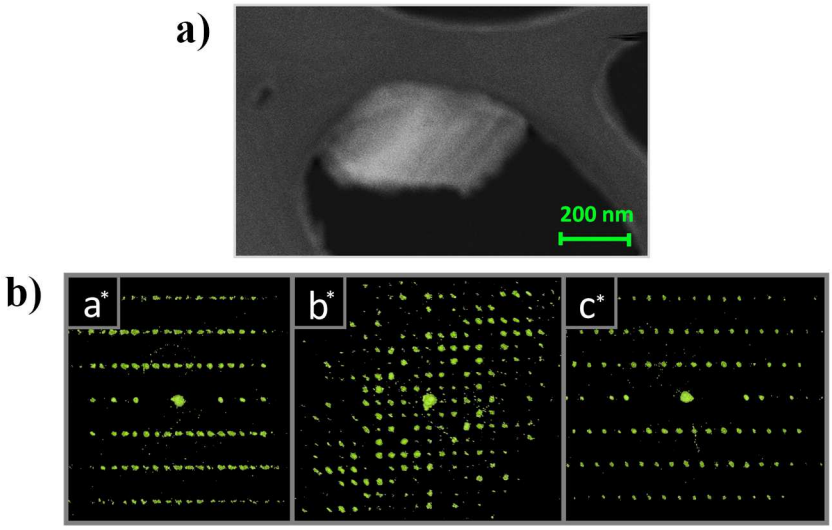

Figure 5.11: (a) HAADF STEM-image of the **TPPM** nanocrystal used for the 3D ED data collection. (b) Projection along the three reciprocal cell directions of the reconstructed reciprocal space for the 3D ED data of **TPPM**.

Remarkably, the data quality was suitable for the dynamical structure refinement of the **TPPM** structure. Dynamical refinement takes into account in the modelling of diffracted intensity the effect of dynamical scattering through a full Bloch wave calculation.[62] The structure is refined together with the thickness of the sample and both the agreement factors and the quality in the structure determination approach single crystal x-ray accuracy.[63] In the case of **TPPM,** dynamical refinement led to an improvement of the structural model and allowed to localize most of the hydrogen atoms (Figure 5.12). This is the first time that a SOF structure has been refined at a high accuracy taking into account dynamical scattering.

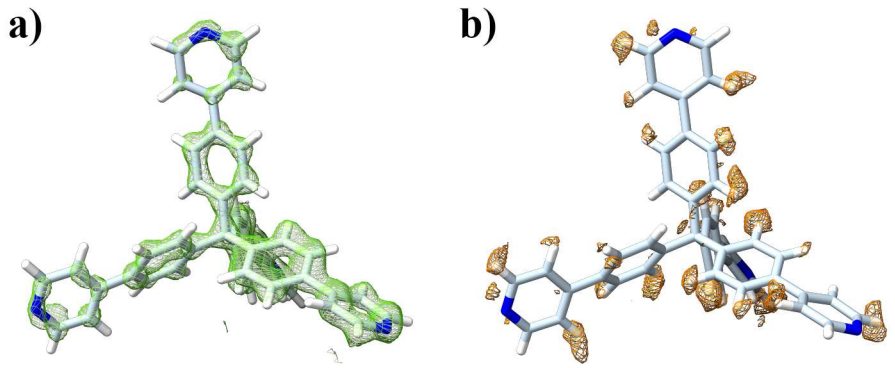

Figure 5.12: (a) Superposition between the molecular unit and the calculated potential map, in the dynamically refined phase of **TPPM**. (b) Superposition between the difference potential map, calculated from a structural model without H atoms, and the **TPPM** molecular unit.

The activated **TPPM**, which is indeed the empty phase (**TPPM-E**), crystallizes in the monoclinic space group C2/*c* like the parent solvates. The biggest changes in the cell parameters involve the *a* axis, which goes from 27.9295(5) to 31.40(6) Å, the β angle, that likewise increases from 120.1390(10) to 133.1(1)° and the volume, which slightly decreases from 3628.2(1) $Å^3$ to 3596(12) $Å^3$ (see Table S5.1).

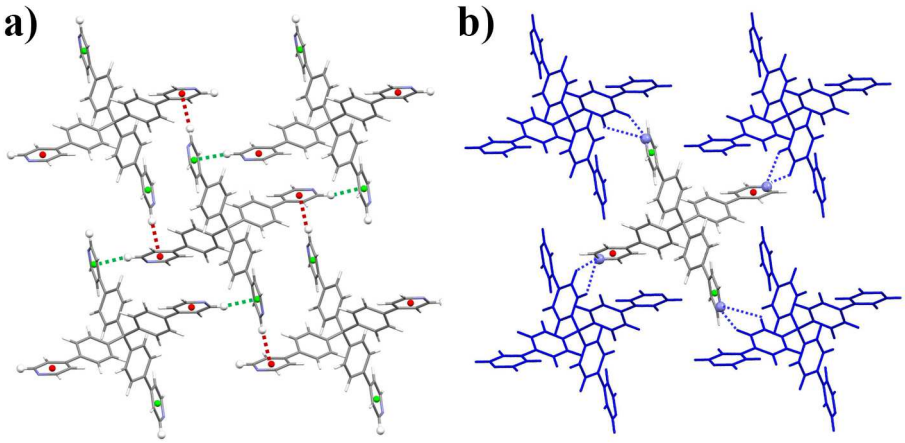

Figure 5.13: View along the *b*-axis direction of the main C-H···centroids (a) and C-H···N (b) interactions, present in the supramolecular framework of the empty form of **TPPM**. The centroids are represented as green (C8A-C12A/N1A, Cg1) and red (C8B-C12B/N1B, Cg2) spheres, respectively.

In the lattice, each **TPPM** forms symmetry-related C11B-H11B···Cg1 and C10A-H10A···Cg2 contacts with four distinct adjacent molecules (Figure 5.13). These interactions are lacking in the solvated forms and are responsible for the more compact structure of the framework. The same central reference molecule is also surrounded by another set of four ligands through weak, C-H···N interactions involving each of the pyridine rings, acting as H-bond acceptors towards the C-H groups of the phenyl moieties. Also in this case, the pattern is rather different from that present in the solvate forms, where each **TPPM** unit behaves both as H-bond donor and acceptor. The different interactions formed in the empty and solvated phase are also evidenced by the Hirshfeld surface analysis shown in Figure 5.14.

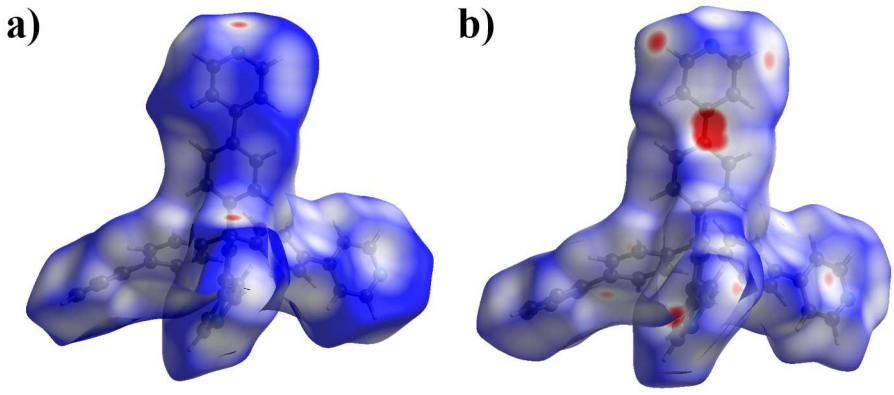

Figure 5.14: Hirshfeld surface comparison between the **TPPM** empty phase (a) and the TPPM·**$CHCl_3$** filled phase (b).

The net result of this crystal-to-crystal phase transition is that of a compact framework in which the original channels become non-connected small voids located among the **TPPM** units; these voids sum up to a volume of *ca.* 145 $Å^3$ (4% of the total unit cell volume) compared to the volume of *ca.* 610 $Å^3$ (17% of the total unit cell volume) occupied by the channels filled with solvent in the solvated form **TPPM·S** (Figure 5.15).

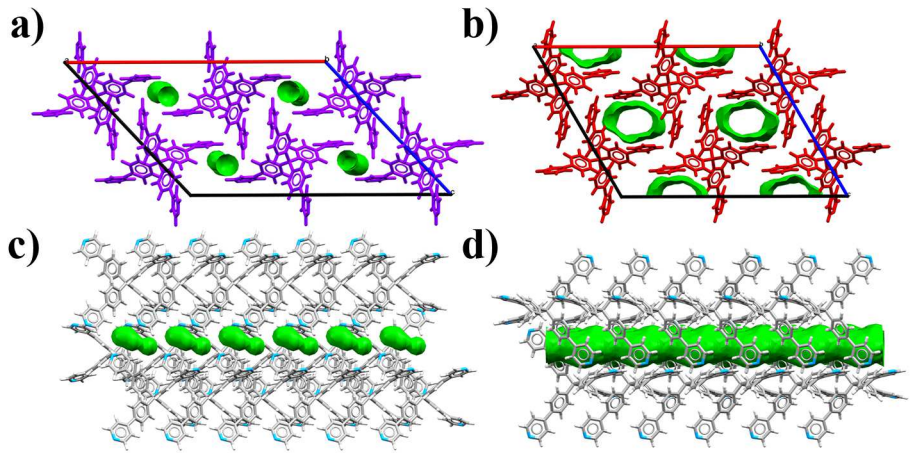

Figure 5.15: Comparison of the crystal lattice for the empty (a, **TPPM-E**) and solvate (b, **TPPM-S**) of **TPPM** and their relative unconnected voids (a) and channels (d). The solvent molecules of the solvate form have been removed for clarity.

Interestingly, this contracted framework (**TPPM-E**) shares common features with the unsolvated form displayed by the **TPPM·CH$_3$CN** crystal structure, in which it results overlapped with its respective solvated phase (Figure 5.8b). Thus, the **TPPM·CH$_3$CN** solvated phase can be seen as a sort of intermediate phase in which, however, the unit cell is that of the solvated form.

5.1.4 Stimuli-responsiveness of TPPM-based SOFs

The desolvation process was also monitored in detail through X-ray powder diffraction analysis. To this purpose, the microcrystalline powder of **TPPM·CHCl$_3$** was used as **TPPM-S** phase reference and measured by a temperature resolved *in situ* X-ray powder diffraction analysis. The **TPPM-S** phase, during the heating treatment, undergoes a crystal-to-crystal phase transition leading to the empty **TPPM** phase. From the temperature-resolved diffractograms it is evident that crystallinity is retained throughout the whole process (see Figure 5.16 and Figure S5.9).

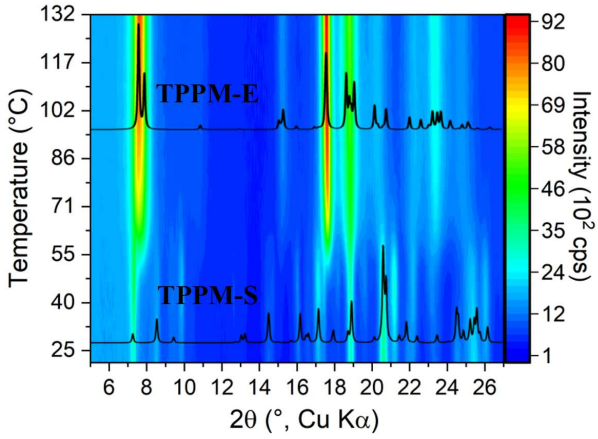

Figure 5.16: Temperature induced desolvation of **TPPM-S** (**TPPM·CHCl₃**) analysed by temperature-resolved *in situ* powder X-ray diffraction, 2D projection along the intensity axis. The two peaks around 7° in the diffractogram of empty **TPPM** differ from the predicted pattern due to preferred orientation phenomena.

The phase transition does not show a continuous distortion of the lattice parameters, but only a reflection intensity changes for the two involved species. LeBail refinement was performed for each collected diffractogram, leading to a temperature-dependent correlation between powder profile parameters and the phase fraction (Figure 5.17 and Figure S5.10).

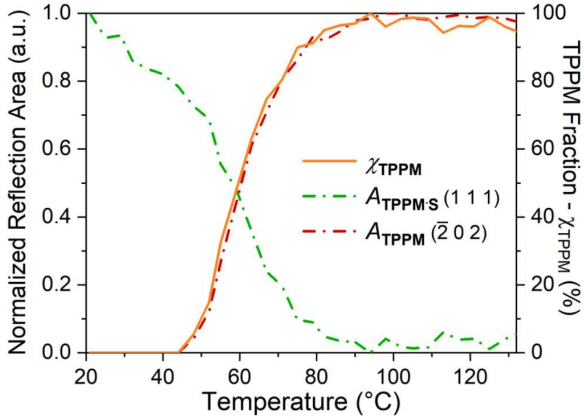

Figure 5.17: Temperature-resolved change in peak area of X-ray (1 1 1) reflection of **TPPM·S** ($A_{TPPM\text{-}S}$) and ($\bar{2}$ 0 2) reflection of **TPPM** (A_{TPPM}). χ_{TPPM} is the fraction of the empty **TPPM** phase.

Interestingly, the dynamic behaviour shown by **TPPM** is reversible. Indeed, when the empty crystalline **TPPM** (**TPPM-E**) is exposed to the vapours of a series of organic solvents, it switches back to the solvate phase **TPPM·S**, as evidenced by PXRD analysis (Figure 5.18 and Figure S5.11).

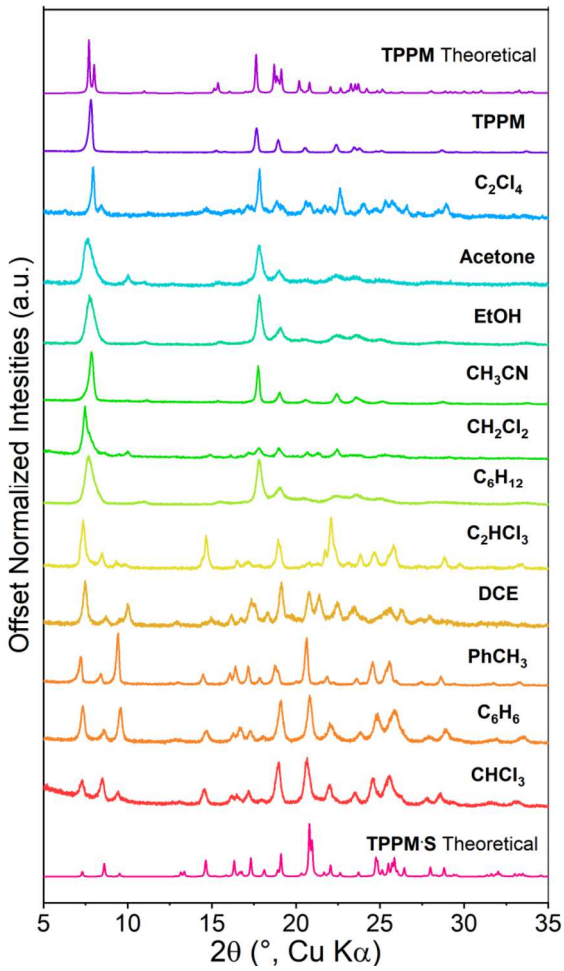

Figure 5.18: Powder X-ray diffractograms after 2 minutes exposure of the **TPPM** phase to vapours of different solvents.

The vapour uptake is fast (completed after *ca.* 2 minutes or less) and selective, as the phase transformation occurs with chloroform, dichloroethane, trichloroethylene, benzene, toluene but not with acetonitrile, ethanol, tetrachloroethylene or acetone. Cyclohexane also triggers the phase

transformation, but its uptake time is much longer (*ca.* 20 minutes). Dichloromethane can be also partially absorbed by empty **TPPM** yielding, however, an unstable phase at room conditions. The affinity towards a group of solvent vapours shown by the SOF was also investigated by ^{1}H NMR spectroscopy through competition experiments. Chloroform and ethanol were selected as representative of the two classes of vapours uptaken and not uptaken by the empty form. The exposure of the **TPPM·EtOH** phase to chloroform vapours for different intervals of time (2 and 20 minutes) caused the progressive substitution of ethanol inside the pores, as shown in the spectra reported in Figure 5.19 (see the disappearance of the signals relative to the ethanol phase and the appearance of the chloroform ones). The reverse uptake did not occur when the crystalline **TPPM·CHCl3** solvate was exposed to EtOH vapours (Figure S5.25).

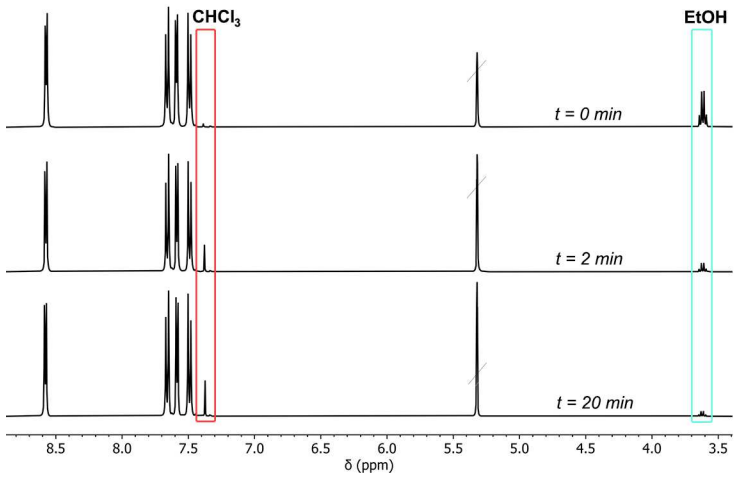

Figure 5.19: Solvent competition studies followed by ^{1}H NMR spectroscopy. The **TPPM·EtOH** phase was exposed to $CHCl_3$ vapours for 2 and 20 minutes. The solid was then dissolved in CD_2Cl_2 with few drops of methanol-d_4. ^{1}H NMR spectra were collected and compared to the starting solvate phase spectra.

The framework stability of the **TPPM-S** phases was investigated through DSC analysis. The characterizations were performed in an open system to minimize possible counterpressure effects. The collected thermograms present an endothermic phase transition, related to the release of guest molecules embedded in the **TPPM** framework (see Figure S5.12). It is worth noticing that the **TPPM·S** phases directly obtained by vapor absorption present higher desorption enthalpies (ΔH_{Des}) than both **TPPM·EtOH** and **TPPM·0.5CH$_3$CN** (Figure 5.20, Figure S5.13) suggesting that thermodynamic stability can play a role in the selectivity of the absorption process.

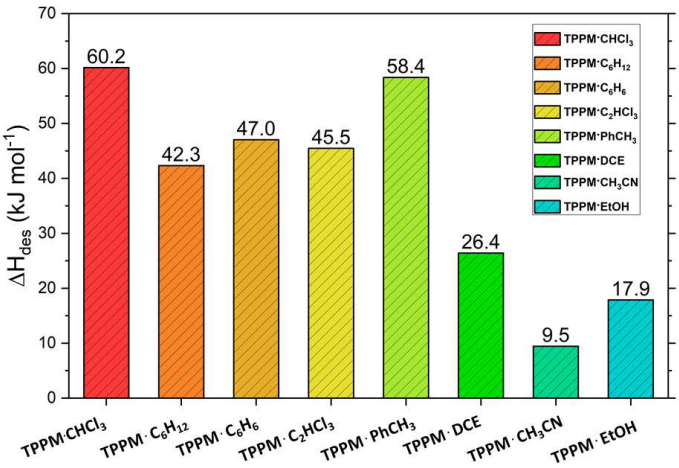

Figure 5.20: Desorption Enthalpies derived from DSC characterization on different **TPPM-S** phases.

The release of solvent molecules during the phase transition was also confirmed by TGA (**Figure S5.14**) which, together with ^{1}H NMR spectroscopy, was also used to determine the amount of absorbed solvent molecules, reported as solvate stoichiometry (Figure S5.15, Figure S5.23 and Figure S5.24). The dynamical behaviour of **TPPM** was studied performing the DSC analysis in a closed system, in which the solvent desorption is followed by the absorption process during the cooling path (Figure 5.21). This experiment was repeated several times to confirm the reversibility of the process; indeed, after each cycle the desorption (ΔH_{Des}) and absorption (ΔH_{Abs}) enthalpies did not

show any significant change. This suggests that also the amount of absorbed and released guest after every repetition remains constant.

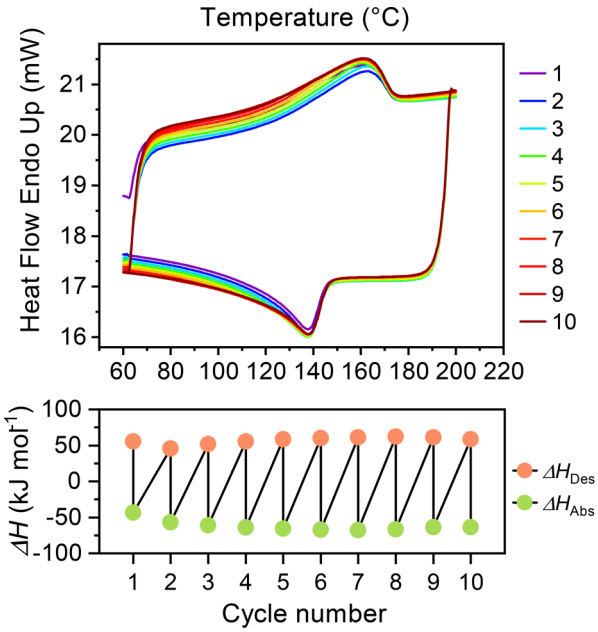

Figure 5.21: Absorption-Desorption cycles performed through DSC analysis in a close system; the **TPPM·CHCl₃** phase was used as reference. (*Top*) Different thermograms collected for each cycle. (*Bottom*) Enthalpy of desorption and absorption reported for each cycle.

To further investigate the selectivity of the guests, their packing coefficient was calculated as the ratio between the guest volume (V_{Guest}) and the volume of the guest-binding site (V) present in the **TPPM·S** phase (see Section 5.3.4 in the SI). This parameter has been proposed by Rebek to predict the best binding accommodation of guests inside molecular capsules in solution, which is reached when the coefficient is *ca.* 55%. [64]

$$PC_{guest}(\%) = \frac{V_{guest}}{V} \cdot 100 \qquad (5.1)$$

where V_{gues} is the guest molecule volume and V is the binding site volume.

Recently, this method has been shown to work nicely also for the absorption of gases inside the pores of supramolecular hosts.[65] Indeed, it is remarkable that in our case, both $CHCl_3$ and DCE show a packing coefficient of 55 and 56%, respectively, and almost all the other guests that are absorbed by **TPPM** present packing coefficients in the range 60-70%. On the contrary, all the solvents that are not uptaken or form unstable host-guest complexes, show a low coefficient packing, typically in the range 35-44%.

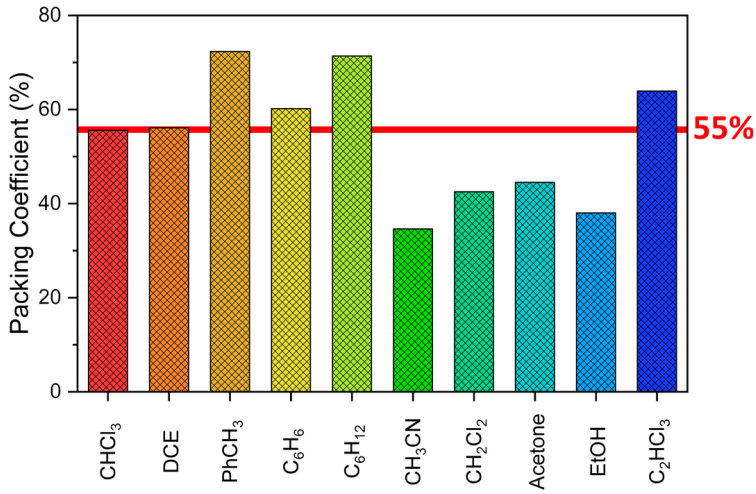

Figure 5.22: Packing coefficients (PC) comparison between the investigated **TPPM-S** phases. PC values are calculated in agreement with the relation proposed by Rebek (Equation 5.1).

The selective vapour uptake prompted us to investigate whether the solid-state spectroscopic properties of **TPPM** are influenced by the nature of the absorbed solvent. With this aim, UV-Vis absorption and emission spectra were recorded on powder samples of **TPPM** in thin layer form before and after their exposure to solvent vapours (Figure S5.27 and Figure S5.33). For all tested samples, the absorption profile (Figure S5.34) was found to be in good agreement with the one obtained for **TPPM** in DCM solution (Figure S5.26). On the contrary, in the emission spectra of the solid samples, the rising of a second, more intense band centred at 480 nm was observed (Figure 5.23a), in

addition to the one at 360 nm characteristic of the solubilized **TPPM**. This behaviour is in line with the formation of excimers in tightly packed crystalline structures of aromatic molecules, as confirmed by the excitation profiles.[66] Interestingly, the ratio between the emission intensity at the two maxima varies among all the series of tested solvates and differs from the **TPPM** empty form (Table S5.5).

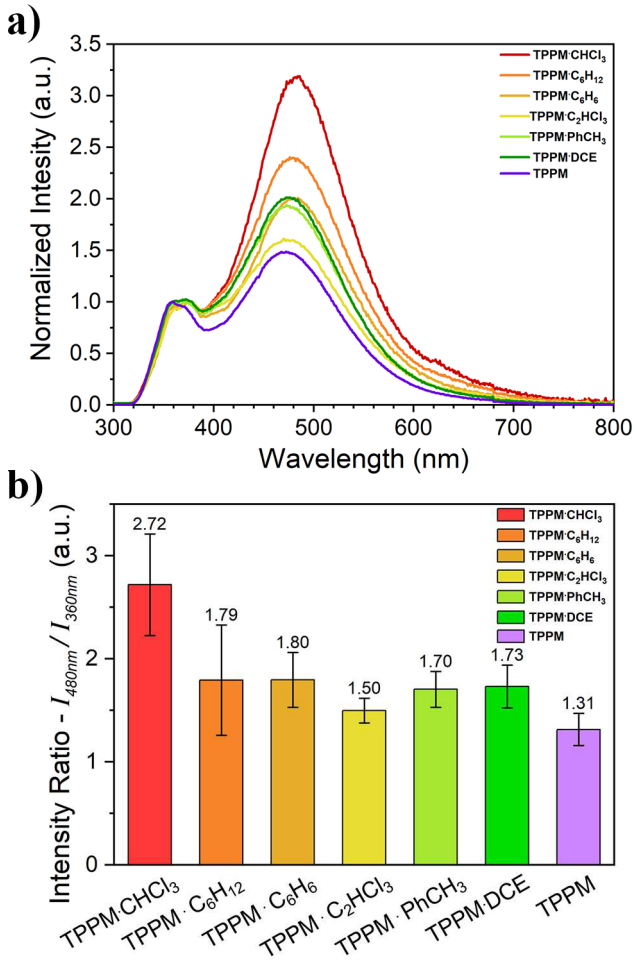

Figure 5.23: (a) Comparison of the solid-state emission spectra of the different **TPPM** solvates; (b) Diagram reporting the mean intensity ratio (I_{480nm}/I_{360nm}) values and their respective standard deviations.

As depicted by the diagram reported in Figure 5.23b, the emission spectra were collected for three different samples and the significance levels for each mean value of intensity ratio was obtained by one-way ANOVA calculation by Tukey Test. Only in the case of **TPPM·CHCl$_3$** a significance level lower than the threshold value of 0.05 was recorded. These results make **TPPM** a potential candidate for the uptake and detection of chloroform vapours in air. As volatile organic compound (VOC), the release of chloroform in the atmosphere resulting from a wide range of industrial activities is of high interest and has a severe impact on both human and environmental health.[67] In this respect, the stability of both **TPPM** and **TPPM-S** in presence of water is of particular relevance, as humidity is the main interferent in environmental monitoring of VOCs.

5.1.5 Conclusions

In summary, the crystal structures of the solvated and empty forms of a crystalline SOF based on the rigid, tetrahedral organic tecton **TPPM** were elucidated. This structural analysis, in which 3D ED has played an essential role, has paved the way for a deeper understanding of the dynamic behaviour of the material. This reversible single-crystal-to-single-crystal phase transition is remarkably triggered by a selective group of organic vapours; the origin of this selectivity has been also elucidated and lies in the difference of packing coefficient. In addition, it was shown that the solid-state fluorescence of **TPPM** is affected by solvent uptake. The combined features of dynamic behaviour and selectivity can be exploited in the recognition of chloroform vapours through fluorescence measurements. This study might be considered as another step towards a better comprehension of stimuli responsive materials held together by weak supramolecular interactions.

5.2 3D Electron Diffraction analysis of a novel, mechanochemically-synthesized SOF based on TPPM

As discussed in Chapter 5.1, the **TPPM**-based SOF exists in two forms: an empty, closed structure containing only small, isolated voids (**TPPM-E**), and an expanded framework endowed with channels that can be occupied by different guests (chloroform, ethanol, benzene, acetonitrile, etc.). In order to obtain the solvated, expanded form (**TPPM-S**), the empty form can be exposed to vapours of specific organic solvents (e.g. chloroform, trichloroethene and benzene) for a few minutes. Another way to obtain the expanded form consists in crystallising the tecton by slow evaporation of a solution with the desired solvent, typically chloroform. Chloroform can then be displaced by soaking the crystals for a couple of days in a different medium, preferably one in which **TPPM** shows very low solubility (such as, for example, ethanol or acetonitrile). An alternative approach consists in using mechanochemistry, an environmentally friendly synthetic strategy that has shown to be green, versatile, and efficient. [68–70] Mechanochemistry often yields microcrystalline materials that cannot be analysed with single-crystal X-ray diffraction methods. While in the past this was a severe obstacle, nowadays it has been demonstrated that this problem can be overcome by using three-dimensional electron diffraction (3D ED) directly on the crude reaction product (see Chapter 4). [60,71,72]

The increased interest induced by the success of 3D ED also triggered the development of dedicated instruments as an alternative to TEM architectures. The second section of this chapter (see Chapter 5.2) the structure solution and refinement of a novel, mechanochemically synthesized **TPPM-S** phase (**TPPM·BnOH**), characterized by partially filled channels, will be presented. The 3D ED analysis of this phase was carried out with the ELDICO ED-1, a novel electron diffractometer specifically designed to collect 3D ED data in a reliable and reproducible way. [73]

5.2.1 Mechanochemical Synthesis of the Novel TPPM-based SOF (TPPM·BnOH)

In order to synthesize the solvated form of the **TPPM**-based SOF, crystals of the empty form (**TPPM-E**; obtained by heating a batch of single crystals of **TPPM·CHCl3** at 100 °C for 2h) were manually ground in the presence of benzyl alcohol. The reaction consists of a liquid-assisted grinding (LAG) in which one of the reagents (BnOH) acts also as a liquid additive. The obtained mechanochemical product resulted to be crystalline, displaying a PXRD profile that could not be indexed as the SOF empty form (Figure 5.24).

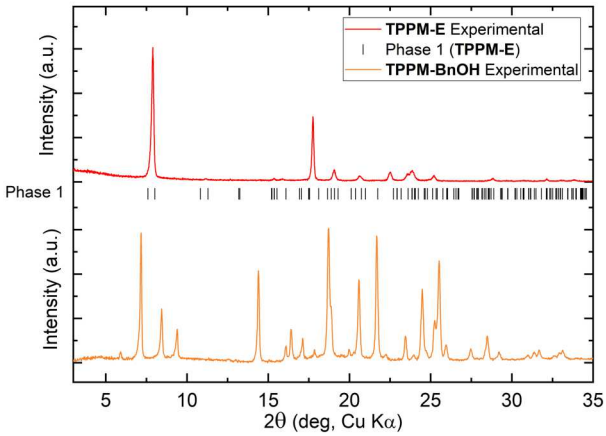

Figure 5.24: Powder X-ray profile of the **TPPM** empty form (red line) and calculated reflections (black sticks), compared to the mechanochemical product (orange line).

A probable strong preferred orientation and the low resolution of X-ray diffraction data hampered a structure solution based on PXRD characterisation and prompted us to try 3D ED. Although loaded with solvent molecules, the compound was stable under the electron beam and full data sets could be automatically collected.

5.2.2 3D ED Characterization of the Mechanochemical Product

The 3D ED analysis was carried out on the ELDICO ED-1 electron diffractometer (see Figure 5.25), a novel instrument designed specifically for an easy access to diffraction experiments and not specifically for imaging (which, on the contrary, is the original application of a TEM). This results in a horizontal setup, unusual for an electrons-based machine, in which the sample rotates around a vertical axis and the number of lenses is limited to just the illumination and scanning system. The diffractometer is assembled out of three crucial components: the electron beam system, the goniometer and a single electron detector. A detailed description of each can be found in Section 5.4 (Supplementary Information-B).

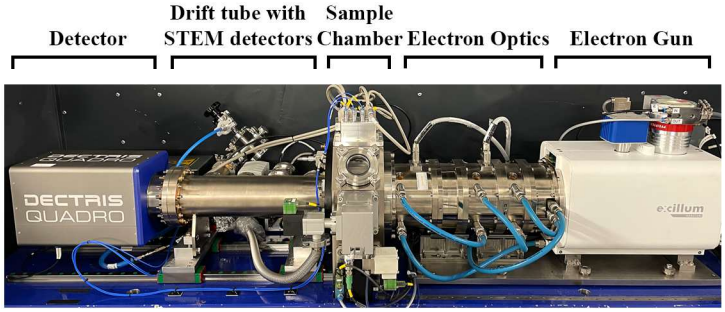

Figure 5.25: Photograph of the ELDICO ED-1 electron diffractometer setup. The sample chamber has an octagonal shape with several ports, of which the goniometer connection, a window, and the load lock for vacuum transfer are visible.

The nanocrystalline powder was directly characterized, as synthesised, through 3D electron diffraction analysis (3D ED). The sample was prepared with the procedure reported in section 5.4.3. The data collection was conducted in continuous rotation mode with a beam diameter of ~750 nm. This modality is analogous to a single-crystal X-ray experiment with an area detector; however, in the case of electrons, the much stronger interaction with matter allows a faster data collection on remarkably smaller crystal volumes compared to X-rays. The 3D ED experiments lasted only few minutes. The

availability of very sensitive and fast single electron detectors like the Dectris QUADRO does not require the use of an intense beam, therefore the total electron dose is minimized. [61] The high mechanical stability of the vertical goniometer guarantees that, after a fine optimization of the eucentric position, the nanocrystal is maintained in a stable position inside the electron beam during the whole rotation.

The crystals suitable for the 3D ED analysis were searched through STEM imaging and their crystal quality was preliminarily checked with a single diffraction pattern, placing the beam on the crystal of interest.

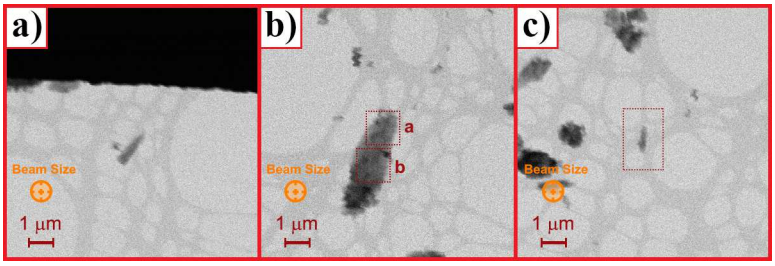

Figure 5.26: STEM-Images of the three **TPPM·BnOH** microcrystals used for the 3D ED data collection. (a): Crystal 1; (b): Crystal 2. The dotted squares highlight the two areas in which data collection 2^a and 2^b were conducted; (c): Crystal 3.

Three different microcrystals were characterised in order to maximize the data completeness (Figure 5.26, Table S5.8). Despite the **TPPM**-based crystals being quite sensitive to the electron beam, as previously checked on a standard TEM, the electron diffractometer configuration allowed a complete 3D ED experiment. Indeed, ED frames were collected over 109° of reciprocal space, with a resolution of 1.2 Å, avoiding the amorphization of the crystals or any visible resolution loss at the end of the experiment (Figure S5.36). For the three analysed crystals, four datasets were collected. The PETS2 software [74] was employed to analyse the diffraction patterns, in order to find the unit cell, index and integrate the reflection intensities.

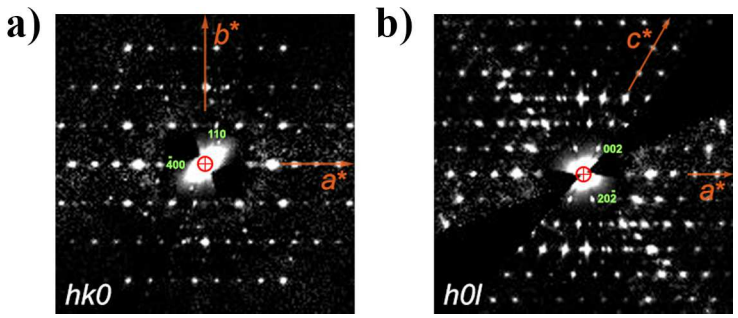

Figure 5.27: Section of the reciprocal space, reconstructed with PETS2 from the 3D ED data. (a) *hk0* reciprocal plane section showing the extinction rule $h + k = 2n$. (b) *h0l* reciprocal plane section showing the angle $\beta^* \approx 61°$ and the reflection condition for the *c* glide plane, $l = 2n$. The reciprocal space sections are calculated on the merged data sets of crystals 1, 2 and 3.

Despite the presence of some spurious reflections coming from other small crystals falling inside the illuminated area, the reconstructed reciprocal space (Figure 5.27) could be unambiguously indexed with a monoclinic C-centred lattice with parameters $a = 27.907(7)$, $b = 7.0195(7)$, $c = 21.592(3)$, $\beta = 118.821(12)$ (Å and °,Table S5.9). The C-centring extinction rule and the *c* glide clearly observed in the *h0l* plane led to the identification of the C1*c*1 extinction symbol compatible with C*c* and C2/*c* space groups. The indexed data were then integrated with the fit profile model of PETS2, in which the mosaicity and resolution dependence of the peak width are refined globally, and then the orientation of each pattern (geometrical optimization) was optimized (Figure S5.37).

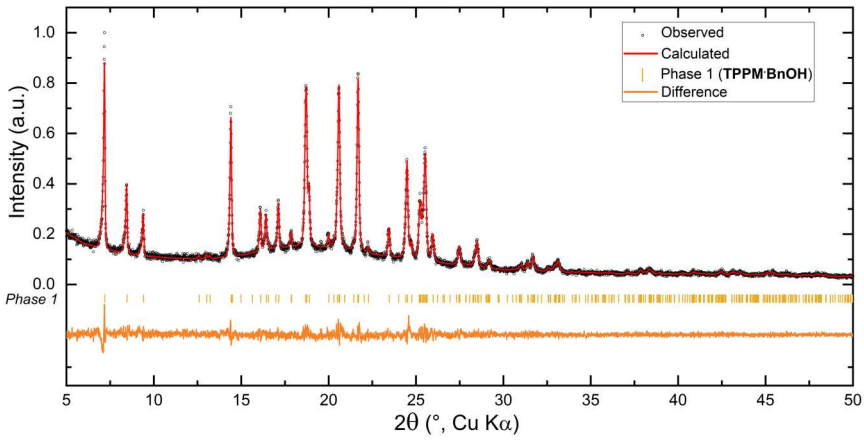

Figure 5.28: Profile fit from LeBail refinement on **TPPM·BnOH**. The shown range is limited to 2ϑ values of 5-50 for clarity, whereas the refinement was carried out in the range 5-75°. The refinement converged to Rp = 5.77%, wRp = 7.68% and GOF = 2.87.

The correct unit cell determination was checked on PXRD data through a LeBail refinement (Figure 5.28). The refinement converges to slightly bigger unit cell parameters with respect to those obtained from the electron diffraction data (Table S5.10). This result can be ascribed to a loss of solvent molecules due to the strong vacuum condition inside the electron diffractometer column. It is well known that porous materials, like MOFs and SOFs, have the capability to release the guest molecules held inside their pores, and this process is accelerated by vacuum and heat. Indeed, under the previously mentioned stimuli, the expanded, solvated form of the **TPPM**-based SOF could easily release guest molecules, such as $CHCl_3$, EtOH, C_6H_6 and CH_3CN (Chapter.5.1.4). [1] However, the fact that the unit cell volume remains significantly larger than that of the empty phase (Table S5.10) indicates that the BnOH release is only partial and the remained molecules in the pores can stabilize the expanded form of the **TPPM**-based SOF also under high vacuum (~10^{-7} mbar) conditions. This is quite unusual for this SOF since with all other solvents the only phase detected in high vacuum was the empty one.

The datasets collected from the analyzed crystals were merged together (using the merging procedure of PETS2), and the structural model was then solved *ab-initio* with standard direct methods in space group C*2/c*. The model was initially refined kinematically, i.e., with the measured intensity considered proportional to the square modulus of the structure factor. The kinematically refined model revealed the formation of a supramolecular network characteristic of the SOF expanded form, [1] in which the **TPPM** molecules are mainly involved in CH···N interactions (Figure 5.29).

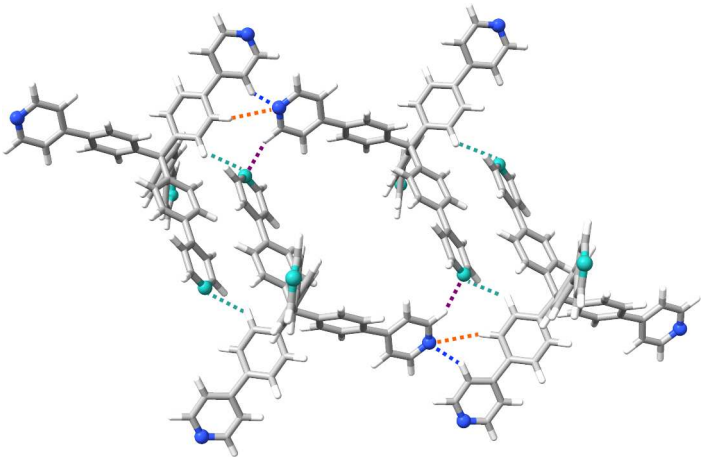

Figure 5.29: View of the main C-H···N interactions in **TPPM·0.5BnOH**. The N atoms involved in the interaction are represented as turquoise (N1A) and blue (N1B) spheres. Solvent molecules have been omitted for clarity. The interactions N1A···C3B, N1B···C9A, N1A···C10B and N1B···C4B are shown by purple, orange, blue and turquoise dashed lines, respectively.

The existence of BnOH molecules inside the pores was highlighted by the difference Fourier map calculation, which shows the presence of residual electrostatic potential in the framework channels (Figure 5.30a). The modelling of the guest molecules embedded in the SOF channels showed them to be disordered over two equivalent positions, each with occupancy of *ca.* 0.25 (Figure 5.31); they were then modelized as rigid body molecules, in a ratio of 1:2 with respect to **TPPM**. The solvent stoichiometry calculated from

thermogravimetric and NMR analysis over the crude product shows a ratio of **TPPM** and BnOH near to 1:1 (Figure S5.41, Figure S5.42). This result confirms that, during the diffraction experiment, a partial removal of BnOH has taken place under vacuum, as suspected from the moderate decrease in the lattice parameters detected with respect to PXRD data.

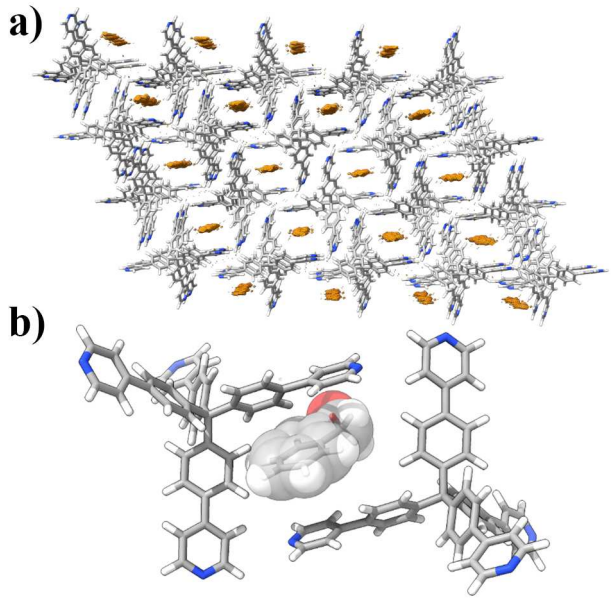

Figure 5.30: (a) Difference Fourier Map calculated on the **TPPM** supramolecular network free of guest molecules. The electrostatic potential is reported as an orange surface (isosurface level 2.5σ[ΔV(r)]), with the nitrogen atoms in blue, carbon atoms in light grey and hydrogen atoms in white. (b) View of the benzyl alcohol guest packed between two **TPPM** molecules in the **TPPM·0.5BnOH** crystal phase. For clarity reasons, only one of the two possible orientations of the BnOH molecule is displayed. The oxygen atoms are represented in red, carbon atoms in grey, nitrogen atoms in blue and hydrogen atoms in white. The solvent molecule is shown in space-filling mode.

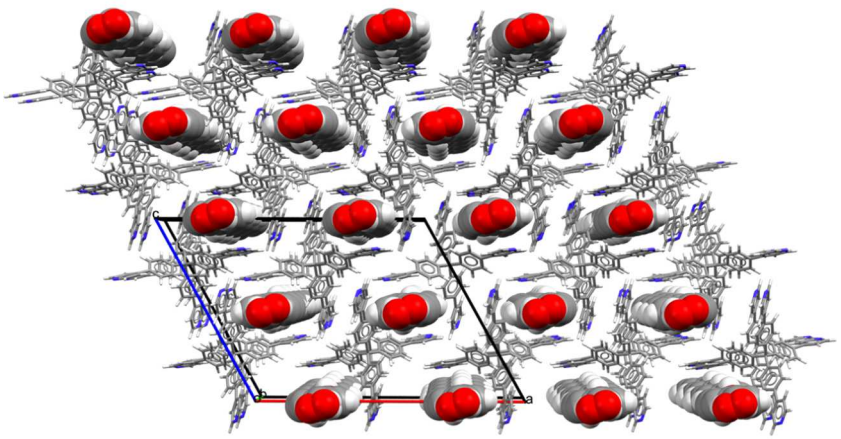

Figure 5.31: The **TPPM·0.5BnOH** structural model oriented along the crystallographic *b*-axis. The oxygen atoms are represented in red, carbon atoms in grey, nitrogen atoms in blue and hydrogen atoms in white. The disordered solvent molecules are shown in space filling mode.

To further improve the **TPPM·0.5BnOH** structural model and have better agreement between the experimental and calculated intensities, a dynamical refinement, which takes into account multiple scattering effects through a full Bloch calculation,[62] is needed. However, if we want to keep the high coverage obtained by merging data from different crystals, we are obliged to perform the refinement against multiple data sets, one for each crystal, since for each different crystal the dynamical effects will be different due to their different thickness. We considered three different crystal data sets (crystal 2^a, 2^b, 3) and refined the structure dynamically against these three data sets simultaneously. Remarkably, the electron diffraction data quality proved suitable for a dynamical refinement and the refinement successfully converged. The dynamical refinement requires to consider and refine, together with the structural model, the thickness of the sample at zero degrees of tilt. In the case of multiple data sets the number of refined thicknesses equals the number of crystals involved (in our case crystal 2^a: 645 Å, crystal 2^b: 578 Å, crystal 3: 738 Å). The dynamical data treatment allowed, as expected, a significant

reduction of the agreement factors: the R_1(obs) value was reduced from 27.47% to 14.42%. The atoms displacement parameters were also refined without any restraints, leading to a structural model that better represents the mobility of the pyridyl rings with respect to the inner phenyl groups (Figure S5.40). From the calculation of the difference Fourier map, it was also possible to detect the positions of 80% of the hydrogen atoms of the **TPPM** molecule (Figure 5.32).

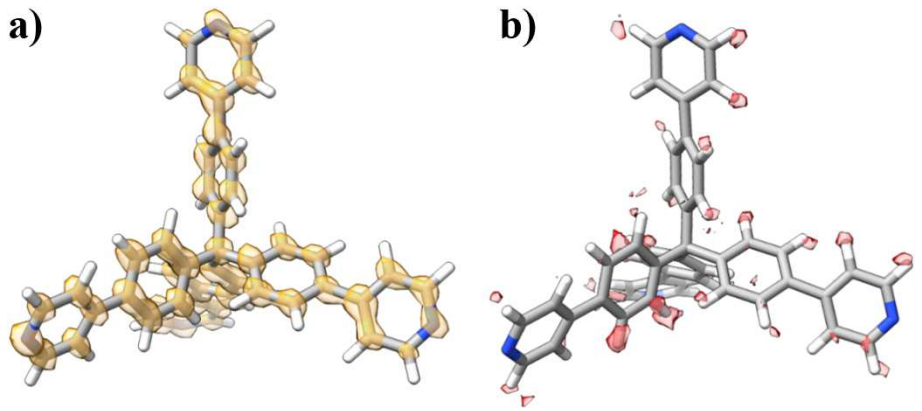

Figure 5.32: (a) Superposition between the calculated potential map and the **TPPM** molecule, in the dynamically refined phase of **TPPM·0.5BnOH**. (b) Superposition between the difference potential map, calculated from the structural model without H atoms, and the **TPPM** molecule from the **TPPM·BnOH** structure after the dynamical refinement. The Fourier map and difference map are represented with an isosurface level of $2\sigma[\Delta V(r)]$.

5.2.3 Conclusions

A new expanded phase of a **TPPM**-based SOF was synthesized by mechanochemical synthesis. The crystal structure of the as-synthesized product was elucidated by 3D ED analysis with a novel electron diffractometer. This is one of the first structures solved with a horizontal electron diffractometer with a completely new design with respect to a standard TEM. The data quality allowed to solve the crystal structure of the SOF discovering that the vacuum inside the instrument was not enough to completely empty the channels. The residual BnOH molecules in the channels could be detected in the difference Fourier maps and their position properly refined. The structure could be also refined dynamically against multiple data sets collected on three crystals. To our knowledge, this is one of the first time in which such a procedure has been successfully attempted.

5.3 Supplementary Information – A (Chapter 5.1)

All commercial reagents and solvents were used as received. Tetrakis(4-bromophenyl)methane, tetrakis(triphenilphenilphospine)palladium(0) end 4-pyridineboronic acid were purchased from TCI Europe. All instrumental details related to the adopted characterization techniques are reported in their respective sections.

5.3.1 Synthetic Procedures

TPPM Synthesis

The synthesis was performed following the procedure reported by Kitagawa et.al.[45] Tetrakis(4-bromophenyl)methane (400 mg, 0.63 mmol) and toluene (15 mL) were added to a 100 mL Schlenk tube, followed by an aqueous solution of sodium carbonate (667 mg, 6.29 mmol, in 5 mL of H_2O) and an ethanol suspension of 4-pyridineboronic acid (546 mg, 85% purity, 3.77 mmol, in 12 mL of ethanol). The mixture was purged with Ar (bubbling for 20 minutes) and tetrakis(triphenylphosphine)palladium(0) (87 mg, 0.07 mmol) was added. The reaction mixture was heated at 90 °C for 3 days under stirring. The mixture was cooled to room temperature and the precipitate was filtered. The off-white solid was washed with H_2O (3 × 3 mL) and dried. Recrystallization from a 9:1 CH_2Cl_2/MeOH mixture afforded TPPM as colorless crystals (240 mg, 61% yield).

^{1}H NMR (400 MHz, CD_2Cl_2) δ (ppm): 8.59 (dd; J_1 = 4.7 Hz, J_2 = 1.85 Hz, 8H), 7.66 (d, J = 8.6 Hz, 8H), 7.58 (dd, J1 = 4.7 Hz, J2 = 1.8 Hz, 8H), 7.49 (d, J = 8.5 Hz, 8H).

Crystallization of TPPM·$CHCl_3$

TPPM (32 mg) was added to 20 mL of $CHCl_3$ in a 100 mL round bottom flask and left to reflux. The clear solution was cooled at room temperature and left to slowly evaporate, in order to obtain colourless needle crystals.

Crystallization of TPPM·C_6H_6

Crystals of **TPPM·C_6H_6** were prepared starting from large crystals of **TPPM·$CHCl_3$**; they were added in a 5-mL scintillation vial with 3 mL of C_6H_6. The TPPM·$CHCl_3$ crystals were left to soak for 3 days yielding the **TPPM·C_6H_6** solvate.

Crystallization of TPPM·EtOH

Crystals of **TPPM·EtOH** were prepared by soaking, following the same procedure described for **TPPM·C_6H_6**, using EtOH instead of C_6H_6.

Crystallisation of TPPM·0.5CH_3CN

Crystals of **TPPM·0.5CH_3CN** were prepared by soaking, following the same procedure described for **TPPM·C_6H_6**, using **CH_3CN** instead of C_6H_6.

Solvent vapour absorption experiment

TPPM crystals were placed in an oven at 100°C to completely remove any traces of the solvent absorbed molecules. The activated **TPPM** crystals were subsequently placed in a closed vessel, previously saturated with vapours of a specific solvent and left for 2 minutes.

5.3.2 Solid-State Characterization

Single-crystal X-ray diffraction (SC-XRD)

The crystal structures of **TPPM·CHCl$_3$**, **TPPM·EtOH**, **TPPM·C$_6$H$_6$** and **TPPM·0.5CH$_3$CN** were determined by X-ray diffraction on single crystals. The structure of the empty form of **TPPM** was solved by 3D Electron Diffraction (see next section). Crystal data and experimental details for data collection and structure refinement are reported in Table S1. Intensity data and cell parameters were recorded at 200(2) K [167(2) K for **TPPM·0.5CH$_3$CN**] on a Bruker D8 Venture PhotonII diffractometer (CuKα radiation λ = 1.54178 Å). The raw frame data were processed using SAINT and SADABS to yield the reflection data files.[75] The structures were solved by Direct Methods using the SHELXT program[76] and refined on F_o^2 by full-matrix least-squares procedures, using SHELXL-2018[77] in the WinGX suite v.2014.1.[78] All non-hydrogen atoms were refined with anisotropic atomic displacements, with the exception of some of the disordered solvents. The hydrogen atoms were included in the refinement at idealized geometry and refined "riding" on the corresponding parent atoms. The weighting schemes used in the last cycle of refinement were $w = 1/ [\sigma^2 F_o^2 + (0.1661P)^2 + 5.9859P]$, $w = 1/ [\sigma^2 F_o^2 + (0.1710P)^2 + 4.3284P]$, $w = 1/ [\sigma^2 F_o^2 + (0.3487P)^2]$, and $w = 1/ [\sigma^2 F_o^2 + (0.2669P)^2]$, where $P = (F_o^2 + 2F_c^2)/3$, for **TPPM·CHCl$_3$**, **TPPM·EtOH**, **TPPM·C$_6$H$_6$** and **TPPM·0.5CH$_3$CN**, respectively. The crystallographic data have been deposited with the Cambridge Crystallographic Data Centre as supplementary publication no. 2194027, 2194028, 2194029 and 2194030.

Table S5.1: Crystallographic data for **TPPM·CHCl$_3$**, **TPPM·EtOH**, **TPPM·C$_6$H$_6$**, **TPPM·0.5CH$_3$CN**, **TPPM·DMF**,[44] **TPPM·DMSO**[45] and **TPPM**.

Formula	**TPPM·CHCl$_3$**	**TPPM·EtOH**	**TPPM·C$_6$H$_6$**	**TPPM·0.5CH$_3$CN**	**TPPM·DMF**	**TPPM·DMSO**	**TPPM**
Formula	$C_{43}H_{32}N_4{\cdot}CHCl_3$	$C_{43}H_{32}N_4{\cdot}C_2H_6O$	$C_{43}H_{32}N_4{\cdot}C_6H_6$	$C_{43}H_{32}N_4{\cdot}0.5(C_2H_3N)$	$C_{43}H_{32}N_4{\cdot}C_3H_7NO$	$C_{43}H_{32}N_4{\cdot}C_2H_6OS$	$C_{43}H_{32}N_4$
Formula weight	748.11	674.81	706.85	649.27	701.84	706.87	628.8
Crystal system	Monoclinic	Monoclinic	Monoclinic	Monoclinic	Monoclinic	Monoclinic	Monoclinic
Space group	C2/c	C2/c	C2/c	C2/c	C2/c	C2/c	C2/c
a/Å	27.9292(5)	28.0868(10)	28.074(2)	28.194(3)	27.985(4)	27.918(3)	31.4066
b/Å	6.9946(1)	7.0429(2)	7.0379(4)	7.0654(7)	7.0302(9)	6.9508(6)	7.1129
c/Å	21.4760(4)	21.2863(8)	21.3400(10)	21.254(3)	21.501(3)	21.315(2)	22.063
a/°	90	90	90	90	90	90	90
β/°	120.139(1)	120.765(1)	120.782(4)	122.335(7)	121.0620(10)	119.427(4)	133.175
g/°	90	90	90	90	90	90	90
V/Å^3	3628.2(1)	3618.1(2)	3622.4(4)	3577.2(7)	3623.55	3602.58	3594.34
Z	4	4	4	4	4	4	4
D$_c$/g cm^{-3}	1.370	1.239	1.296	1.206	1.286	1.303	1.162
F(000)	1552	1424	1488	1364	1480	1488	1320
μ/mm^{-1}	2.598	0.580	0.585	0.552	0.078	0.134	-
$\vartheta_{min,max}$/°	3.66, 79.57	3.66, 72.43	3.66, 72.50	3.71, 59.2	3.02, 25.00	2.19, 30.05	0.12, 1.2
Reflections collected/unique	42954 / 3913	38183 / 3582	39587 / 3592	14926/2569	16397 / 3169	38910 / 5272	31938
	[R(int) = 0.0380]	[R(int) = 0.0579]	[R(int) = 0.0693]	[R(int) = 0.0855]	[R(int) = 0.0497]	[R(int) = 0.0343]	
R [Fo>4s(Fo)]^a, wR$_2$^{a}	0.0796, 0.2499	0.0706, 0.2362	0.0955, 0.3452	0.1089, 0.3152	0.0451, 0.1057	0.0604, 0.1530	0.1148, 0.1302

$^a R_1 = \Sigma||F_o|-|F_c||/\Sigma|F_o|$, $wR_2 = [\Sigma[w(F_o^2 - F_c^2)^2]/\Sigma[w(F_o^2)^2]]^{1/2}$

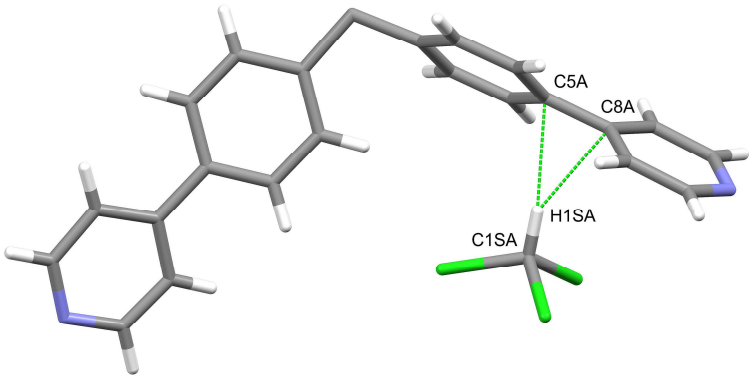

Figure S5.1: Detail of the C-H···$C_{aromatic}$ interactions in **TPPM·CHCl$_3$**. C1S··C5A and·C1S-H1S···C5A: 3.365(3) Å and 166.9(5)°; C1S··C8A and·C1S-H1S···C8A: 3.209(2) Å and 150.0(6)°.

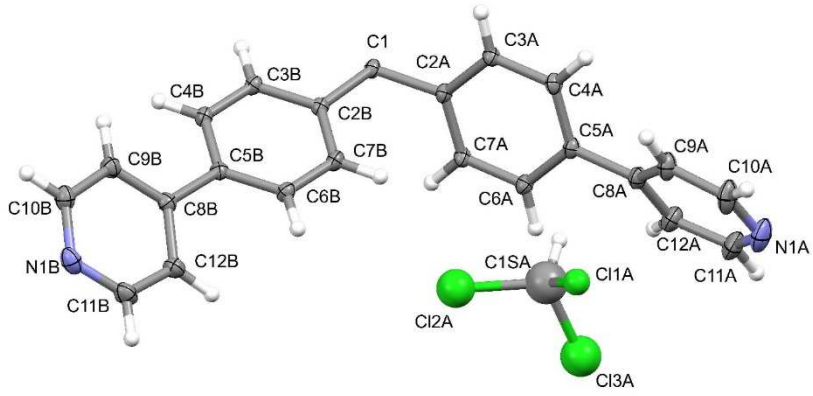

Figure S5.2: Ortep view of the asymmetric unit of **TPPM·CHCl$_3$**. Only one possible orientation for chloroform is shown for clarity.

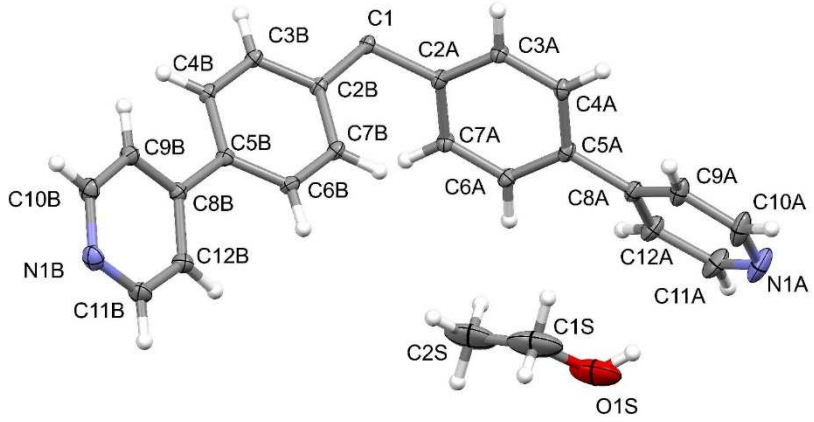

Figure S5.3: Ortep view of the asymmetric unit of **TPPM·EtOH**. Only one orientation of ethanol is shown for clarity.

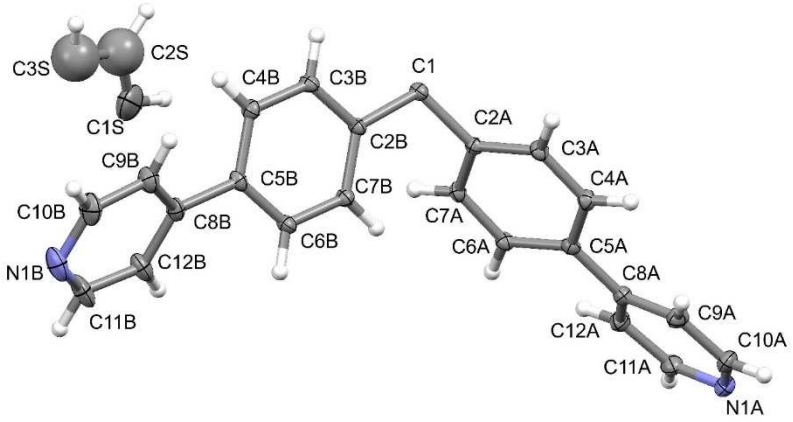

Figure S5.4: Ortep view of the asymmetric unit of **TPPM·C_6H_6**.

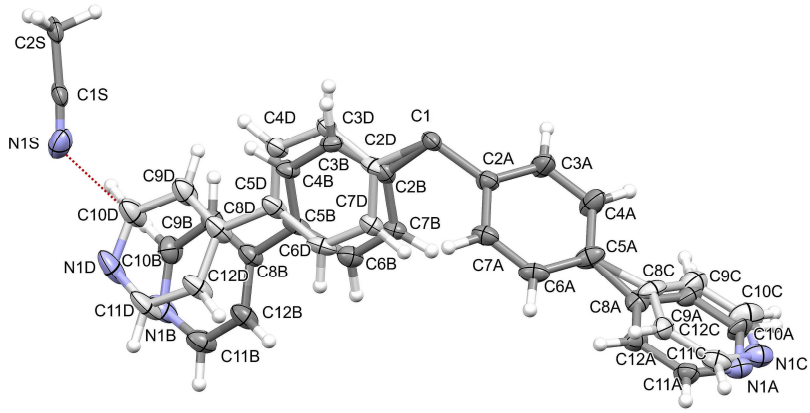

Figure S5.5: Ortep view of the asymmetric unit of **TPPM·0.5CH$_3$CN.** The second orientation of **TPPM** is shown in light grey. The C10B-H10B···N1S interaction [3.439(3) Å; 123.7(4)°] is shown as a red dotted line.

Hirshfeld surface analysis

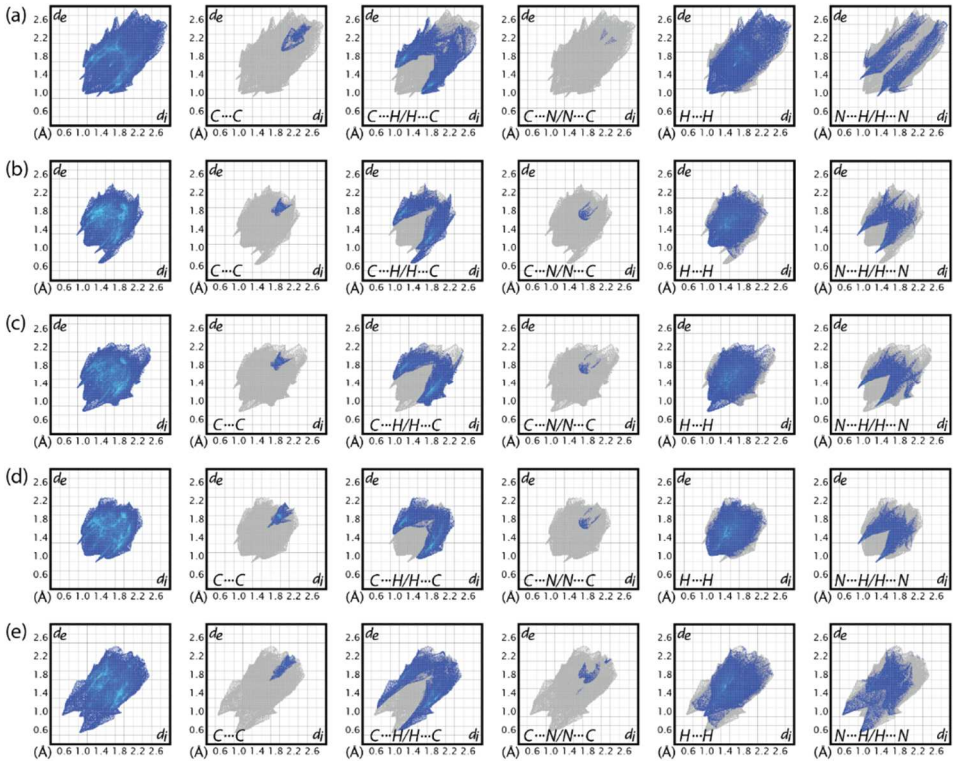

Figure S5.6: Comparison of the fingerprint plots of (a) **TPPM** in the empty form and in (b) **TPPM·CHCl$_3$**, (c) **TPPM·EtOH**, (d) **TPPM·C$_6$H$_6$** and (e) **TPPM·0.5CH$_3$CN**.

Table S5.2: Percentage of the interaction shown in the fingerprint plots.

Interaction	Empty	Chloroform	Ethanol	Benzene	CH$_3$CN-Filled
C···H/H···C	33.5	28.2	31.3	31.5	33.5
C···C	2.2	2.1	2	4.2	2.6
C···N/N···C	0.1	0.6	0.4	0.5	0.9
N···H/H···N	17.2	14.5	14.6	14.5	18.4
H···H	47	41.8	48.6	49.3	44.6
O···C/C···O	-	-	0.5	-	-
O···H/H···O	-	-	2.6	-	-
C···Cl/Cl···C	-	4.2	-	-	-
Cl···H/H···Cl	-	8.3	-	-	-
Cl···N/N···Cl	-	0.3		-	-

3D Electron Diffraction (3D ED)

Scanning transmission electron microscopy imaging and 3D electron diffraction have been carried out on a Zeiss Libra 120 transmission electron microscope, equipped with a LaB_6 thermionic source operating at 120 kV (λ=0.0335 Å) and a Timepix single-electron detector by ASI for collecting diffraction patterns in low dose mode. 3D electron diffraction data were collected on single nanocrystals in nanodiffraction mode with a parallel electron beam of 150 nm in diameter. The diffraction patterns were collected in stepwise mode, with an angular step of 1° covering an angular range of 120°. The data collection was carried out in precession mode with a parallel beam precessing on a cone surface with a 1° semiangle aperture (PEDT protocol), in order to increase the reciprocal space integration. Imaging was carried out in STEM mode with a high angular dark field detector (HAADF). Crystal data and experimental details for data collection and structure refinement are reported in Table S5.1. The 3D ED data were analysed using the software PETS.[74] Ab-initio structure determination of **TPPM** was performed by Standard Direct Methods using the SIR2019 package.[79] Data were initially refined with a fully kinematical approximation, i.e. neglecting dynamical scattering and assuming that I_{hkl} is proportional to $|F_{hkl}|^2$. Least-squares structure refinement was performed with the software SHELXL-2014[77] interfaced with ShelXle.[80] The kinematically refined structure was subsequently refined taking into account the dynamical diffraction theory (multiple scattering) of electrons. The diffraction data were properly integrated for the dynamical refinement using PETS. Dynamical refinement of **TPPM** was carried out with the software suite Jana2006.[81] Crystallographic data for **TPPM** have been deposited with the Cambridge Crystallographic Data Centre as supplementary publication no. 2194031.

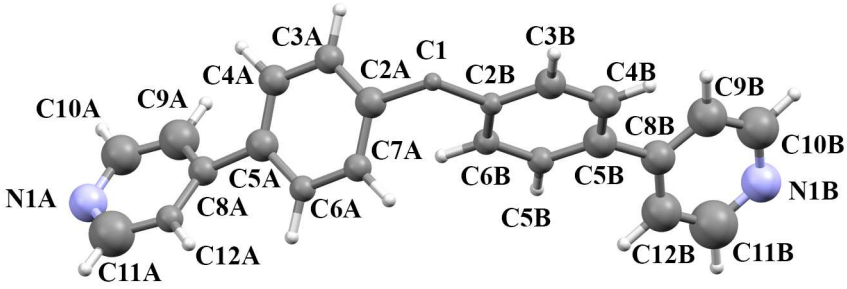

Figure S5.7: Ortep view of the asymmetric unit of **TPPM**.

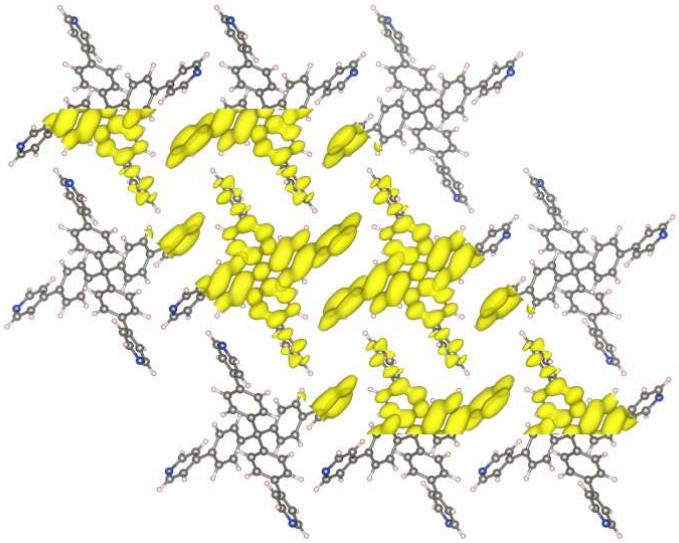

Figure S5.8. Electrostatic potential map of the **TPPM** structural model, visualized as isosurface within the unit cell border. The potential map is calculated from the dynamically refined structure by Fourier map calculation.

Powder X-ray Diffraction (PXRD)

The PXRD patterns of the samples were collected using Ni-filtered Cu Kα radiation ($\lambda_{K\alpha1}$ = 1.5406 Å, $\lambda_{K\alpha2}$ = 1.5444 Å), on a Rigaku SmartLab XE diffractometer equipped with a HyPix-3000 detector. The data were preliminarily processed with SmartLab Studio II (by Rigaku). Standard PXRD patterns were collected in Bragg-Brentano geometry in the 2ϑ range 5-35°, placing the sample on a silicon zero background specimen holder. Temperature-resolved *in situ* data collections were performed using a TTK 600 temperature chamber by Anton Paar, collecting each pattern in a 2ϑ range of 5-27° in 5 minutes during the heating ramp (1°C min^{-1}).

The LeBail refinement on powder X-ray diffraction data, from temperature-resolved analysis, was carried out with Jana2006.[81] The background was described by manually-picked points, the unit cells were defined from single crystal data (SC-XRD or 3D ED) and the profile parameters were obtained by cyclic refinements on the entire dataset. The convergence residual values of each diffraction pattern are reported in Table S3. The diffraction profile temperature is the mean value between initial and final data collection temperatures. Each diffractogram, collected during the temperature resolved experiment, was analyzed through LeBail refinement. The profile data obtained from the refinement were used for the phase fraction estimation of **TPPM·S** (**TPPM·CHCl3**) and empty **TPPM**. For both phases, a characteristic reflection was selected: (-202) for **TPPM** at 2ϑ = 8.02° and (111) for **TPPM·S** at 2ϑ = 14.39°. The phase fraction calculation was performed comparing the peak area of the characteristic reflection for each powder diffraction pattern, in accordance with Equation S5.1.

$$\chi_{TPPM}(T) = \frac{A_{TPPM}(T)}{A_{TPPM}(T) + A_{TPPM-S}(T)} \cdot 100 \qquad \text{(S5.1)}$$

where $\chi_{TPPM}(T)$ is the **TPPM** phase fraction at the temperature T, while $A_{TPPM}(T)$ and $A_{TPPM\text{-}S}(T)$ are the areas of the (-202) and (111) reflections, respectively, for **TPPM** and **TPPM·CHCl3** at the temperature T.

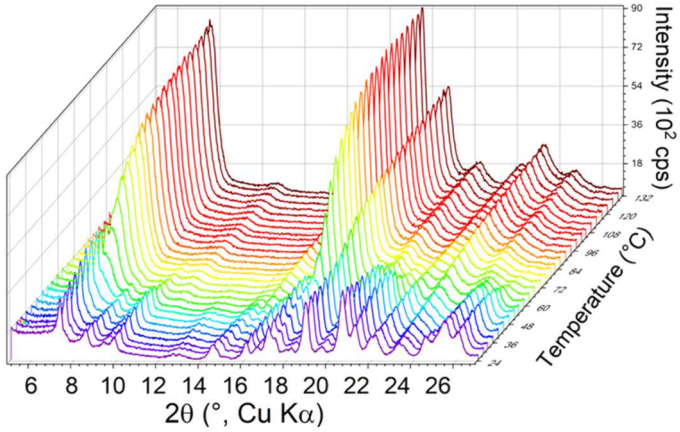

Figure S5.9: X-ray powder profile series collected during the temperature-resolved analysis.

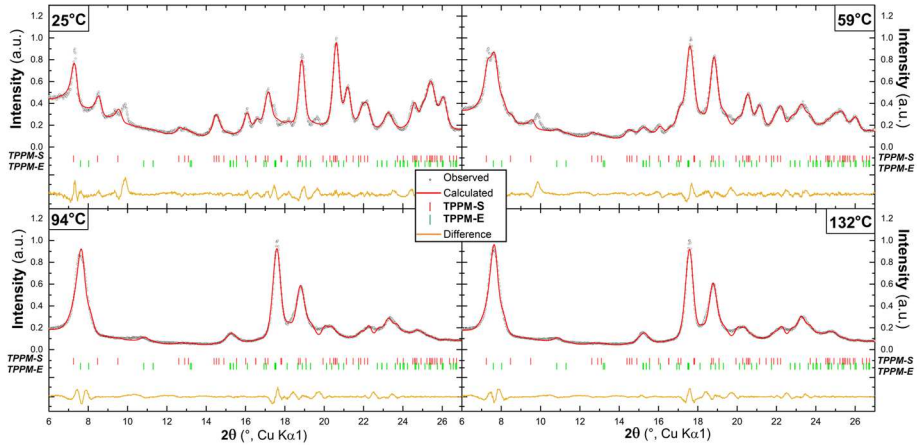

Figure S5.10: Profile fit from LeBail refinement performed on specific diffractograms at characteristic temperatures of the PXRD desorption monitoring experiment. The convergence residual values are reported in Table S5.3.

Table S5.3: Profile parameters of Le Bail refinement for each diffractogram collected during the temperature-resolved experiment.

Temperature (°C)	R_p (%)	R_{wp} (%)
21	5.4844	7.9947
25	5.4121	8.0852
29	5.5843	8.3577
32	5.7252	8.8281
36	5.7962	9.1395
40	6.1616	9.7719
44	6.0805	10.053
48	5.9376	9.7978
52	5.4259	9.2085
55	5.1261	8.2017
59	5.0332	7.3885
63	5.0167	6.9963
67	5.1857	7.0132
71	5.4371	7.4023
75	5.4544	7.346
79	5.4411	7.3796
82	5.4497	7.3435
86	5.5465	7.4895
90	5.4314	7.2961
94	5.3235	7.2297
98	5.3435	7.1588
102	5.2542	7.1246
105	5.2839	7.1011
109	5.1544	6.9531
113	5.2909	7.008
117	5.3109	7.0219
121	5.1686	6.8925
125	5.2629	6.9829
129	5.2704	6.8826
132	5.2591	6.9453

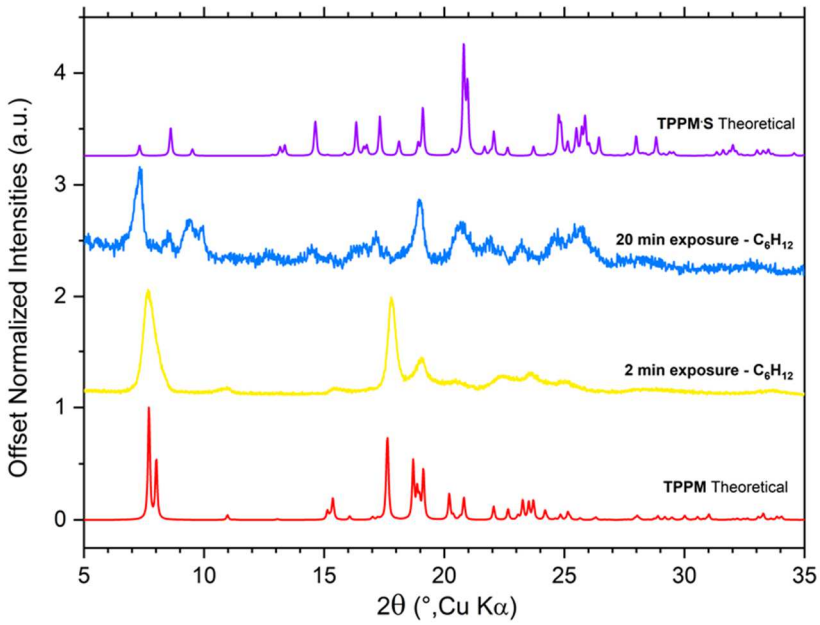

Figure S5.11: Powder X-ray diffractograms of **TPPM** after 2 min and 20 min of exposure to cyclohexane vapors.

5.3.3 Thermal Characterizations

Differential Scanning Calorimetry (DSC)

Differential scanning calorimetry analyses were performed with a Perking Elmer instrument, model DSC6000. The desorption analyses were performed in holed pans with a heating rate of 5°C min^{-1} in a temperature range of 30-220 °C. The cyclic absorption-desorption experiment was performed in a closed pan with a heating rate of 10 °C min^{-1} in a temperature range of 60-200°C.

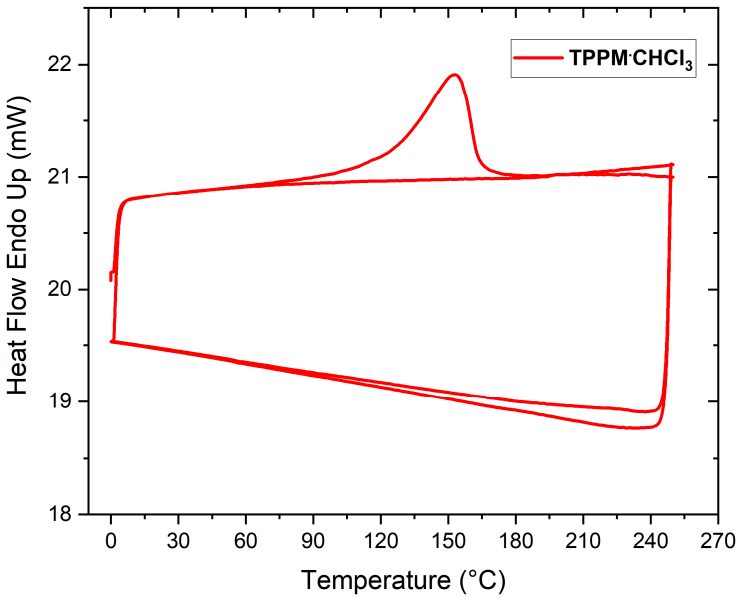

Figure S5.12: DSC thermogram of the **TPPM·$CHCl_3$** phase, performed with two heating-cooling cycles to highlight the stability of the **TPPM** phase after solvent removal.

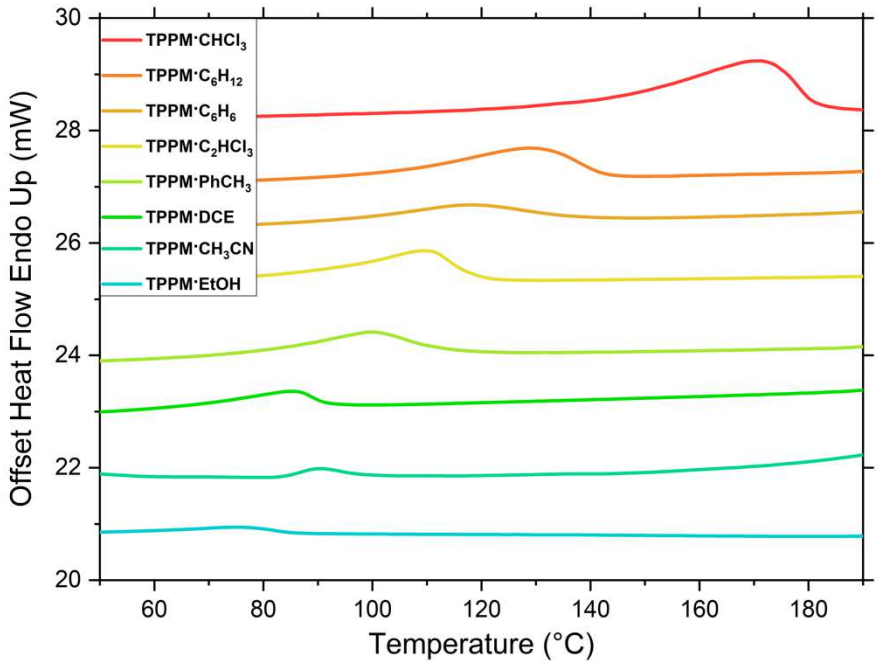

Figure S5.13: Comparison of the thermograms of various **TPPM** solvates highlighting the different heats of desorption; only the heating ramps have been reported. The dichloroethane solvate (**TPPM·DCE**) presents an intermediate value of ΔH_{Des} that can probably be related to its low pore occupancy.

Thermogravimetric Analysis (TGA)

Thermogravimetric analyses were performed with a Perking Elmer instrument, model TGA 8000. The desorption process leading to the weight loss was performed under a heating rate of 5°C min^{-1} in a temperature range of 30-220 °C.

Relation adopted for the solvate stoichiometry (SS^{TGA}) calculation from TGA data:

$$SS^{TGA} = \frac{\Delta W(\%) \cdot (MW_{TPPM} + MW_{Guest})}{MW_{Guest}} \quad \text{(S5.2)}$$

where $\Delta W(\%)$ is the measured weight loss percentage, while MW_{TPPM} and MW_{Guest} are the **TPPM** and Guest molar weight, respectively.

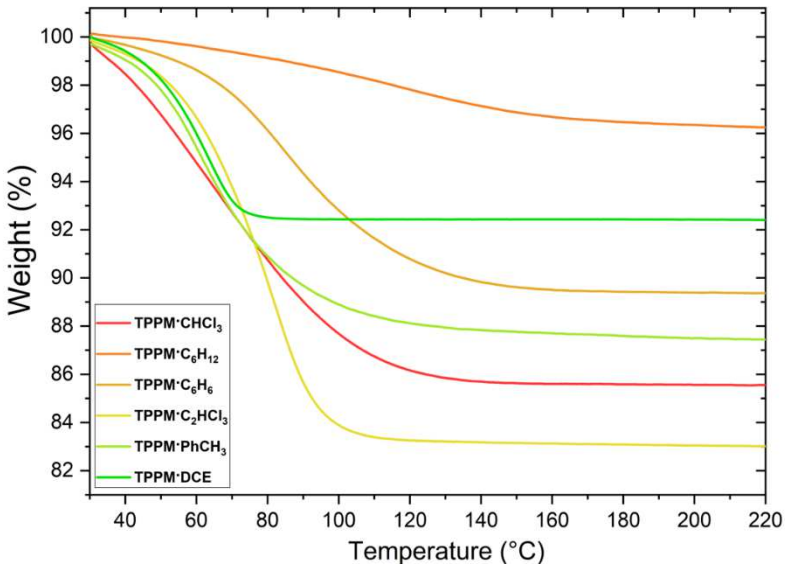

Figure S5.14: Comparison of the thermogravimetric path for different **TPPM-S** forms.

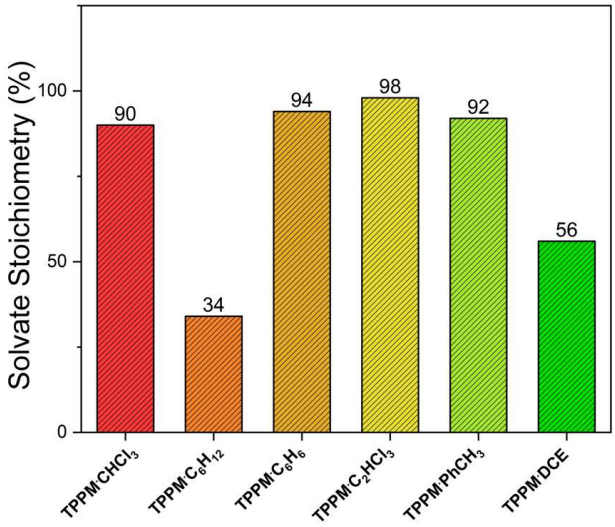

Figure S5.15: Comparison of the solvate stoichiometry among the **TPPM** solvates. The solvate stoichiometry (SS^{TGA}) was estimated from TGA data using Equation S5.2.

5.3.4 Packing Coefficients Calculation

The packing coefficients were calculated as the ratio between the guest volume (V_{Guest}) and the volume of the guest binding site (V) present in the **TPPM-S** phase (Equation S5.3). Guest volumes were calculated combining the van der Waals Volume (v_W) with the probe (radius 1.2 Å) excluded volume (v_{Pex}), using the MoloVol program.[82] The guest binding site volume in the **TPPM-S** phase was calculated dividing the potential void volume by the Z value of the crystal structures. The **TPPM-S** potential void volume was calculated by the program Mercury,[83] using a probe with a radius of 1.2 Å, considering the frameworks of the **TPPM-S** crystal structures from which the solvent molecules were removed (15.5 % of the unit cell, 565 Å^{-3}).

$$PC_{Guest} = \frac{V_{Guest}}{V} \cdot 100 \qquad \text{(S5.3)}$$

where PC_{Guest} is the Guest packing coefficient, V the Guest volume and V the cavity (guest binding site) volume (V = 140.5 Å^{-3}).

The guest volume was calculated as follows:

$$V_{Guest} = v_W + v_{Pex} \qquad \text{(S5.4)}$$

where v_W is the guest van der Waals volume and v_{Pex} the probe excluded volume.

Table S5.4: Solvents volumes and Packing Coefficients.

Solvent	v_w (Å^{-3})	v_{Pex} (Å^{-3})	V_{guest} (Å^{-3})	PC_{guest} (%)
$CHCl_3$	76.23	1.83	78.06	55.56
DCE	76.78	2.01	78.79	56.08
$PhCH_3$	99.92	1.70	101.62	72.33
C_6H_6	84.03	0.53	84.56	60.18
C_6H_{12}	97.15	3.16	100.31	71.39
CH_3CN	48.34	0.29	48.63	34.61
CH_2Cl_2	59.72	0.94	60.67	42.50
Acetone	62.53	1.72	64.25	44.50
EtOH	52.28	1.12	53.40	38.01
C_2HCl_3	87.78	2.01	89.79	63.91

5.3.5 NMR Characterization

The ^{1}H NMR spectra were collected in CD_2Cl_2 with few drops of methanol-d_4, in order to completely solubilize the **TPPM** molecule, on a Bruker AC400 Avance.

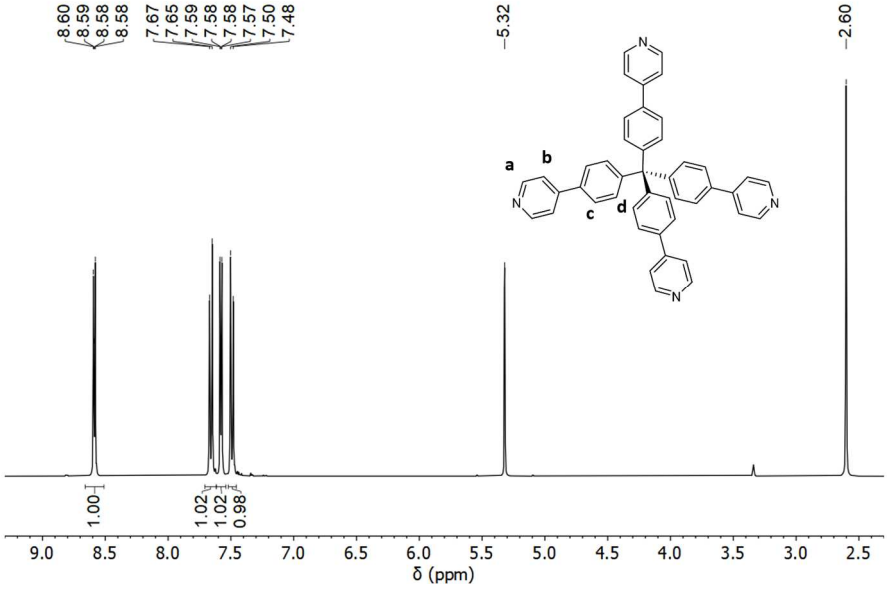

Figure S5.16: ^{1}H NMR spectrum of **TPPM** (400 MHz, CD_2Cl_2) δ (ppm): 8.59 (dd; J_1 = 4.7 Hz, J_2 = 1.85 Hz, 8H, a), 7.66 (d, J = 8.6 Hz, 8H, c), 7.58 (dd, J1 = 4.7 Hz, J2 = 1.8 Hz, 8H, b), 7.49 (d, J = 8.5 Hz, 8H, d).

Solvent loading determination by ^{1}H-NMR spectroscopy performed on TPPM-S phases

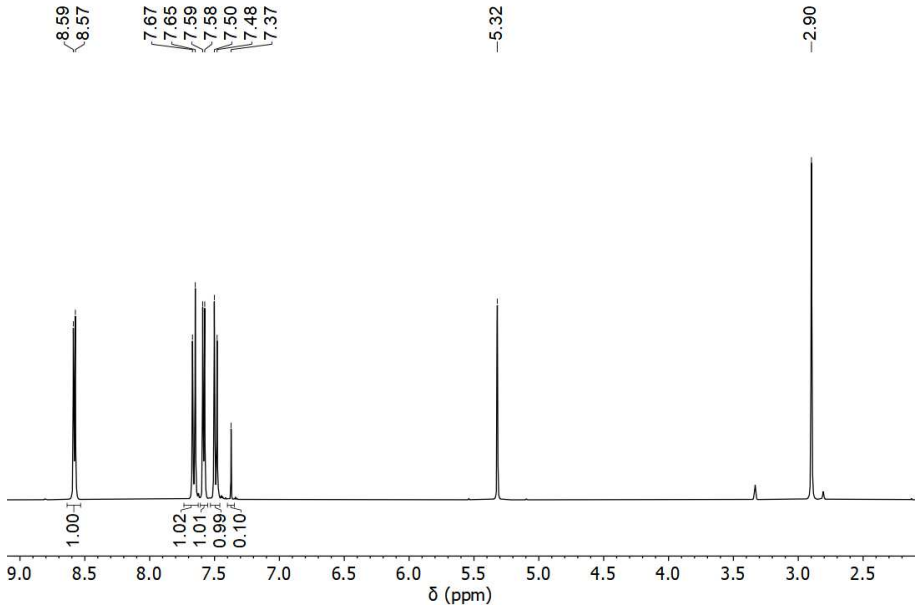

Figure S5.17: ^{1}H NMR spectrum of **TPPM·CHCl$_3$** collected in CD_2Cl_2.

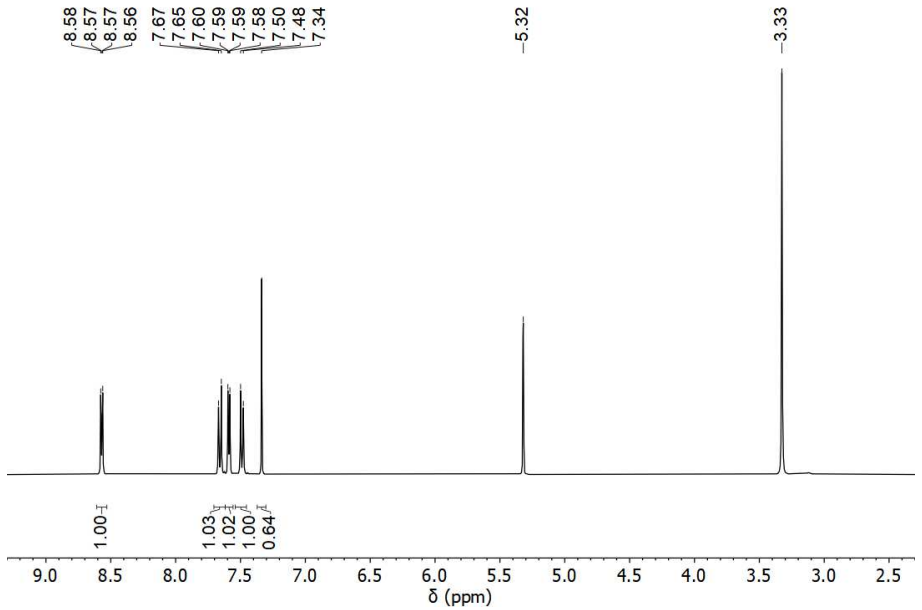

Figure S5.18: ^{1}H NMR spectrum of **TPPM·C$_6$H$_6$** collected in CD_2Cl_2.

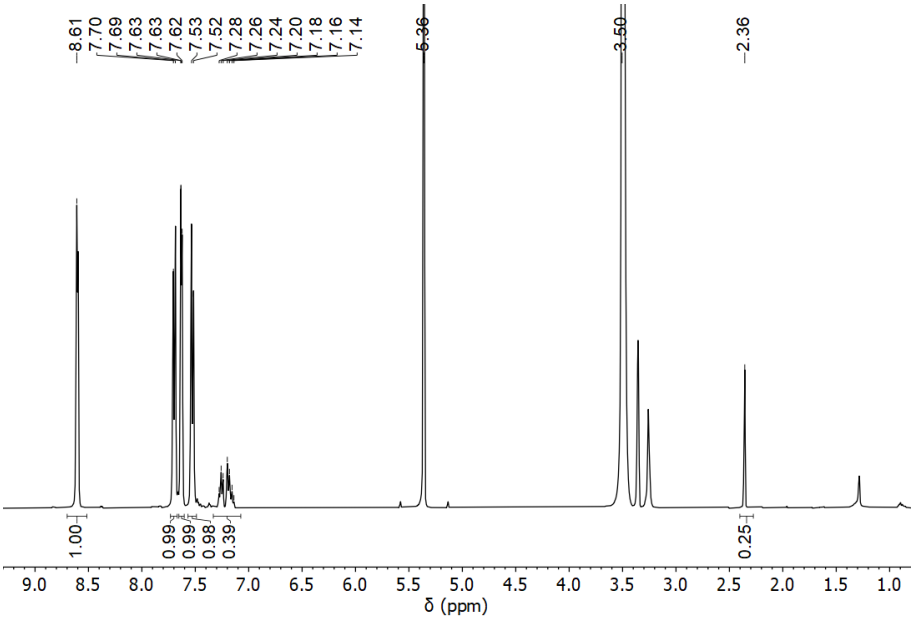

Figure S5.19: ^{1}H NMR spectrum of **TPPM·PhCH$_3$** collected in CD_2Cl_2.

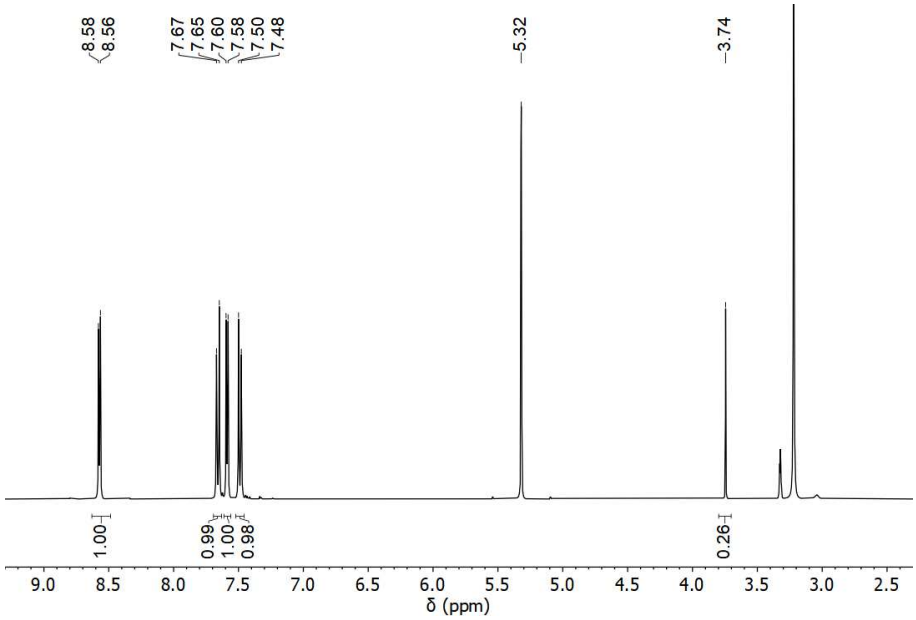

Figure S5.20: ^{1}H NMR spectrum of **TPPM·DCE** collected in CD_2Cl_2.

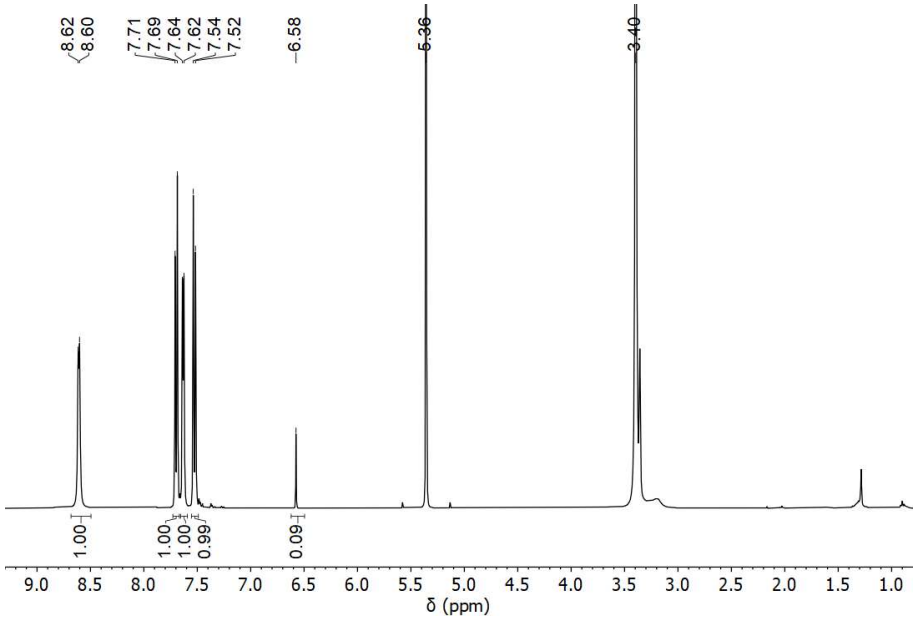

Figure S5.21: ^{1}H NMR spectrum of **TPPM·C_2HCl_3** solvate collected in CD_2Cl_2.

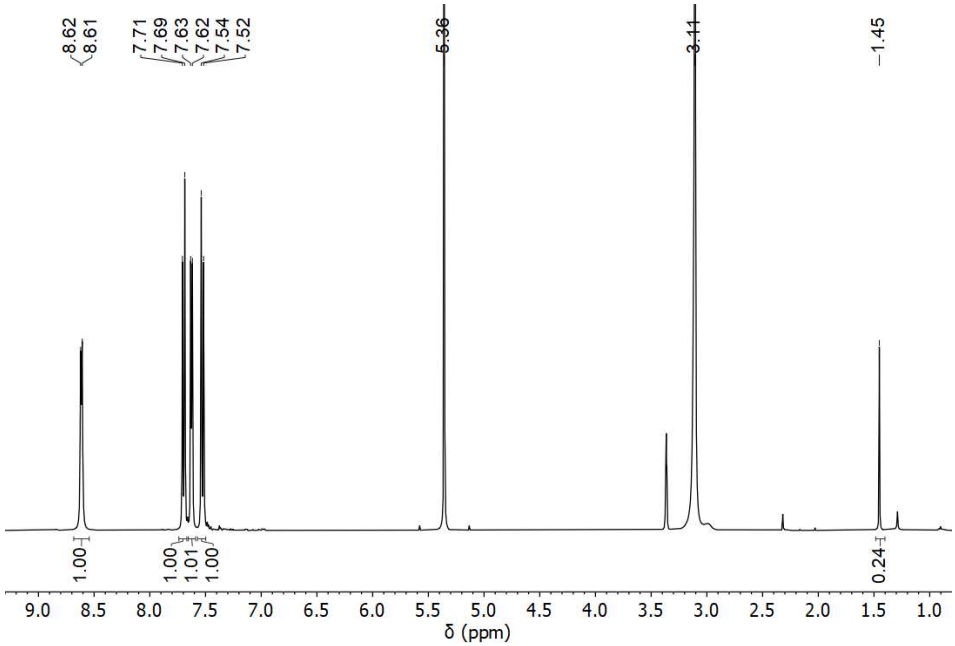

Figure S5.22: ^{1}H NMR spectrum of **TPPM·$C_{12}H_{12}$** collected in CD_2Cl_2.

The solvate stoichiometry (SS^{NMR}) was estimated from ^{1}H NMR data according to following equation:

$$SS^{NMR} = \frac{I_{Guest} \cdot n_{TPPM}}{I_{TPPM} \cdot n_{Guest}} \quad (S5.5)$$

Where I_{Guest} and I_{TPPM} are the integral associated to guest and TPPM diagnostic peaks, respectively; n is the number of hydrogen atoms related to the diagnostic peak of interest.

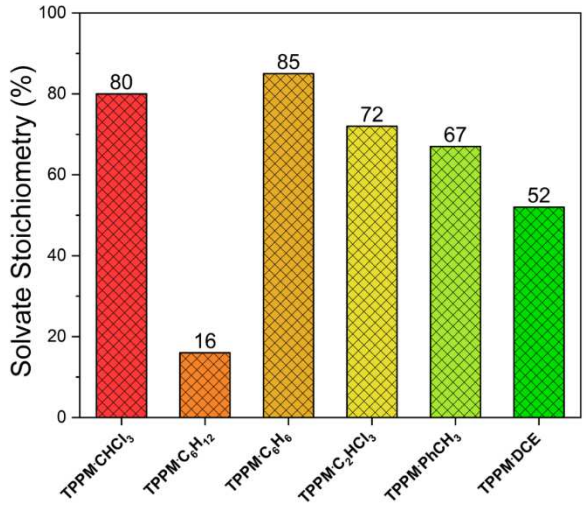

Figure S5.23: Comparison of the solvate stoichiometry among the different **TPPM** solvates.

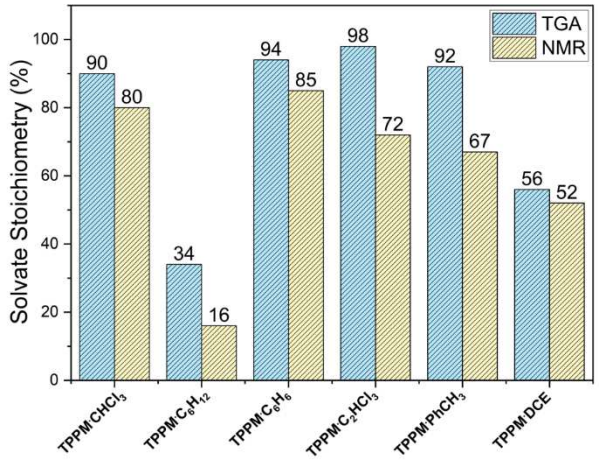

Figure S5.24: Comparison of SS^{TGA} and SS^{NMR} for different **TPPM** solvates.

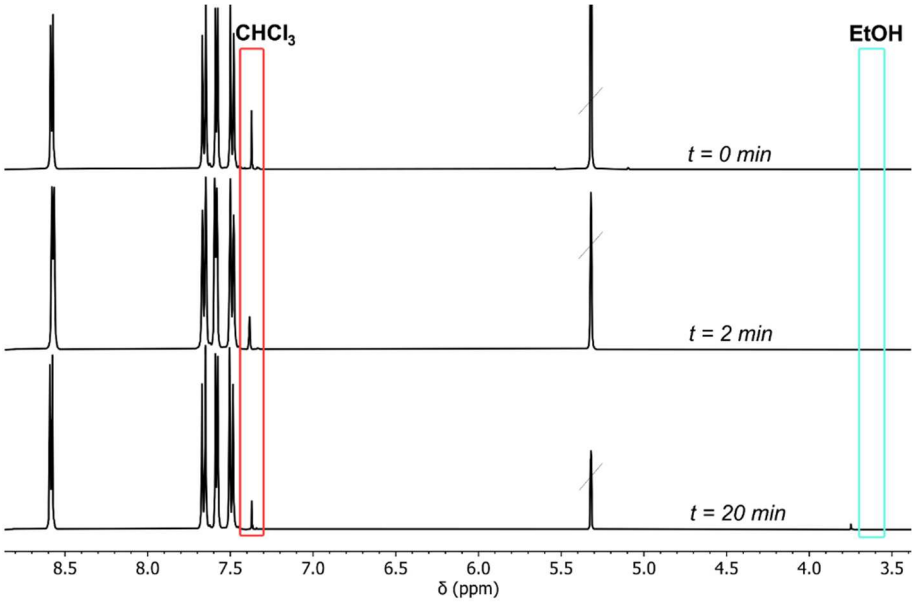

Figure S5.25: Solvent competition studies followed by ^{1}H NMR spectroscopy. The **TPPM·CHCl$_3$** phase was exposed to EtOH vapours for 2 and 20 minutes. The solid was then dissolved in CD_2Cl_2 with few drops of methanol-d_4. ^{1}H NMR spectra were collected and compared to the one of the initials solvate.

5.3.6 Spectroscopic Characterization

UV-Vis (UltraViolet-Visible) absorption spectra were collected using a PerkinElmer Lambda650 spectrophotometer. The solid samples were prepared spreading the sample on a quartz plate to produce a thin layer. Absorption spectra were collected in transmission, with the light beam orthogonal to the sample, using air as reference. Liquid samples were analysed as diluted solution ($\approx 10^{-6}$) in DCM:MeOH (95:5).

Fluorescence measurements were performed on a FLS1000 Edinburgh Fluorometer; the samples were prepared in the same way of the UV-Vis analysis. Emission spectra on solid samples were collected on thinner layers with respect to the absorption spectra, to minimize the inner-filter effects and to obtain an excitation profile comparable to the absorption spectra. Fluorescence analyses were performed placing the quartz support at 45° with respect to the excitation beam and tilted off the vertical. Furthermore, long pass filters were employed in the emission path ($\lambda_{cut\text{-}off}$[emission] = 330 nm, $\lambda_{cut\text{-}off}$[excitation] = 455 nm).

The solid-state spectroscopic characterization was performed on the **TPPM-S** phases directly obtained by vapor absorption from the empty **TPPM** phase.

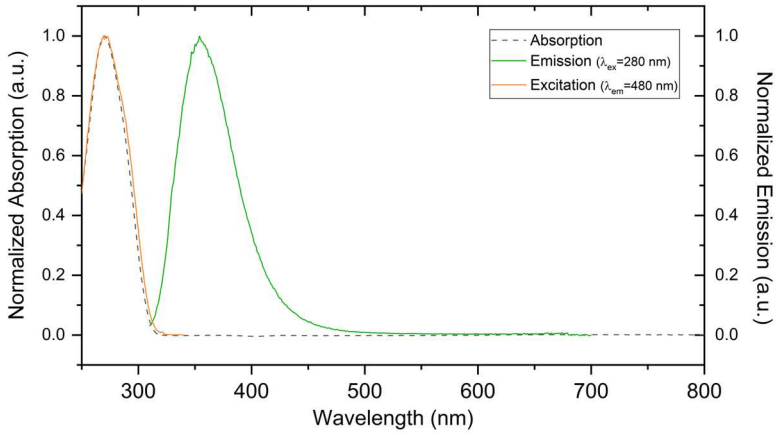

Figure S5.26: Absorption, excitation, and emission spectra of the empty **TPPM** phase in DCM:MeOH (95:5) solution.

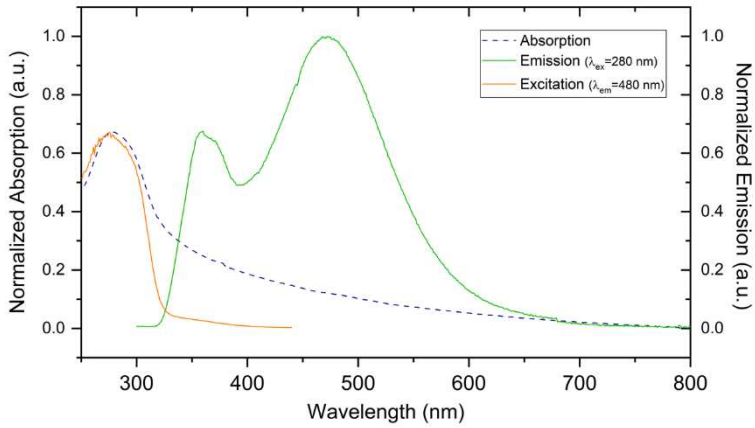

Figure S5.27: Absorption, excitation, and emission spectra of the empty **TPPM** phase in the solid state.

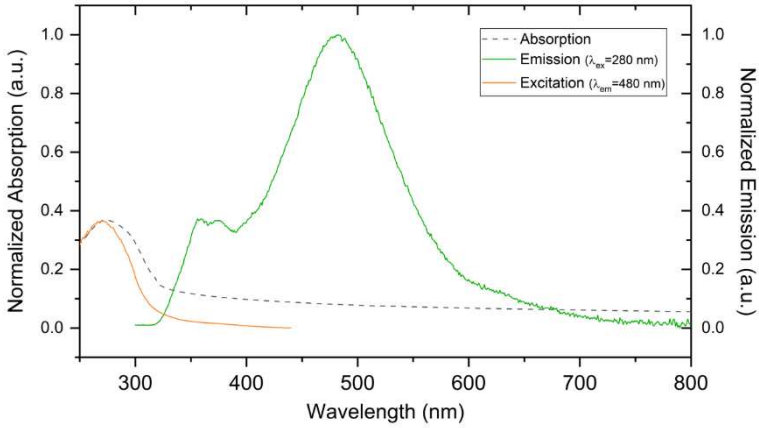

Figure S5.28: Absorption, excitation, and emission spectra of **TPPM·$CHCl_3$** in the solid state.

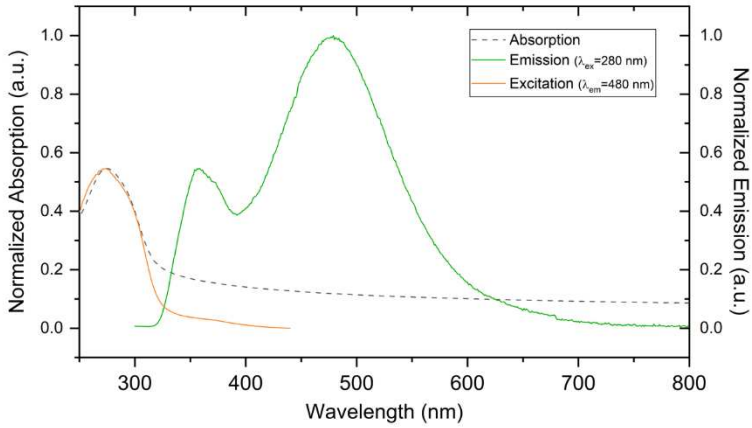

Figure S5.29: Absorption, excitation, and emission spectra of the **TPPM·C_6H_6** phase in the solid state.

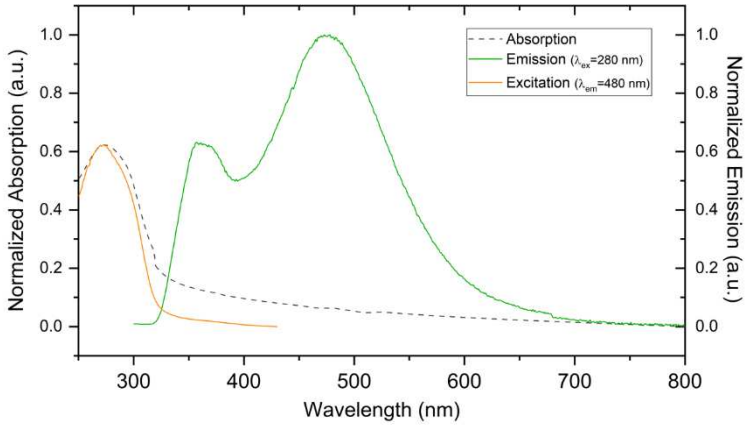

Figure S5.30: Absorption, excitation, and emission spectra of **TPPM·$PhCH_3$** in the solid state.

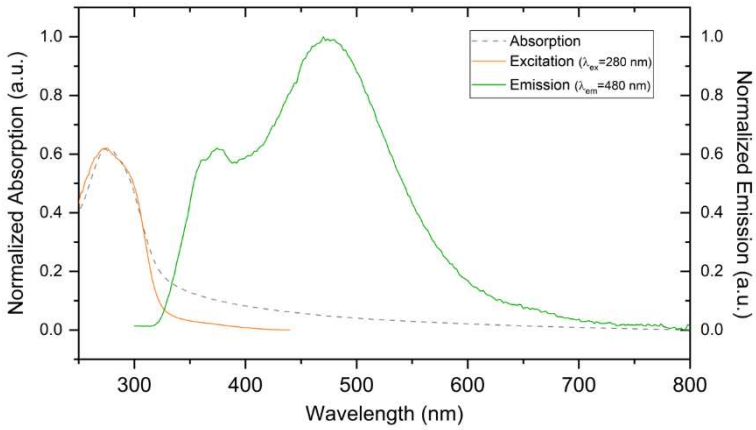

Figure S5.31: Absorption, excitation, and emission spectra of **TPPM·C_2HCl_3** in the solid state.

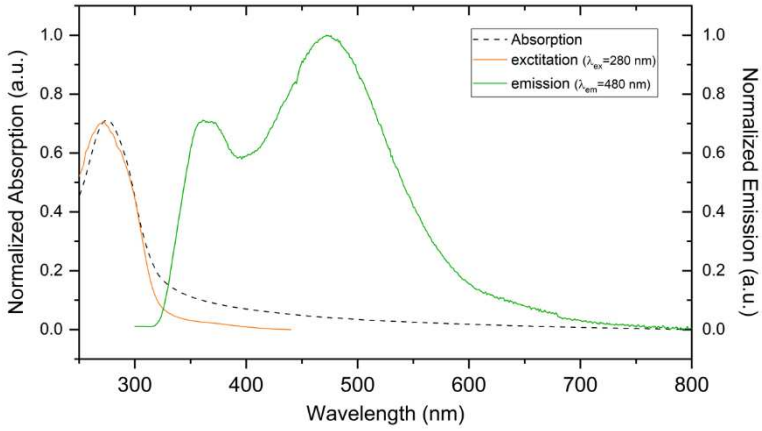

Figure S5.32: Absorption, excitation, and emission spectra of **TPPM·C_6H_{12}** in the solid state.

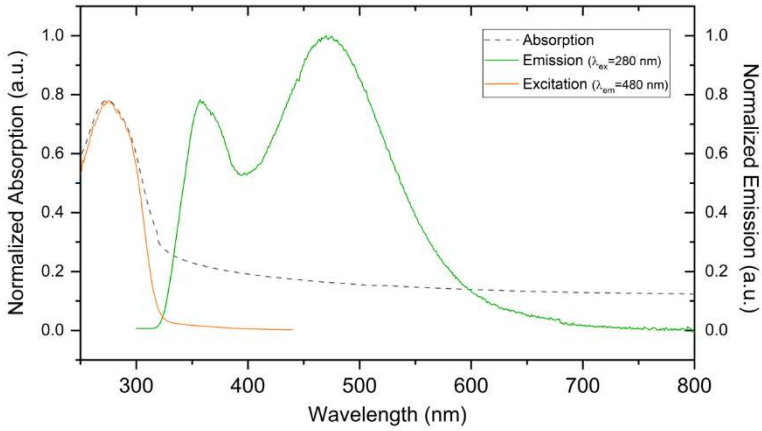

Figure S5.33: Absorption, excitation, and emission spectra of **TPPM·DCE** in the solid state.

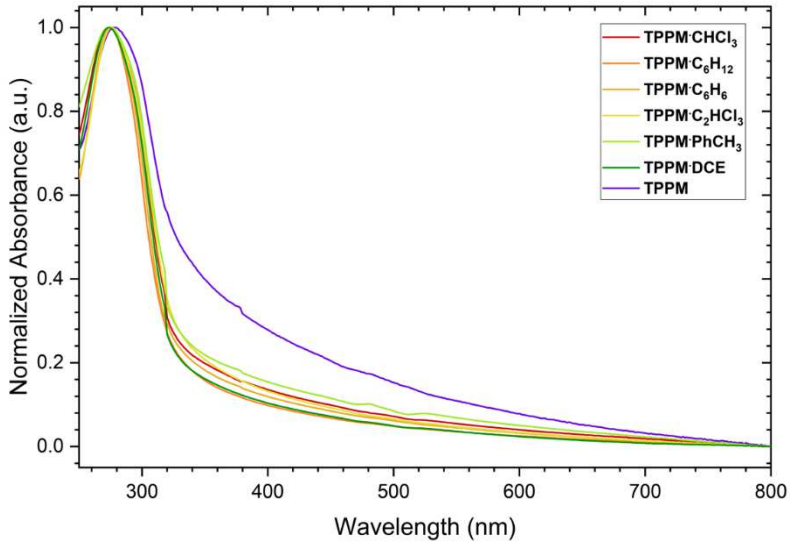

Figure S5.34: Comparison of the absorption spectra at the solid state for the different **TPPM** phases.

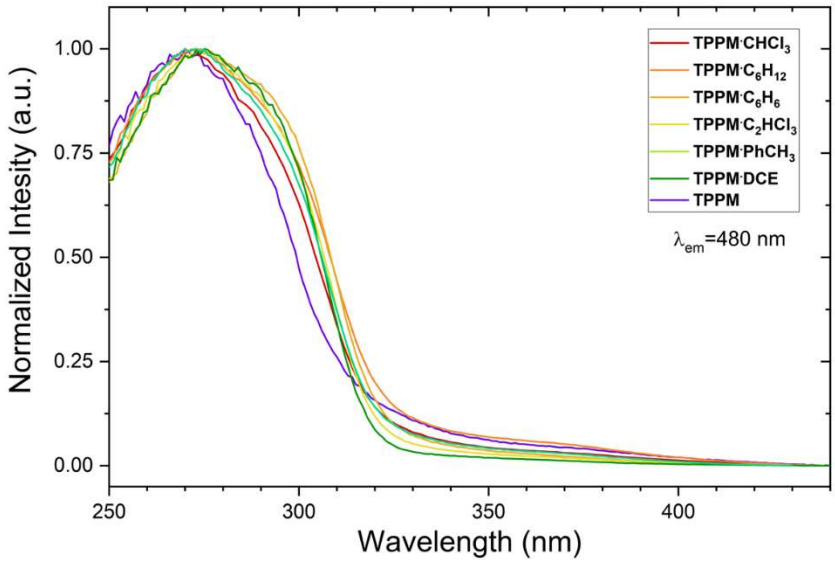

Figure S5.35: Comparison of the excitation spectra at the solid state for the different **TPPM** phases.

Table S5.5: Emission Ratio value for each **TPPM** phase characterized by solid-state spectroscopic methods. To perform a statistical analysis, the emission spectra were collected for three different samples.

TPPM-SOF Crystal Phase	Ratio I_{480nm}/I_{360nm}	Mean Value	Standard Deviation
TPPM·CHCl$_3$	2.21035	2.71874	0.49312
	2.75085		
	3.19502		
TPPM·C$_6$H$_{12}$	1.56512	1.79224	0.5353
	1.40794		
	2.40366		
TPPM·C$_6$H$_6$	1.49289	1.79589	0.26564
	1.90603		
	1.98874		
TPPM·C$_2$HCl$_3$	1.6129	1.4968	0.12073
	1.50557		
	1.37193		
TPPM·PhCH$_3$	1.5791	1.70348	0.17374
	1.94918		
	1.58215		
TPPM·DCE	1.64479	1.72997	0.20764
	1.96666		
	1.57846		
TPPM	1.17315	1.31384	0.15554
	1.48086		
	1.2875		

Table S5.6: Significance levels for each group obtained by one-way ANOVA calculation by Tukey Test, using 0.05 as significance level.

	TPPM·$CHCl_3$	TPPM·C_6H_{12}	TPPM·C_6H_6	TPPM·C_2HCl_3	TPPM·$PhCH_3$	TPPM·DCE	TPPM
TPPM·$CHCl_3$							
TPPM·C_6H_{12}	0.041						
TPPM·C_6H_6	0.042	1					
TPPM·C_2HCl_3	0.0054	0.91	0.91				
TPPM·$PhCH_3$	0.022	1	1	0.98			
TPPM·DCE	0.027	1	1	0.97	1		
TPPM	0.0015	0.55	0.55	0.99	0.75	0.69	

5.4 Supplementary Information – B (Chapter 5.2)

5.4.1 Synthetic Procedures

The TPPM synthesis was carried out following the procedure reported in the literature (see Section 5.3.1). [84]

The mechanochemical reactions were conducted with the addition of a small amount of liquid; this synthetic approach is called "Liquid Assisted Grinding" (LAG). The amount of liquid added to the reaction mixture and the total mass of the solid fraction is related to the parameter η (see in Chapter 4.4.1 the Equation 4.1). [85]

Mechanochemical Synthesis of TPPM·BnOH

TPPM (29.5 mg, 0.047 mmol) and BnOH (18 μL, 0.17 mmol) were placed into an agate mortar of 6 cm in diameter. The mixture was manually ground with a pestle for 20 min ($\eta = 0.61$) and then the mechanochemical crude was left in an open container for 1 hour to evaporate the remaining traces of LAG additive.

5.4.2 Powder X-ray Diffraction (PXRD)

The PXRD patterns of the samples were collected using Ni-filtered Cu K radiation ($\lambda_{K\alpha1}$ = 1.5406 Å, $\lambda_{K\alpha2}$ = 1.5444 Å), on a Rigaku SmartLab XE diffractometer equipped with a HyPix-3000 detector. The data were processed with SmartLab Studio II (by Rigaku). PXRD patterns were collected in Bragg-Brentano geometry in the 2ϑ range 5-75°, placing the sample on a silicon zero background specimen holder. The LeBail refinement on powder X-ray diffraction data was conducted with Jana2020.[81] Manually selected points were used to describe the background, single crystal data (3D ED) were used to define the unit cell, and cyclic refinements on the entire dataset were used to generate the profile parameters. The peak profile was modelled as a Pseudo-Voight function, corrected due to axial divergence asymmetry and it is cut outside 20*FMWH range. The refinement converged to Rp = 5.77%, wRp = 7.68% and GOF = 2.87 (Figure 5.28).

Table S5.7: Unit cell parameters obtained from the LeBail Refinement on the powder X-ray diffraction data (PXRD).

	PXRD
a (Å)	28.469(2)
b (Å)	7.0652(4)
c (Å)	21.774(1)
α (°)	90
β (°)	120.481(4)
γ (°)	90
Vol (Å^3)	3774.33(3)

5.4.3 3D Electron Diffraction (3D ED)

Sample Preparation

The preparation of a sample suitable for 3D ED analysis was conducted using directly the mechanochemical reaction crude (see S1.2). The nanocrystalline powder of **TPPM·BnOH** was placed on a microscope glass and a TEM sample grid (Cu square grid, 300 mesh, holey carbon film) was gently pressed on it.

Electron Diffractometer

3D electron diffraction analysis and scanning transmission electron microscopy imaging have been carried out on an ELDICO ED-1 electron diffractometer. A photograph of the setup is reported in Figure 5.25. The electron gun is made with a self-ramping up beam system having a thermionic LaB_6 source which produces a 160 keV electron beam. The beam is shaped by multiple condenser lenses; however, no lens is located close to the sample chamber and no projector lenses are used to project the diffraction pattern onto the detector.[86] The condenser lenses are accompanied by several deflectors and among those is a pair of scanning coils that allow STEM imaging. There is only one aperture for both applicable modes, STEM imaging and diffraction. In STEM mode a focussed beam with diameters from 30-40 nm can be realized. The distance of the last condenser lens to the sample is ca. 35 mm, which was designed to leave space for further attachments, but also to have a rather large focal length, which means that even out of the focal plane a remarkable depth and sharpness of the images can be achieved, e.g. when images with a large field of view of a tilted or bent grid are recorded. In diffraction mode (parallel beam) recommended beam diameters are in the range from 300 to 950 nm with beam divergences in the range from 0.15 to 0.05 mrad, respectively.

The goniometer, which can mount a standard TEM grid, is equipped with four linear axes and one rotation axis which is vertical [87]. The construction

of the goniometer allows to bring any position on a mounted grid into the point of intersection between rotation axis and the diffraction mode's electron beam (the usual eucentric point in a standard TEM). The movement of the goniometer (especially the sample rotation) is not restricted by any close-by optical elements. The detector is a hybrid pixel detector (Dectris QUADRO) which allows for continuous rotation experiments by its fast readout and neglectable dead time of 100 ns. Due to the fixed sample to detector distance and to the absence of any projection system compared to a TEM, once the detector distance is calibrated with a standard, no daily calibration is necessary and quite precise undistorted measurements of the reciprocal space geometry can be performed retrieving precise unit cell parameters.

The crystals suitable for the 3D ED analysis are searched through STEM imaging and their crystal quality is preliminarily checked with a single diffraction pattern, placing the beam on the crystal of interest. During the analysis, the diffraction patterns are collected while the crystal is rotating, in accordance with the continuous-rotation data collection protocol.

Data Collection and Analysis

Electron diffraction data were collected on different microcrystals illuminated with a parallel electron beam of 750 nm in diameter. The diffraction patterns were recorded with a continuous rotation data collection protocol (cRED), which consists of a continuous scan of the reciprocal space, in this case, up to a maximum of 109° with an angular integration of 0.50° and one second of exposure time per frame. The position of the object on the TEM grid was assessed through STEM imaging. The eucentric height and the in-plane stability of the crystal were corrected through specific routines implemented in the software integrated with the instrument. Three different crystals were analyzed in total, and two data collections were performed in different regions of the Crystal 2.

The collected diffraction data of each crystal were separately handled using the PETS2 software.[74] The reflection data were indexed determining also the orientation matrix, subsequently was performed the optimization of the frame orientation and the reflection intensities were integrated. Furthermore, the diffraction data were combined together using the PETS2 merging tool, which increased the completeness of the reflection data. The reflection intensities were treated with Jana2020 and the symmetrically equivalent reflections were averaged. The merged reflection dataset was used for the *ab-initio* structure determination, performed by Standard Direct Methods using the SHELXT software.[76] The data were initially refined with a fully kinematical approximation, which consists in neglecting the dynamical scattering phenomena and assuming that I_{hkl} is directly proportional to $|F_{hkl}|^2$. The least-squares refinement was performed with the software SHELXL-2014 [77] interfaced with Olex2.[88] The position of the solvent molecule was assessed from the calculation of the difference electrostatic potential map, with a resolution of 0.1 Å. The solvent molecules resulted disordered, so they were refined as a rigid body with an occupancy of 0.25. The amount of BnOH molecules inferred from the refined occupancy is in agreement with the calculated number of electrons from the solvent mask calculation. The solvent mask was calculated with Olex2 on the crystal structure with unmodelled BnOH molecules (Figure S5.38). The calculation led to 12 electrons per asymmetric unit (theoretical number: 14.5 electrons).

For the dynamical refinement, the reflections were integrated considering a rotation semiangle ($\Delta\alpha$) of 0.25° (corresponding to half of the angular integration step). The integrated intensities were combined together in virtual frames with the PETS2 software. Each virtual frame is composed of the sum of 8 experimental frames (N_F), for a covered semi-tilt range of 2° ($\Delta\alpha_v = N_F\Delta\alpha$), and the number of overlapping frames (N_O) was imposed to 4. The dynamical refinement was conducted considering the unit cell obtained from the crystal 2^b data. It was carried out using the Jana2020 software [81]

simultaneously on crystal 2^a, 2^b and 3 datasets (Table S5.9). The dataset from crystal 1 was omitted due to quality reasons. Moreover, the dynamical refinement was performed after an initial optimization of the crystal thickness and frame geometry. The crystal structure was then refined together with the crystal thickness of the respective crystals of each data collection.

Table S5.8: Angular coverage of the data collections performed on the analysed microcrystals. The reported values were obtained after a frame-by-frame fine tuning of the geometrical parameters, performed with the PETS2 software.

	Crystal 1	Crystal 2^a	Crystal 2^b	Crystal 3
Starting Angle (°)	-69.90	-30.19	-69.73	-3.05
Ending Angle (°)	28.97	39.14	39.39	64.79
Angular Range (°)	98.87	69.33	109.11	67.85
Estimated total dose (e/Å^2)	2.75	1.92	3.03	1.89

*Two different data collections have been conducted on crystal 2. 2^a: first data collection on crystal 2; 2^b: second data collection on crystal 2. Estimated total dose based on 0.0139 e A-2 s-1 dose rate at an emission current of 20 µA.

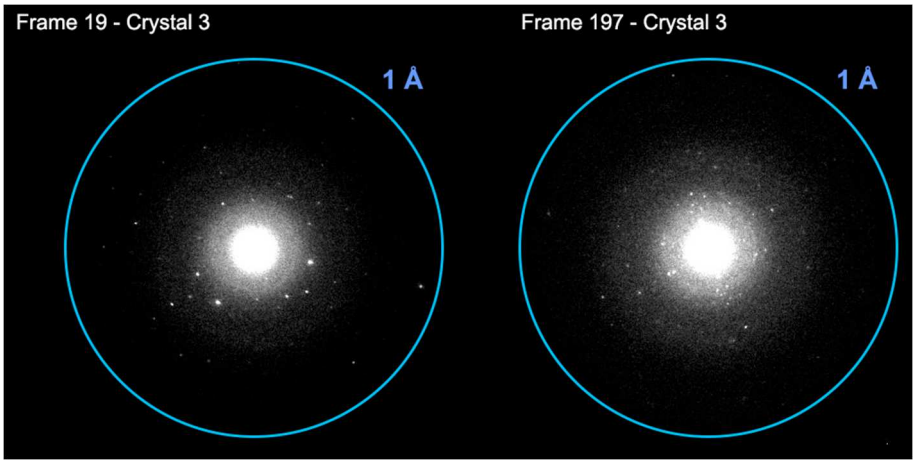

Figure S5.36: Electron diffraction patterns from the data collection on crystal 3. The figure shows two distinct diffraction patterns at the start (left) and end (right) of the data collection. The blue circle highlights in the resolution of 1Å.

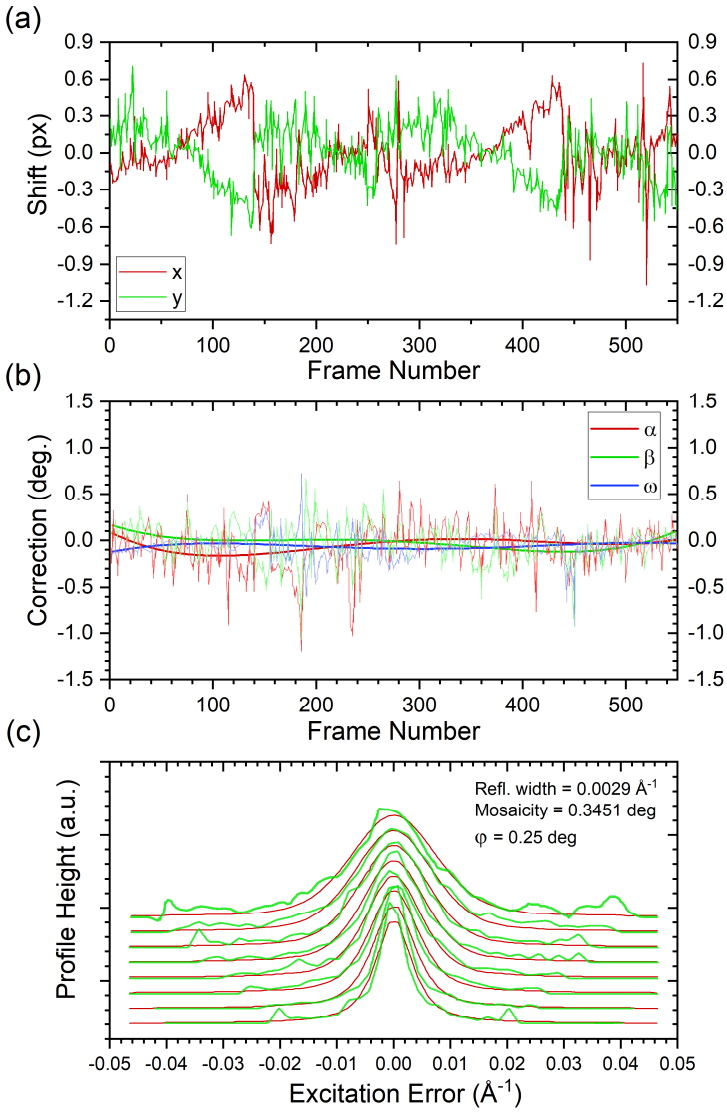

Figure S5.37: (a) Plot of the shift of the pattern centre. From the centre shift it is possible to distinguish the four datasets used in the data reduction process. (b) Plots of the geometrical corrections applied to each diffraction pattern. ω: angle comprised between the tilt axis and the positive horizontal axis of the image. α: tilt angle. β: second tilt angle. (c) Plot of rocking curve (RC) profiles of the merged datasets. The lowest curve corresponds to the average RC in the range 0.2 to 0.3 $Å^{-1}$, the next curves are obtained after a step of 0.1 $Å^{-1}$ until 0.9 to 1 $Å^{-1}$. The red curve is the calculated RC profile while the green line represents the experimental profile.

Table S5.9: Unit cell parameters obtained from the analysed crystals.

	Crystal 1	**Crystal 2**[a]	**Crystal 2**[b]	**Crystal 3**	**Merged**
a (Å)	27.98(1)	27.95(1)	27.946(7)	27.90(1)	27.907(7)
b (Å)	7.014(1)	7.019(1)	7.0236(5)	7.023(2)	7.0195(7)
c (Å)	21.72(1)	21.555(7)	21.610(3)	21.57(1)	21.592(3)
α (°)	90	90	90	90	90
β (°)	118.81(3)	118.62(3)	119.031(14)	118.67(4)	118.821(12)
γ (°)	90	90	90	90	90
Vol (Å^3)	3734.0(4)	3712.5(3)	3708.7(12)	3705.1(4)	3705.9(12)
Indexed (%)	59.51	76.30	67.52	65.16	68.80
R_{int}(obs) (%)	12.01	11.54	9.93	11.22	24.06
Completeness (%)	73	51	78	69	82
Redundancy	2.44	1.99	2.51	2.74	2.61

The indexed cells belong to an mC Bravais class.

Table S5.10: Comparison between the unit cell parameters from 3D ED analysis and from the LeBail refinement on PXRD data.

	3D ED	3D ED	PXRD
	TPPM-E	**TPPM·0.5BnOH**	**TPPM·BnOH**
a (Å)	31.4066	27.907(7)	28.469(2)
b (Å)	7.1129	7.0195(7)	7.0652(4)
c (Å)	22.063	21.592(3)	21.774(1)
α (°)	90	90	90
β (°)	133.175	118.821(12)	120.481(4)
γ (°)	90	90	90
Vol (Å^3)	3594.3(4)	3705.9(12)	3774.33(3)

The indexed cells belong to an mC Bravais class.

Table S5.11: Crystal data and structure refinement for the **TPPM·0.5BnOH** phase from the merged datasets at the kinematical theory level.

Empirical formula	$C_{48.5}H_{35.5}N_4O_{0.5}$
Formula weight	682.35
Temperature/K	293(2)
Crystal system	Monoclinic
Space group	C2/c
a/Å	27.907(7)
b/Å	7.0195(5)
c/Å	21.592(3)
α/°	90
β/°	118.821(14)
γ/°	90
Volume/Å^3	3705.9(12)
Z	4
ρ_{calc}g/cm^3	1.223
F(000)	1434
Crystal size/mm^3	Crystal 1: 0.0015 × 0.00055 × 0.00032 Crystal 2: 0.0042 × 0.0015 × 0.00058 Crystal 3: 0.001 × 0.0004 × 0.00025
Radiation	Electrons (λ = 0.02851 Å)
2ϑ range for data collection/°	0.16 to 1.922
Index ranges	$-32 \le h \le 32$, $-8 \le k \le 8$, $-22 \le l \le 25$
Reflections collected	7491
Independent reflections	2636 [R_{int}= 0.2406, R_{sigma}= 0.1983]
Data/restraints/parameters	2636/54/132
Goodness-of-fit on F^2	1.958
Final R indexes [I>=2σ (I)]	R_1= 0.2747, wR_2= 0.5723
Final R indexes [all data]	R_1= 0.3073, wR_2= 0.5886

$R_1 = \Sigma \| |F_o| - |F_c| \| / \Sigma |F_o|$, $wR_2 = [\Sigma[w(F_o^2-F_c^2)^2]/\Sigma[w(F_o^2)^2]]^{1/2}$

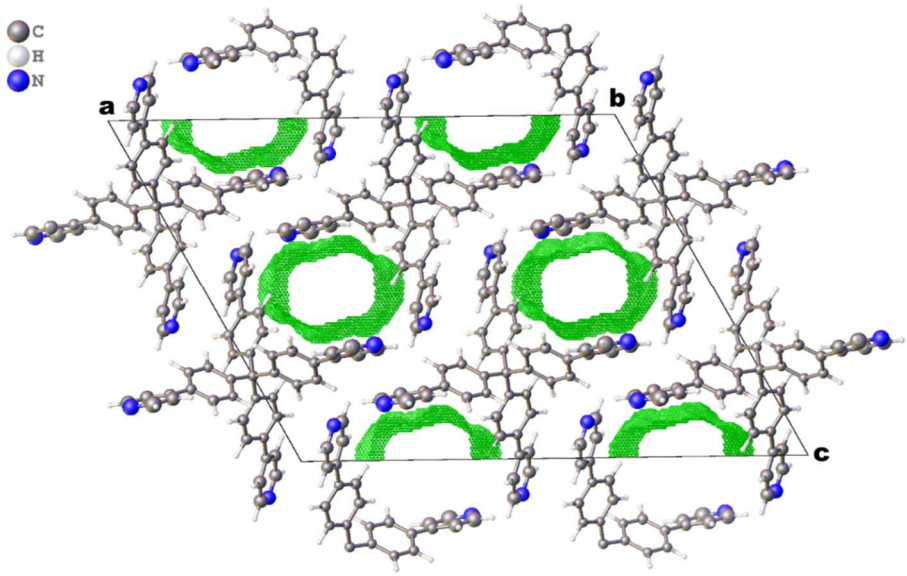

Figure S5.38: Representation of the solvent mask as a green surface along the crystallographic *b*-axis direction.

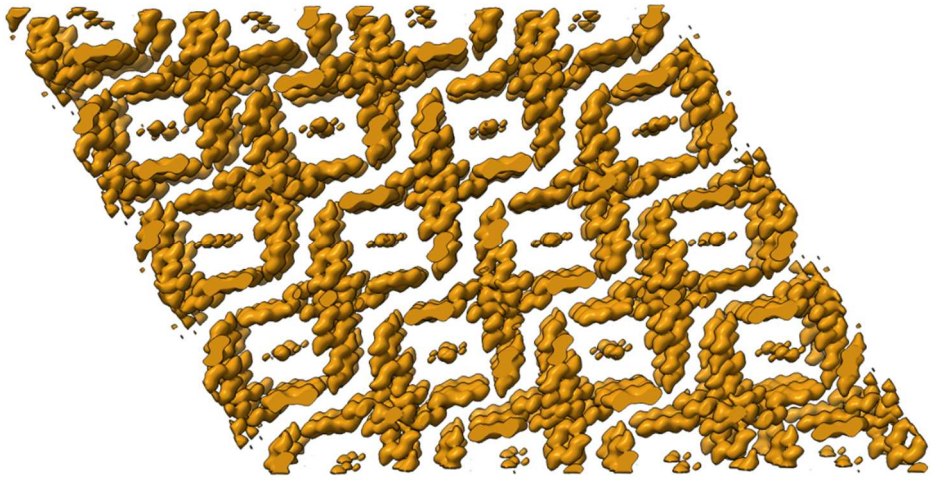

Figure S5.39: Electrostatic potential map of the **TPPM** structural model, visualized as isosurface within the unit cell borders. The potential map is calculated from the dynamically refined structure by Fourier map calculations.

Table S5.12: Crystal data and structure refinement for the **TPPM·0.5BnOH** phase from the dataset simultaneously refined at the dynamical theory level.

Empirical formula	$C_{48.5}H_{35.5}N_4O_{0.5}$
Formula weight	682.35
Temperature/K	293(2)
Crystal system	Monoclinic
Space group	C2/c
a/Å	27.946(7)
b/Å	7.0236(5)
c/Å	21.610(3)
α/°	90
β/°	119.031(14)
γ/°	90
Volume/Å^3	3708.7(12)
Z	4
ρ_{calc}g/cm^3	1.223
F(000)	1434
Crystal size/mm^3	Crystal 1: 0.0015 × 0.00055 × 0.00032 Crystal 2: 0.0042 × 0.0015 × 0.00058 Crystal 3: 0.001 × 0.0004 × 0.00025
Radiation	Electrons (λ = 0.02851 Å)
2ϑ range for data collection/°	0.16 to 1.922
Index ranges	-26 ≤ h ≤ 27, -6 ≤ k ≤ 6, -21 ≤ l ≤ 20
Reflections collected	15678
Independent reflections	3291 [R_{int}= 0.2406, R_{sigma}= 0.1983]
Data/restraints/parameters	3291/50/210
Goodness-of-fit on F^2	3.9081
Final R indexes [I>=3σ (I)]	R_1= 0.1442, wR_2= 0.1479
Final R indexes [all data]	R_1= 0.2031, wR_2= 0.1532

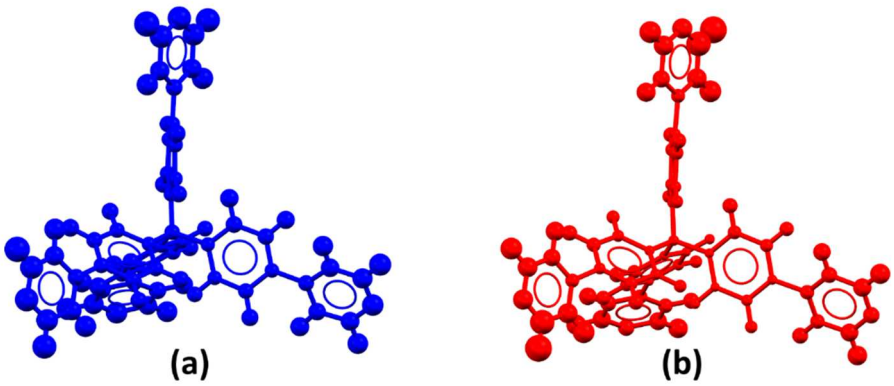

Figure S5.40: View of the **TPPM** molecule in a ball a stick representation, in which the radius of the sphere is directly proportional to U_{iso} values. (a) Kinematical refinement; (b) Dynamical refinement.

5.4.4 Thermogravimetric Analysis (TGA)

The thermogravimetric analysis of **TPPM·BnOH** was conducted on a Perkin Elmer Instrument, model TGA 8000. The desorption process of the guest molecules was followed in the temperature range 30-350°C with a heating rate of 10°C min^{-1} under nitrogen flux.

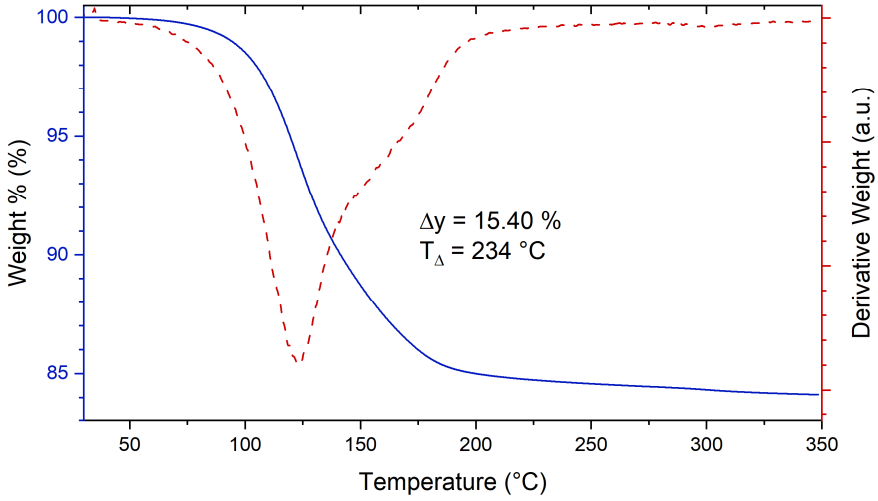

Figure S5.41: Thermogravimetric path recorded on the **TPPM·BnOH** crystal phase. The blue line corresponds to the weigh percentage on temperature, while the red dashed line is the first derivative of the weight percentage.

The solvate stoichiometry (SS^{TGA}) was calculated from the weight loss, in order to define the **TPPM**/BnOH ratio at atmospheric conditions (Equation 5.2). The SS^{TGA} of the **TPPM·BnOH** phase, at room conditions, resulted close to 1.

5.4.5 NMR Characterization

The ^{1}H NMR spectra were collected in CD_2Cl_2 with few drops of methanol-d4, in order to obtain a clear solution of **TPPM**, on a Bruker AC400 Avance. The solvate stoichiometry (SS^{NMR}) from ^{1}H NMR data was calculated in accordance with Equation 5.5.

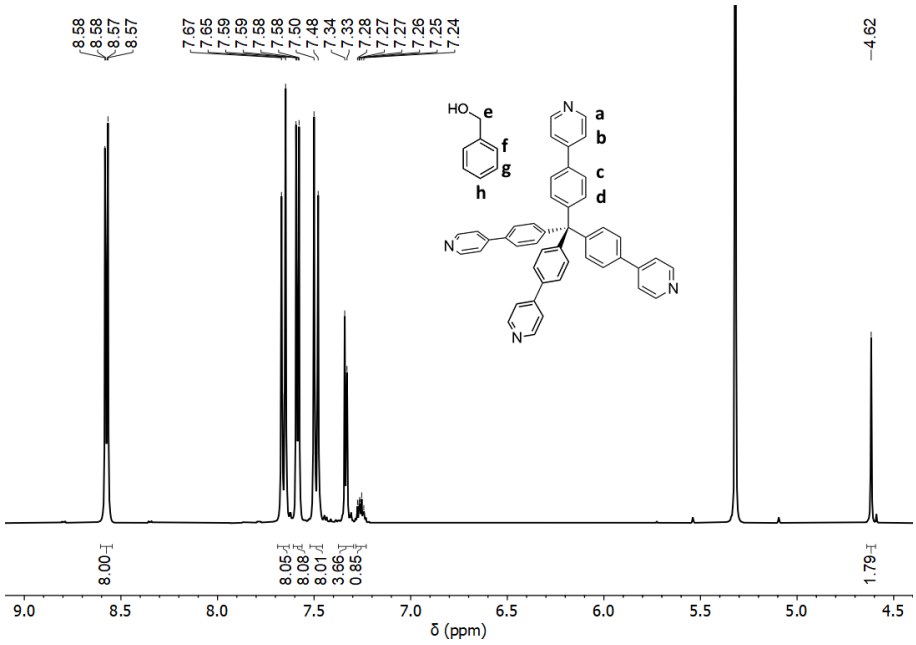

Figure S5.42: ^{1}H NMR spectrum of **TPPM·BnOH** (400 MHz, CD_2Cl_2) δ (ppm): 8.57 (dd, J_1 = 4.7 Hz, J_2 = 1.7 Hz, 8H, a), 7.66 (d, J = 8.6 Hz, 8H, c), 7.59 (dd, J_1 =4.8 Hz, J_2 = 1.7 Hz, 8H, b), 7.49 (d, J = 8.6 Hz, 8H, d), 7.33 (m, 4H, f + g), 7.26 (m, 1H, h), 4.62 (s, 2H, e).

Bibliography:

[1] D. Marchetti, F. Portone, F. Mezzadri, E. Dalcanale, M. Gemmi, A. Pedrini, C. Massera, "Selective and Reversible Solvent Uptake in Tetra-4-(4-pyridyl)phenylmethane-based Supramolecular Organic Frameworks", *Chem. - Eur. J.* 28 (2022) e202202977. https://doi.org/10.1002/chem.202202977.

[2] D. Marchetti, A. Pedrini, C. Massera, M.D. Faye Diouf, C. Jandl, G. Steinfeld, M. Gemmi, "3D electron diffraction analysis of a novel, mechanochemically synthesized supramolecular organic framework based on tetrakis-4-(4-pyridyl)phenylmethane", *Acta Crystallogr. B Struct. Sci. Cryst. Eng. Mater.* 79 (2023) 432–436. https://doi.org/10.1107/S2052520623007680.

[3] J.L. Atwood, L.J. Barbour, A. Jerga, "A New Type of Material for the Recovery of Hydrogen from Gas Mixtures", *Angew. Chem. Int. Ed.* 43 (2004) 2948–2950. https://doi.org/10.1002/anie.200353559.

[4] W. Yang, A. Greenaway, X. Lin, R. Matsuda, A.J. Blake, C. Wilson, W. Lewis, P. Hubberstey, S. Kitagawa, N.R. Champness, M. Schröder, "Exceptional Thermal Stability in a Supramolecular Organic Framework: Porosity and Gas Storage", *J. Am. Chem. Soc.* 132 (2010) 14457–14469. https://doi.org/10.1021/ja1042935.

[5] J. Lü, C. Perez-Krap, M. Suyetin, N.H. Alsmail, Y. Yan, S. Yang, W. Lewis, E. Bichoutskaia, C.C. Tang, A.J. Blake, R. Cao, M. Schröder, "A Robust Binary Supramolecular Organic Framework (SOF) with High CO_2 Adsorption and Selectivity", *J. Am. Chem. Soc.* 136 (2014) 12828–12831. https://doi.org/10.1021/ja506577g.

[6] T. Ishi-i, H. Tanaka, H. Koga, Y. Tanaka, T. Matsumoto, "Near-infrared fluorescent organic porous crystal that responds to solvent vapors", *J. Mater. Chem. C.* 8 (2020) 12437–12444. https://doi.org/10.1039/D0TC03261A.

[7] M. Mastalerz, I.M. Oppel, "Rational Construction of an Extrinsic Porous Molecular Crystal with an Extraordinary High Specific Surface Area", *Angew. Chem. Int. Ed.* 51 (2012) 5252–5255. https://doi.org/10.1002/anie.201201174.

[8] J. Luo, J.-W. Wang, J.-H. Zhang, S. Lai, D.-C. Zhong, "Hydrogen-bonded organic frameworks: design, structures and potential applications", *CrystEngComm.* 20 (2018) 5884–5898. https://doi.org/10.1039/C8CE00655E.

[9] R.-B. Lin, Y. He, P. Li, H. Wang, W. Zhou, B. Chen, "Multifunctional porous hydrogen-bonded organic framework materials", *Chem. Soc. Rev.* 48 (2019) 1362–1389. https://doi.org/10.1039/C8CS00155C.

[10] P. Li, M.R. Ryder, J.F. Stoddart, "Hydrogen-Bonded Organic Frameworks: A Rising Class of Porous Molecular Materials", *Acc. Mater. Res.* 1 (2020) 77–87. https://doi.org/10.1021/accountsmr.0c00019.

[11] B. Wang, R.-B. Lin, Z. Zhang, S. Xiang, B. Chen, "Hydrogen-Bonded Organic Frameworks as a Tunable Platform for Functional Materials", *J. Am. Chem. Soc.* 142 (2020) 14399–14416. https://doi.org/10.1021/jacs.0c06473.

[12] N.G. White, "Amidinium···carboxylate frameworks: predictable, robust, water-stable hydrogen bonded materials", *Chem. Commun.* 57 (2021) 10998–11008. https://doi.org/10.1039/D1CC04782E.

[13] B. Yu, S. Geng, H. Wang, W. Zhou, Z. Zhang, B. Chen, J. Jiang, "A Solid Transformation into Carboxyl Dimers Based on a Robust Hydrogen-Bonded Organic Framework for Propyne/Propylene Separation", *Angew. Chem. Int. Ed.* 60 (2021) 25942–25948. https://doi.org/10.1002/anie.202110057.

[14] J.-X. Wang, J. Pei, X.-W. Gu, Y.-X. Lin, B. Li, G. Qian, "Efficient CO_2/CO separation in a stable microporous hydrogen-bonded organic framework", *Chem. Commun.* 57 (2021) 10051–10054. https://doi.org/10.1039/D1CC03438C.

[15] Y. Yang, L. Li, R.-B. Lin, Y. Ye, Z. Yao, L. Yang, F. Xiang, S. Chen, Z. Zhang, S. Xiang, B. Chen, "Ethylene/ethane separation in a stable hydrogen-bonded organic framework through a gating mechanism", *Nat. Chem.* 13 (2021) 933–939. https://doi.org/10.1038/s41557-021-00740-z.

[16] Y. Liu, H. Wu, L. Guo, W. Zhou, Z. Zhang, Q. Yang, Y. Yang, Q. Ren, Z. Bao, Hydrogen-Bonded Metal–Nucleobase Frameworks for Efficient Separation of Xenon and Krypton, *Angew. Chem. Int. Ed.* 61 (2022). https://doi.org/10.1002/anie.202117609.

[17] L. Ma, Y. Xie, R.S.H. Khoo, H. Arman, B. Wang, W. Zhou, J. Zhang, R. Lin, B. Chen, An Adaptive Hydrogen-Bonded Organic Framework for the Exclusive Recognition of *p* -Xylene, *Chem. - Eur. J.* 28 (2022). https://doi.org/10.1002/chem.202104269.

[18] P. Cui, E. Svensson Grape, P.R. Spackman, Y. Wu, R. Clowes, G.M. Day, A.K. Inge, M.A. Little, A.I. Cooper, "An Expandable Hydrogen-Bonded Organic Framework Characterized by Three-Dimensional

Electron Diffraction", *J. Am. Chem. Soc.* 142 (2020) 12743–12750. https://doi.org/10.1021/jacs.0c04885.

[19] B. Wang, R. He, L.-H. Xie, Z.-J. Lin, X. Zhang, J. Wang, H. Huang, Z. Zhang, K.S. Schanze, J. Zhang, S. Xiang, B. Chen, "Microporous Hydrogen-Bonded Organic Framework for Highly Efficient Turn-Up Fluorescent Sensing of Aniline", *J. Am. Chem. Soc.* 142 (2020) 12478–12485. https://doi.org/10.1021/jacs.0c05277.

[20] X. Ding, Z. Liu, Y. Zhang, G. Ye, J. Jia, J. Chen, "Binary Solvent Regulated Architecture of Ultra-Microporous Hydrogen-Bonded Organic Frameworks with Tunable Polarization for Highly-Selective Gas Separation", *Angew Chem Int Ed.* 61 (2022) e202116483. https://doi.org/10.1002/anie.202116483.

[21] M. Zhang, J. Samanta, C. Ke, "Assembling Guests as Cyclic Tetramers in a Porous Hydrogen-Bonded Organic Framework", *Crystal Growth & Design.* 22 (2022) 3421–3427. https://doi.org/10.1021/acs.cgd.2c00217.

[22] P. Sozzani, S. Bracco, A. Comotti, L. Ferretti, R. Simonutti, "Methane and Carbon Dioxide Storage in a Porous van der Waals Crystal", *Angew. Chem. Int. Ed.* 44 (2005) 1816–1820. https://doi.org/10.1002/anie.200461704.

[23] T.-H. Chen, I. Popov, W. Kaveevivitchai, Y.-C. Chuang, Y.-S. Chen, O. Daugulis, A.J. Jacobson, O.Š. Miljanić, "Thermally robust and porous noncovalent organic framework with high affinity for fluorocarbons and CFCs", *Nat. Commun.* 5 (2014) 5131. https://doi.org/10.1038/ncomms6131.

[24] B. Ji, D. Zhang, R. Liang, G. Kang, Q. Zhu, D. Deng, "Selective Binding and Removal of Aromatic Guests in a Porous Halogen-Bonded Organic Framework", *Crystal Growth & Design.* 21 (2021) 482–489. https://doi.org/10.1021/acs.cgd.0c01212.

[25] B.J. Eckstein, L.C. Brown, B.C. Noll, M.P. Moghadasnia, G.J. Balaich, C.M. McGuirk, "A Porous Chalcogen-Bonded Organic Framework", *J. Am. Chem. Soc.* 143 (2021) 20207–20215. https://doi.org/10.1021/jacs.1c08642.

[26] W. Yang, R. Jiang, C. Liu, B. Yu, X. Cai, H. Wang, "Triptycene-Based Porous Chalcogen-Bonded Organic Frameworks", *Crystal Growth & Design.* 21 (2021) 6497–6503. https://doi.org/10.1021/acs.cgd.1c00942.

[27] G. Gong, J. Zhao, Y. Chen, F. Xie, F. Lu, J. Wang, L. Wang, S. Chen, An amino-type halogen-bonded organic framework for the selective adsorption of aliphatic acid vapors: insight into the competitive

interactions of halogen bonds and hydrogen bonds, *J. Mater. Chem. A.* 10 (2022) 10586–10592. https://doi.org/10.1039/D2TA00628F.

[28] C. Chen, H. Guan, H. Li, Y. Zhou, Y. Huang, W. Wei, M. Hong, M. Wu, "A Noncovalent π-Stacked Porous Organic Molecular Framework for Selective Separation of Aromatics and Cyclic Aliphatics", *Angew. Chem. Int. Ed.* 61 (2022) e202201646. https://doi.org/10.1002/anie.202201646.

[29] G.R. Krishna, R. Devarapalli, G. Lal, C.M. Reddy, "Mechanically Flexible Organic Crystals Achieved by Introducing Weak Interactions in Structure: Supramolecular Shape Synthons", *J. Am. Chem. Soc.* 138 (2016) 13561–13567. https://doi.org/10.1021/jacs.6b05118.

[30] Z. Liu, L. Zhang, D. Sun, "Stimuli-responsive structural changes in metal–organic frameworks", *Chem. Commun.* 56 (2020) 9416–9432. https://doi.org/10.1039/D0CC03197F.

[31] P. She, Y. Qin, X. Wang, Q. Zhang, "Recent Progress in External-Stimulus-Responsive 2D Covalent Organic Frameworks", *Adv. Mater.* 34 (2022) 2101175. https://doi.org/10.1002/adma.202101175.

[32] C.C. Sun, C.M. Reddy, "Mechanically responsive crystalline materials", *CrystEngComm.* 23 (2021) 5683–5685. https://doi.org/10.1039/D1CE90102H.

[33] J.L. Atwood, L.J. Barbour, A. Jerga, B.L. Schottel, "Guest Transport in a Nonporous Organic Solid via Dynamic van der Waals Cooperativity", *Science*. 298 (2002) 1000–1002. https://doi.org/10.1126/science.1077591.

[34] Z. Wang, N. Sikdar, S.-Q. Wang, X. Li, M. Yu, X.-H. Bu, Z. Chang, X. Zou, Y. Chen, P. Cheng, K. Yu, M.J. Zaworotko, Z. Zhang, "Soft Porous Crystal Based upon Organic Cages That Exhibit Guest-Induced Breathing and Selective Gas Separation", *J. Am. Chem. Soc.* 141 (2019) 9408–9414. https://doi.org/10.1021/jacs.9b04319.

[35] L.J. Barbour, "Crystal porosity and the burden of proof", *Chem. Commun*. (2006) 1163. https://doi.org/10.1039/b515612m.

[36] R. Natarajan, L. Bridgland, A. Sirikulkajorn, J.-H. Lee, M.F. Haddow, G. Magro, B. Ali, S. Narayanan, P. Strickland, J.P.H. Charmant, A.G. Orpen, N.B. McKeown, C.G. Bezzu, A.P. Davis, "Tunable Porous Organic Crystals: Structural Scope and Adsorption Properties of Nanoporous Steroidal Ureas", *J. Am. Chem. Soc.* 135 (2013) 16912–16925. https://doi.org/10.1021/ja405701u.

[37] J.K. Zaręba, "Tetraphenylmethane and tetraphenylsilane as building units of coordination polymers and supramolecular networks – A focus on

tetraphosphonates", *Inorg. Chem. Commun.* 86 (2017) 172–186. https://doi.org/10.1016/j.inoche.2017.10.013.

[38] A. Pedrini, D. Marchetti, R. Pinalli, C. Massera, "Stimuli-Responsive, Dynamic Supramolecular Organic Frameworks", *ChemPlusChem*. 88 (2023) e202300383. https://doi.org/10.1002/cplu.202300383.

[39] X. Wang, M. Simard, J.D. Wuest, "Molecular Tectonics. Three-Dimensional Organic Networks with Zeolitic Properties", *J. Am. Chem. Soc.* 116 (1994) 12119–12120. https://doi.org/10.1021/ja00105a089.

[40] J.-H. Fournier, T. Maris, M. Simard, J.D. Wuest, "Molecular Tectonics. Hydrogen-Bonded Networks Built from Tetraphenols Derived from Tetraphenylmethane and Tetraphenylsilane", *Crystal Growth & Design.* 3 (2003) 535–540. https://doi.org/10.1021/cg034043d.

[41] J.-H. Fournier, T. Maris, J.D. Wuest, W. Guo, E. Galoppini, "Molecular Tectonics. Use of the Hydrogen Bonding of Boronic Acids To Direct Supramolecular Construction", *J. Am. Chem. Soc.* 125 (2003) 1002–1006. https://doi.org/10.1021/ja0276772.

[42] D. Laliberté, T. Maris, J.D. Wuest, "Molecular tectonics. Use of urethanes and ureas derived from tetraphenylmethane and tetraphenylsilane to build porous chiral hydrogen-bonded networks", *Can. J. Chem.* 82 (2004) 386–398. https://doi.org/10.1139/v03-208.

[43] I. Bassanetti, S. Bracco, A. Comotti, M. Negroni, C. Bezuidenhout, S. Canossa, P.P. Mazzeo, L. Marchió, P. Sozzani, "Flexible porous molecular materials responsive to CO_2, CH_4 and Xe stimuli", *J. Mater. Chem. A.* 6 (2018) 14231–14239. https://doi.org/10.1039/C8TA02211A.

[44] C.B. Caputo, V.N. Vukotic, N.M. Sirizzotti, S.J. Loeb, "A tetrapyridine ligand with a rigid tetrahedral core forms metal–organic frameworks with PtS type architecture", *Chem. Commun.* 47 (2011) 8545. https://doi.org/10.1039/c1cc12188j.

[45] H. Kitagawa, H. Ohtsu, M. Kawano, "Kinetic Assembly of a Thermally Stable Porous Coordination Network Based on Labile CuI Units and the Visualization of I_2 Sorption", *Angew. Chem. Int. Ed.* 52 (2013) 12395–12399. https://doi.org/10.1002/anie.201306776.

[46] H. Kitagawa, H. Ohtsu, A.J. Cruz-Cabeza, M. Kawano, "Isolation and evolution of labile sulfur allotropes *via* kinetic encapsulation in interactive porous networks", *IUCrJ.* 3 (2016) 232–236. https://doi.org/10.1107/S2052252516008423.

[47] H. Ohtsu, M. Okuyama, T. Nakajima, M. Iwamura, K. Nozaki, D. Hashizume, M. Kawano, "Through-Space Charge Transfer in Copper

Coordination Networks with Copper-Halide Guest Anions", *Inorg. Chem.* 60 (2021) 9273–9277. https://doi.org/10.1021/acs.inorgchem.1c01451.

[48] Gaussian 09, Revision D.01, Frisch, M. J.; Trucks, G. W.; Schlegel, H. B.; Scuseria, G. E.; Robb, M. A.; Cheeseman, J. R.; Scalmani, G.; Barone, V.; Petersson, G. A.; Nakatsuji, H.; Li, X.; Caricato, M.; Marenich, M.; Bloino, J.; Janesko, B. G.; Gomperts, R.; Mennucci, B.; Hratchian, H. P.; Ortiz, J. V.; Izmaylov, A. F.; Sonnenberg, J. L.; Williams-Young, D.; Ding, F.; Lipparini, F.; Egidi, F.; Goings, J.; Peng, B.; Petrone, A.; Henderson, T.; Ranasinghe, D.; Zakrzewski, V. G.; Gao, J.; Rega, N.; Zheng, G.; Liang, W.; Hada, M.; Ehara, M.; Toyota, K.; Fukuda, R.; Hasegawa, J.; Ishida, M.; Nakajima, T.; Honda, Y.; Kitao, O.; Nakai, H.; Vreven, T.; Throssell, K.; Montgomery, J. A.; Peralta, Jr., J. E.; Ogliaro, F.; Bearpark, M.; Heyd, J. J.; Brothers, E.; Kudin, K. N.; Staroverov, V. N.; Keith, T.;. Kobayashi, R.; Normand, J.; Raghavachari, K.; Rendell, A.; Burant, J. C.; Iyengar, S. S.; Tomasi, J.; Cossi, M.; Millam, J. M.; Klene, M.; Adamo, C.; Cammi, R.; Ochterski, J. W.; Martin, R. L.; Morokuma, K.; Farkas, O.; Foresman, J. B., Fox, D. J. Gaussian, Inc., Wallingford CT, 2016.

[49] P.A. Wood, T.S.G. Olsson, J.C. Cole, S.J. Cottrell, N. Feeder, P.T.A. Galek, C.R. Groom, E. Pidcock, "Evaluation of molecular crystal structures using Full Interaction Maps", *CrystEngComm.* 15 (2013) 65–72. https://doi.org/10.1039/C2CE25849H.

[50] A.I. Kitaigorodskii, "The principle of close packing and the condition of thermodynamic stability of organic crystals", *Acta Cryst.* 18 (1965) 585–590. https://doi.org/10.1107/S0365110X65001391.

[51] D. Holden, S.Y. Chong, L. Chen, K.E. Jelfs, T. Hasell, A.I. Cooper, "Understanding static, dynamic and cooperative porosity in molecular materials", *Chem. Sci.* 7 (2016) 4875–4879. https://doi.org/10.1039/C6SC00713A.

[52] C. Massera, M. Melegari, E. Kalenius, F. Ugozzoli, E. Dalcanale, "Supramolecular Control of Single-Crystal-to-Single-Crystal Transformation through Selective Guest Exchange", *Chem. Eur. J.* 17 (2011) 3064–3068. https://doi.org/10.1002/chem.201003407.

[53] W. Xiao, C. Hu, M.D. Ward, "Guest Exchange through Single Crystal–Single Crystal Transformations in a Flexible Hydrogen-Bonded Framework", *J. Am. Chem. Soc.* 136 (2014) 14200–14206. https://doi.org/10.1021/ja507689m.

[54] P. Li, H.D. Arman, H. Wang, L. Weng, K. Alfooty, R.F. Angawi, B. Chen, "Solvent Dependent Structures of Melamine: Porous or Nonporous?", *Crystal Growth & Design*. 15 (2015) 1871–1875. https://doi.org/10.1021/acs.cgd.5b00039.

[55] S.A. Boer, L. Conte, A. Tarzia, M.T. Huxley, M.G. Gardiner, D.R.T. Appadoo, C. Ennis, C.J. Doonan, C. Richardson, N.G. White, "Water Sorption Controls Extreme Single-Crystal-to-Single-Crystal Molecular Reorganization in Hydrogen Bonded Organic Frameworks", *Chem. - Eur. J.* 28 (2022) e202201929. https://doi.org/10.1002/chem.202201929.

[56] C.R. Groom, I.J. Bruno, M.P. Lightfoot, S.C. Ward, "The Cambridge Structural Database", *Acta Crystallogr. B Struct. Sci. Cryst. Eng. Mater.* 72 (2016) 171–179. https://doi.org/10.1107/S2052520616003954.

[57] P.R. Spackman, M.J. Turner, J.J. McKinnon, S.K. Wolff, D.J. Grimwood, D. Jayatilaka, M.A. Spackman, "*CrystalExplorer*: a program for Hirshfeld surface analysis, visualization and quantitative analysis of molecular crystals", *J. Appl. Crystallogr.* 54 (2021) 1006–1011. https://doi.org/10.1107/S1600576721002910.

[58] T. Gruene, J.T.C. Wennmacher, C. Zaubitzer, J.J. Holstein, J. Heidler, A. Fecteau-Lefebvre, S. De Carlo, E. Müller, K.N. Goldie, I. Regeni, T. Li, G. Santiso-Quinones, G. Steinfeld, S. Handschin, E. van Genderen, J.A. van Bokhoven, G.H. Clever, R. Pantelic, "Rapid Structure Determination of Microcrystalline Molecular Compounds Using Electron Diffraction", *Angew. Chem. Int. Ed.* 57 (2018) 16313–16317. https://doi.org/10.1002/anie.201811318.

[59] M. Gemmi, E. Mugnaioli, T.E. Gorelik, U. Kolb, L. Palatinus, P. Boullay, S. Hovmöller, J.P. Abrahams, "3D Electron Diffraction: The Nanocrystallography Revolution", *ACS Cent. Sci.* 5 (2019) 1315–1329. https://doi.org/10.1021/acscentsci.9b00394.

[60] D. Marchetti, F. Guagnini, A.E. Lanza, A. Pedrini, L. Righi, E. Dalcanale, M. Gemmi, C. Massera, "Combined Approach of Mechanochemistry and Electron Crystallography for the Discovery of 1D and 2D Coordination Polymers", *Crystal Growth & Design.* 21 (2021) 6660–6664. https://doi.org/10.1021/acs.cgd.1c01058.

[61] M. Gemmi, A.E. Lanza, "3D electron diffraction techniques", *Acta Crystallogr. B Struct. Sci. Cryst. Eng. Mater.* 75 (2019) 495–504. https://doi.org/10.1107/S2052520619007510.

[62] L. Palatinus, V. Petříček, C.A. Corrêa, "Structure refinement using precession electron diffraction tomography and dynamical diffraction:

theory and implementation", *Acta Crystallogr. A Found. Adv.* 71 (2015) 235–244. https://doi.org/10.1107/S2053273315001266.

[63] L. Palatinus, P. Brázda, P. Boullay, O. Perez, M. Klementová, S. Petit, V. Eigner, M. Zaarour, S. Mintova, "Hydrogen positions in single nanocrystals revealed by electron diffraction", *Science*. 355 (2017) 166–169. https://doi.org/10.1126/science.aak9652.

[64] S. Mecozzi, J. Rebek, Jr., "The 55 % Solution: A Formula for Molecular Recognition in the Liquid State", *Chem. - Eur. J.* 4 (1998) 1016–1022. https://doi.org/10.1002/(SICI)1521-3765(19980615)4:6<1016::AID-CHEM1016>3.0.CO;2-B.

[65] V.I. Nikolayenko, D.C. Castell, D.P. van Heerden, L.J. Barbour, "Guest-Induced Structural Transformations in a Porous Halogen-Bonded Framework", *Angew. Chem. Int. Ed.* 57 (2018) 12086–12091. https://doi.org/10.1002/anie.201806399.

[66] F.M. Winnik, "Photophysics of preassociated pyrenes in aqueous polymer solutions and in other organized media", *Chem. Rev.* 93 (1993) 587–614. https://doi.org/10.1021/cr00018a001.

[67] L. Spinelle, M. Gerboles, G. Kok, S. Persijn, T. Sauerwald, "Review of Portable and Low-Cost Sensors for the Ambient Air Monitoring of Benzene and Other Volatile Organic Compounds", *Sensors*. 17 (2017) 1520. https://doi.org/10.3390/s17071520.

[68] J.L. Howard, Q. Cao, D.L. Browne, "Mechanochemistry as an emerging tool for molecular synthesis: what can it offer?", *Chem. Sci.* 9 (2018) 3080–3094. https://doi.org/10.1039/C7SC05371A.

[69] F. Gomollón-Bel, "Ten Chemical Innovations That Will Change Our World: IUPAC identifies emerging technologies in Chemistry with potential to make our planet more sustainable", *Chem. Int.* 41 (2019) 12–17. https://doi.org/10.1515/ci-2019-0203.

[70] K.J. Ardila-Fierro, J.G. Hernández, "Sustainability Assessment of Mechanochemistry by Using the Twelve Principles of Green Chemistry", *ChemSusChem*. 14 (2021) 2145–2162. https://doi.org/10.1002/cssc.202100478.

[71] S. Biswas, S. Banerjee, M.A. Shlain, A.A. Bardin, R.V. Ulijn, B.L. Nannenga, A.M. Rappe, A.B. Braunschweig, "Photomechanochemical control over stereoselectivity in the [2 + 2] photodimerization of acenaphthylene", *Faraday Discuss.* 241 (2023) 266–277. https://doi.org/10.1039/D2FD00122E.

[72] T. Sasaki, T. Nakane, A. Kawamoto, T. Nishizawa, G. Kurisu, "Microcrystal electron diffraction (MicroED) structure determination of a mechanochemically synthesized co-crystal not affordable from solution crystallization", *CrystEngComm.* 25 (2023) 352–356. https://doi.org/10.1039/D2CE01522F.

[73] P. Simoncic, E. Romeijn, E. Hovestreydt, G. Steinfeld, G. Santiso-Quiñones, J. Merkelbach, "Electron crystallography and dedicated electron-diffraction instrumentation", *Acta Crystallogr. E Cryst. Commun.* 79 (2023) 410–422. https://doi.org/10.1107/S2056989023003109.

[74] L. Palatinus, P. Brázda, M. Jelínek, J. Hrdá, G. Steciuk, M. Klementová, "Specifics of the data processing of precession electron diffraction tomography data and their implementation in the program *PETS2.0"*, *Acta. Crystallogr. B Struct. Sci. Cryst. Eng. Mater.* 75 (2019) 512–522. https://doi.org/10.1107/S2052520619007534.

[75] (a) SADABS Bruker AXS; Madison, Wisconsin, USA, 2004; "SAINT, Software Users Guide", Version 6.0; Bruker Analytical X-ray Systems, Madison, WI, (1999); (b) Sheldrick, G. M. "SADABS v2.03: Area-Detector Absorption Correction". University of Göttingen, Germany, (1999).

[76] G.M. Sheldrick, "*SHELXT* – Integrated space-group and crystal-structure determination", *Acta Crystallogr. A Found. Adv.* 71 (2015) 3–8. https://doi.org/10.1107/S2053273314026370.

[77] G.M. Sheldrick, "Crystal structure refinement with *SHELXL"*, *Acta Crystallogr. C Struct. Chem.* 71 (2015) 3–8. https://doi.org/10.1107/S2053229614024218.

[78] L.J. Farrugia, "*WinGX* suite for small-molecule single-crystal crystallography", *J. Appl. Crystallogr.* 32 (1999) 837–838. https://doi.org/10.1107/S0021889899006020.

[79] M.C. Burla, R. Caliandro, B. Carrozzini, G.L. Cascarano, C. Cuocci, C. Giacovazzo, M. Mallamo, A. Mazzone, G. Polidori, "Crystal structure determination and refinement *via SIR2014"*, *J. Appl. Crystallogr.* 48 (2015) 306–309. https://doi.org/10.1107/S1600576715001132.

[80] C.B. Hübschle, G.M. Sheldrick, B. Dittrich, "*ShelXle*: a Qt graphical user interface for *SHELXL"*, *J. Appl. Crystallogr.* 44 (2011) 1281–1284. https://doi.org/10.1107/S0021889811043202.

[81] V. Petříček, M. Dušek, L. Palatinus, "Crystallographic Computing System JANA2006: General features", *Z. Kristallogr. Cryst. Mater.* 229 (2014) 345–352. https://doi.org/10.1515/zkri-2014-1737.

[82] J.B. Maglic, R. Lavendomme, "*MoloVol*: an easy-to-use program for analyzing cavities, volumes and surface areas of chemical structures", *J. Appl Crystallogr.* 55 (2022) 1033–1044. https://doi.org/10.1107/S1600576722004988.

[83] C.F. Macrae, I. Sovago, S.J. Cottrell, P.T.A. Galek, P. McCabe, E. Pidcock, M. Platings, G.P. Shields, J.S. Stevens, M. Towler, P.A. Wood, "*Mercury 4.0*: from visualization to analysis, design and prediction", *J. Appl. Crystallogr.* 53 (2020) 226–235. https://doi.org/10.1107/S1600576719014092.

[84] H. Kitagawa, H. Ohtsu, M. Kawano, "Kinetic Assembly of a Thermally Stable Porous Coordination Network Based on Labile CuI Units and the Visualization of I_2 Sorption", *Angew. Chem. Int. Ed.* 52 (2013) 12395–12399. https://doi.org/10.1002/anie.201306776.

[85] T. Friščić, S.L. Childs, S.A.A. Rizvi, W. Jones, "The role of solvent in mechanochemical and sonochemical cocrystal formation: a solubility-based approach for predicting cocrystallisation outcome", *CrystEngComm*. 11 (2009) 418–426. https://doi.org/10.1039/B815174A.

[86] Niebel, H., van den Berg, C., Steinfeld, G., van Veen, A. & Tuohimaa, T. (2021). *European Patent Office*. EP21191210.0., n.d.

[87] Garbuglia, F. & Steinfeld, G. (2022). *European Patent Office*. EP22192609.0.

[88] O.V. Dolomanov, L.J. Bourhis, R.J. Gildea, J.A.K. Howard, H. Puschmann, "*OLEX2*: a complete structure solution, refinement and analysis program", *J. Appl. Crystallogr.* 42 (2009) 339–341. https://doi.org/10.1107/S0021889808042726.

6 Diamondoids Flexibles TPPM-Copper Paddle wheels based MOFs

This chapter will discuss the synthesis and characterisation of a novel class of flexible TPPM-based Metal-Organic Frameworks (MOFs), with a particular focus on the structural investigation of the involved crystalline structures. As elucidated in Chapter 5 (Figure 5.1), the tetra-4-(4-pyridil)phenylmethane (**TPPM**) molecule in the presence of metal centres, due to its four rigid pyridyl wings, can acts as a tetrahedral ligand. The use of **TPPM** as an organic linker for MOFs synthesis has been already discussed in the literature. [1–4] Herein we describe the utilisation of **TPPM** with different metal nodes (Cu(II) paddle wheels) [5] in order to achieve highly interpenetrated MOFs with a diamond-like network featuring dynamic behaviour. Moreover, the framework functionalization through the introduction of specific fluorinated secondary building units (SBUs), and its effects on the absorption of specific fluorinated guests will also be discussed.

6.1 Introduction

Metal-organic frameworks (MOFs) are a class of crystalline porous materials, formed by combining metal-based secondary building units (SBUs) with specific organic linkers through relatively strong bonds (reticular material synthesis). MOFs exhibit a broad range of potential applications, including gas storage, separations, and catalysis. [6–15] The chemical composition and shape of their building units can be largely varied leading to materials that offer unique properties, making them the subject of extensive study and industrial applications. [16–18]

The MOF design was facilitated by the introduction of the SBU concept (**Figure 6.1**), in which pre-synthesised units are linked together by rigid organic molecules. [5]

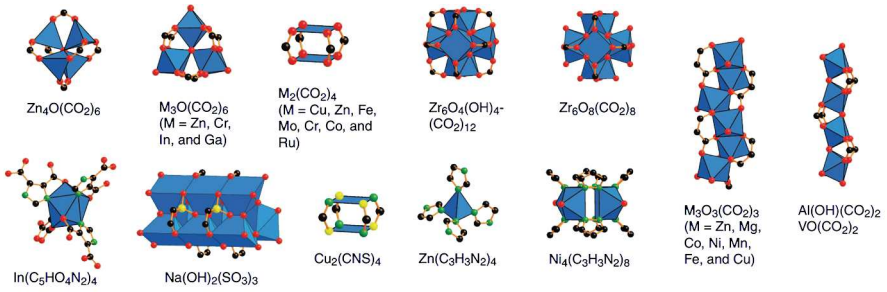

Figure 6.1: Representation of the most common inorganic secondary building units (SBUs). [5]

The class of **TPPM**-based MOFs described in this chapter is characterized by the employment of $M_2(CO_2)_4$ SBUs, in which Copper(II) acts as the metal centre. This class of SBUs, known as Cu(II) paddle-wheels, usually gives rise to 2D or 3D networks through polytopic carboxylate linkers and can present ligands coordinated to the metal in their apical position. In this work, the SBU's carboxylate linkers are constituted by monotopic ligands while the **TPPM** molecules interact with the Cu(II) centres in their apical positions. As will be detailed in Section 6.2, the resulting linear SBU combined with the **TPPM** tetrahedral geometry leads to diamond-like networks (**dia**).

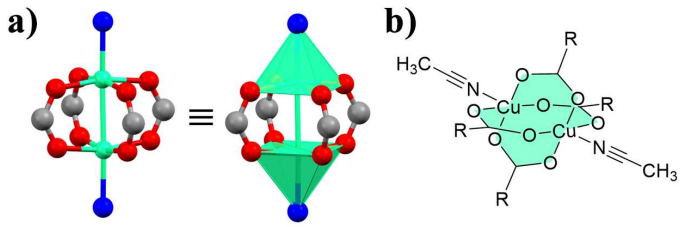

Figure 6.2: (a) Schematic representation of a Cu(II)paddle-wheel characterized by two ligands in its apical positions. (b) Example of a Cu(II)paddle-wheel with ACN molecules fulfilling the Cu(II) coordination sphere. The carboxylate groups are represented with a generic residual group (R).

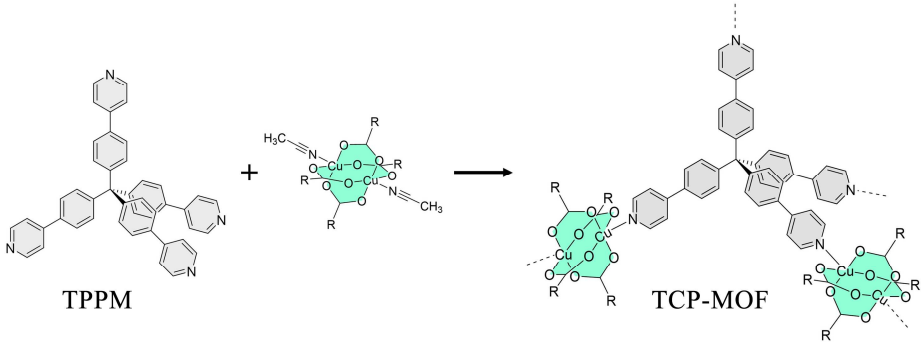

Figure 6.3: Generalized reaction between **TPPM** and $[Cu_2(RCO_2)_4(ACN)_2]$ as Cu(II)paddle-wheel source, to obtain a **TCP-MOF**.

There are multiple reasons behind the employment of Cu(II)paddle-wheels composed of monotopic carboxylate (Figure 6.2). Indeed, their apical ligands are usually neutrally charged as are the **TPPM** molecules. This facilitates the network formation through a simple ligand exchange process. Furthermore, the resulting **dia**-net displays the carboxylate residual functions oriented inside the framework's channels (Figure 6.4c). Since the residual groups connected to the COO^{2-} function do not take part in the network formation, they can be easily modified in order to obtain different isoreticular MOFs based on TPPM and Cu(II) paddle-wheels (**TCP-MOF**, Figure 6.3).

The **TCP-MOF** framework is usually characterized by a **dia**-net with wide pores of ~40Å in diameter (Figure 6.4a). This high internal empty volume results drastically reduced by the interpenetration of multiple networks,

leading to stable and flexible crystal structures, with well-defined channels (Figure 6.4c). The interpenetration plays an additional role in the system's flexibility, adding additional degrees of freedom as inter-framework movements. [19]

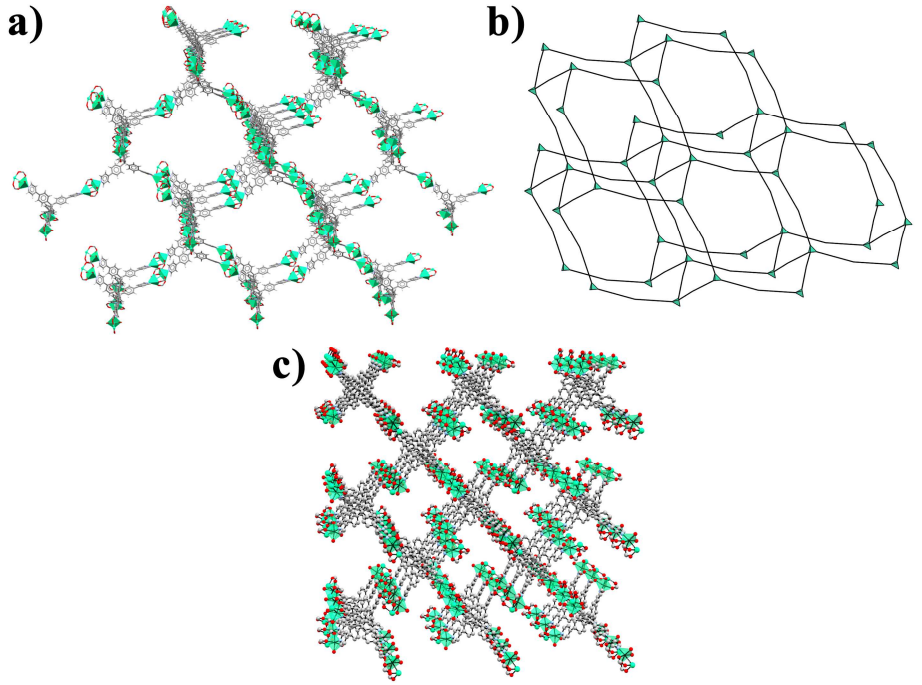

Figure 6.4: Comparison between a single **TCP-MOF** network (a), the resulting **dia**-net (b), and a multi-interpenetrated network with well-defined channels (c).

TCP-MOFs can undergo a crystal-to-crystal phase transition, between open pore and closed pore forms, after the removal of guest molecules embedded in their pores. This phase transition can be induced by applying external stimuli such as temperature or pressure changes, in analogy to the dynamical behaviour of **TPPM** crystals. [20] However, after the phase transitions, **TCP-MOFs** retain their well-defined framework of coordinative interactions (Figure 6.5); they can be classified as third-generation MOFs, a class of materials characterized by framework dynamicity, which is an essential prerequisite for responsiveness towards external stimuli.

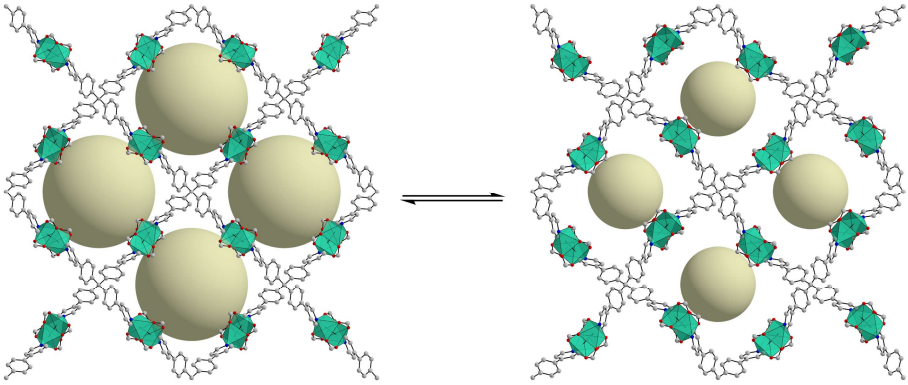

Figure 6.5: Example of a reversible crystal-to-crystal phase transition of a generic **TCP-MOF**, between an open pore (*left*) and a closed pore (*right*) form. The R groups of the SBUs (which would point inside the channels) and hydrogen atoms have been omitted for clarity reasons.

In **TCP-MOFs**, the residual groups bonded to the SBUs are disposed facing the framework's channels (see Figure 6.5). This introduces another variable in the design of this class of MOFs. Indeed, the properties of these materials can be additionally tuned by changing the carboxylic ligand involved in the SBUs (R-COOH). The last sections of this chapter will be focused on the introduction of C-F bonds in the TCP-MOF framework, to obtain fluorinated MOFs (F-MOF). The insertion of fluorinated groups in the MOF structure could confer several advantages in terms of interactions with specific guest molecules, such as relevant fluorinated pollutants. [21]

6.2 Results and Discussion

6.2.1 Synthesis and Characterization of TCP-MOF1

In order to obtain a crystalline phase of **TCP-MOF1**, two different solutions containing **TPPM** and $[Cu_2(AcCO_2)_4(ACN)_2]$, in a solvent mixture of n-BuOH/$CHCl_3$ (1:1 v/v), were placed in contact through a layering process and heated at 90°C for 2 days (**Scheme 6.1**). The layering approach resulted to be essential to synthesise a crystalline product. At the end of the reaction, the contact region between the two layers presented large green crystals suitable for SC-XRD analysis (Figure S6.1).

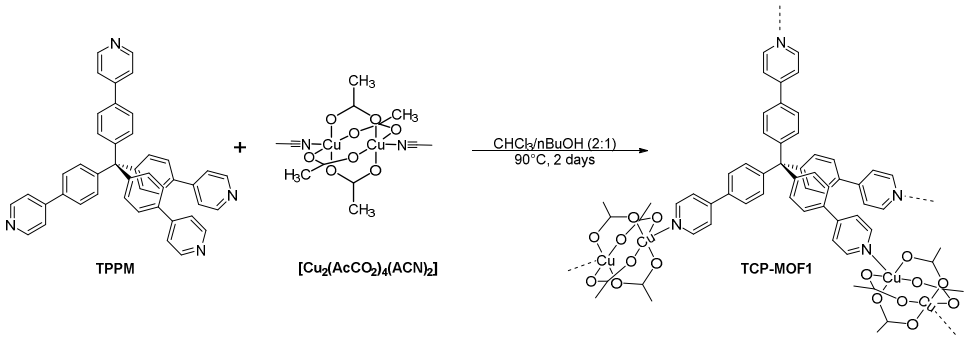

Scheme 6.1: Synthesis of **TCP-MOF1.**

At 200 K, **TCP-MOF1** crystallizes in a tetragonal and non-centrosymmetric space group ($P\bar{4}$), with the following unit cell parameters $a,b = 26.0049(15)$ Å, $c = 7.3356(5)$ Å (Table S6.1). Its framework is composed of **TPPM** molecules coordinated, through all their pyridyl functionalities, to the Cu(II) centres of the SBUs in their apical positions. Thus, the obtained MOF presents a 3D polymeric net with $\{TPPM[Cu_2(AcCO_2)_4]_2\}_n$ as repeating units (Figure 6.6). From the X-ray diffraction data, it was also possible to model a $CHCl_3$ and an n-BuOH molecule, both in proximity to the framework backbone (Figure S6.2). The **TCP-MOF1** presents a diamond-like network (**dia**-net, as calculated by ToposPro software) [22] eight times interpenetrated (Figure 6.7). The eight interlaced networks result aligned along the

crystallographic *c*-axis with an average distance of 7.3356(5) Å (Figure S6.3). This permits the extension of channels along that direction, accounting for ~45.7% of the unit cell volume (2267.37 $Å^3$, as calculated by Mercury4 software). [23]

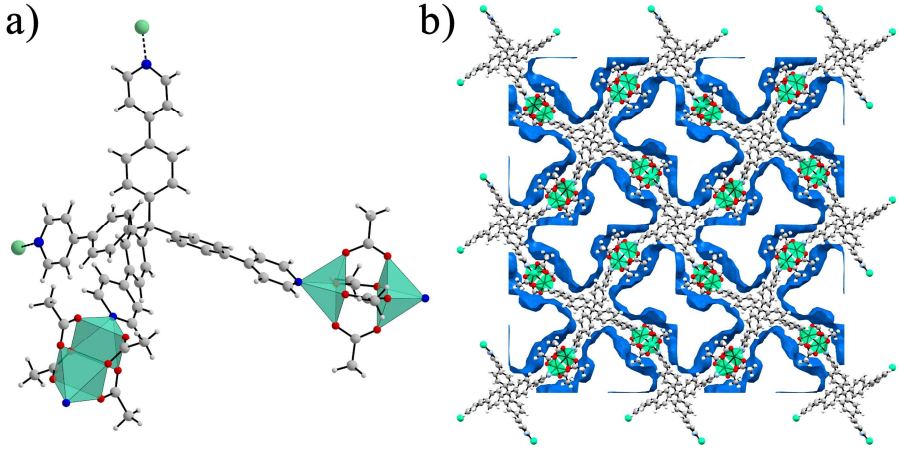

Figure 6.6: (a) Polymeric repeating unit of **TCP-MOF1**. (b) Crystal structure expansion (oriented along the crystallographic *b*-axis) and related channels as blue surfaces. Copper atoms are represented as green polyhedral while oxygen, nitrogen and carbon atoms as red, blue and grey spheres, respectively. The solvent molecules have been removed for clarity.

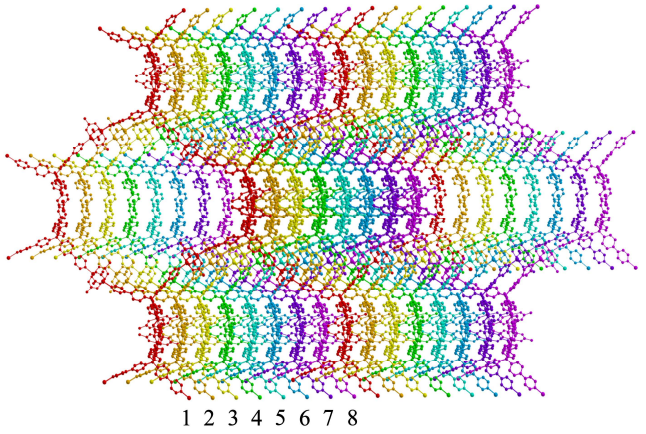

Figure 6.7: Expanded view of the **TCP-MOF1** structure. The eight interpenetrated networks are represented in different colours. Solvent molecules have been omitted for clarity.

Interestingly, at 300 K, **TCP-MOF1** crystals display different lattice parameters, suggesting the occurrence of a temperature-induced single-crystal to single-crystal phase transition (Figure 6.8). A complete SC-XRD analysis was carried out at 300 K, highlighting the presence of a tetragonal centrosymmetric space group ($P\,4/n$) and $a,b = 27.389(9)$ Å, $c = 7.304(2)$ Å as unit cell parameters (Table S6.2). It is worth to mention that, in such conditions, the thermal motion reduces the structure quality, in terms of ADPs values and modelling of solvent molecules. This **TCP-MOF1** structure displays the phenyl rings disordered on two different positions. Moreover, the 300 K form presents larger unit cell values with a volume increased by 518.42 $Å^3$ with respect to the 200 K form. This cell expansion also affects the calculated virtual void, which, in this case, is around 53.1% of the unit cell volume (2908.93 $Å^3$).

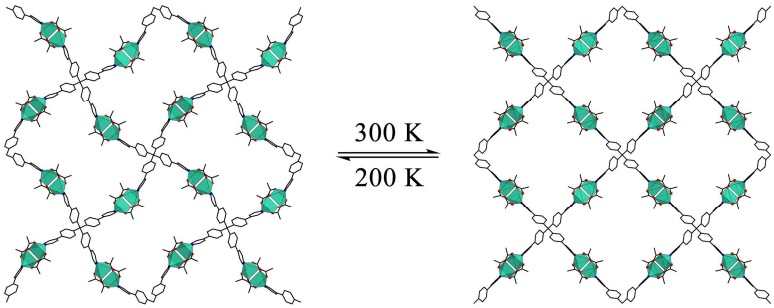

Figure 6.8: TCP-MOF1 single-crystal to single-crystal phase transition. Hydrogen atoms, disordered fragments and solvent molecules have been omitted for clarity. Copper atoms are represented as green polyhedra while oxygen and nitrogen atoms as red and blue spheres, respectively.

At 300K, the system displays square-shaped channels, wherein the SBU centroids distances are equal for both d_1 and d_2 (Figure 6.9a). The geometry of these channels changes when the temperature is lowered to 200K. Indeed, the channels undergo a contraction of d_1 and an elongation of d_2, subsequently leading to a reduction in the pore section area (Figure 6.9b). The distortion of these channels occurs through a rotation of the **TPPM** ligands, causing a misalignment between their pyridyl-phenyl wings and the vertical axis of the SBU (**Figure S6.7**).

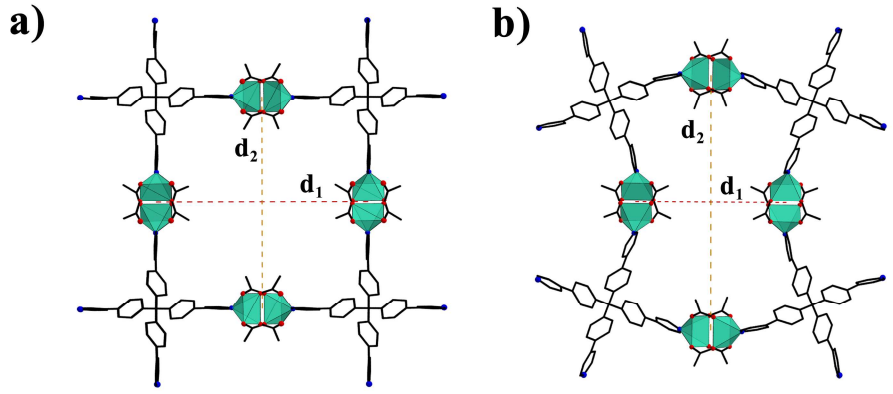

Figure 6.9: Comparison of the two pore geometries in **TCP-MOF1** at 300K (a) and 200K (b), both oriented along the *c*-axis. The distances between the SBU centroids are depicted as red (d_1) and orange (d_2) dashed lines. d_1(a) = d_2(a) = 19.367(5) Å, d_1(b) = 13.6644(6) Å; d_2(b) = 23.1122(9) Å. Hydrogen atoms, disordered fragments and solvent molecules have been omitted for clarity.

To further investigate if this phase transition could also occur through a solvent removal process, crystals of **TCP-MOF1** were placed under vacuum (~10^{-3} bar) for 20 minutes at 300K. However, the obtained product resulted completely amorphous. Moreover, when exposed to atmospheric conditions for two of hours, **TCP-MOF1** drastically loses crystallinity leading to a partially amorphous product (Figure S6.9).

In summary, the **TCP-MOF1** phase exhibits a highly interpenetrated network and undergoes a temperature-induced single-crystal to single-crystal phase transition (Figure 6.8). This process is characterized by the contraction of the framework when the system reaches 200K, highlighting the presence of a potentially flexible framework. Nevertheless, because of its susceptibility to the extraction of embedded guest molecules, **TCP-MOF1** can be categorized as a first-generation MOF (Figure S6.9).

6.2.2 Synthesis and Characterization of TCP-MOF2

To enhance the stability of the **TCP-MOF** framework against the removal of guest molecules, a new SBU was introduced. The acetate ligand was therefore substituted with benzoate, in order to increase the inter- and intra-framework interactions. The resulting SBU of general formula $[Cu_2(PhCO_2)_4(ACN)_2]$ was synthesized following the procedure reported in the supplementary information section. **TCP-MOF2** was then synthesized in DMF from a mixture of **TPPM**, $[Cu_2(PhCO_2)_4(ACN)_2]$ and benzoic acid, left at 90°C for 3 days. The excess of benzoic acid acts as a modulating agent decelerating the reaction speed, a requisite condition for achieving a crystalline material.

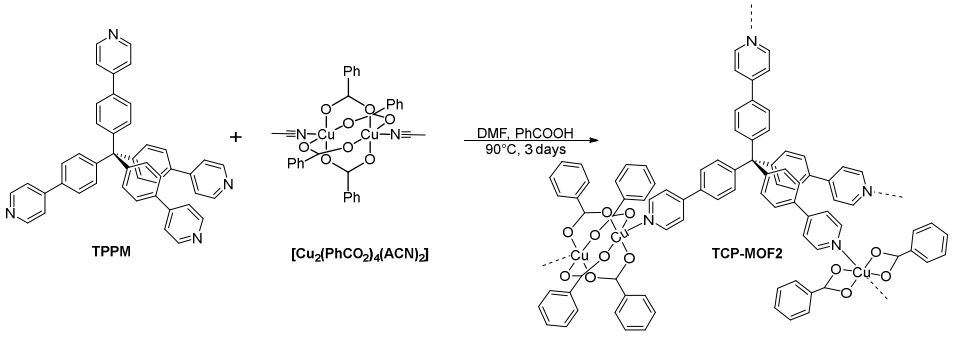

Scheme 6.2: Synthesis of **TCP-MOF2.**

The obtained product crystallizes in micrometric crystals (Figure S6.10), whose PXRD profile does not correspond to any known structure. The small crystalline domains hamper any SC-XRD diffraction characterization, requiring the usage of 3D electron diffraction (3D ED). Due to the beam

sensitivity of the material, the analysis was carried out using a special low-dose setup, in which the electron dose is below 0.05 el·s^{-1} Å^2. The diffraction patterns were collected following a peculiar continuous rotation (cRED) protocol, in which the parallel electron beam is scanning on a square area of 300x300nm^2 (see Chapter 2.2) During the STEM-cRED data collection protocol, the diffracted electrons pass through the high-angle annular dark field (HAADF) STEM detector allowing the live-tracking of the crystal. In the meantime, the Timepix single electron detector, placed below the HAADF, is collecting the electron diffraction patterns. [24] The 3D ED analysis was carried out on two different crystals, in order to improve data completeness. The PETS2 software [25] was employed to analyse the diffraction patterns and subsequently find the unit cell, index, and integrate the reflection intensities. From the reciprocal space reconstruction, the sample was indexed in the monoclinic primitive lattice with parameters a = 25.534(7) Å, b = 7.485(3) Å, c = 22.287(9) Å, β = 98.81(3) ° (Table S6.6). The unit cell determination from 3D ED data was checked on PXRD data through Le Bail refinement (Figure 6.10), revealing a distinct congruence between the two analyses (Table S6.4).

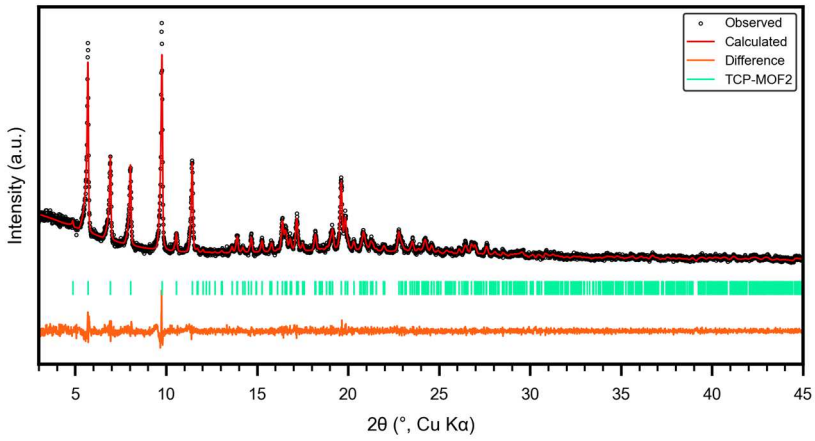

Figure 6.10: Profile fit from Le Bail refinement on **TCP-MOF2**. The refinement converged to Rp = 6.85%, wRp = 8.69% and GOF = 6.37.

The indexed data were integrated up to 0.80 Å of resolution and the structural model was solved *ab initio* through the Superflip software. [26] The obtained model was refined kinematically, revealing the formation of the **TPPM**-based MOF **TCP-MOF2** (Figure 6.12a). **TCP-MOF2** presents a diamond-like network eight times interpenetrated (as calculated by ToposPro software), [22] in analogy to **TCP-MOF1**.

Interestingly, in this product, the framework connectivity comprises **{TPPM[Cu$_2$(PhCO$_2$)$_4$][Cu(PhCO$_2$)$_2$]}$_n$** repeating units (Figure 6.11a), in which **TPPM** molecules are respectively coordinated to Cu(II)paddle-wheels (Figure 6.11b) and Cu(II) octahedral complexes (Figure 6.11c). In both metal nodes, the **TPPM** molecules result coordinated in metals' apical positions, while the benzoate ligands are disposed along the equatorial ones.

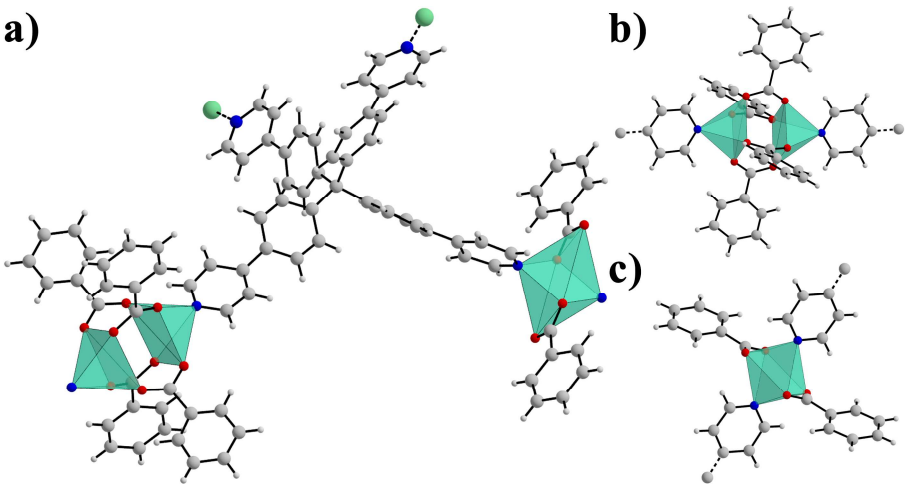

Figure 6.11: Polymeric repeating unit of **TCP-MOF2** (a), Copper(II) paddle-wheel (b) and octahedral complex (c). Copper atoms are represented as green polyhedra while oxygen, nitrogen, and carbon atoms as red, blue and grey spheres, respectively. The solvent molecules have been removed for clarity.

The resulting crystal structure exhibits channels oriented along the crystallographic *b*-axis, accounting for 16.7% of the unit cell volume (703.92 $Å^3$, Figure 6.12b). From the kinematical refinement it was possible to determine the solvent molecules embedded in those channels (Figure 6.12c). Thus, the **TCP-MOF2** asymmetric unit was modelized with a single DMF molecule presenting an occupancy of 0.5. The partial occupancy of these solvent molecules is also supported by TGA analysis, which shows a weight loss attributable to a DMF stoichiometry of 0.35 (Figure S6.20).

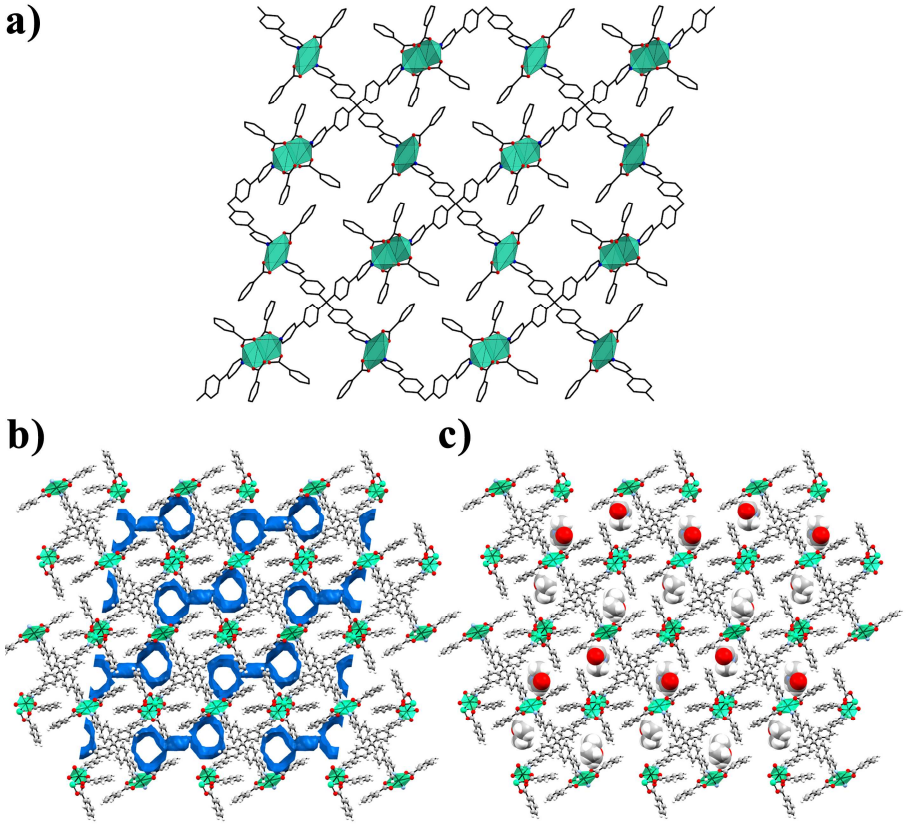

Figure 6.12: Crystal structure expansion of **TCP-MOF2** oriented along the crystallographic *b*-axis (a) with its relative channels as blue surfaces (b) and with the DMF molecules embedded in the frameworks channels (c). Copper atoms are represented as green polyhedra while oxygen, nitrogen and carbon atoms as red, blue and grey spheres, respectively. In (a) the solvent molecules and hydrogen atoms have been removed for clarity.

In contrast to **TCP-MOF1,** the **TCP-MOF2** phase results stable under atmospheric conditions also after days of exposure. Thus, to investigate its stability upon the removal of the solvent molecules trapped in its channels, **TCP-MOF2** was heated at 130°C for 1 day. The resulting product is crystalline and exhibits a PXRD profile that differs from the diffractogram of the initial sample (Figure 6.13). This result suggests the formation of a new, unknown crystalline phase after the thermal treatment (**TCP-MOF2**(E)). Further characterization will be focused on the crystal structure termination of this novel phase obtained from **TCP-MOF2**.

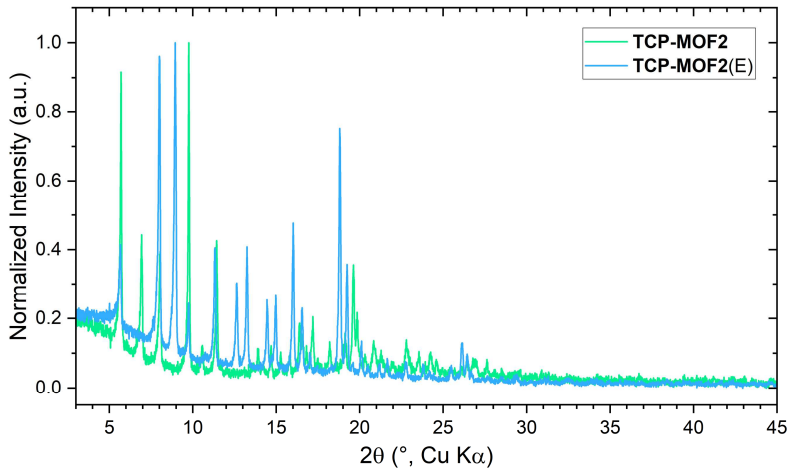

Figure 6.13: Comparison between the PXRD profile of **TCP-MOF2** and **TCP-MOF2(**E).

6.2.3 Synthesis and Characterization of TCP-MOF3

Diverse reaction conditions were tested with the aim to obtain a **TCP-MOF** based on $[Cu_2(PhCO_2)_4]$ units only, and with the same connectivity displayed by **TCP-MOF1**. A novel crystalline phase was obtained after layering different solutions containing **TPPM**, benzoic acid and $[Cu_2(PhCO_2)_4(ACN)_2]$, in a solvent mixture of $^{i}PrOH/CHCl_3$ (1:1 v/v) while heating the system at 50°C for 3 days (Scheme 6.3). The layering approach and the usage of benzoic acid, as modulating agent, resulted to be essential to obtain a crystalline product.

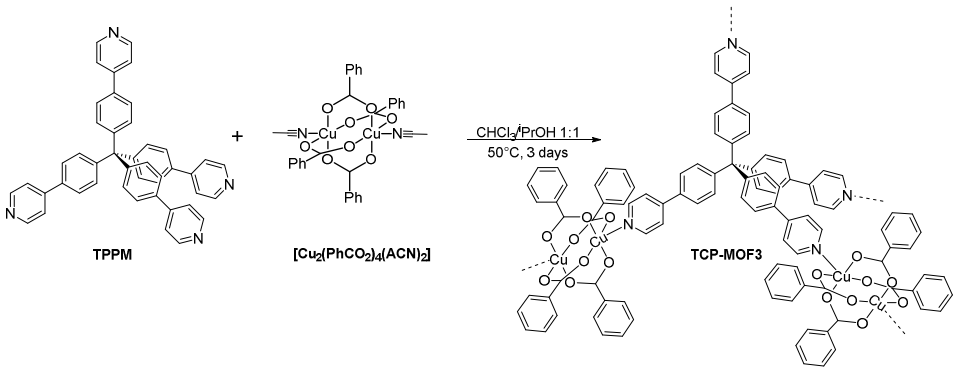

Scheme 6.3: Solvothermal synthesis of **TCP-MOF3.**

The resulting product was obtained as rod-shaped micrometric crystals (Figure S6.11a), whose PXRD profile did not correspond to any known structure. Due to the presence of small crystalline domains, 3D electron diffraction (3D ED) was employed for the structural characterization. The analysis was carried out using the special low-dose setup adopted also for the structure elucidation of **TCP-MOF2** (electron dose below 0.05 $el \cdot s^{-1} \cdot Å^2$). The diffraction patterns were collected following a PEDT data collection protocol (see. Chapter 2.2). From the reciprocal space reconstruction a tetragonal lattice was identified, with space group $P\,\bar{4}b2$ and unit cell parameters a = 22.974(8) Å and c = 9.005(4) Å (Table S6.7). The indexed reflections were then integrated and the crystal structure was solved *ab initio* and kinematically refined, revealing the presence of a 3D coordination polymer

based on **TPPM** and Cu(II)paddle-wheels (**TCP-MOF3**, Figure 6.14), of general formula **{TPPM[Cu$_2$(PhCO$_2$)$_4$]$_2$}$_n$**. The repeating units form a diamond-like network (**dia**-net) that is eight times interpenetrated, [22] as the previously described **TCP-MOFs**. Moreover, by orienting the **TCP-MOF3** along the crystallographic *c*-axis it is possible to distinguish the phenyl rings of the SBUs protruding outside the polymeric network. In **TCP-MOF3**, as anticipated for this particular type of MOF, the substituent of the carboxylic acids constituting the SBUs are positioned toward the centre of the channels, in which guest molecules can be entrapped (Figure 6.15a). Unlike **TCP-MOF1**, this structure does not feature open channels along the *c*-axis. Instead, it displays small and isolated void regions, which constitute the 2.9% of the unit cell volume (126.75 Å^3, Figure 6.15b).

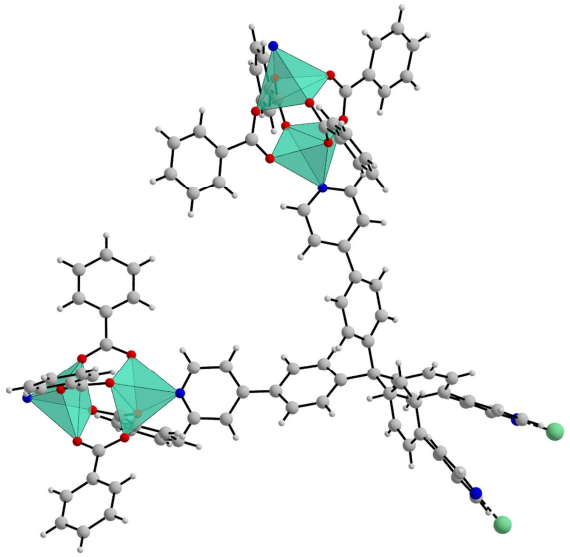

Figure 6.14: Polymeric repeating unit of **TCP-MOF3**. Copper atoms are represented as green polyhedra while oxygen, nitrogen, and carbon atoms as red, blue and grey spheres, respectively.

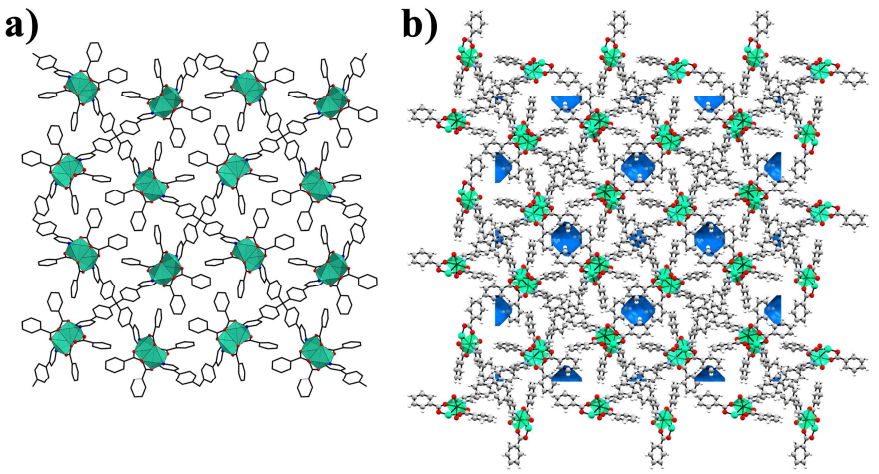

Figure 6.15: Crystal structure expansion of **TCP-MOF3** oriented along the crystallographic *c*-axis (a) with its relative isolated voids as blue surfaces (b). Copper atoms are represented as green polyhedra while oxygen, nitrogen and carbon atoms are shown as red, blue and grey spheres, respectively.

The comparison between the calculated **TCP-MOF3** PXRD profile, calculated from the 3D ED model, and the experimental one, reveals that they derive from different crystal structures (Figure 6.16). Moreover, the experimental PXRD diffractogram seems to be correlated to a crystal lattice with a slightly larger unit cell. The calculated diffractogram was named **TCP-MOF3**(Empty Phase) since it does not contain solvent molecules trapped in its framework.

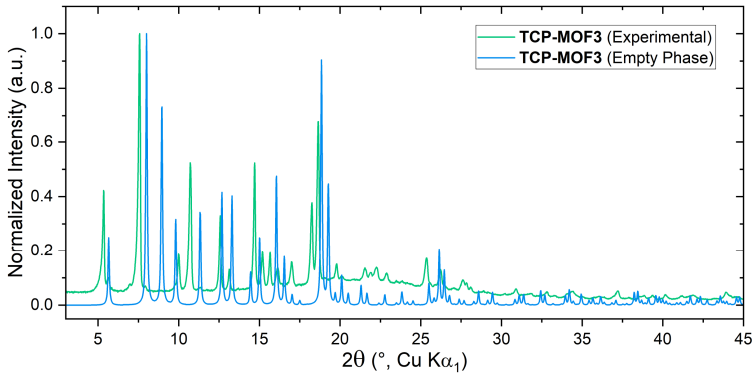

Figure 6.16: Comparison between the experimental and calculated PXRD profile of **TCP-MOF3**.

The empty phase of **TCP-MOF3** was also compared to the **TCP-MOF1**-200K phase, revealing similarities in both frameworks. As illustrated in Figure 6.17, the **TCP-MOF3** structure exhibits two Cu(II)paddle-wheels along the (200) plane that are closer together compared to those positioned on the ($\bar{2}$00) plane. In **TPC-MOF1**, at 200K, this asymmetry in the distanced between the centroids of SBUs was responsible of a reduction in pore size. Therefore, the empty phase of **TCP-MOF3** can be considered as a contracted form of a TCP-MOF constituted of **{TPPM[$Cu_2(PhCO_2)_4$]$_2$}$_n$** repeating units.

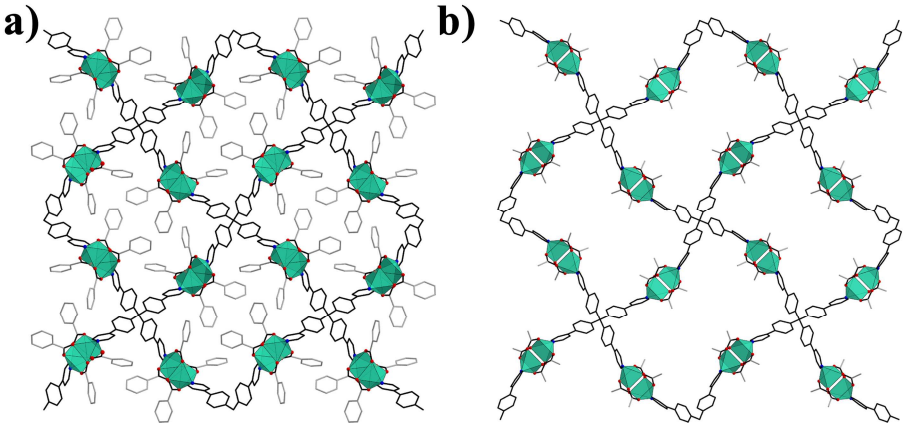

Figure 6.17: Comparison between the crystal structure of **TCP-MOF3**-Empty Phase (a) and **TCP-MOF2**-200K (b), both oriented along the crystallographic *c*-axis. Phenyl ring and methyl groups have been coloured in grey, to highlight the similarities of their frameworks.

To assess the framework flexibility of this material upon the removal of guest molecules, it was first necessary to isolate the expanded, solvated phase of **TCP-MOF3**, assuming that the initial empty phase was the contracted form. The product obtained from the reaction reported in Scheme 6.3 was thus soaked in BnOH for a day, in order to fill its pores with a high-boiling solvent. This step was intended to prevent the extraction of guest molecules during the 3D ED analysis, which is carried out under the high vacuum conditions of a TEM column (10^{-10} bar, see Chapter 5.2). Interestingly, the

same material could also be directly synthesized through a mechanochemical approach. The reaction was conducted in a mixer mill operating at 20 Hz, for 30 minutes and using BnOH as liquid additive (Scheme 6.4). This environmentally friendly approach is also very effective in terms of yield, allowing to achieve larger quantities of **TCP-MOF3** in few minutes. However, the mechanochemical product is less crystalline than the solvothermal one (Figure 6.18). For this reason, the 3D ED analysis was carried out on the product obtained from the soaking process.

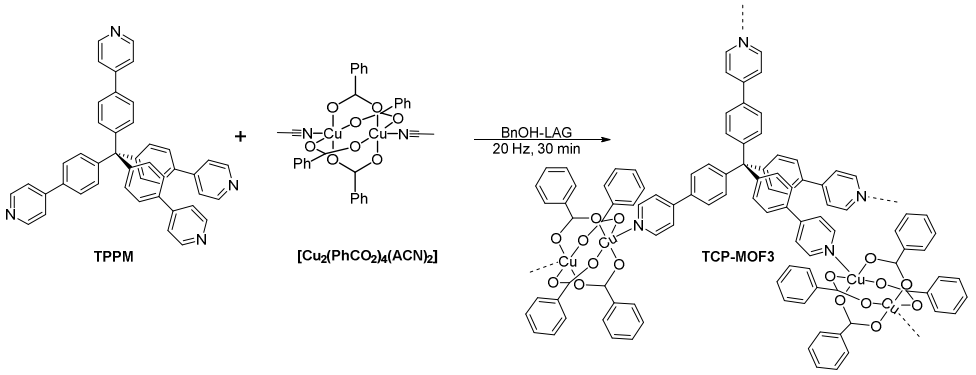

Scheme 6.4: Mechanochemical synthesis of **TCP-MOF3.**

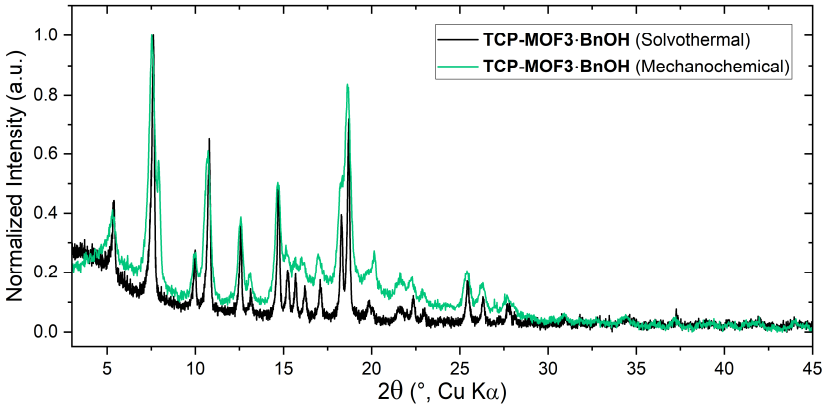

Figure 6.18: Superposition of the PXRD profiles of the **TCP-MOF3·BnOH** crystals obtained through soaking and mechanosythesis.

The 3D ED data collection was conducted on a single nanocrystal (Figure S6.11) through a STEM-cRED data collection protocol. The reconstructed reciprocal space was exhibiting a different symmetry with respect to the

contracted phase of **TCP-MOF3**. The collected data were indexed with a tetragonal unit cell in the $P\,4/n$ space group, featuring the cell parameters $a = 23.043(5)$ Å and $c = 8.803(2)$ Å. The structure could be solved *ab initio* and refined with a kinematical approach. The resulting structure corresponds to a MOF with the same connectivity of the empty, contracted form of **TCP-MOF3** (Figure 6.19, Table S6.8, Figure S6.16).

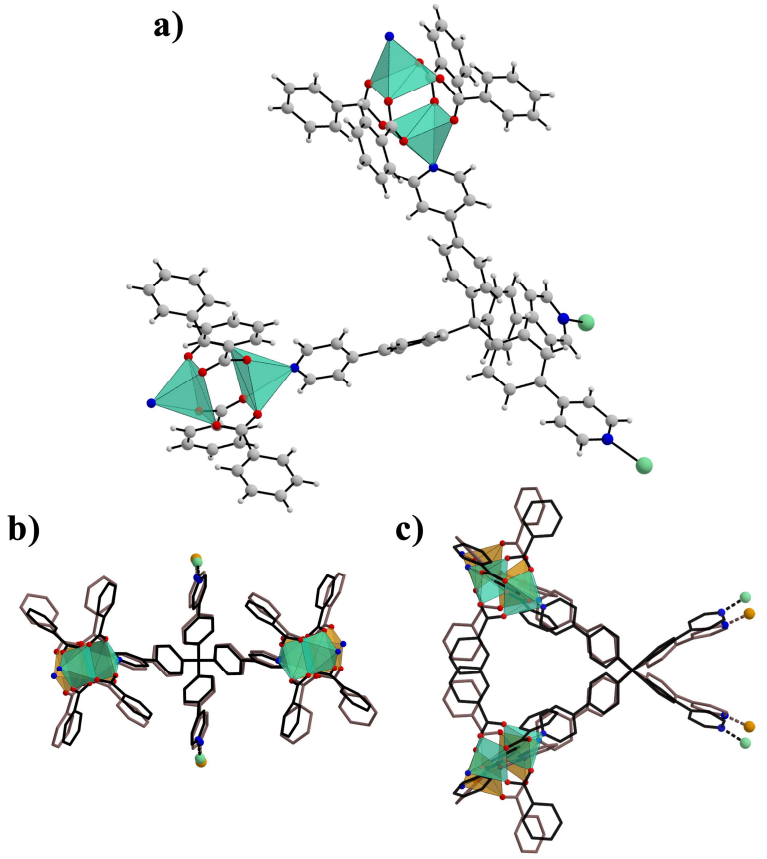

Figure 6.19: Polymeric repeating unit of **TCP-MOF3·BnOH** (a) and its superpositions with the **TCP-MOF3** empty phase, oriented along the crystallographic *c* and *b* axes (b and c) respectively Copper atoms are represented as green and orange polyhedra for **TCP-MOF3·BnOH** and the **TCP-MOF** empty phase, respectively. Oxygen, nitrogen, and carbon atoms as red, blue, and grey spheres, respectively.

If compared to the empty phase, the **{TPPM[Cu$_2$(PhCO$_2$)$_4$]$_2$}$_n$** repeating units show differences in their conformational arrangement. Indeed, in this new phase, the pyridyl-phenyl wings are slightly distorted, leading to a shift in the position of the metal nodes (Figure 6.19b-c). Along the *a* and *b* axes, the centroids of the Cu(II)paddle-wheels are now equally distanced, resulting in a square-like geometry comparable to the **TCP-MOF1** 300K phase (Figure 6.20). This positional change of the SBU induces a rearrangement of their phenyl substituents, leading to the opening of pores that run along the *c*-axis (10.7% of the unit cell volume, 501.9 Å^3, Figure 6.21). Thus, the **TCP-MOF3·BnOH** can be considered as the **TCP-MOF3** expanded phase.

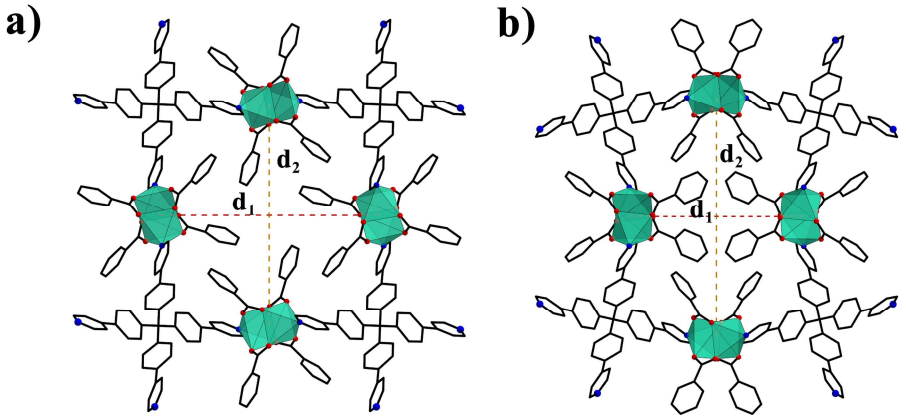

Figure 6.20: Comparison of the SBUs centroids distances in **TCP-MOF3·BnOH** and **TCP-MOF3** empty phase, both oriented along the *c*-axis. The distances between the centroids are depicted as red (d_1) and orange (d_2) dashed lines. d_1(a) = d_2(a) = 16.294(3) Å, d_1(b) = 13.202(3) Å; d_2(b) = 18.015(5) Å. Hydrogen atoms have been omitted for clarity.

Moreover, the calculated PXRD profile of the **TCP-MOF3·BnOH** phase was in agreement with the experimental pattern. To further confirm the comparison, a Le Bail refinement was conducted staring from the 3D ED lattice parameter (Figure 6.22). The resulting unit cell values showed $a,b = 23.2663(8)$ Å and $c = 8.8096(5)$ Å, indicating the congruence of the two crystal systems (Table S6.5).

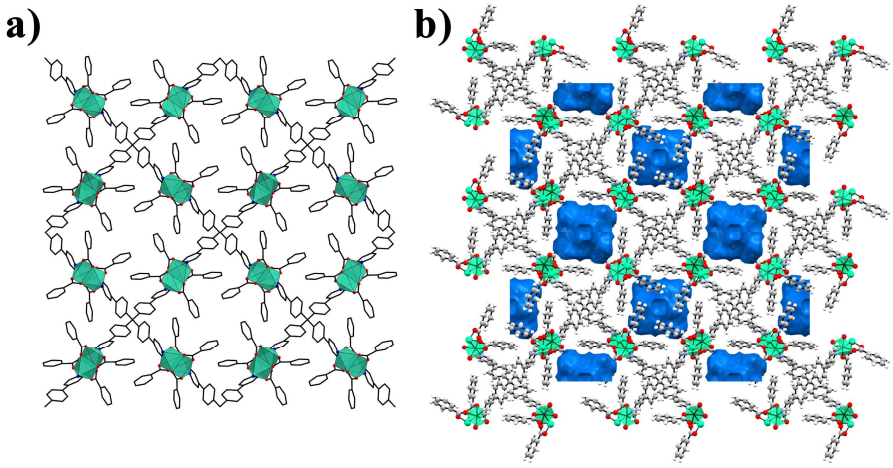

Figure 6.21: Crystal structure expansion of **TCP-MOF3·BnOH** oriented along the crystallographic *c*-axis (a) with its relative isolated voids as blue surfaces (b).

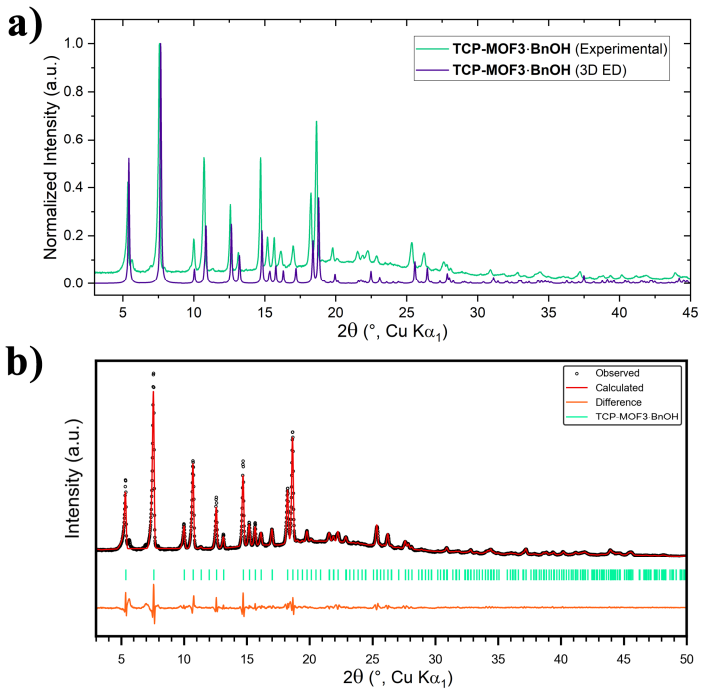

Figure 6.22: PXRD profile comparison between the experimental and calculated patterns of **TCP-MOF3·BnOH** (a). Profile fit from Le Bail refinement on **TCP-MOF3·BnOH**. The shown range is limited to 2θ values of 3-50 for clarity, whereas the refinement was carried out in the range 3-94°. The refinement converged to Rp = 3.39%, wRp = 6.05% and GOF = 2.29.

From the kinematical refinement it was not possible to modelise the solvent molecules embedded in the channels of the structure. Moreover, a TGA analysis conducted on this material showed the removal of the solvent molecules before its thermal degradation. The solvent stoichiometry (SS^{TGA}) calculated from its weight loss resulted being around six molecules of BnOH for repeating unit (Figure S6.21). However, this value of SS^{TGA} is too high to solely correspond to the removal of solvent molecules trapped in the MOF channels. Indeed, from the first derivative of the TGA thermogram we can clearly distinguish the presence of two different processes at 90 and 114°C. The excess of BnOH and the presence of two thermal desorption processes might be correlated to a fraction of solvent trapped on the surfaces of the **TCP-MOF3** nanocrystals.

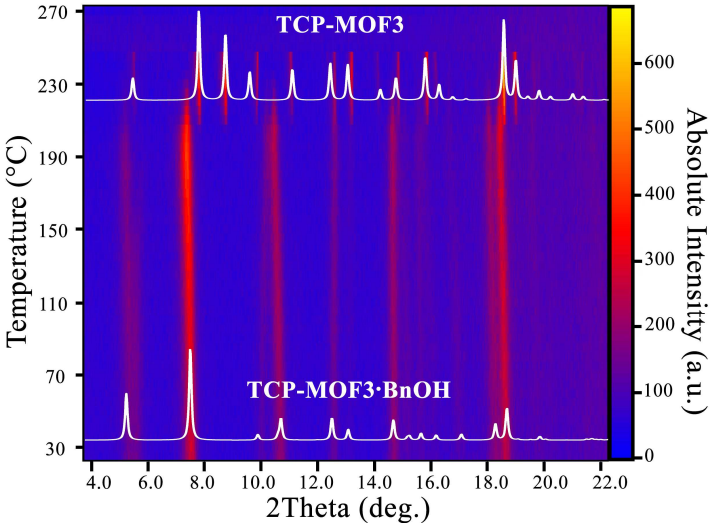

Figure 6.23: Temperature induced guest removal of **TCP-MOF3·BnOH** analysed by temperature-resolved *in situ* powder X-ray diffraction, 2D projection along the intensity axis.

A temperature-resolved *in situ* PXRD analysis was conducted to investigate the presence of a phase transition between the **TCP-MOF3** empty phase and **TCP-MOF3·BnOH**. From the temperature-resolved diffractograms it is evident the presence of a phase transition around 180°C, followed by the

amorphization of the sample at 250°C. The discrepancies in temperature between TGA and the temperature-resolved *in situ* PXRD analysis, might be correlated to the different conditions in which they have been carried out. Nevertheless, from Figure 6.23 we can clearly distinguish that such phase transition involves the transformation of **TCP-MOF3·BnOH** in **TCP-MOF3**. It is reasonable to associate this transformation to a temperature-induced desolvation process, moving from an expanded, filled phase (**TCP-MOF3·BnOH**) to an empty contracted one (**TCP-MOF3**). In the case of the 3D ED analysis conducted on the as-synthesized **TCP-MOF3** (Scheme 6.3), the contracted form (Figure 6.15) is likely obtained due to the extraction of the guest molecules induced by the high vacuum conditions in the TEM column. In summary, the obtained results suggest that the phase transition between the expanded and the contracted forms of **TCP-MOF3** can be triggered by the extraction of guest molecules trapped in the pores, achieved by applying heat or under vacuum (Figure 6.24).

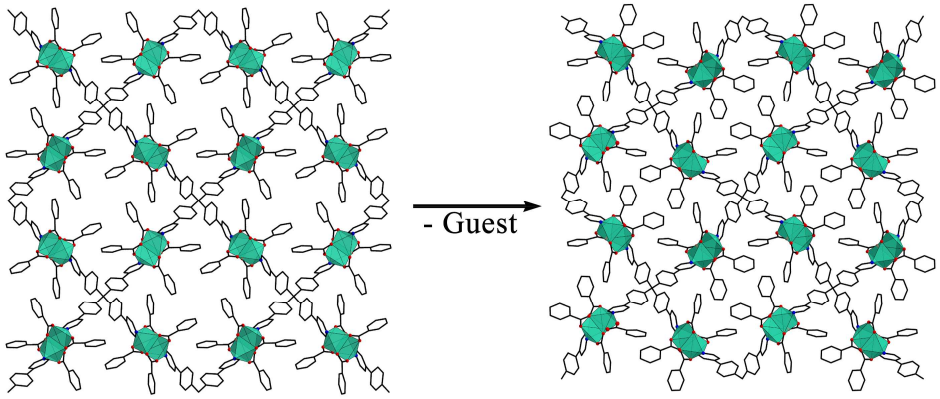

Figure 6.24: Schematization of the phase transition between **TCP-MOF3·BnOH** (*left*) and **TCP-MOF3** (*right*) after the removal of guest molecules. Hydrogen atoms have been omitted for clarity. Copper atoms are represented as green polyhedra while oxygen and nitrogen atoms as red and blue spheres, respectively.

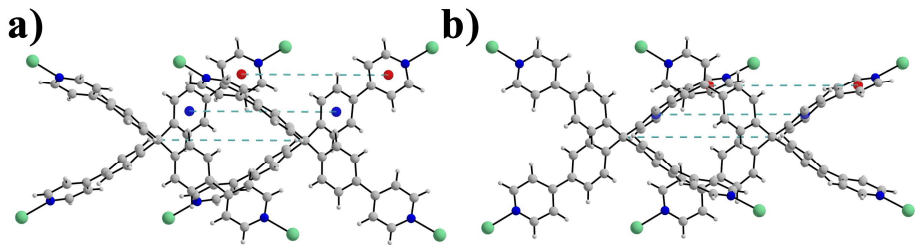

Figure 6.25: View of the principal inter-framework distances along the *c*-axis for the two **TPPM** fragments in the asymmetric unit of **TCP-MOF3·BnOH** (a) and of the **TCP-MOF3** empty phase (b). The rings centroids of the pyridyl and phenyl rings are represented in red and blue, respectively. The three distances (turquoise dashed lines) are equal for both fragments and equivalent to 8.303(3) Å for **TCP-MOF3·BnOH** and 9.005(4) Å for the **TCP-MOF3** empty phase, respectively.

The observed phase transition denotes the presence of a flexible framework, capable to rearrange its nets after the desolvation process. In order to compensate the reduction of interactions after the guest extraction, the material undergoes an overall conformational rearrangement of its **TPPM** pyridyl-phenyl arms, followed by an increase in inter-framework distances between the interlaced nets (**Figure 6.25**, Figure S6.19). Remarkably, the obtaining of a crystalline contracted form upon guest removal allows to classify **TCP-MOF3** as a third-generation MOF. [20]

Gas sorption measurements have been conducted on the **TCP-MOF3** contracted phase, in collaboration with the group of Prof. Ocean Cheung from Uppsala University. The nitrogen adsorption isotherm reveals the presence of an initial Langmuir-like adsorption region, which reflects the presence of micropores. The subsequent increase of the amount of nitrogen adsorbed is ascribable to the presence of mesopores, followed at the end by a pronounced interparticle condensation (Figure 6.26). The analysis also revealed a pore volume value of 0.29 $cm^3\ g^{-1}$, which is in line with the predicted value of 0.285 $cm^3\ g^{-1}$ (calculation performed with the pore analyser tool in Mercury software). [23] However, the experimental surface area values were found to be almost the double of the expected ones (Table 6.1). This is probably

correlated to the presence of a large contribution of interparticle condensation in the total amount of gas adsorbed. Moreover, from the pore size plot it is possible to distinguish the presence of a bimodal distribution, related to pores with diameters of 0.74 and 0.85 nm. These pore size values are compatible with the calculated value of 0.56 nm, considering the material flexibility and the different characterization conditions, in term of temperature and pressure.

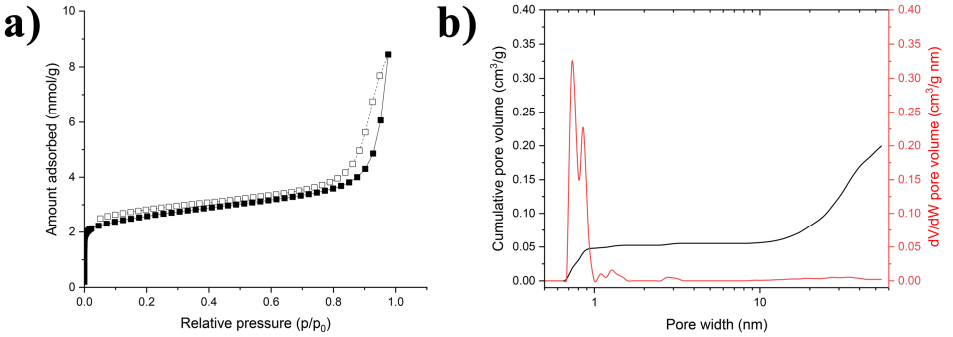

Figure 6.26: Nitrogen adsorption isotherms of **TCP-MOF3** recorded at liquid N_2 temperature (a), and its relative pore size distribution and cumulative pore volume plots (b).

Table 6.1: Comparison between the experimental and calculated values of surface area, pore diameter and pore volume for **TCP-MOF3**.

	Experimental	Calculated
SSA_{BET} (m^2 g^{-1})	206.3	84.96
$SSA_{Langmuir}$ (m^2 g^{-1})	260.0	
Pore volume (cm^3)	0.29	0.285
Peak pore size (nm)	0.74, 0.85	0.56

The nitrogen adsorption displayed in the microporous region in Figure 6.26a, is endorsed by a value of pore volume compatible to the **TCP-MOF3** expanded phase This result indicates that the **TCP-MOF3** empty phase can be converted to the filled one when exposed to nitrogen already at small relative pressures, underlining the reversibility of the conversion process between its empty and contracted forms (Figure 6.27).

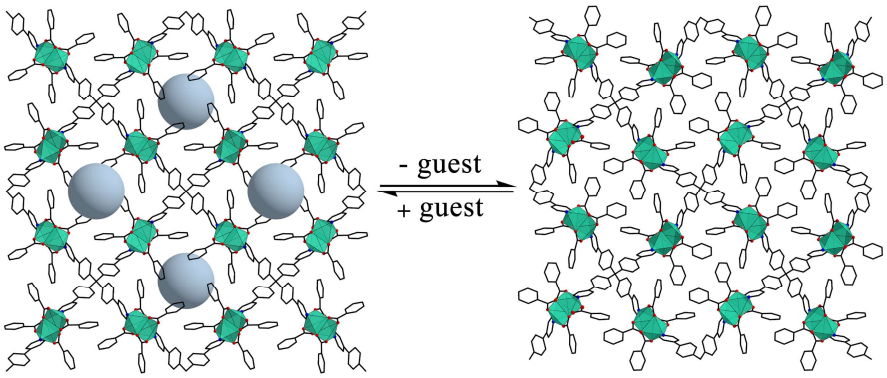

Figure 6.27: Schematic representation of the reversible process between **TCP-MOF3** expanded (*left*) and contracted (*right*) forms. The **TCP-MOF3** expanded form was depicted with light-blue spheres embedded in its pores, to represent the guest molecules.

Subsequently, **TCP-MOF3** was tested for the gas sorption of greenhouse gases such as CO_2, CH_4 and SF_6 (Figure 6.28). The obtained results highlighted a pronounced adsorption of SF_6 al low pressure that suggest a moderate affinity of the framework towards this gas. Therefore, the next steps in our investigation were directed to the synthesis of a fluorinated **TCP-MOF,** isoreticular with **TCP-MOF3**, with the aim of studying the role of the fluorination on the affinity of the materials towards the adsorption of CO_2 and SF_6.

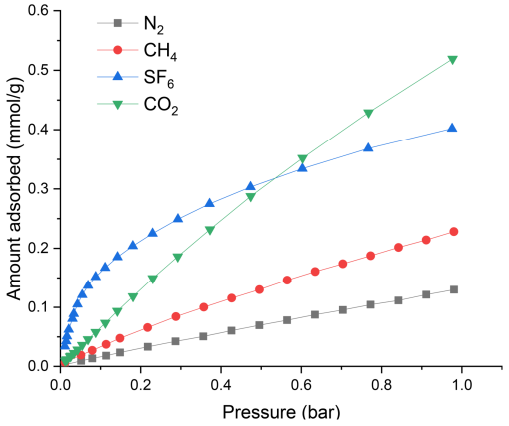

Figure 6.28: N_2, CH_4, SF_6 and CO_2 gas adsorption isotherms of **TCP-MOF3** measured at 293K.

6.2.4 Synthesis and characterization of fluorinated TCP-MOFs

This section is focused on the synthesis of two fluorinated **TCP-MOFs**, that were found to be isotericular to **TCP-MOF2** and **TCP-MOF3**, respectively. The fluorine atoms were inserted in the framework through the functionalization of the carboxylic ligands of the original SBU; by substituting the benzoate ligands in $[Cu_2(PhCO_2)_4(ACN)_2]$ with 4-fluoro benzoate (p-$FPhCO_2^-$) the analogous complex $[Cu_2(p\text{-}FPhCO_2)_4(ACN)_2]$ was obtained (Figure 6.29).

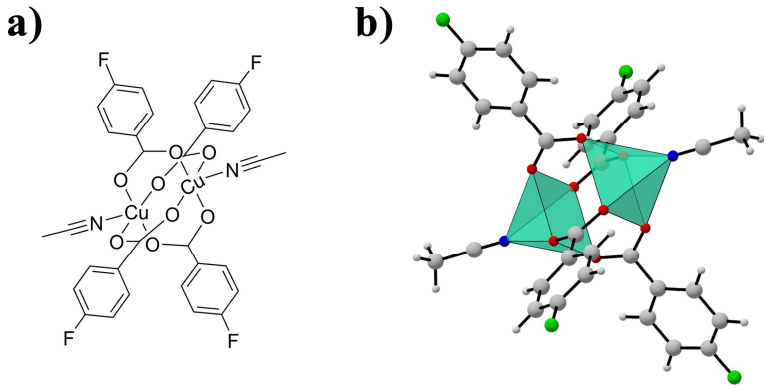

Figure 6.29: Molecular sketch (a) and molecular structure from SC-XRD data (b) of the $[Cu_2(p\text{-}FPhCO_2)_4(ACN)_2]$ complex.

The new MOFs were also compared to their not-fluorinated analogous in terms of absorption of specific guest molecules.

Synthesis and characterization of TCP-MOF4, the fluorinated version of TCP-MOF2

The synthesis of **TCP-MOF4** was conducted under analogous condition to those employed for the solvothermal synthesis of **TCP-MOF3**. Thus, three different solutions were used, containing **TPPM**, *p*-fluoro benzoic acid (*p*-FBzA) and $[Cu_2(p\text{-}FPhCO_2)_4(ACN)_2]$, respectively, in a solvent mixture of $^{i}PrOH/CHCl_3$. The above-mentioned solutions were then placed in contact by layering and heated up at 80°C for 3 days (Scheme 6.5). Any attempt to synthesize **TCP-MOF4** in the same reaction conditions of **TCP-MOF2** generally led to an amorphous product. while the use of a large amount of *p*-FBzA as modulating agent was shown to play an important role in obtaining a crystalline product. This indicates that small modifications of the SBU precursor drastically change its reactivity to obtain this class of metal-organic frameworks.

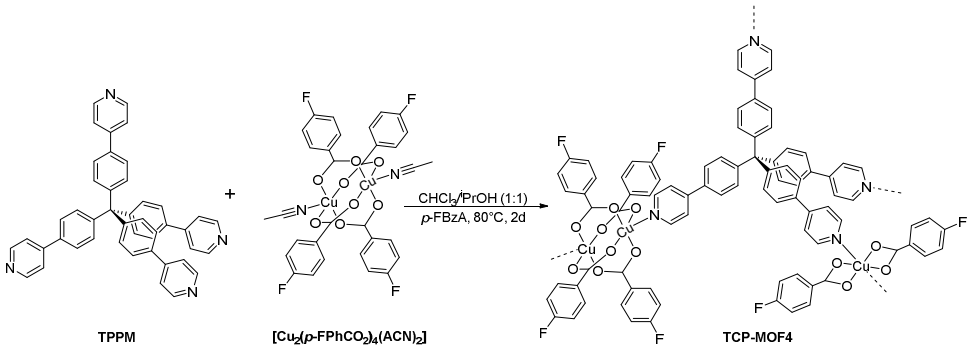

Scheme 6.5: Synthesis of **TCP-MOF4**.

TCP-MOF4 exhibits a distinct PXRD pattern showing similarities to the powder profile of **TCP-MOF2**. Its micrometric crystals were characterized through 3D ED analysis. The data collection was carried out following the STEM-cRED protocol.

The diffraction patterns were combined together and the reciprocal space reconstructed, indicating a monoclinic system in the space group $P\,2/n$ with lattice parameters $a = 25.632(11)$ Å, $b = 7.653(2)$ Å, $c = 23.063(9)$ Å, $\beta = 98.12(3)$ Å. The unit cell obtained is quite close to the **TCP-MOF2,** as evidenced by the peak coincidence between the two PXRD patterns (Figure 6.30, Table 6.2).

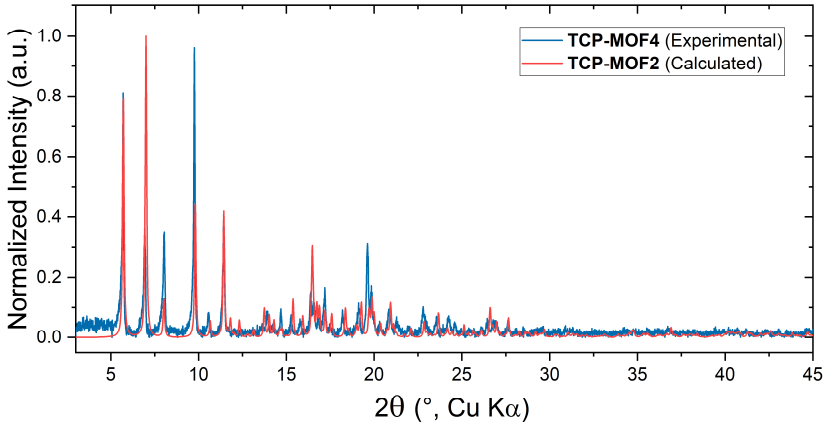

Figure 6.30: PXRD profile comparison between the experimental data of **TCP-MOF4** and the calculated pattern of **TCP-MOF2**.

Table 6.2: Unit cell parameter comparison between **TCP-MOF2** and **TCP-MOF4.**

	TCP-MOF2	**TCP-MOF4**
a (Å)	25.534(7)	25.632(11)
b (Å)	7.485(3)	7.653(2)
c (Å)	22.287(9)	23.063(9)
α (°)	90	90
β (°)	98.81(3)	98.12(3)
γ (°)	90	90
Vol ($Å^3$)	4674.2(3)	4768.8(6)

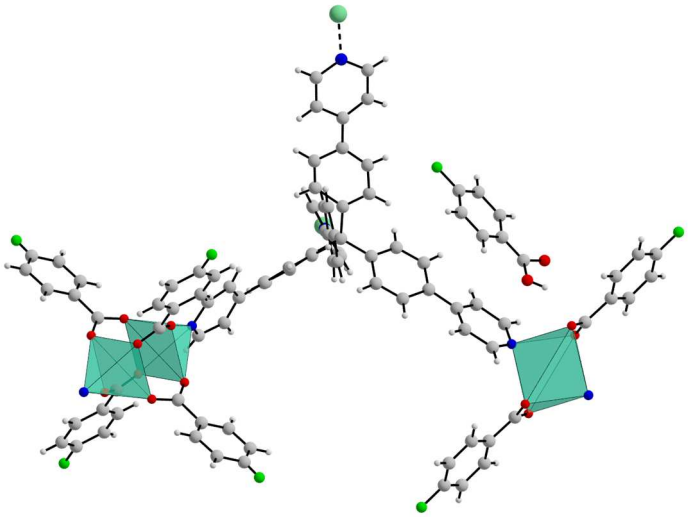

Figure 6.31: Polymeric repeating unit of **TCP-MOF4**.

The indexed reflections were then integrated, and the crystal structure resolved through ab initio methods. The kinematical refinement revealed the presence of a fluorinate metal-organic framework isoreticular to **TCP-MOF2** of general formula **{TPPM[Cu$_2$(*p*-FPhCO$_2$)$_4$][Cu(*p*-FPhCO$_2$)$_2$]}$_n$** (Figure 6.31, Figure 6.32a-b). The channel of **TCP-MOF4** resulted partially occupied by *p*-FBzA molecules (site occupancy 0.75), which are involved in H-bond interactions with the polymeric backbone of the structure. The resulting channels are oriented along the crystallographic *b*-axis, accounting for 16.7% of the unit cell volume (748.95 Å^3) which is the same percentage of virtual void found in **TCP-MOF2** (Figure 6.32c-d). The presence of F atoms appears to have no impact on the pore size of **TCP-MOF4**. In both structures, the channels are divided in two cavities delimited on one side by **TPPM** molecules and on the other side by the aryl substituents of the carboxylic groups coordinated to the metal centres. In **TCP-MOF2**, these aromatic moieties interact with each other through CH$^{\cdots}\pi$ contacts, whereas in **TCP-MOF4** they interact *via* C-H$^{\cdots}$F interactions.

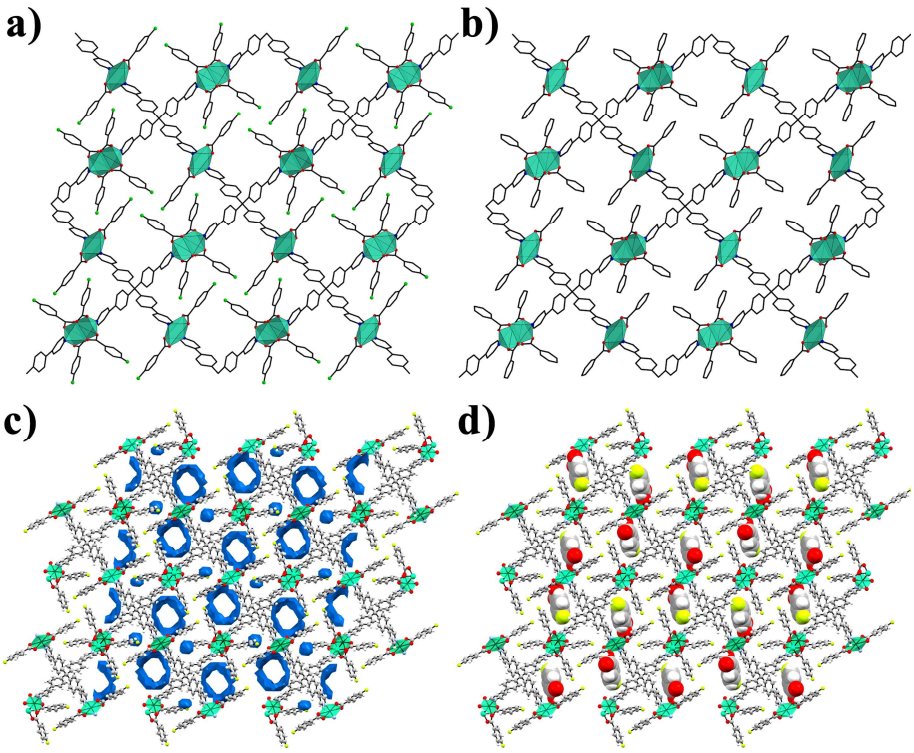

Figure 6.32: Crystal structure expansion of **TCP-MOF4** (a) and **TCP-MOF2** (b) both oriented along their crystallographic *b*-axis. Calculated channels of **TCP-MOF4** as blue surfaces (c) and packing expansion showing the *p*-FBzA molecules embedded in the framework (d). Copper atoms are represented as green polyhedra while oxygen, nitrogen, fluorine and carbon atoms are shown as red, blue, green and grey spheres, respectively.

The electrostatic potential running along the cavities was then calculated for both **TCP-MOF2** and **TCP-MOF4**. The calculation was carried out with the Material Studio software suite [27], using the DMol3 package with a m061 functional (Figure 6.33). The potential maps thus obtained for both frameworks show the negative charge surrounding the carboxylic oxygen facing the inner side of the cavities. Furthermore, **TCP-MOF4** displays an additional negative potential in proximity of the fluorine atoms, with an increase of the negative charged regions along the cavity of this framework.

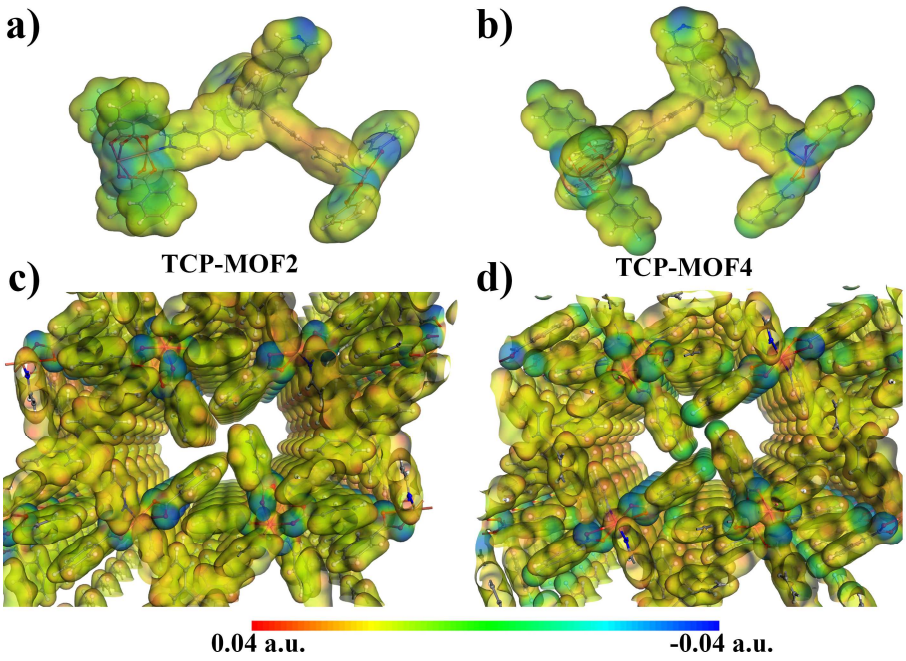

Figure 6.33: Potential electrostatic surfaces of the repeating unit and of the expanded structure for **TCP-MOF2** (a,c) and **TCP-MOF4** (b,d). The expanded structures have been oriented along the crystallographic *b*-axis, to emphasize the potential along the channels. The surfaces have been calculated at the m061 level of theory using the DMol3 package of Material Studio software. [27]

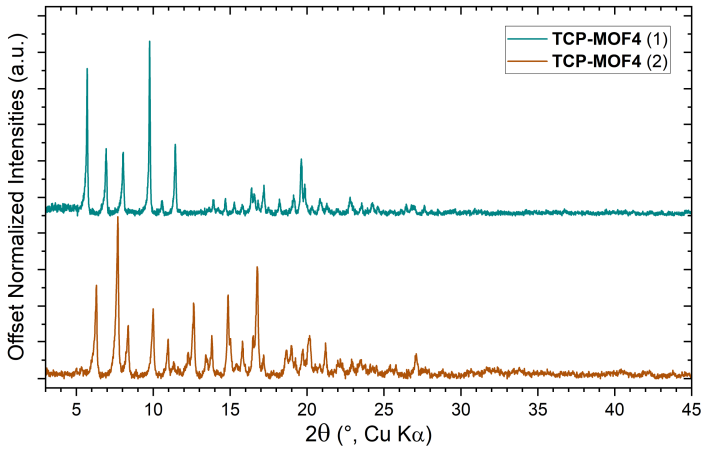

Figure 6.34: PXRD profile comparison between the **TCP-MOF4** filled phase (1) and the washed products (2).

In order to remove the *p*-FBzA molecules contained in the **TCP-MOF4** channels, the as-synthesized product was washed with chloroform. Interestingly, after a few hours from this process, the material presented a different PXRD pattern from the initial one (Figure 6.34). To investigate the reason behind this change, a temperature-resolved *in situ* PXRD analysis was carried out on the crude product. The analysis revealed that upon heating, **TCP-MOF4** undergoes a phase transition: around 170°C, a crystalline phase appears with a powder profile similar to the pattern of the washed product (Figure 6.35). This result suggests that after the removal of the guest molecules embedded in the channels, the **TCP-MOF4** framework maintain its crystallinity, leading to a new (likely) contracted phase. The absence of guest molecules in washed **TCP-MOF4** was also confirmed by TGA analysis, since the thermogram only displayed a weight loss at 332 °C related to the thermal degradation of the material. Further characterization will be carried out to elucidate the crystal structure of this new phase.

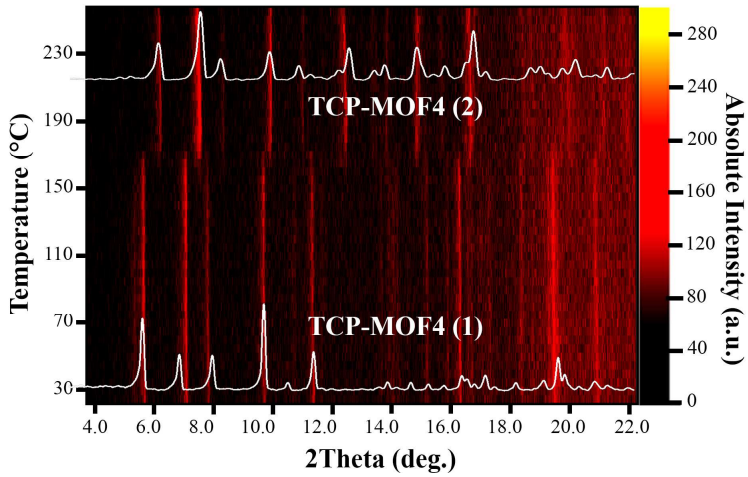

Figure 6.35: Temperature-induced guest removal of **TCP-MOF4** analysed by temperature-resolved *in situ* powder X-ray diffraction; 2D projection along the intensity axis.

The fluorinated **TCP-MOF4** exhibits a moderate stability in water. Its crystallinity was confirmed even after soaking into an aqueous suspension for seven days.

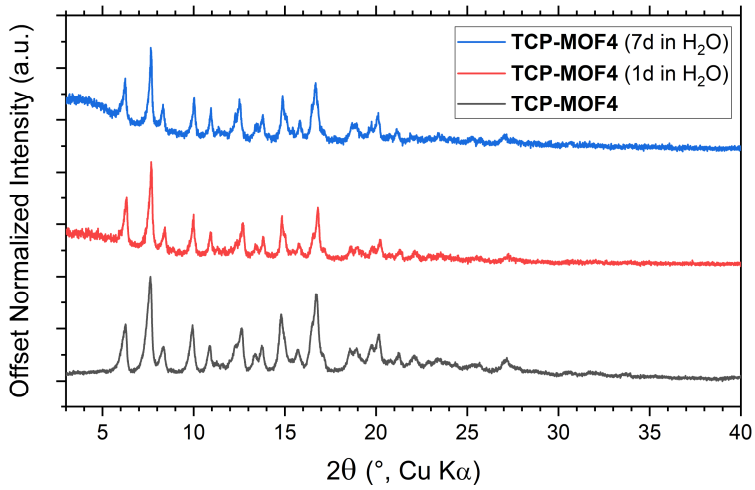

Figure 6.36: Stability experiment on **TCP-MOF4** in water. The experiment was conducted on the washed product to prevent any contamination from the guest molecules contained in the raw material.

After confirming its stability in aqueous media, a preliminary experiment was carried out to test the role of fluorination in **TCP-MOF4** toward the adsorption of fluorinated compounds in water. The sodium salts of perfluorobutanoic acid (**NaPFB**) and perfluorooctanoic acid (**NaPFO**) were selected as target molecules. Then, the capability of **TCP-MOF4** to adsorb PFAS from water was compared to that of its not-fluorinated counterpart (**TCP-MOF2**). Initially, the MOFs were exposed to a 5 mM solution of each target molecules for 24 h. Subsequently, the solid was recovered and washed with distilled water. The presence of PFAS was then estimated through ^{19}F-NMR after digesting the solid with a DCl/D_2O (2:8) solution. Neither **TCP-MOF2** nor **TCP-MOF4** were found to absorb **NaPFB** (Figure S6.24, Figure S6.26). However, **TCP-MOF4** demonstrated the capability to adsorb a moderate amount of **NaPFO**, estimated to be around 25.4±0.5% in moles

(Figure 6.37, Figure S6.30). In contrast, the ^{19}F-NMR of **TCP-MOF2** showed no signals associated with the presence of **NaPFO**, suggesting a lack of affinity for this class of pollutants (Figure S6.25).

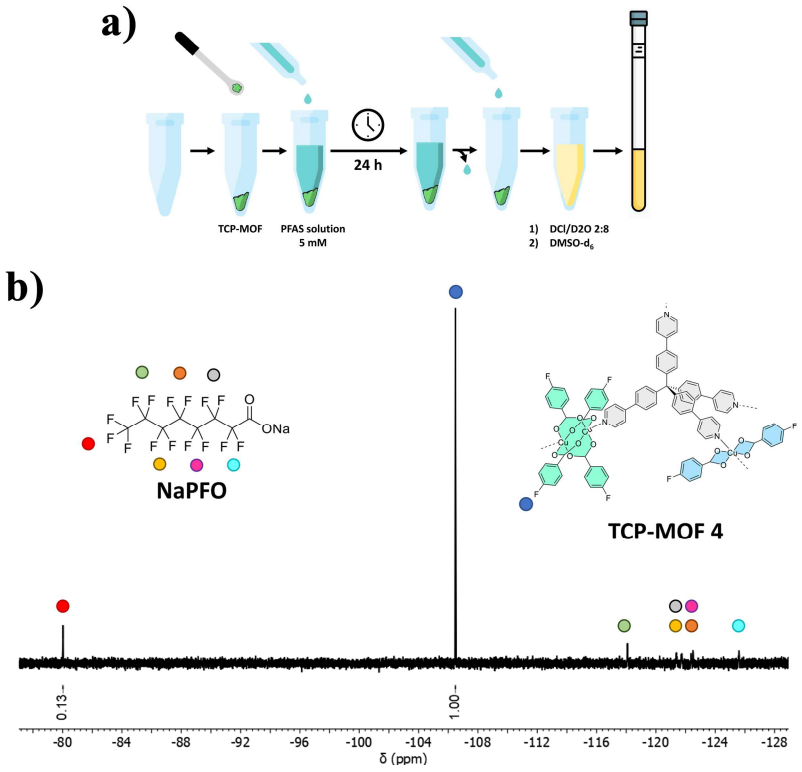

Figure 6.37: Schematic representation of the PFAS exposure experiment (a). ^{19}F-NMR spectrum of **TCP-MOF4** after the exposure to the **NaPFO** solution (b). Details of the experiment have been reported in the dedicated section of the supplementary information.

A portion of the **TCP-MOF4** that has been exposed to the **NaPFO** solution, was characterized by PXRD analysis to check the presence of any structural changes after the adsorption experiment (Figure 6.38). The obtained powder profile differs from the initial one and appears to be the combination of the two **TCP-MOF4** phases described in Figure 6.34. As the PFAS exposure experiment started from the crystalline phase supposed to be the contracted form of **TCP-MOF4**, the observation of a fraction correlated to the filled phase of **TCP-MOF4** suggests that this material can expands its framework when exposed to specific guest molecules. Moreover, the partial absorption of **NaPFO** was supported by the incomplete conversion to the **TCP-MOF4** expanded form during the adsorption experiment. The results suggest that the adsorption process takes place primarily at the surface of the material. To determine the nature of this adsorption phenomenon, further investigations are required.

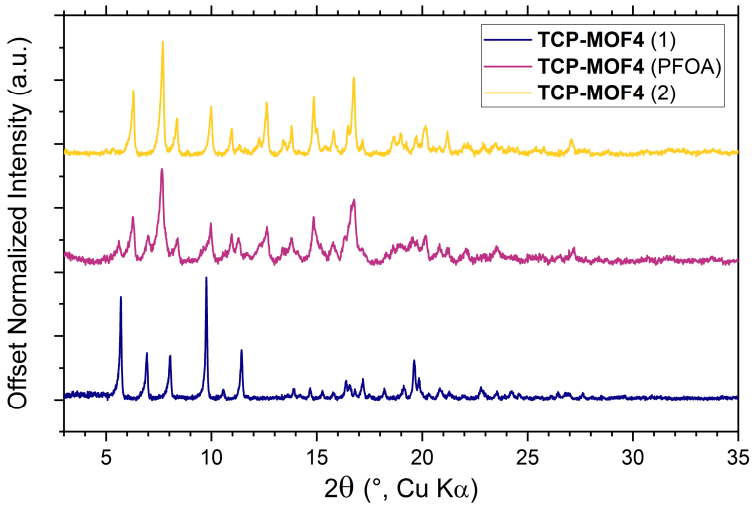

Figure 6.38: PXRD profile comparison between the **TCP-MOF4** filled phase (1), washed phase (2) and after the **NaPFO** adsorption experiment.

Synthesis and characterization of TCP-MOF5, the fluorinated version of TCP-MOF3

TCP-MOF5 was synthesized with the aim of creating a fluorinated metal-organic framework isoreticular to **TCP-MOF3**. The objective was to compare their properties towards the adsorption of greenhouse gases.

TCP-MOF5 was synthesized using a different approach compared to the synthetic methods employed for the previously described TCP-MOFs. **TPPM** and $[Cu_2(p\text{-}FPhCO_2)_4(ACN)_2]$ were suspended in *o*-Dichloro Benzene (*o*-DCB) and left under stirring at 140°C for 3 hours (**Scheme 6.6**). Under these conditions, a crystalline product was achieved without the employment of *p*-FBzA as a modulating agent. The crude product was washed at room temperature with chloroform and characterized through PXRD analysis.

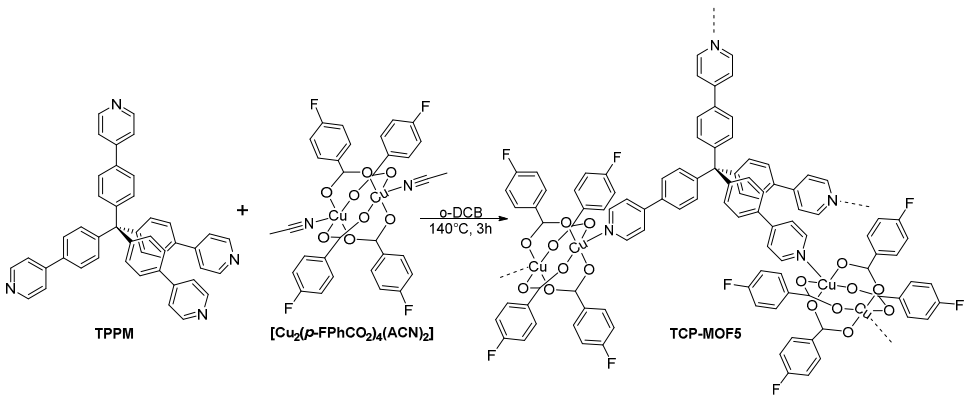

Scheme 6.6: Synthesis of **TCP-MOF5**.

The PXRD pattern of the product displays similarities to the powder profile of **TCP-MOF3·BnOH**, with peaks slightly shifted towards low 2θ values. This suggests a potential increase of the unit cell parameters (Figure 6.39). The micrometric crystals of the product were then characterized through 3D ED analysis in cRED mode. The diffraction patterns were combined, and the reciprocal space was reconstructed, indicating a tetragonal system in the space group $P\,4/n$ with lattice parameters $a = 24.387(11)$ Å, $c = 8.284(5)$ Å. The indexed reflection data confirmed the presence of a unit

cell that is slightly broader compared to the expanded phase of **TCP-MOF3** (**Table 6.3**).

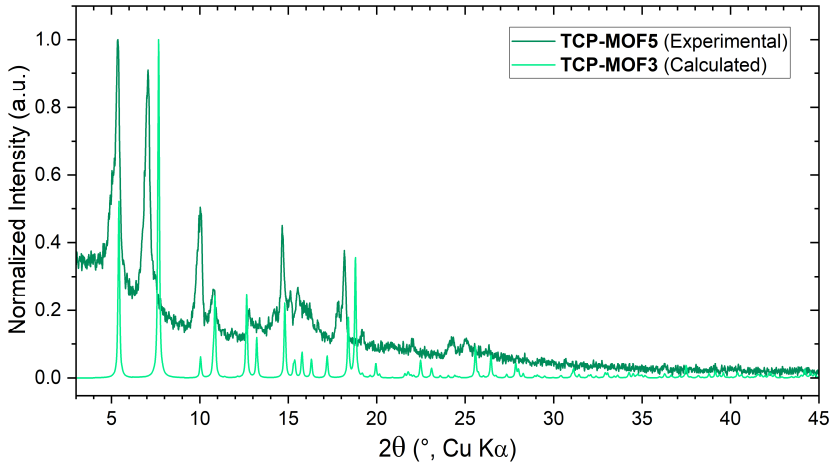

Figure 6.39: PXRD profile comparison between the reaction product **TCP-MOF5** and the calculated pattern of **TCP-MOF3**.

Table 6.3: Unit cell parameter comparison between **TCP-MOF2** and **TCP-MOF4.**

	TCP-MOF3	**TCP-MOF5**
a (Å)	23.043(5)	24.387(11)
b (Å)	23.043(5)	24.387(11)
c (Å)	8.803(2)	8.284(5)
α (°)	90	90
β (°)	90	90
γ (°)	90	90
Vol ($Å^3$)	4674.2(18)	4927(4)

The reflections were integrated, and the structure was solved using *ab initio* methods, followed by a kinematical refinement. The resulting structure corresponds to a MOF with an identical polymeric backbone as **TCP-MOF3**, but containing Cu(II) paddle-wheels with *p*-fluoro benzoate ligands (Figure 6.40). **TCP-MOF5** has general formula **{TPPM[Cu_2(*p*-FPhCO_2)$_4$]$_2$}$_n$** and displays an eight-fold interpenetrated diamond-like network. The crystal

structure exhibits channels running along the crystallographic *c*-axis, likely occupied by unmodelled solvent molecules, constituting the 12.5% of the unit cell volume (614 $Å^3$, Figure 6.42). The PXRD pattern, calculated from the structural model obtained by 3D ED, corresponds to the pattern of the bulk reaction product (Figure 6.41).

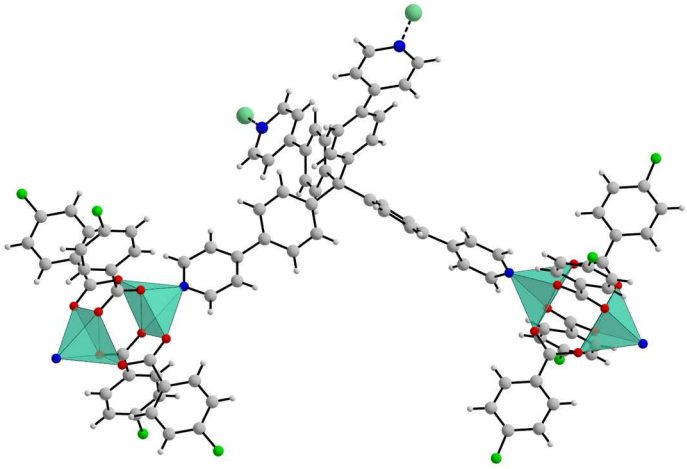

Figure 6.40: Polymeric repeating unit of **TCP-MOF5**

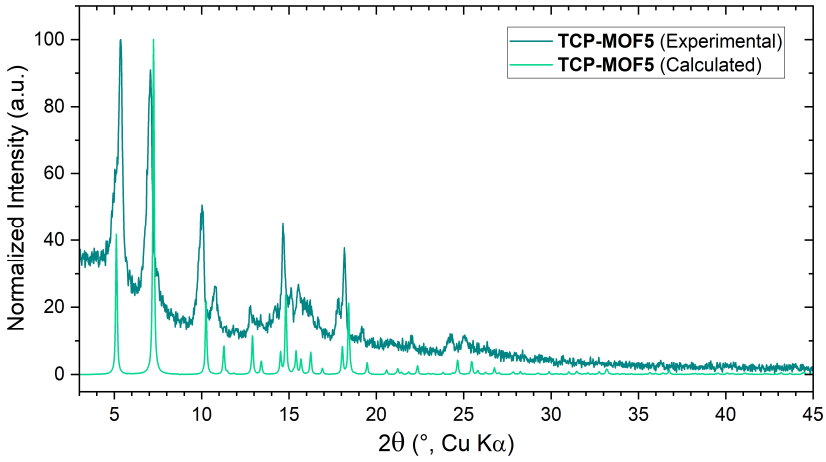

Figure 6.41: PXRD profile comparison between the **TCP-MOF5** reaction product and the calculated pattern from its structural model solved by 3D ED.

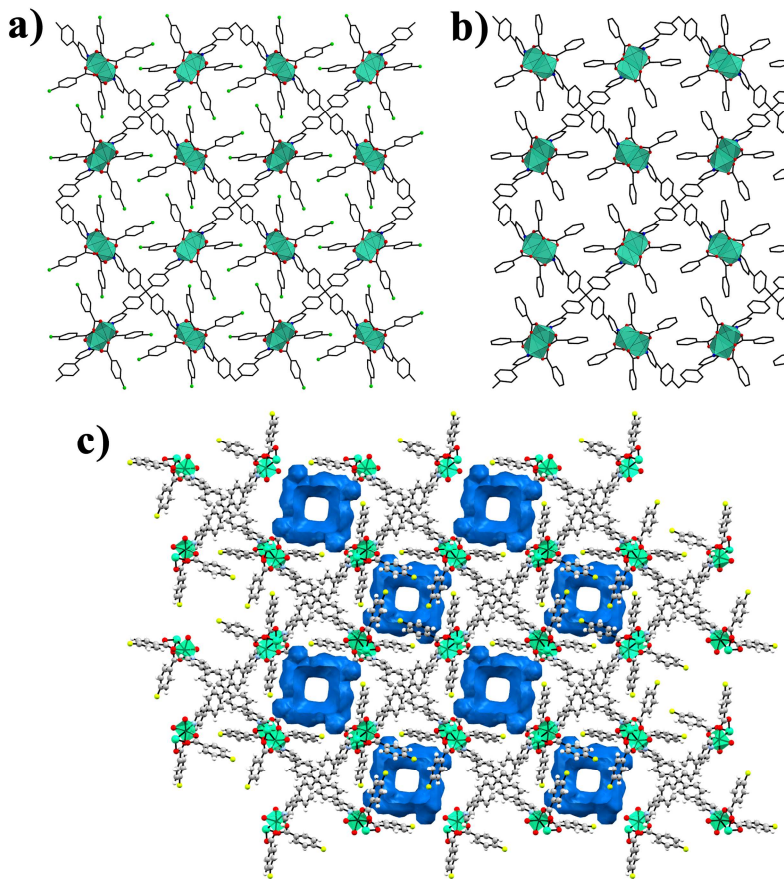

Figure 6.42: Crystal structure expansion of **TCP-MOF5** (a) and **TCP-MOF3** (b) both oriented along their crystallographic *b*-axis. The calculated channels of **TCP-MOF5** have been represented as blue surfaces (c). Copper atoms are represented as green polyhedral while oxygen, nitrogen, fluorine, and carbon atoms are shown as red, blue, green and grey spheres, respectively.

The electrostatic potential map of the entire framework was calculated for both **TCP-MOF3** and **TCP-MOF5** (Figure 6.43). The calculation reveals an enhancement of the negative charge surrounding the cavities in **TCP-MOF5**, with respect to **TCP-MOF3**. In both frameworks, the aryl groups are packed together through π-π staking, forming rods of aromatic groups along the channel walls. In **TCP-MOF5**, the mono-fluorinated rings approach the neighbouring groups, establishing CH···F interactions and positioning the

F atoms on the edges of the cavities. The pores of these frameworks are surrounded by the aryl substituents of the SBUs, amplifying the effect of the fluorinated groups on their electrostatic potential, with respect to the **TCP-MOF2-4** series.

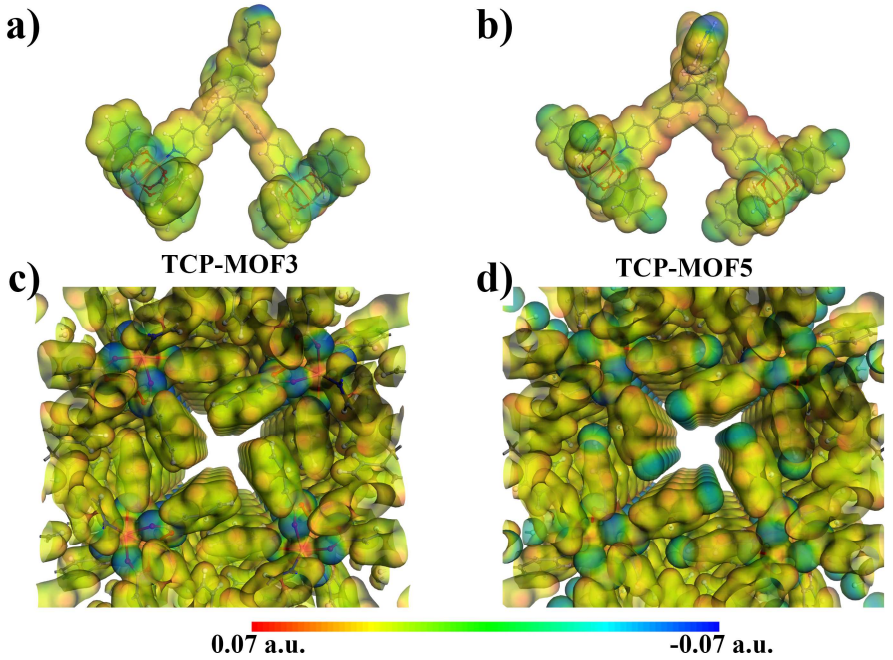

Figure 6.43: Potential electrostatic surfaces of the repeating unit and of the expanded structure for **TCP-MOF3** (a,c) and **TCP-MOF5** (b,d). The expanded structures have been oriented along the crystallographic *c*-axis, to emphasize the potential along the channels. The surfaces have been calculated at the m061 level of theory using the DMol3 package of Material Studio software. [27]

To characterize the thermal stability of the product, a TGA analysis was then carried out, revealing a weight loss of the 3.16% until 130°C followed by thermal degradation around 325°C. Subsequently, **TCP-MOF5** was heated to 150°C under vacuum, to completely evacuate solvent molecules from its pores. Gas sorption measurements were conducted on the activated **TCP-MOF5**, in collaboration with the group of Prof. Ocean Cheung form Uppsala University. The nitrogen adsorption isotherm reveals the presence of an initial

Langmuir-like adsorption region, which reflects the presence of micropores. The subsequent rise in the amount of adsorbed nitrogen can be attributed to a more pronounced presence of mesopores, ending in an interparticle condensation (Figure 6.44). The analysis displays a pore volume value of 0.25 cm^3 g^{-1}, which is in line with the predicted value of 0.287 cm^3 g^{-1} (calculation performed with the pore analyser tool in Mercury software). [23] Moreover, experimental surface area values were found in line with the expected ones (Table 6.4). Lastly, from the pore size plot, pores with a diameter of 1.4 nm were estimated, a value which does not match with the **TCP-MOF5** crystal structure.

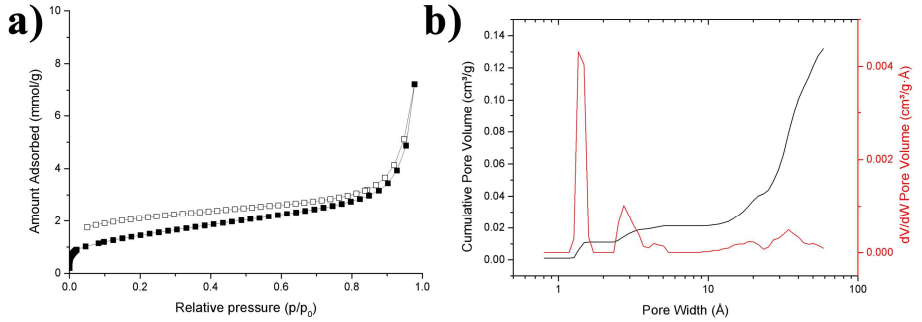

Figure 6.44: Nitrogen adsorption isotherm of **TCP-MOF5** recorded at liquid N_2 temperature (a), and its relative pore size distribution and cumulative pore volume plots (b).

Table 6.4: Comparison between the experimental and calculated values of surface area, pore diameter and pore volume for **TCP-MOF5**.

	Experimental	Calculated
SSA_{BET} (m^2 g^{-1})	117	147.26
$SSA_{Langmuir}$ (m^2 g^{-1})	150	
Pore volume (cm^3)	0.25	0.287

TCP-MOF5 was then tested for the gas sorption of greenhouse gases, including CO_2, CH_4 and SF_6 (Figure 6.45). In contrast to **TCP-MOF3**, the obtained results do not evidence a pronounced adsorption of SF_6 al low pressure. The CO_2 adsorption is slightly increased compared to **TCP-MOF3**, possibly due to electrostatic potential charge separation along the channels. These difference in the electrostatic potentials and the presence of alternating C-H and C-F groups can promote interactions with the quadrupole moment of the gas. [28]

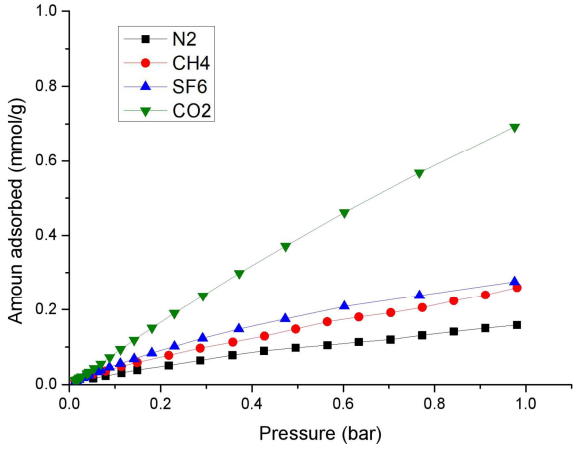

Figure 6.45: N_2, CH_4, SF_6 and CO_2 gas adsorption isotherms of **TCP-MOF5** measured at 293K.

As observed for **TCP-MOF3**, the material displays a nitrogen adsorption in the microporous region (Figure 6.44a) and the measured pore volume value is comparable to the **TCP-MOF5** filled phase. These results suggest that the activated **TCP-MOF5** can be converted back to the expanded phase when exposed to nitrogen, already at small relative pressures. Nevertheless, the structural characterization of **TCP-MOF5** is currently in a preliminary stage, and further characterization will be focused on discovering the presence of its corresponding contracted phase and verifying the reversibility of the conversion process with the expanded form.

6.3 Conclusions

In this chapter a new series of metal-organic frameworks was investigated, composed by **TPPM** molecules connected to Cu(II) paddle wheels (**TCP-MOFs**) and based on a highly interpenetrated diamond-like network. The special arrangement of the building blocks allows to tune the properties of these MOFs through the modification of the carboxylic ligands surrounding the SBUs. Initially, the influence of the SBUs on the flexibility of the framework was demonstrated by the development of a first-generation TCP-MOF (**TCP-MOF1**) and its analogous third-generation MOF (**TCP-MOF3**). Through fluorination of the SBUs, two series of isoreticular **TCP-MOFs** (**TCP-MOF1** and **TCP-MOF3**, **TCP-MOF2** and **TCP-MOF4**) were identified and their different properties investigated. 3D ED analysis played a crucial role in the structure elucidation of these materials, indeed 5 out of 7 **TCP-MOFs** structures required this technique to be solved. The possibility to analyse micro- or nanometric crystal as single crystals, through the 3D electron diffraction technique, allowed to focalize the synthetic efforts on exploring a wide chemical space instead of growing large crystals. This research might be considered as a further step in the exploration of flexible metal-organic frameworks, highlighting the potential of implementing 3D ED analysis in their structural characterization to enhance their development process.

6.4 Supplementary Information

6.4.1 Synthetic Procedures

$[Cu_2(CH_3CO_2)_4(ACN)_2]$ Synthesis

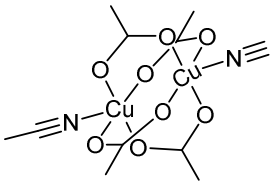

$[Cu_2(CH_3CO_2)_4(ACN)_2]$

The synthesis was conducted solubilizing copper acetate monohydrate (500 mg) in 200 mL of ACN. Molecular sieves (3 Å) were added to the solution. After 2h, the solution was filtered, and the solvent evaporated under reduced pressure. The product was obtained as large dark-green crystals suitable for single crystal X-ray diffraction. The solid state analysis confirmed the structure of the paddle-wheel of general formula $[Cu_2(CH_3CO_2)_4(ACN)_2]\cdot ACN$ (quantitative yield, CSD ref. code: HILNUL). [29]

$[Cu_2(PhCO_2)_4(ACN)_2]$ Synthesis

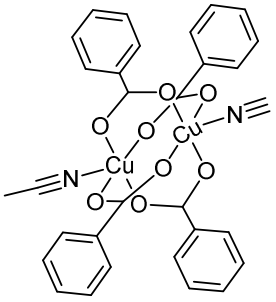

$[Cu_2(PhCO_2)_4(ACN)_2]$

The synthesis was conducted by mixing into an agate mortar benzoic acid (500 mg, 4.1 mmol) and sodium hydroxide (164 mg, 4.1 mmol). Then, 500 µL of water were added and a liquid assisted grinding (LAG) was performed for

10 minutes. In the meantime, copper sulphate pentahydrate (511 mg, 2.1 mmol) was added to 5 mL of water and sonicated for 20 minutes until complete solubilization. The mechanochemical product was then solubilized in 10 mL of water and the copper sulphate solution was added, immediately obtaining a blue precipitate. The mixture was cooled into an ice bath and the precipitated was filtered. The obtained solid was subsequently solubilized in 200 mL of ACN and molecular sieves (3 Å) were added to the mixture. After 2h, the reaction mixture was filtered, and the solvent evaporated under reduced pressure. The product was then recrystalized at 4°C, isolating blue crystals suitable for single crystal X-ray diffraction. The solid state analysis confirmed the structure of the paddle-wheel of general formula **$[Cu_2(PhCO_2)_4(ACN)_2]\cdot ACN$** (376 mg, 51% yield, CSD ref. code: QILXOY). [30]

$[Cu_2(p\text{-}FPhCO_2)_4(ACN)_2]$ Synthesis

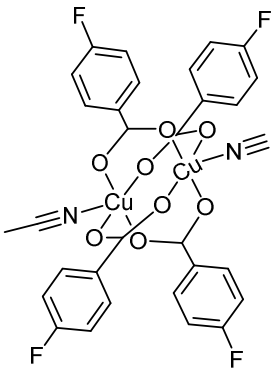

$[Cu_2(p\text{-}FPhCO_2)_4(ACN)_2]$

The synthesis was conducted by mixing into an agate mortar 4-fluoro benzoic acid (500 mg, 3.6 mmol) and sodium hydroxide (142.7 mg, 3.6 mmol). Then, 500 µL of water were added and a liquid assisted grinding (LAG) was performed for 10 minutes. In the meantime, copper sulphate pentahydrate (445.5 mg, 1.8 mmol) was added to 5 mL of water and sonicated for 20 minutes until complete solubilization. The mechanochemical product was then

solubilized in 10 mL of water and the copper sulphate solution was added, immediately obtaining a blue precipitate. The mixture was cooled into an ice bath and the precipitated was filtered. The obtained solid was subsequently solubilized in 200 mL of ACN and molecular sieves (3 Å) were added to the mixture. After 2h, the reaction mixture was filtered, and the solvent evaporated under reduced pressure. The product was then recrystallized at 4°C, isolating blue crystals suitable for single crystal X-ray diffraction (Table S6.3, Figure S6.8). The solid-state analysis confirmed the structure of the paddle-wheel of general formula **[Cu_2(*p*-FPhCO_2)$_4$(ACN)$_2$]** (407 mg, 52% yield).

TPPM Synthesis

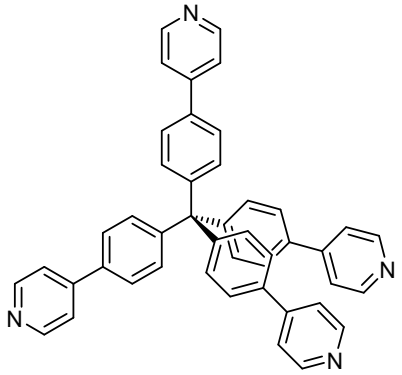

TPPM

The TPPM synthesis was carried out following the procedure reported in Chapter 5.3.1 and in the literature. [2]

TCP-MOF1 Synthesis

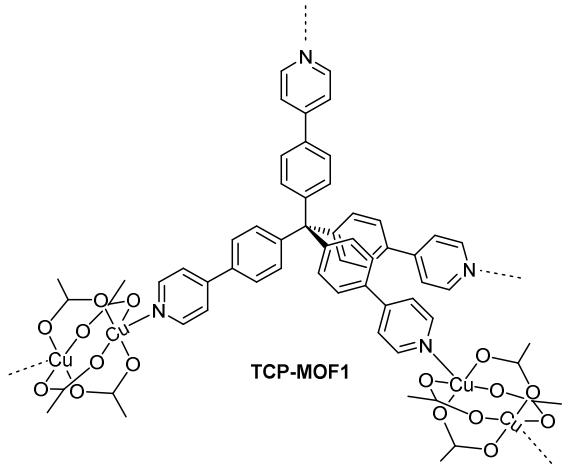

The **TCP-MOF1** synthesis was conducted solubilizing the **TPPM** molecule (3.34 mg, 5.31 µmol) in 3.2 mL of a $CHCl_3$/n-BuOH 2:1 solution, and **$[Cu_2(CH_3CO_2)_4(ACN)_2]\cdot ACN$** (5.12 mg, 10.75 µmol) into 2.8 mL of a $CHCl_3$/n-BuOH 1:2 solution. The solution of **TPPM** was then placed into a glass tube with a Teflon screw cap, then the **$[Cu_2(CH_3CO_2)_4(ACN)_2]\cdot ACN$** solution was carefully added, in order to obtain two different layers. The reaction was then heated at 90° C for 2 days, obtaining large crystals suitable for SC-XRD diffraction analysis (Figure S6.2, Figure S6.5, Table S6.1, Table S6.2).

TCP-MOF2 Synthesis

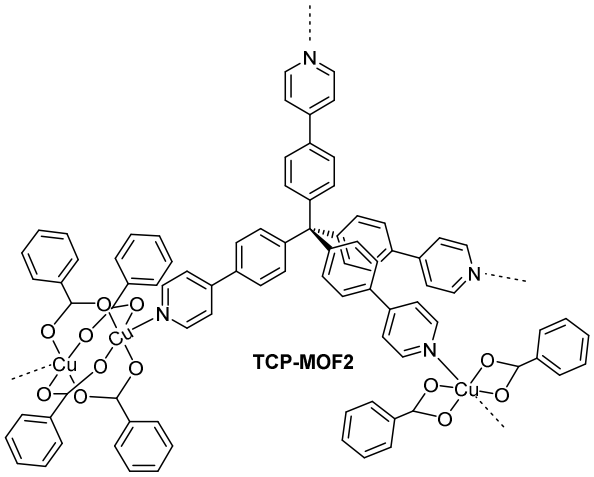

The **TCP-MOF2** synthesis was carried out adding the **TPPM** molecule (6.67 mg, 10.6 µmol), **$[Cu_2(PhCO_2)_4(ACN)_2]\cdot ACN$** (15.34 mg, 21.17 µmol), benzoic acid (149.56 mg, 1.22 mmol), and 10 mL of DMF into a glass tube with a Teflon screw cap. The mixture was then heated up to 90°C for 3 days. The reaction crude was then washed with a $CHCl_3$/MeOH 9:1 solution and dried under reduced pressure. The product appears as a light-blue powder, that was characterized through HAADF-STEM, 3D ED, PXRD and TGA analysis (Table S6.6, Figure S6.14, Figure S6.20, Figure S6.10).

TCP-MOF3 Solvothermal Synthesis

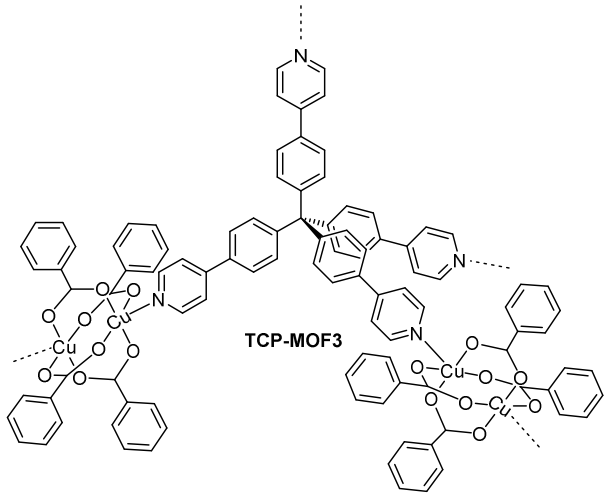

The **TCP-MOF3** synthesis was conducted solubilizing the **TPPM** molecule (2.90 mg, 4.61 µmol) in 2.8 mL of a $CHCl_3$/^{i}PrOH 2:1 solution, benzoic acid (15.4 mg, 12.61 µmol) into 1.5 mL of a $CHCl_3$/ ^{i}PrOH 1:1 solution, and **$[Cu_2(PhCO_2)_4(ACN)_2]\cdot ACN$** (6.97 mg, 9.62 µmol) into 2.8 mL of a $CHCl_3$/ ^{i}PrOH 1:2 solution. The solution of **TPPM** was then placed into a glass tube with a Teflon screw cap, then the benzoic acid solution, followed by the **$[Cu_2(PhCO_2)_4(ACN)_2]\cdot ACN$** solution, were carefully added, in order to obtain three different layers. The reaction was then heated at 50° C for 3 days. The obtained green powder was then rinsed with a $CHCl_3$/MeOH 9:1 solution and dried under reduced pressure. The product was then characterized through HAADF-STEM, 3D ED and PXRD analysis (Table S6.7, Table S6.8, Figure S6.11, Figure S6.15, Figure S6.16).

TCP-MOF3 Mechanochemical Synthesis

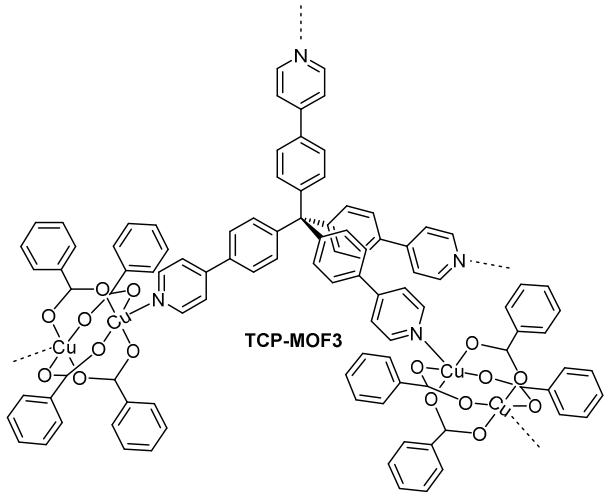

The mechanochemical synthesis of **TCP-MOF3** was carried out placing the **TPPM** molecule (29.5 mg, 46.9 µmol), **$[Cu_2(PhCO_2)_4(ACN)_2]\cdot ACN$** (66.2 mg, 91.3 µmol) and 50 µL of benzyl alcohol into an agate jar with two 5 mm agate spheres. The mixture was ground into a Retsch mixer mill MM 400 operating at 20 Hz form 30 min. The grinding crude was left in an open container to evaporate the remaining traces of LAG additive. The obtained green powder was then washed with a $CHCl_3$/MeOH 9:1 solution, dried under reduced pressure and characterized through PXRD analysis.

TCP-MOF4 Synthesis

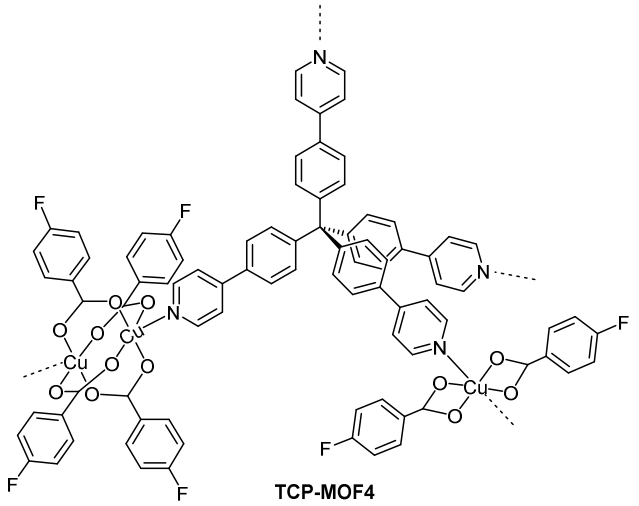

TCP-MOF4

The **TCP-MOF4** synthesis was conducted solubilizing the **TPPM** molecule (3.11 mg, 4.95 µmol) in 3.0 mL of a $CHCl_3$/^{i}PrOH 2:1 solution, benzoic acid (8.78 mg, 62.7 µmol) into 2.5 mL of a $CHCl_3$/ ^{i}PrOH 1:1 solution, and **[Cu2(*p*-FPhCO2)4(ACN)2]** (7.29 mg, 9.53 µmol) into 3 mL of a $CHCl_3$/ ^{i}PrOH 1:2 solution. The solution of **TPPM** was then placed into a glass tube with a Teflon screw cap, then the benzoic acid solution followed by the [Cu_2(p-**FPhCO2)4(ACN)2]·ACN** solution were carefully added, in order to obtain three different layers. The reaction was then heated at 80° C for 2 days. The obtained green powder was then rinsed with a $CHCl_3$/MeOH 9:1 solution and dried under reduced pressure. The product was then characterized through HAADF-STEM, 3D ED, PXRD and TGA analysis (Table S6.9, Figure S6.12, Figure S6.17, Figure S **6.22**).

TCP-MOF5 Synthesis

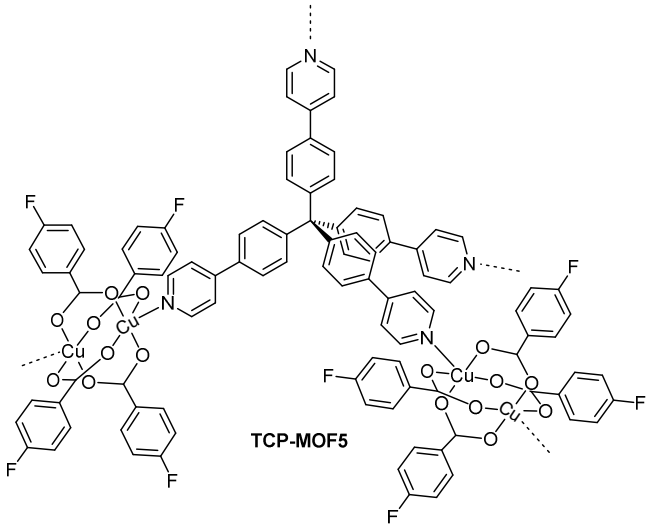

The **TCP-MOF5** synthesis was carried out adding the **TPPM** molecule (7.44 mg, 11.8 µmol), **[Cu$_2$(*p*-FPhCO$_2$)$_4$(ACN)$_2$]** (18.50 mg, 24.16 µmol) and 20 mL of o-DCB into a glass tube with a Teflon screw cap. The mixture was then heated up to 140°C for two hours. The reaction crude was then washed with a $CHCl_3$/MeOH 9:1 solution and dried under reduced pressure. The product appears as a green powder, that was characterized through HAADF-STEM, 3D ED, PXRD and TGA analysis (Table S6.10, Figure S6.13, Figure S6.18, Figure S6.23).

6.4.2 Structural Characterization

Single Crystal X-ray Diffraction (SC-XRD)

The crystal structures of **TCP-MOF1** were determined by X-ray diffraction on single crystals. Crystal data and experimental details for data collection and structure refinement are reported in Table S6.1. Intensity data and cell parameters were recorded at 200(2) K and 300(2) K, respectively, for the contracted and expanded phase, on a Bruker D8 Venture PhotonII diffractometer (CuKα radiation λ = 1.54178 Å). The raw frame data were processed using SAINT and SADABS to yield the reflection data files. [31] The structures were solved by Direct Methods using the SHELXT program[32] and refined on F_o^2 by full-matrix least-squares procedures, using SHELXL-2018[33] in the WinGX suite v.2014.1.[34] All non-hydrogen atoms were refined with anisotropic atomic displacements, with the exception of some of the disordered solvents. The hydrogen atoms were included in the refinement at idealized geometry and refined "riding" on the corresponding parent atoms. The weighting schemes used in the last cycle of refinement were $w = 1/ [\sigma^2 F_o^2 + (0.2000P)^2]$ and $w = 1/ [\sigma^2 F_o^2 + (0.5108P)^2]$, where $P = (F_o^2 + 2F_c^2)/3$, for **TCP-MOF1 200K** and **TCP-MOF1 300K**, respectively.

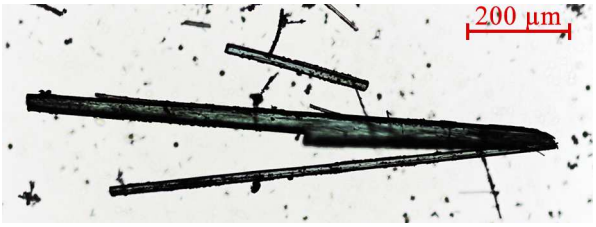

Figure S6.1: Optical Microscope image of **TCP-MOF1** crystals.

Table S6.1: Crystallographic information for **TCP-MOF1 200K**

Empirical formula	$C_{45}H_{30}N_4O_4Cl_3Cu$
Formula weight	860.62
Temperature/K	200(2)
Crystal system	tetragonal
Space group	*P*-4
a/Å	26.0049(15)
b/Å	26.0049(15)
c/Å	7.3356(5)
α/°	90
β/°	90
γ/°	90
Volume/Å^3	4960.7(7)
Z	4
ρ_{calc}g/cm^3	1.152
μ/mm^{-1}	2.432
F(000)	1760.0
Radiation	CuKα (λ = 1.54178)
2ϑ range for data collection/°	3.398 to 118.23
Index ranges	-28 ≤ h ≤ 28, -28 ≤ k ≤ 28, -6 ≤ l ≤ 8
Reflections collected	25468
Independent reflections	7111 [R_{int} = 0.1146, R_{sigma} = 0.0925]
Data/restraints/parameters	7111/0/469
Goodness-of-fit on F^2	1.372
Final R indexes [I>=2σ (I)] [a]	R_1 = 0.1362, wR_2 = 0.3461
Final R indexes [all data] [a]	R1 = 0.1569, wR2 = 0.3647

[a] $R_1 = \Sigma \| F_o | - | F_c \| / \Sigma | F_o |$, $wR_2 = [\Sigma[w(F_o^2-F_c^2)^2]/\Sigma[w(F_o^2)^2]]^{1/2}$

Table S6.2: Crystallographic information for **TCP-MOF1 300K**

Empirical formula	$C_{61}H_{56}N_4O_{16}Cu_4$
Formula weight	1355.25
Temperature/K	299(2)
Crystal system	tetragonal
Space group	*P*4/n
a/Å	27.389(9)
b/Å	27.389(9)
c/Å	7.304(2)
α/°	90
β/°	90
γ/°	90
Volume/Å^3	5479(4)
Z	2
ρ_{calc}g/cm^3	0.821
μ/mm^{-1}	1.203
F(000)	1388.0
Radiation	CuKα (λ = 1.54178)
2ϑ range for data collection/°	4.562 to 109.9
Index ranges	-28 ≤ h ≤ 28, -25 ≤ k ≤ 28, -7 ≤ l ≤ 6
Reflections collected	19208
Independent reflections	3392 [R_{int} = 0.1478, R_{sigma} = 0.1169]
Data/restraints/parameters	3392/3/230
Goodness-of-fit on F^2	1.002
Final R indexes [I>=2σ (I)] [a]	R_1 = 0.2011, wR_2 = 0.5269
Final R indexes [all data] [a]	R_1 = 0.2989, wR_2 = 0.6229

[a] $R_1 = \Sigma \| F_o | - | F_c \| / \Sigma | F_o |$, $wR_2 = [\Sigma[w(F_o^2-F_c^2)^2]/\Sigma[w(F_o^2)^2]]^{1/2}$

Table S6.3: Crystallographic information for **$[Cu_2(p\text{-}FPhCO_2)_4(ACN)_2]$**

Empirical formula	$C_{32}H_{22}Cu_2F_4N_2O_8$
Formula weight	765.59
Temperature/K	200.00(10)
Crystal system	triclinic
Space group	*P*-1
a/Å	10.1124(4)
b/Å	10.3357(4)
c/Å	10.4275(4)
α/°	71.530(4)
β/°	70.551(4)
γ/°	67.444(4)
Volume/Å^3	926.42(7)
Z	1
ρ_{calc}g/cm^3	1.372
μ/mm^{-1}	1.214
F(000)	386.0
Radiation	Mo Kα (λ = 0.71073)
2ϑ range for data collection/°	4.494 to 61.014
Index ranges	-14 ≤ h ≤ 14, -14 ≤ k ≤ 14, -14 ≤ l ≤ 14
Reflections collected	39860
Independent reflections	5631 [R_{int} = 0.0644, R_{sigma} = 0.0295]
Data/restraints/parameters	5631/0/218
Goodness-of-fit on F^2	1.086
Final R indexes [I>=2σ (I)] [a]	R_1 = 0.0428, wR_2 = 0.1147
Final R indexes [all data] [a]	R_1 = 0.0445, wR_2 = 0.1161

[a] $R_1 = \Sigma \| F_o | - | F_c \| / \Sigma | F_o |$, $wR_2 = [\Sigma[w(F_o^2-F_c^2)^2]/\Sigma[w(F_o^2)^2]]^{1/2}$

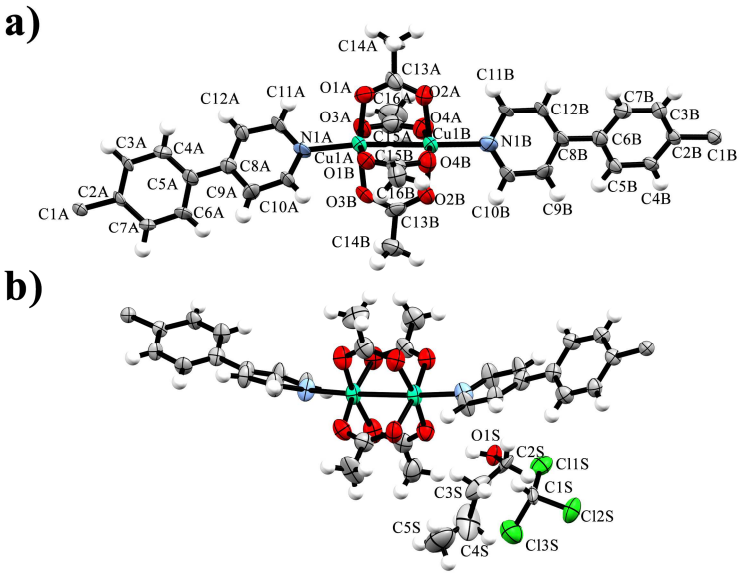

Figure S6.2: Ortep view of the asymmetric unit of **TCP-MOF1** at 200K (probability level 50%). To highlight all the atoms involved, the asymmetric unit is represented in two different orientations. In (a), solvent molecules have been removed for clarity.

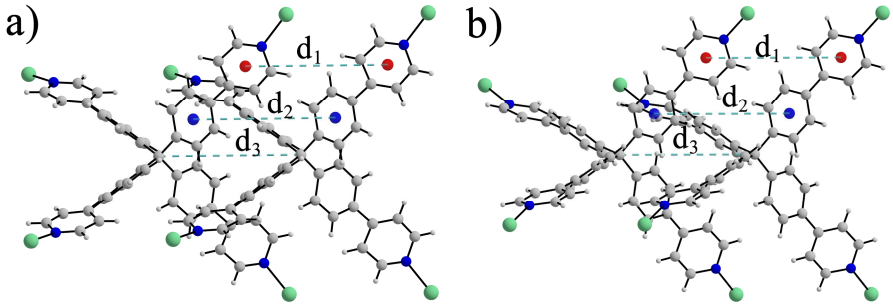

Figure S6.3: View of the principal inter-framework distances that occur along the *c*-axis for the two **TPPM** fragments in the asymmetric unit of **TCP-MOF1** at 200K (see **Figure S6.2**): A (a) and B (a) . Pyridyl rings and phenyl rings centroids are represented in red and blue, respectively. The distances $\mathbf{d_1}$ (pyridyl centroids distances), $\mathbf{d_2}$ (phenyl centroid distances) and $\mathbf{d_3}$ (C1 distances) are equal for both fragments and equivalent to 7.3356(5) Å.

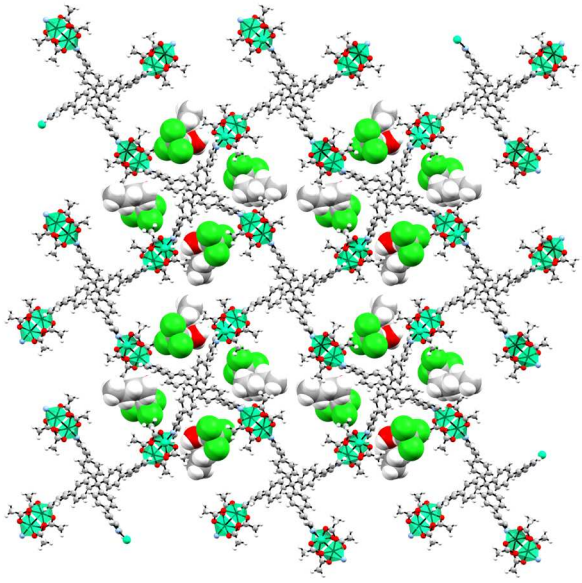

Figure S6.4: Packing of the **TCP-MOF1** crystal structure oriented along the crystallographic *c*-axis. Copper atoms are represented as green ellipsoids, while the solvent molecules embedded in the channel are depicted as CPK models.

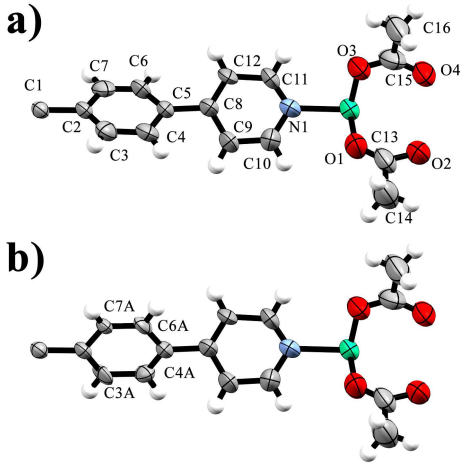

Figure S6.5: Ortep view of the asymmetric unit of **TCP-MOF1** at 300K (probability level 30%). Two different views of the structure are reported, to highlight the presence of positional disorder on the **TPPM** phenyl ring.

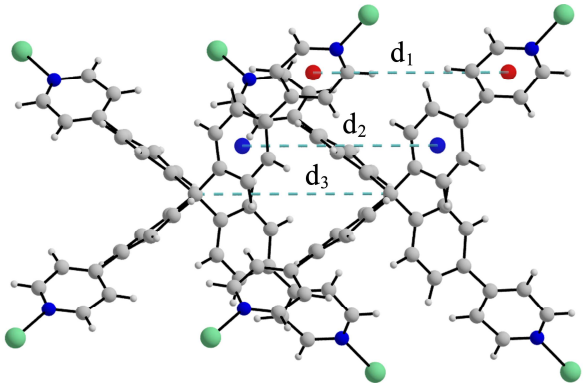

Figure S6.6: View of the principal inter-framework distances that occur along the *c*-axis for the two **TPPM** fragments in the asymmetric unit of **TCP-MOF1** at 300K. Pyridyl rings and phenyl rings centroids are represented in red and blue, respectively. The distances $\mathbf{d_1}$ (pyridyl centroids distances), $\mathbf{d_2}$ (phenyl centroid distances) and $\mathbf{d_3}$ (C1 distances) are equal for both fragments and equivalent to 7.304(2) Å.

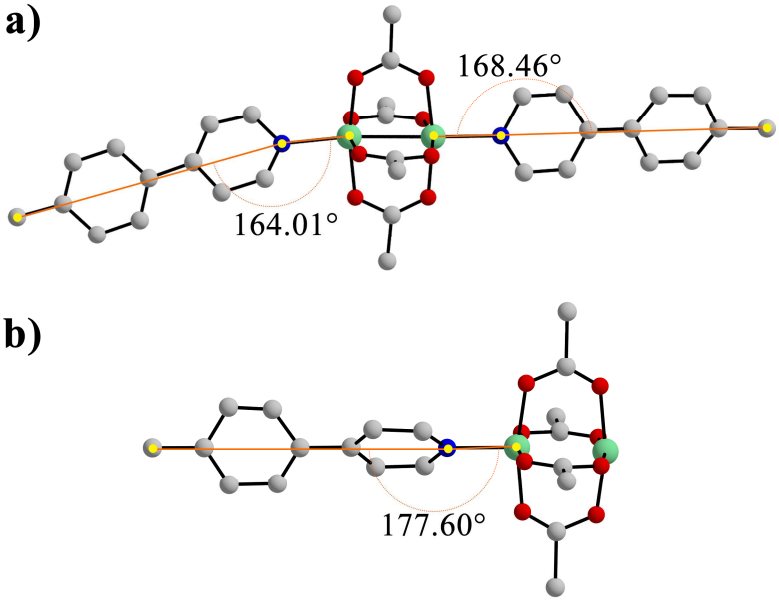

Figure S6.7: Asymmetric unit of **TCP-MOF1** at 200K (a) and 300K (b). In the figure, the angle between C1-N1-Cu1 is reported, to highlight the differences in terms of coordination geometry between both structures.

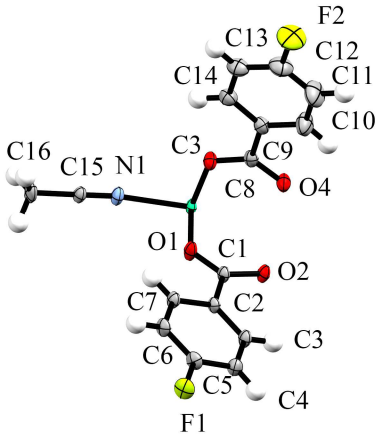

Figure S6.8: Ortep view of the asymmetric unit of **[Cu_2(*p*-FPhCO_2)$_4$(ACN)$_2$]** (probability level 30%).

Powder X-ray Diffraction (PXRD)

The powder X-ray diffraction data used for refinement analysis were collected in 0.3 mm borosilicate glass capillary, using Cu Kα1 radiation (λ=1.5406 Å) on a STOE Stadi P equipped with a Ge (111) Johansson focussing monochromator from STOE & Cie and a Mythen2 1K detector from Dectris. Data were preliminarily processed with WinXPOW (by STOE & Cie). The LeBail refinement on powder X-ray diffraction data was conducted with Jana2020.[35] Manually selected points were used to describe the background, single crystal data (3D ED) were used to define the unit cell, and cyclic refinements on the entire dataset were used to generate the profile parameters. The peak profile was modelled as a Pseudo-Voight function, corrected due to axial divergence asymmetry and cut outside 20*FMWH range.

Temperature-resolved *in situ* data collections were performed using a High Temperature Attachment for capillaries provided by STOE, collecting each diffraction pattern in a 2ϑ range of 3.7°- 22.2° every 10°C with a heating ramp of 10°C/min.

The PXRD patterns of the remaining samples were collected using Ni-filtered Cu K radiation ($\lambda_{K\alpha1}$ = 1.5406 Å, $\lambda_{K\alpha2}$ = 1.5444 Å), on a Rigaku SmartLab XE diffractometer equipped with a HyPix-3000 detector. The data were collected in Bragg-Brentano geometry and processed with SmartLab Studio II (by Rigaku).

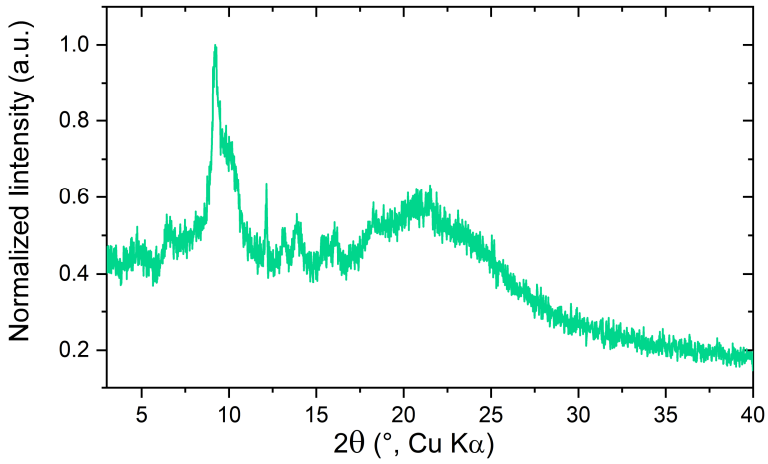

Figure S6.9: PXRD profile of **TPC-MOF1** after the 2 hours of exposure at atmospheric conditions.

Table S6.4: Comparison between the unit cell parameters from 3D ED analysis and from the Le Bail refinement on PXRD data, for the **TCP-MOF2** structure.

	3D ED	**PXRD**
a (Å)	25.534(7)	25.743(2)
b (Å)	7.485(3)	7.5507(8)
c (Å)	22.287(9)	22.229(2)
α (°)	90	90
β (°)	98.81(3)	99.039(4)
γ (°)	90	90
Vol ($Å^3$)	4209.3(3)	4266.4(5)

Table S6.5: Comparison between the unit cell parameters from 3D ED analysis and from the Le Bail refinement on PXRD data, for the **TCP-MOF3·BnOH** structure.

	3D ED	**PXRD**
a (Å)	23.043(5)	23.2663(8)
b (Å)	23.043(5)	23.2663(8)
c (Å)	8.803(2)	8.8096(5)
α (°)	90	90
β (°)	90	90
γ (°)	90	90
Vol ($Å^3$)	4674.2(3)	4768.8(6)

3D Electron Diffraction (3D ED) and TEM analysis

Scanning transmission electron microscopy imaging and 3D electron diffraction were carried out on a Zeiss Libra 120 transmission electron microscope, equipped with a LaB_6 thermionic source operating at 120 kV (λ=0.0335 Å) and a Timepix single-electron detector by ASI for collecting diffraction patterns in low dose mode. 3D electron diffraction data were collected on single nanocrystals in nanodiffraction mode with a parallel electron beam of 150 nm in diameter. Imaging was carried out in STEM mode with a high angular dark field detector (HAADF). The 3D ED data were analysed using the software PETS.[25] The ab-initio structure determination of **TCP-MOF2** was performed using the Superflip [26] package, while SHELXT was used for **TCP-MOF3**, **TCP-MOF3·BnOH**, **TCP-MOF4** and **TCP-MOF5**.[32] Data were refined with a fully kinematical approximation, *i.e.* neglecting dynamical scattering and assuming that I_{hkl} is proportional to $|F_{hkl}|^2$. Least-squares structure refinement was performed with the software SHELXL-2014 [33] interfaced with Olex2.[36]

Table S6.6: Crystallographic information for **TCP-MOF2**

Empirical formula	$C_{45}H_{34.5}Cu_{1.5}N_{2.5}O_{6.5}$
Formula weight	809.60
Temperature/K	293(2)
Crystal system	Monoclinic
Space group	*P*2/n
a/Å	25.534(7)
b/Å	7.485(3)
c/Å	22.287(9)
α/°	90
β/°	98.81(3)
γ/°	90
Volume/Å^3	4209.3(3)
Z	4
ρ_{calc}g/cm^3	1.278
F(000)	696
Radiation	Electrons (λ = 0.0335 Å)
2ϑ range for data collection/°	0.124 to 2.382
Index ranges	-31 ≤ h ≤ 31, -9 ≤ k ≤ 9, -27 ≤ l ≤ 27
Reflections collected	22319
Independent reflections	7993 [R_{int}= 0.3403, R_{sigma}= 0.2904]
Data/restraints/parameters	7993/73/210
Goodness-of-fit on F^2	1.336
Final R indexes [I>=2σ (I)] [a]	R_1= 0.2917, wR_2= 0.5871
Final R indexes [all data] [a]	R_1= 0.4137, wR_2= 0.5871

[a] $R_1 = \Sigma \| F_o | - | F_c \| / \Sigma | F_o |$, $wR_2 = [\Sigma[w(F_o^2-F_c^2)^2]/\Sigma[w(F_o^2)^2]]^{1/2}$

Table S6.7: Crystallographic information for **TCP-MOF3**

Empirical formula	$C_{25.25}H_{18}CuNO_4$
Formula weight	462.97
Temperature/K	293(2)
Crystal system	tetragonal
Space group	*P*-4*b*2
a/Å	22.074(8)
b/Å	22.074(8)
c/Å	9.005(4)
α/°	90
β/°	90
γ/°	90
Volume/Å^3	4388(4)
Z	8
ρ_{calc}g/cm^3	1.402
F(000)	695.0
Radiation	Electrons (λ = 0.0335 Å)
2ϑ range for data collection/°	0.122 to 1.706
Index ranges	-15 ≤ h ≤ 15, -18 ≤ k ≤ 19, -8 ≤ l ≤ 7
Reflections collected	6431
Independent reflections	1617 [R_{int} = 0.3149, R_{sigma} = 0.2032]
Data/restraints/parameters	1617/86/126
Goodness-of-fit on F^2	1.718
Final R indexes [I>=2σ (I)] [a]	R_1 = 0.2029, wR_2 = 0.4125
Final R indexes [all data] [a]	R_1 = 0.2591, wR_2 = 0.4458

[a] $R_1 = \Sigma \| F_o | - | F_c \| / \Sigma | F_o |$, $wR_2 = [\Sigma[w(F_o^2-F_c^2)^2]/\Sigma[w(F_o^2)^2]]^{1/2}$

Table S6.8: Crystallographic information for **TCP-MOF3·BnOH**

Empirical formula	$C_{25.25}H_{18}CuNO_4$
Formula weight	462.97
Temperature/K	293(2)
Crystal system	tetragonal
Space group	*P*4/n
a/Å	23.043(5)
b/Å	23.043(5)
c/Å	8.803(2)
α/°	90
β/°	90
γ/°	90
Volume/Å^3	4674.2(18)
Z	8
ρ_{calc}g/cm^3	1.309
F(000)	695
Radiation	Electrons (λ = 0.0335 Å)
2ϑ range for data collection/°	0.118 to 2.02
Index ranges	-24 ≤ h ≤ 24, -18 ≤ k ≤ 19, -9 ≤ l ≤ 9
Reflections collected	9252
Independent reflections	2565 [R_{int} = 0.3536, R_{sigma} = 0.2548]
Data/restraints/parameters	2565/192/258
Goodness-of-fit on F^2	1.470
Final R indexes [I>=2σ (I)] [a]	R_1 = 0.2344, wR_2 = 0.5105
Final R indexes [all data] [a]	R_1 = 0.2836, wR_2 = 0.5600

[a] $R_1 = \Sigma \| F_o | - | F_c \| / \Sigma | F_o |$, $wR_2 = [\Sigma[w(F_o^2-F_c^2)^2]/\Sigma[w(F_o^2)^2]]^{1/2}$

Table S6.9: Crystallographic information for **TCP-MOF4**

Empirical formula	$C_{48.75}H_{31.75}Cu_{1.5}F_{3.75}N_2O_{7.5}$
Formula weight	932.11
Temperature/K	293(2)
Crystal system	monoclinic
Space group	*P*2/n
a/Å	25.632(11)
b/Å	7.653(2)
c/Å	23.063(9)
α/°	90
β/°	98.12(3)
γ/°	90
Volume/Å^3	4478(3)
Z	4
ρ_{calc}g/cm^3	1.382
F(000)	682.0
Radiation	Electrons (λ = 0.0335 Å)
2ϑ range for data collection/°	0.104 to 2.132
Index ranges	-28 ≤ h ≤ 28, -8 ≤ k ≤ 8, -25 ≤ l ≤ 25
Reflections collected	14073
Independent reflections	4477 [R_{int} = 0.3812, R_{sigma} = 0.3348]
Data/restraints/parameters	4477/29/217
Goodness-of-fit on F^2	1.335
Final R indexes [I>=2σ (I)] [a]	R_1 = 0.2558, wR_2 = 0.5176
Final R indexes [all data] [a]	R_1 = 0.3841, wR_2 = 0.5956

[a] $R_1 = \Sigma \| F_o | - | F_c \| / \Sigma | F_o |$, $wR_2 = [\Sigma[w(F_o^2-F_c^2)^2]/\Sigma[w(F_o^2)^2]]^{1/2}$

Table S6.10: Crystallographic information for **TCP-MOF5**

Empirical formula	$C_{25.25}CuF_2NO_4$
Formula weight	4920.00
Temperature/K	293(2)
Crystal system	Tetragonal
Space group	*P*4/n
a/Å	24.387(11)
b/Å	24.387(11)
c/Å	8.284(5)
α/°	90
β/°	90
γ/°	90
Volume/Å^3	4927(4)
Z	8
ρ_{calc}g/cm^3	1.658
F(000)	711
Radiation	Electrons (λ = 0.0335 Å)
2ϑ range for data collection/°	0.158 to 1.478
Index ranges	-18 ≤ h ≤ 18, -18 ≤ k ≤ 18, -6 ≤ l ≤ 6
Reflections collected	9907
Independent reflections	1177 [R_{int} = 0.3297, R_{sigma} = 0.2312]
Data/restraints/parameters	1177/56/87
Goodness-of-fit on F^2	1.696
Final R indexes [I>=2σ (I)] [a]	R_1 = 0.2929, wR_2 = 0.6023
Final R indexes [all data] [a]	R_1 = 0.3670, wR_2 = 0.6599

[a] $R_1 = \Sigma \| F_o | - | F_c \| / \Sigma | F_o |$, $wR_2 = [\Sigma[w(F_o^2-F_c^2)^2]/\Sigma[w(F_o^2)^2]]^{1/2}$

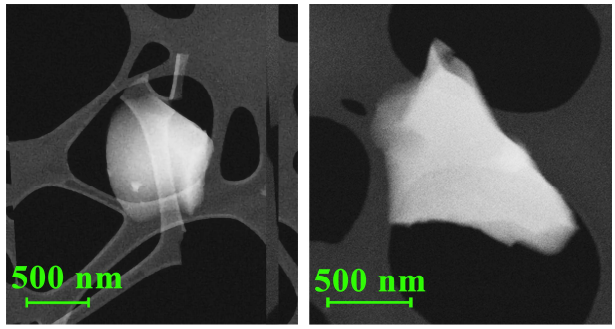

Figure S6.10: HAADF-STEM image of the **TCP-MOF2** nanocrystals used for the 3D ED data collection.

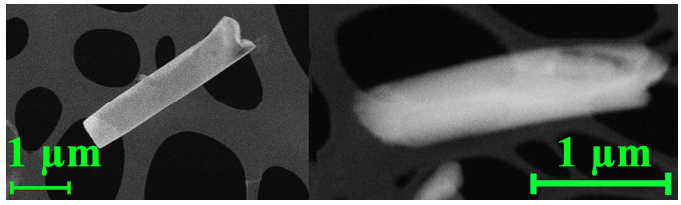

Figure S6.11: HAADF-STEM image of the **TCP-MOF3** nanocrystals used for the 3D ED data collection. (*right*) **TCP-MOF3** empty phase, (*left*) **TCP-MOF3·BnOH** phase.

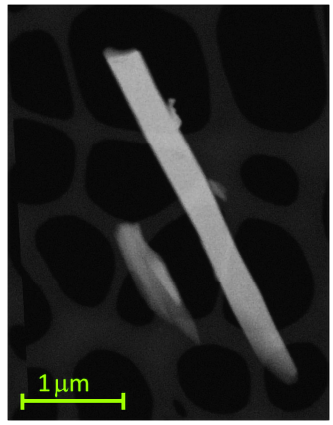

Figure S6.12: HAADF-STEM image of the **TCP-MOF4** nanocrystals used for the 3D ED data collection.

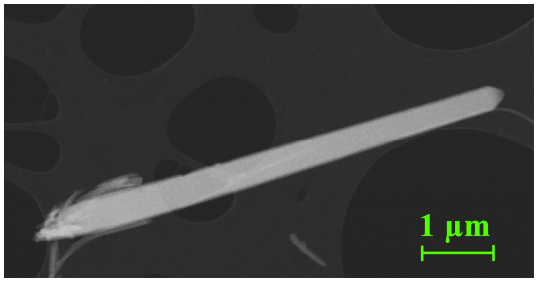

Figure S6.13: HAADF-STEM image of the **TCP-MOF5** nanocrystals used for the 3D ED data collection.

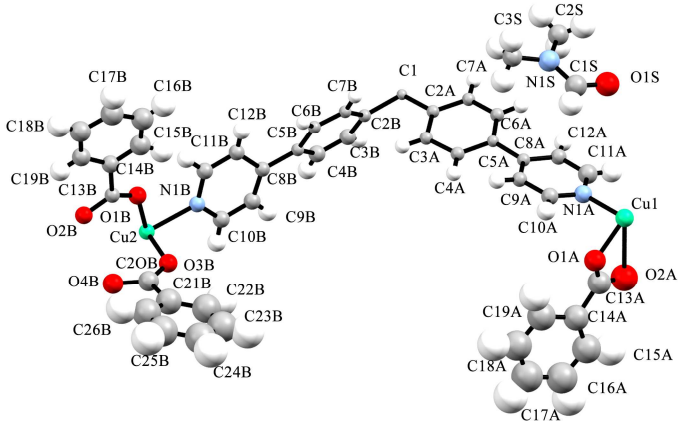

Figure S6.14: Ortep view of the asymmetric unit of **TCP-MOF2** (probability level 50%).

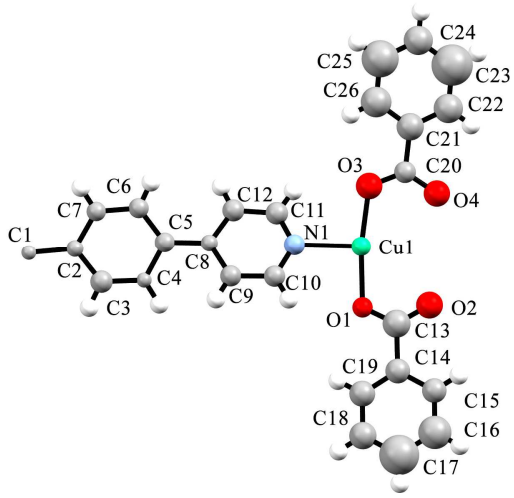

Figure S6.15: Ortep view of the asymmetric unit of **TCP-MOF3** empty phase (probability level 30%).

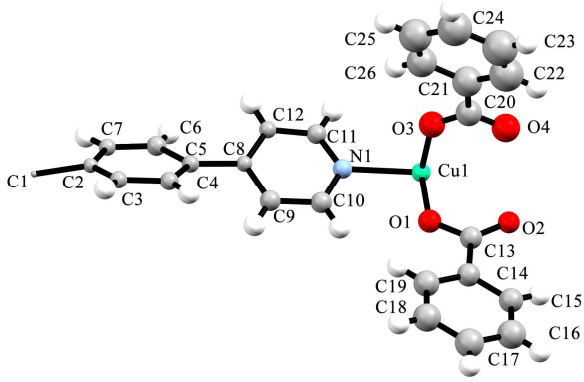

Figure S6.16: Ortep view of the asymmetric unit of **TCP-MOF3·BnOH** (probability level 30%).

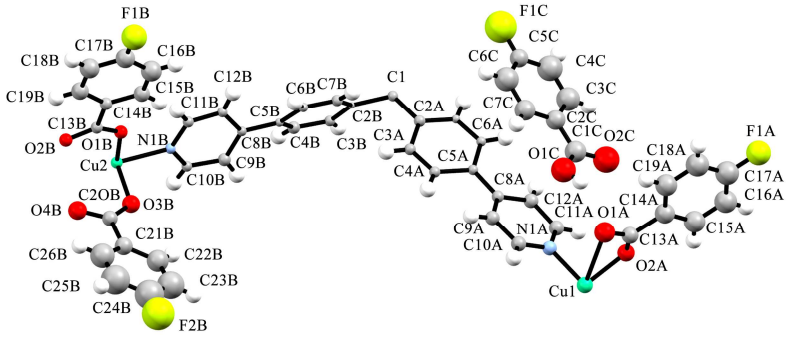

Figure S6.17: Ortep view of the asymmetric unit of **TCP-MOF4** (probability level 30%).

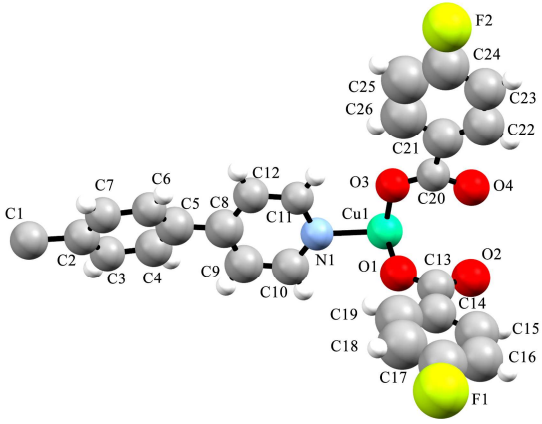

Figure S6.18: Ortep view of the asymmetric unit of **TCP-MOF5** (probability level 30%).

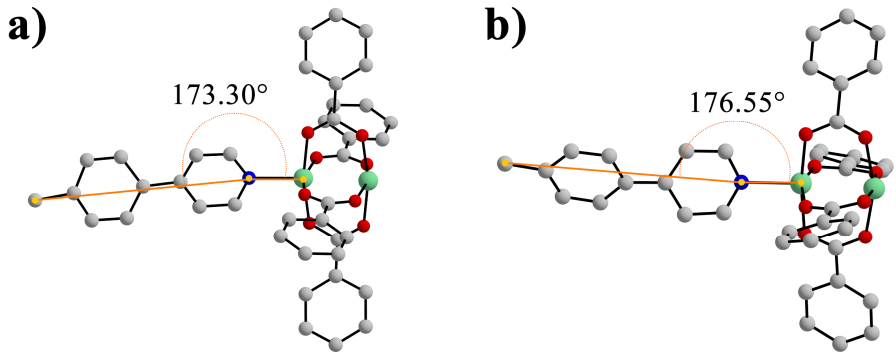

Figure S6.19: Asymmetric unit of **TCP-MOF3·BnOH** (a) and **TCP-MOF3** empty phase (b). In the figure, the angle between C1-N1-Cu1 is reported, to highlight the differences in terms of coordination geometry between both crystal structures.

6.4.3 Thermogravimetric Analyses (TGA)

The thermogravimetric analyses were conducted on a Perkin Elmer Instrument, model TGA 8000. The experiments were carried out in the temperature range 30-550°C with a heating rate of 20°C min^{-1} under air flux.

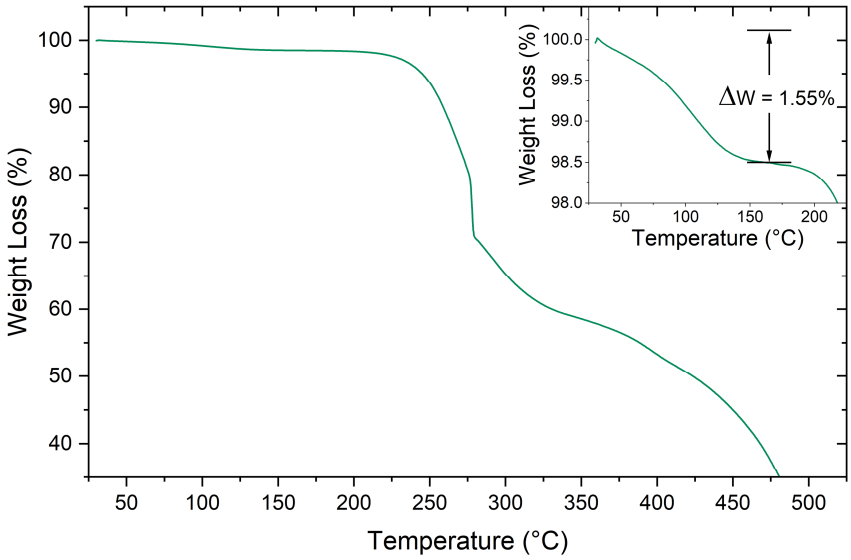

Figure S6.20: Thermogravimetric path recorded on the **TCP-MOF2** crystal phase.

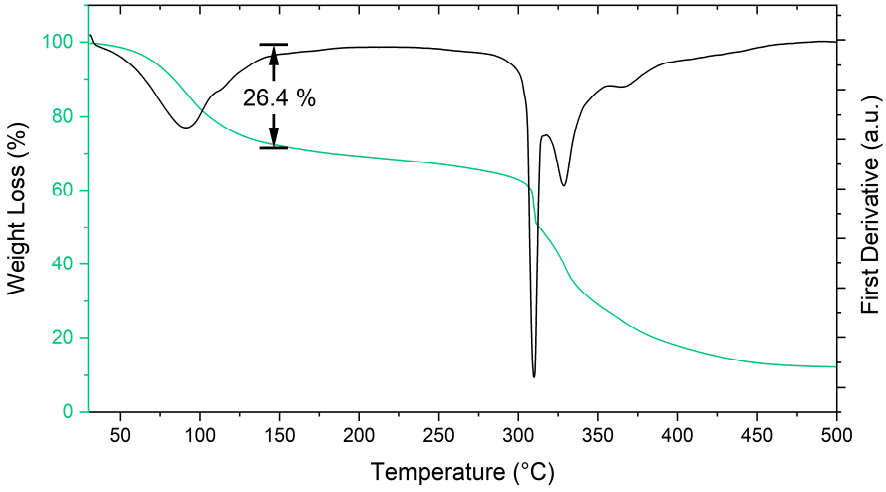

Figure S6.21: Thermogravimetric path recorded on the **TCP-MOF3** crystal phase.

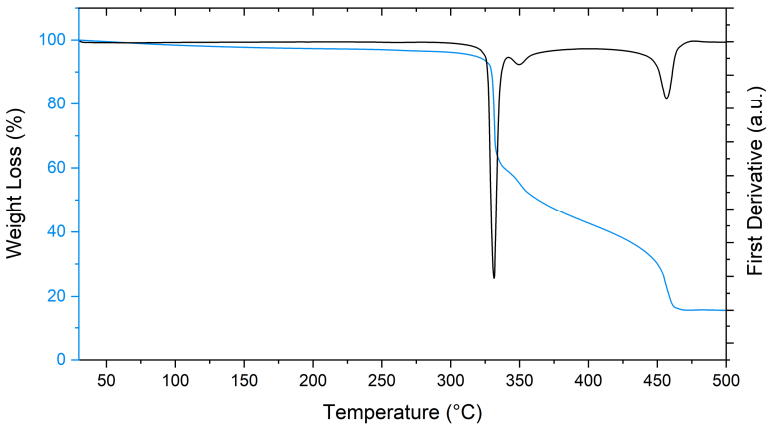

Figure S 6.22: Thermogravimetric path recorded on the **TCP-MOF4** crystal phase after the washing process.

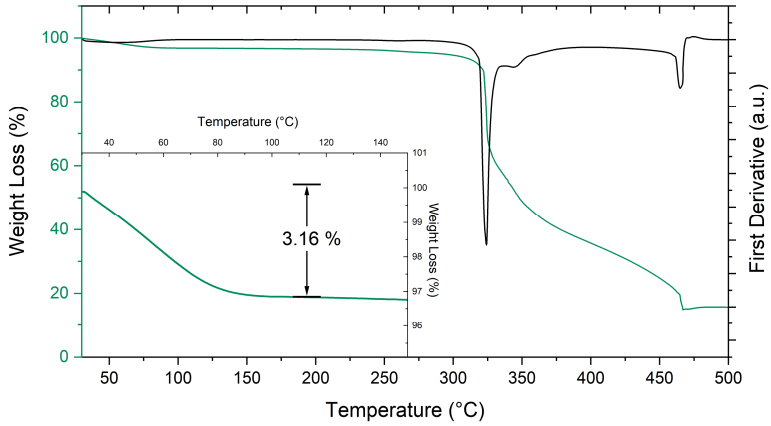

Figure S6.23: Thermogravimetric path recorded on the **TCP-MOF5** crystal phase.

6.4.4 Gas sorption

The gas sorption measurements were carried out at Uppsala University by Professor Ocean Cheung. The gas sorption measurements were performed on a Micromeritics ASAP202 surface analyser. Before gas sorption measurements, the as-synthesized MOFs were activated under dynamical vacuum at 150°C.

6.4.5 PFAS adsorption experiment on TCP-MOF2 and TCP-MOF4

The ^{19}F NMR spectra were collected in 450µL of DMSO-d6 with 50µL of DCl/D2O (2:8), in order to completely digest the material and hamper the influence of the paramagnetic Cu(II) ions. The analysis was conducted on a Jeol 600 MHz ECZ600R. The **TCP-MOF2** spectra were recorder with the addition of 50µL of 0.03 mM aqueous solution of trifluoro ethanol as internal standard.

The adsorption experiment was carried out in triplicate for both **TCP-MOF2** and **TCP-MOF4**. The procedure consisted in placing about 1 mg of the MOF into a 1.5mL Eppendorf vial, followed by the addition of 1 mL of a 5mM solution of **NaPFB** or **NaPFO**. After 24 hours, the aqueous solution was removed by centrifugation and the solid was rinsed two times with distilled water. Then, 50mL of a DCl/D2O (2:8) solution were added to the solid in order to completely destroy its polymeric network. Subsequently, the product was completely solubilized in DMSO-d6 and characterized through ^{19}F NMR spectroscopy.

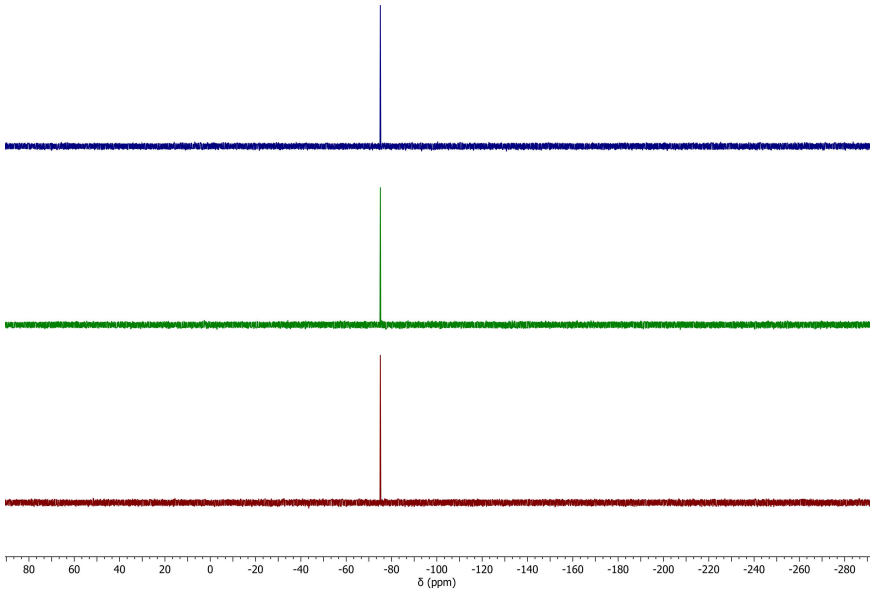

Figure S6.24: ^{19}F NMR spectra of **TCP-MOF2** after the exposure to the **NaPFB** solution. (565 MHz, DMSO-d_6) δ (ppm): -75.8 (t, J = 8.8 Hz, 3F, TFE).

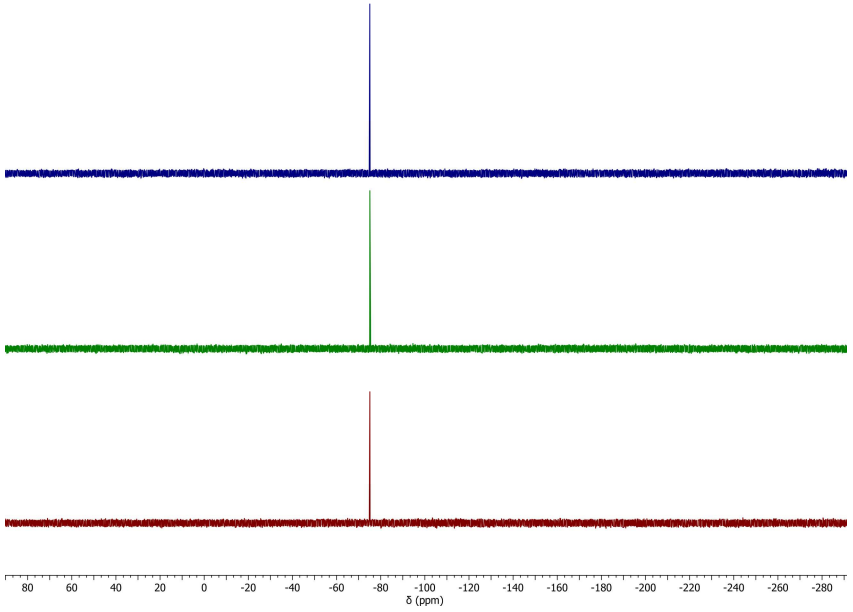

Figure S6.25: ^{19}F NMR spectra of **TCP-MOF2** after the exposure to the **NaPFO** solution. (565 MHz, DMSO-d_6) δ (ppm): -75.8 (t, J = 8.8 Hz, 3F, TFE).

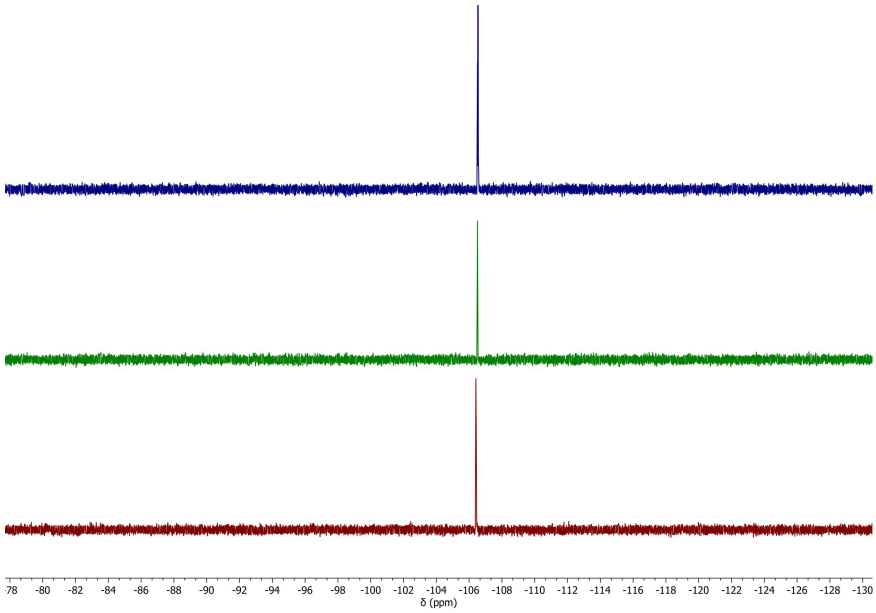

Figure S6.26: ^{19}F NMR spectra of **TCP-MOF4** after the exposure to the **NaPFB** solution. (565 MHz, DMSO-d$_6$) δ (ppm): -106.5 (m, 6F, *p*-FBzA from **TCP-MOF4**).

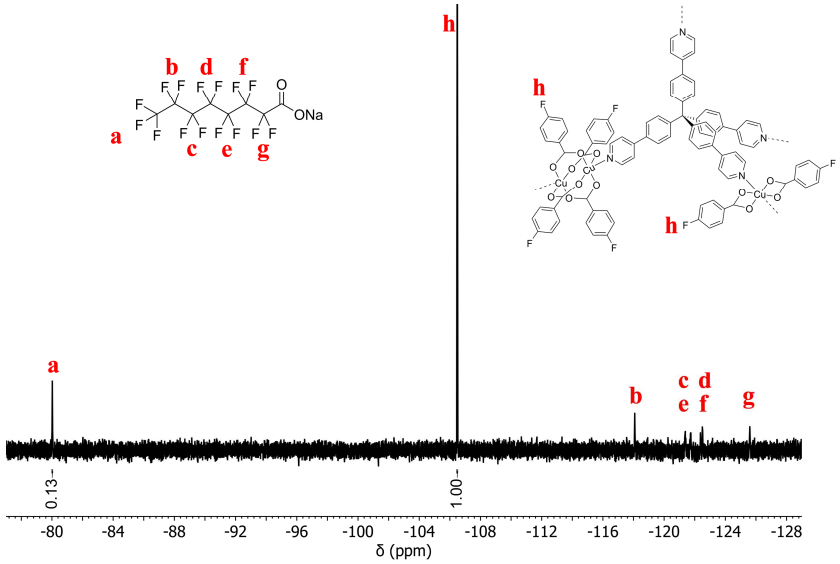

Figure S6.27: ^{19}F NMR spectrum of **TCP-MOF4** after the exposure to the **NaPFO** solution, first experiment. (565 MHz, DMSO-d$_6$) δ (ppm): -80.4 (t, J = 9.70 Hz, 3F, a), -106.5 (m, 6F, h), -118.1 (m, 2F, b), -121.4 (m, 2F, c), -121.7(m, 2F, d), -122.4 (m, 2F, e), -122.5 (m, 2F, f), -125.6 (m, 2F, g).

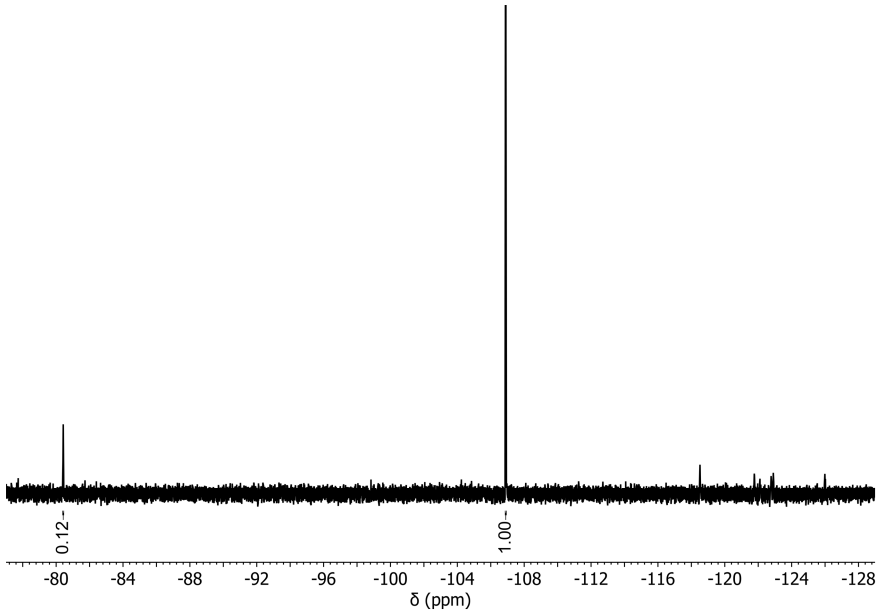

Figure S6.28: ^{19}F NMR spectrum of **TCP-MOF4** after the exposure to the **NaPFO** solution, second experiment.

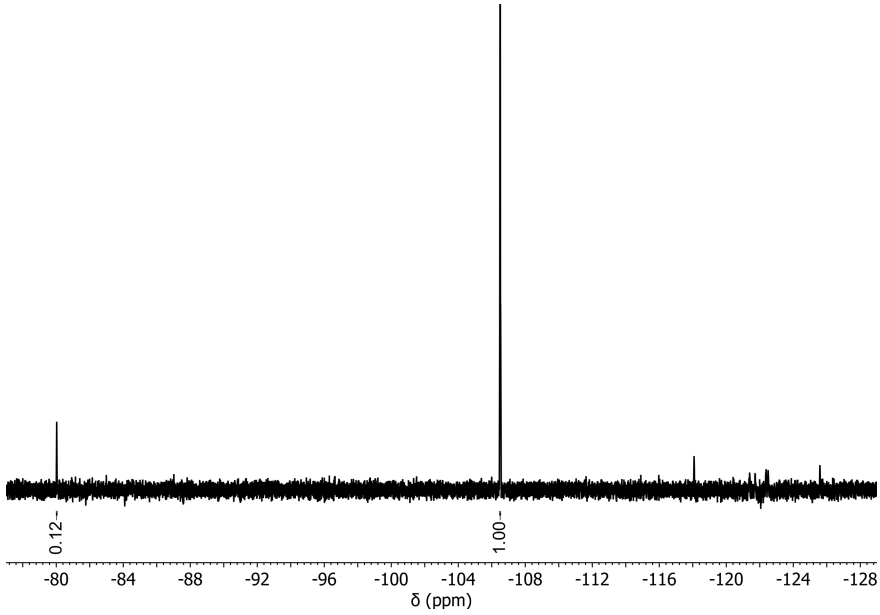

Figure S6.29: ^{19}F NMR spectrum of **TCP-MOF4** after the exposure to the **NaPFO** solution, third experiment.

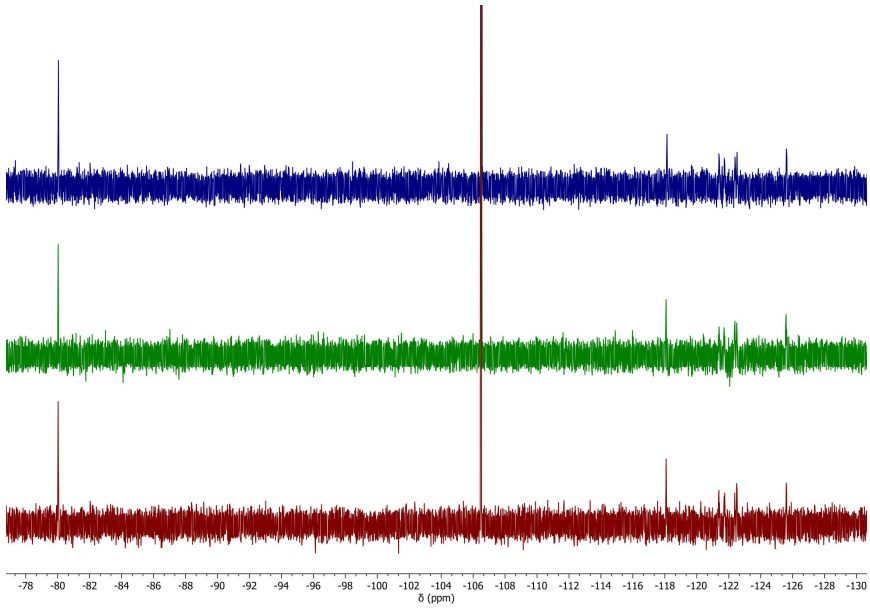

Figure S6.30: ^{19}F NMR spectra of **TCP-MOF4** after the exposure to the **NaPFO** solution, stacked view of the three experiments.

Bibliography:

[1] C.B. Caputo, V.N. Vukotic, N.M. Sirizzotti, S.J. Loeb, "A tetrapyridine ligand with a rigid tetrahedral core forms metal–organic frameworks with PtS type architecture", *Chem. Commun.* 47 (2011) 8545. https://doi.org/10.1039/c1cc12188j.

[2] H. Kitagawa, H. Ohtsu, M. Kawano, "Kinetic Assembly of a Thermally Stable Porous Coordination Network Based on Labile CuI Units and the Visualization of I 2 Sorption", *Angew. Chem. Int. Ed.* 52 (2013) 12395–12399. https://doi.org/10.1002/anie.201306776.

[3] H. Kitagawa, H. Ohtsu, A.J. Cruz-Cabeza, M. Kawano, "Isolation and evolution of labile sulfur allotropes *via* kinetic encapsulation in interactive porous networks", *IUCrJ* 3 (2016) 232–236. https://doi.org/10.1107/S2052252516008423.

[4] H. Ohtsu, M. Okuyama, T. Nakajima, M. Iwamura, K. Nozaki, D. Hashizume, M. Kawano, "Through-Space Charge Transfer in Copper Coordination Networks with Copper-Halide Guest Anions", *Inorg. Chem.* 60 (2021) 9273–9277. https://doi.org/10.1021/acs.inorgchem.1c01451.

[5] H. Furukawa, K.E. Cordova, M. O'Keeffe, O.M. Yaghi, "The Chemistry and Applications of Metal-Organic Frameworks", *Science* 341 (2013) 1230444. https://doi.org/10.1126/science.1230444.

[6] O.M. Yaghi, M. O'Keeffe, N.W. Ockwig, H.K. Chae, M. Eddaoudi, J. Kim, "Reticular synthesis and the design of new materials", *Nature* 423 (2003) 705–714. https://doi.org/10.1038/nature01650.

[7] R. Freund, S. Canossa, S.M. Cohen, W. Yan, H. Deng, V. Guillerm, M. Eddaoudi, D.G. Madden, D. Fairen-Jimenez, H. Lyu, L.K. Macreadie, Z. Ji, Y. Zhang, B. Wang, F. Haase, C. Wöll, O. Zaremba, J. Andreo, S. Wuttke, C.S. Diercks, "25 Years of Reticular Chemistry", *Angew. Chem. Int. Ed.* 60 (2021) 23946–23974. https://doi.org/10.1002/anie.202101644.

[8] R.B. Getman, Y.-S. Bae, C.E. Wilmer, R.Q. Snurr, "Review and Analysis of Molecular Simulations of Methane, Hydrogen, and Acetylene Storage in Metal–Organic Frameworks", *Chem. Rev.* 112 (2012) 703–723. https://doi.org/10.1021/cr200217c.

[9] K. Sumida, D.L. Rogow, J.A. Mason, T.M. McDonald, E.D. Bloch, Z.R. Herm, T.-H. Bae, J.R. Long, "Carbon Dioxide Capture in Metal–Organic Frameworks", *Chem. Rev.* 112 (2012) 724–781. https://doi.org/10.1021/cr2003272.

[10] M.P. Suh, H.J. Park, T.K. Prasad, D.-W. Lim, "Hydrogen Storage in Metal–Organic Frameworks", *Chem. Rev.* 112 (2012) 782–835. https://doi.org/10.1021/cr200274s.

[11] A. Schneemann, V. Bon, I. Schwedler, I. Senkovska, S. Kaskel, R.A. Fischer, "Flexible metal–organic frameworks", *Chem. Soc. Rev.* 43 (2014) 6062–6096. https://doi.org/10.1039/C4CS00101J.

[12] H. Wu, Q. Gong, D.H. Olson, J. Li, "Commensurate Adsorption of Hydrocarbons and Alcohols in Microporous Metal Organic Frameworks", *Chem. Rev.* 112 (2012) 836–868. https://doi.org/10.1021/cr200216x.

[13] L.E. Kreno, K. Leong, O.K. Farha, M. Allendorf, R.P. Van Duyne, J.T. Hupp, "Metal–Organic Framework Materials as Chemical Sensors", *Chem. Rev.* 112 (2012) 1105–1125. https://doi.org/10.1021/cr200324t.

[14] W. Zhang, R.-G. Xiong, "Ferroelectric Metal–Organic Frameworks", *Chem. Rev.* 112 (2012) 1163–1195. https://doi.org/10.1021/cr200174w.

[15] P. Horcajada, R. Gref, T. Baati, P.K. Allan, G. Maurin, P. Couvreur, G. Férey, R.E. Morris, C. Serre, "Metal–Organic Frameworks in Biomedicine", *Chem. Rev.* 112 (2012) 1232–1268. https://doi.org/10.1021/cr200256v.

[16] H.-C. Zhou, J.R. Long, O.M. Yaghi, "Introduction to Metal–Organic Frameworks", *Chem. Rev.* 112 (2012) 673–674. https://doi.org/10.1021/cr300014x.

[17] U. Mueller, M. Schubert, F. Teich, H. Puetter, K. Schierle-Arndt, J. Pastré, "Metal–organic frameworks—prospective industrial applications", *J. Mater. Chem.* 16 (2006) 626–636. https://doi.org/10.1039/B511962F.

[18] M. Jacoby, "Heading to Market with MOFs: For Metal-Organic Frameworks, lab-scale research is brisk as commercialization begins", *Chem. Eng. News Archive* 86 (2008) 13–16. https://doi.org/10.1021/cen-v086n034.p013.

[19] D. Jędrzejowski, M. Pander, W. Nitek, W. Bury, D. Matoga, "Turning Flexibility into Rigidity: Stepwise Locking of Interpenetrating Networks in a MOF Crystal through Click Reaction", *Chem. Mater.* 33 (2021) 7509–7517. https://doi.org/10.1021/acs.chemmater.1c02451.

[20] S. Kitagawa, M. Kondo, "Functional Micropore Chemistry of Crystalline Metal Complex-Assembled Compounds", *Bull. Chem. Soc. Jpn.* 71 (1998) 1739–1753. https://doi.org/doi.org/10.1246/bcsj.71.1739.

[21] D. Morelli Venturi, F. Costantino, "Recent advances in the chemistry and applications of fluorinated metal–organic frameworks (F-MOFs)", *RSC Adv.* 13 (2023) 29215–29230. https://doi.org/10.1039/D3RA04940J.

[22] V.A. Blatov, A.P. Shevchenko, D.M. Proserpio, "Applied Topological Analysis of Crystal Structures with the Program Package ToposPro", *Crystal Growth & Design* 14 (2014) 3576–3586. https://doi.org/10.1021/cg500498k.

[23] C.F. Macrae, I. Sovago, S.J. Cottrell, P.T.A. Galek, P. McCabe, E. Pidcock, M. Platings, G.P. Shields, J.S. Stevens, M. Towler, P.A. Wood, "*Mercury 4.0*: from visualization to analysis, design and prediction", *J. Appl. Crystallogr.* 53 (2020) 226–235. https://doi.org/10.1107/S1600576719014092.

[24] I. Nederlof, E. Van Genderen, Y.-W. Li, J.P. Abrahams, "A Medipix quantum area detector allows rotation electron diffraction data collection from submicrometre three-dimensional protein crystals", *Acta Crystallogr. D Biol. Crystallogr.* 69 (2013) 1223–1230. https://doi.org/10.1107/S0907444913009700.

[25] L. Palatinus, P. Brázda, M. Jelínek, J. Hrdá, G. Steciuk, M. Klementová, "Specifics of the data processing of precession electron diffraction tomography data and their implementation in the program *PETS2.0"*, *Acta Crystallogr. B Struct. Sci. Cryst. Eng. Mater.* 75 (2019) 512–522. https://doi.org/10.1107/S2052520619007534.

[26] L. Palatinus, G. Chapuis, "*SUPERFLIP* – a computer program for the solution of crystal structures by charge flipping in arbitrary dimensions", *J. Appl. Crystallogr.* 40 (2007) 786–790. https://doi.org/10.1107/S0021889807029238.

[27] M. Meunier, S. Robertson, "*Materials Studio* 20th anniversary", Mol. Simul. 47 (2021) 537–539. https://doi.org/10.1080/08927022.2021.1892093.

[28] J. Perego, C.X. Bezuidenhout, A. Pedrini, S. Bracco, M. Negroni, A. Comotti, P. Sozzani, "Reorientable fluorinated aryl rings in triangular channel Fe-MOFs: an investigation on CO_2 –matrix interactions", *J. Mater. Chem. A* 8 (2020) 11406–11413. https://doi.org/10.1039/D0TA02529A.

[29] M. Ghassemzadeh, K. Aghapoor, B. Neumiiller, Synthesis and Crystal Structure of $[Cu_2(OAc)_4(NCMe)_2] \cdot 2MeCN$, Z. Natur. B 53 (1998) 774–776. https://doi.org/10.1515/znb-1998-0718.

[30] N. Lah, G. Giester, P. Šegedin, A. Murn, K. Podlipnik, I. Leban, "Two dimeric Cu ^{II} benzoate derivatives solvated with acetonitrile", *Acta Crystallogr. C Cryst. Struct. Commun.* 57 (2001) 546–548. https://doi.org/10.1107/S0108270101003183.

[31] (a) SADABS Bruker AXS; Madison, Wisconsin, USA, 2004; "SAINT, Software Users Guide", Version 6.0; Bruker Analytical X-ray Systems, Madison, WI, (1999); (b) Sheldrick, G. M. "SADABS v2.03: Area-Detector Absorption Correction". University of Göttingen, Germany, (1999).

[32] G.M. Sheldrick, "*SHELXT* – Integrated space-group and crystal-structure determination", *Acta Crystallogr. A Found. Adv.* 71 (2015) 3–8. https://doi.org/10.1107/S2053273314026370.

[33] G.M. Sheldrick, "Crystal structure refinement with *SHELXL"*, *Acta Crystallogr. C Struct. Chem.* 71 (2015) 3–8. https://doi.org/10.1107/S2053229614024218.

[34] L.J. Farrugia, "*WinGX* suite for small-molecule single-crystal crystallography", *J. Appl. Crystallogr.* 32 (1999) 837–838. https://doi.org/10.1107/S0021889899006020.

[35] V. Petříček, M. Dušek, L. Palatinus, "Crystallographic Computing System JANA2006: General features", *Z. Kristallogr. Cryst. Mater.* 229 (2014) 345–352. https://doi.org/10.1515/zkri-2014-1737.

[36] O.V. Dolomanov, L.J. Bourhis, R.J. Gildea, J.A.K. Howard, H. Puschmann, "*OLEX2*: a complete structure solution, refinement and analysis program", *J. Appl. Crystallogr.* 42 (2009) 339–341. https://doi.org/10.1107/S0021889808042726.

7 Bismuth-based MOFs and their structural investigation through 3D ED analysis

This chapter discusses the research project that was carried out during an exchange period at Stockholm University, under the supervision of Prof. Andrew Kentaro Inge. The main topic focuses on the synthesis and characterisation of bismuth(III)-based Metal-Organic Frameworks. The chapter is divided into two sections, which differ for the ligands employed in the synthesis of the final materials. The first section describes the synthesis of two novel Bismuth tricarboxylate MOFs under green conditions, using 4,4′,4″-nitrilotrisbenzoic acid (**H_3NTB**) as the organic linker and Bi(III) as the medal node. In both cases, the crystal structure was solved through 3D Electron diffraction analysis and then refined against powder X-ray diffraction data. The second section aims the synthesis of bismuth-based MOFs using the protocatechuic acid as a ligand. This part also discusses a peculiar Bi-π interaction discovered in Bi-Protocatechuate 2D coordination polymers and how its formation can be prevented to achieve a 3D network.

7.1 Introduction

Bismuth-based Metal-Organic Frameworks (Bi-MOFs) are a promising type of reticular materials that have attracted attention due to their fascinating properties and functionalities. However, this particular class of MOFs is still in an emerging stage of development due to constraints posed by the variety of coordination environments and the low solubility of Bi(III) cations. [1,2] In the last decade, there has been a growing interest in researching MOFs that incorporate main group metals such as Bi, Sn, Al, and In. Bismuth is a promising candidate due to its low cost and minimal environmental impact. [3,4] Furthermore, several Bi-MOFs have demonstrated favourable properties in catalysis, energy storage, biomedical imaging, drug delivery, sensing, and the adsorption and separation of gases. [3,5–10] Bismuth is a non-toxic and noncarcinogenic metal that typically has an oxidation state of +3 in most of its complexes. [11] Bi-MOFs generally exhibit infinitely large SBUs, such as rods and layers, which result in hybrid structures consisting of both organic and inorganic networks. [12] However, the growth of Bi-MOFs remains a significant challenge due to the tendency of Bi^{3+} to form layered dense frameworks with relatively limited porosity. [12]

The first section of this chapter focuses on the synthesis of Bi-MOFs based on a tritopic carboxylate ligand. The first studies on Bi-MOFs based on tritopic carboxylate ligands regard the CAU-7, CAU-17, and SU-100 materials. [12–14] The building block of these materials comprises 1,3,5-benzenetrisbenzoic acid (**H_3BTB**), 1,3,5-trisbenzoic acid (**H_3BTC**) and biphenyl-3,4′,5-tricarboxylic acid (**H_3BPT**), respectively (Scheme 7.1).

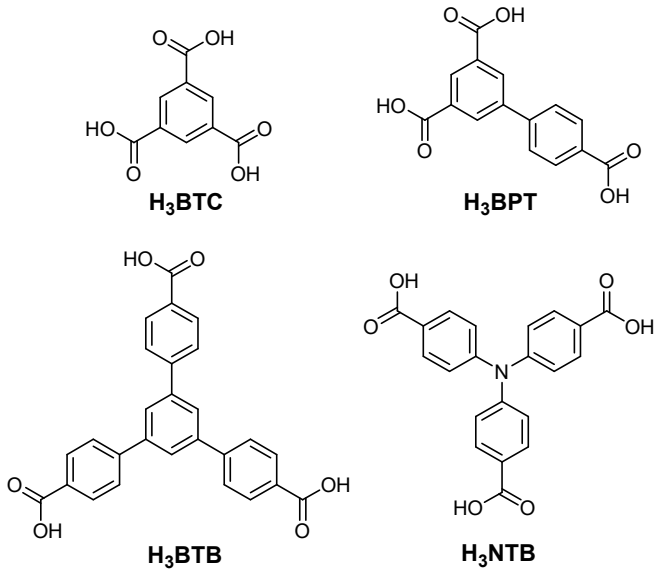

Scheme 7.1: Likers used for CAU-17 (**H3BTC**), SU-100(**H3BPT**), CAU-7 (**H3BTB**) and in this chapter (**H3NTB**).

This project has investigated the use of 4,4′,4″-nitrilotrisbenzoic acid (**H3NTB**) as a tritopic ligand for the synthesis of novel Bi-MOFs. **H3NTB** is a ligand employed in various metal-organic reticular materials based on different metal centres. However, its combination with bismuth has not been explored until now. The novel Bi-NTB MOFs have been synthesized in relatively green and fast conditions, leading to two new microcrystalline materials. In both cases, the structural characterization was carried out on single microcrystals using the 3D Electron Diffraction technique (3D ED).

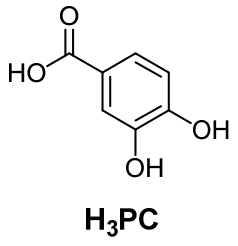

Scheme 7.2: Molecular sketch of the protocatechuic acid (H_3PC).

The second section of this chapter regards the synthesis of reticular metal-organic materials based on protocatechuic acid (**H_3PC**), a phenolic acid bioavailable in nature, with antioxidant and anti-inflammatory properties (Scheme 7.2). [15,16] Although bismuth compounds have been used historically in cosmetics and medicine, [17,18] the combination of this metal with **H_3PC** in metal-organic materials has not yet been investigated. Furthermore, the PC^{3-} molecule has only recently been documented as an organic building block in MOF synthesis. [19] Indeed, the Cambridge Structural Database (CSD) only reports a single MOF based on PC^{3-} linkers, and none of the deposited metal-organic PC-based materials includes bismuth as a metal centre. This is a preliminary study on the synthesis of reticular materials based on PC^{3-} and Bi^{3+} as building blocks.

7.2 Synthesis and characterization of Bi-MOFs based on the H_3NTB ligand – Bi(NTB)MOFs

Bi(NTB) MOFs were synthesized using solvothermal conditions with relatively fast reaction times due to the high reactivity between the building blocks. It is important not to extend the reaction times to prevent side reactions that can occur at the high temperature of the synthesis. The first Bi-MOFs based on the NTB^{3-} linker (**Bi(NTB)-MOF1**) was obtained from the reaction between **H_3NTB** and $Bi(NO_3)_3{\cdot}5H_2O$, in aqueous solution of acetic acid (10% v/v) at 140°C for 2 hours (Scheme 7.3). The reaction crude was washed with acetic acid (20% v/v) and methanol, isolating a microcrystalline powder with a well-defined PXRD pattern (Figure S7.1).

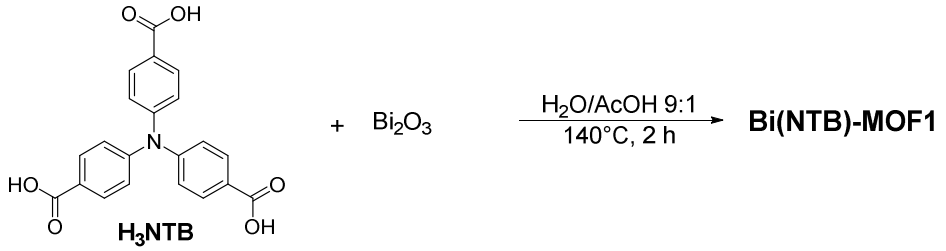

Scheme 7.3: Synthesis of **Bi(NTB)-MOF1**.

Its crystal structure was subsequently elucidated through 3D Electron Diffraction , using a TEM operating in SAED, equipped with Medipix single electron detector, [20] and working in a special low-dose setup. The data collection was carried out in continuous rotation mode and by controlling the TEM through the Instamatic software. [21] Three different crystals were analysed and the gathered data combined and analysed through the XDS package, [22] highlighting the presence of a orthorhombic unit cell in the $Pca2_1$ space group, with parameters: $a = 19.071(6)$ Å, $b = 15.159(4)$ Å, $c = 7.813(2)$ Å. The indexed data were integrated, the crystal structure resolved *ab initio* and kinematically refined. The resulting crystal structure exhibits a polymeric network with general formula **$\{Bi(NTB)\}_n$** (Figure S7.7).

The polymeric network comprises fully deprotonated **NTB^{3-}** molecules coordinated to Bi^{3+} centres. These linkers employ two of their benzoic arms as bidentate chelating ligands, while the remaining one acts as bidentate μ_2-bridging ligand (Figure 7.1).

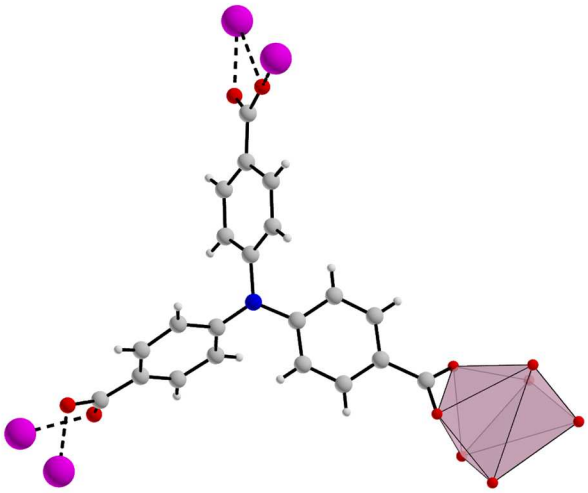

Figure 7.1: Repeating unit of **Bi(NTB)-MOF1.** Bismuth with its coordination environment is represented as a magenta polyhedron, while the Bi^{3+} ions coordinating the other arms of the NTB molecule are depicted as magenta spheres connected through dashed bonds. Oxygen, nitrogen, carbon, and hydrogen atoms are reported as red, blue, grey, and white spheres, respectively.

The bismuth centres have a coordination number of 7; one of the oxygens (O2B) involved in a chelation on a Bi^{3+} cation also interacts with a neighbouring metal centre. This yields rod-like SBUs oriented along the crystallographic *c*-axis, which are composed of bismuth polyhedra linked together by the presence of a common vertex (Figure 7.2). This is consistent with the versatility in the coordination number of bismuth cations, spanning from 6 to 9, and exhibiting Bi-O distances within the range of 2.2-3 Å. [14] Moreover, the structure displays narrow channels of voids (8.5% of the total unit cell volume, 191 $Å^3$) disposed parallel to the corrugate Bi-O rods (as calculated using Mercury software). [23] However, the kinematical refinement

conducted on the 3D ED data did not reveal any structural information about possible guest molecules embedded in these channels (Figure 7.3a). The lack of solvent molecules, that should be trapped in the framework channels, may be related to their removal under the high vacuum conditions present in the TEM.

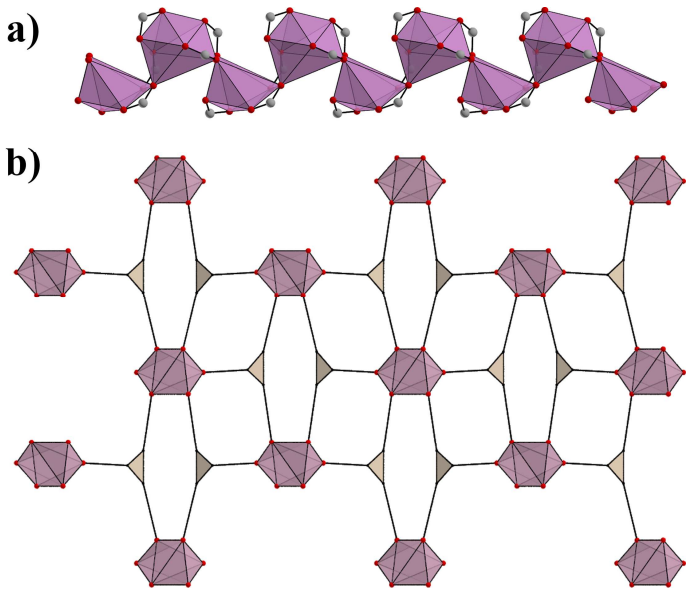

Figure 7.2: (a) Bismuth polyhedra, which share an oxygen atom at their vertices, leading to rod-shaped SBUs. (b) Simplified net of **Bi(NTB)-MOF1** oriented along the *c*-axis, in which the linker molecules are represented as yellow triangles (see also Figure S7.9).

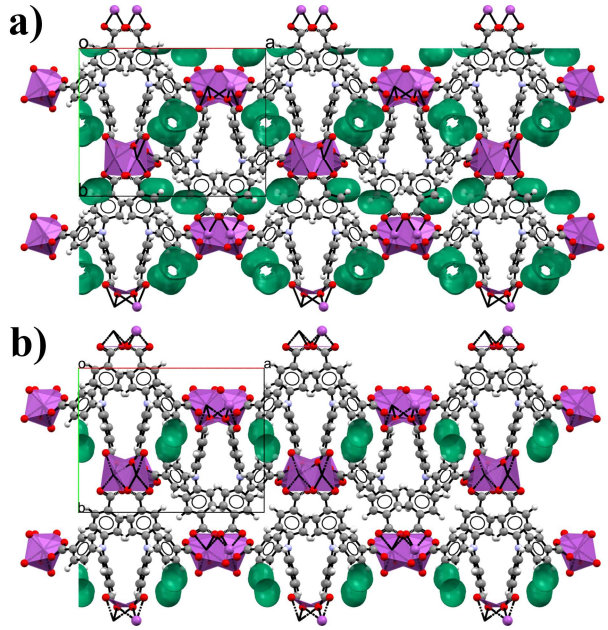

Figure 7.3: Comparison between the **Bi(NTB)-MOF1** structural model from 3D ED analysis (a) and from the Rietveld refinement of PXRD data (b). Both structures have been represented oriented along their crystallographic *c*-axis.

The PXRD profile calculated from the structural model solved by 3D ED was subsequently compared to the experimental PXRD data collected on the bulk (Figure 7.4a). While the comparison revealed some correspondence in the relative intensities of the diffraction peaks. However, the positions of the diffraction peaks in the calculated diffractogram were slightly shifted towards lower 2θ values compared to the experimental pattern. Rietveld refinement was then performed on the PXRD data to gain a better understanding of the overall structure of **Bi(NTB)-MOF1** at ambient conditions (Figure 7.4b). As expected, starting from the kinematically refined structure, the PXRD refinement revealed a reduction in the unit cell volume (Table 7.1) and consequently a contraction of the **Bi(NTB)-MOF1** framework (Figure 7.5). Thus, the structure obtained from the Rietveld refinement no longer displays channels along the *c*-axis. Instead, it exhibits isolated void regions that occupy 2.4% of the unit cell volume (43 $Å^3$, Figure 7.3b).

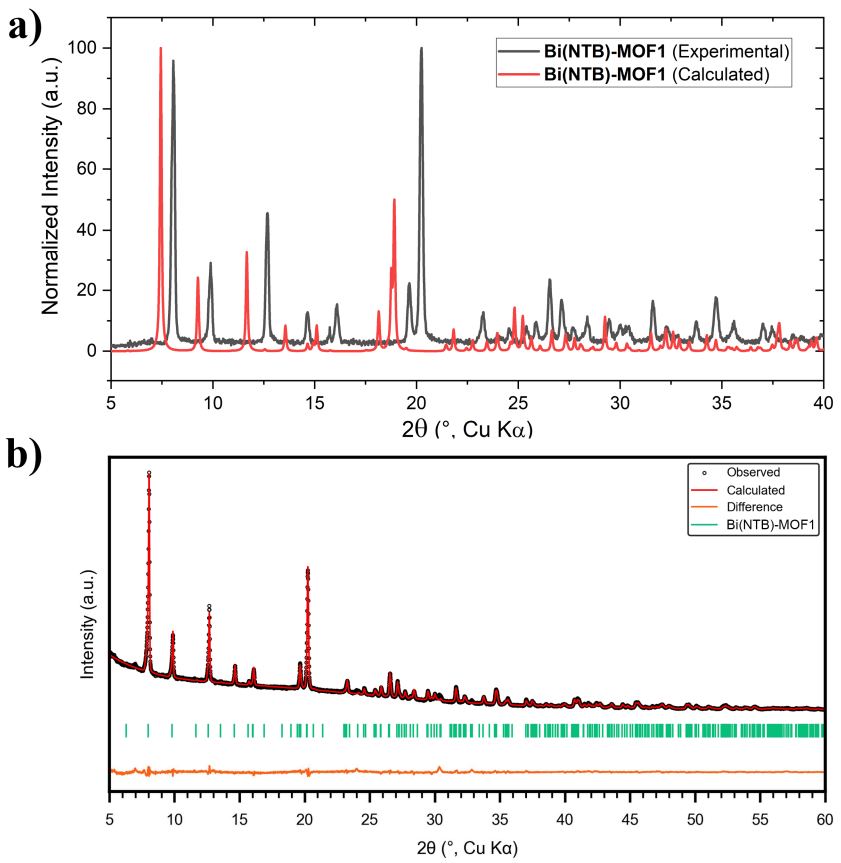

Figure 7.4: (a) PXRD profile comparison between the pattern calculated from the 3D ED model and the experimental one. The PXRD data collection was carried out using a variable slits measurement in a Bragg-Brentano geometry. (b) Profile fit form Rietveld refinement of **Bi(NTB)-MOF1**. The shown range is limited to 2θ values of 5-70° for clarity, whereas the refinement was carried out in the range 5-90°. The refinement converged to Rp = 2.72 % and wRp = 3.76 %.

These differences in structural parameters might be associated with various factors, such as the different temperature and pressure at which the analyses were carried out. Additionally, a more consistent factor could be a non-optimal calibration of the instrumental parameters of the TEM in which the 3D ED data collection was conducted. This phenomenon was also observed, although to a slightly different magnitude, in the following

structures, and therefore further studies will be required to identify its cause. Remarkably, this result demonstrates how these two crystallographic techniques can be combined to compensate for each other's weaknesses and obtain the structural model that better represents the analysed system.

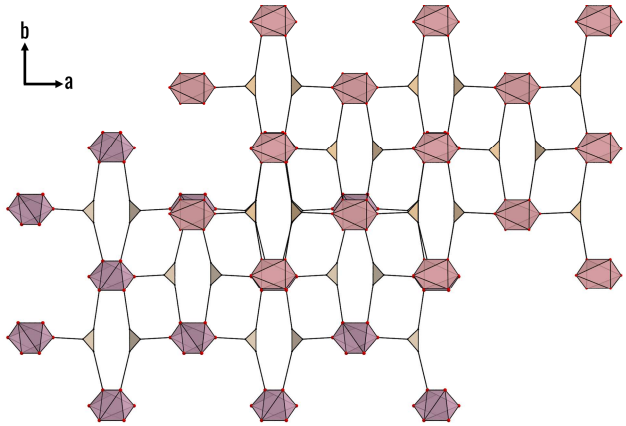

Figure 7.5: Comparison between the simplified net related to the **Bi(NTB)-MOF1** model obtained from 3D ED (*magenta*) and from the Rietveld refinement(*purple*).

Table 7.1: Comparison of the unit cell parameters obtained from 3D ED analysis and from the Rietveld refinement on PXRD data for the **Bi(NTB)-MOF1** structure.

	3D ED	**PXRD**
a (Å)	19.071(6)	18.0256(4)
b (Å)	15.159(4)	14.0138(2)
c (Å)	7.813(2)	7.35376(15)
α (°)	90	90
β (°)	90	90
γ (°)	90	90
Vol ($Å^3$)	2258.7(11)	1834.70(6)

As a further step in the development of this class of materials, the reaction conditions were adjusted to achieve a material with higher porosity and less densely packed then **Bi(NTB9)-MOF1**. Thus, a second material was isolated by performing the solvothermal synthesis with $Bi(NO_3)_3 \cdot 5H_2O$ and using

methanol as solvent (Scheme 7.4). After 20 minutes at 120°C, the reaction crude was washed with methanol and a crystalline powder was isolated. The powder diffraction pattern of the new product was differerent from the profile of **Bi(NTB)-MOF1**, suggesting the formation of a new crystalline phase (Figure 7.6).

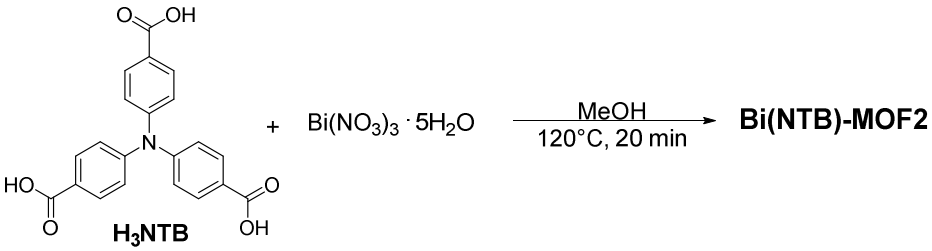

Scheme 7.4: Synthesis of **Bi(NTB)-MOF2**.

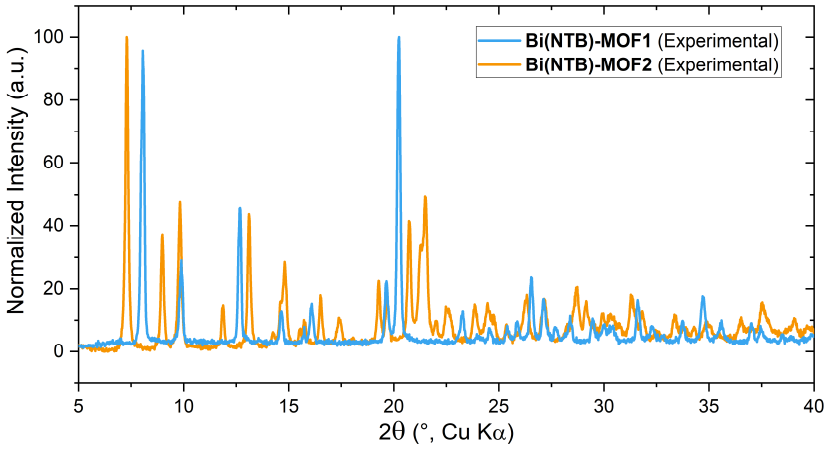

Figure 7.6: PXRD profile comparison between the experimental pattern of **Bi(NTB)-MOF1** and **Bi(NTB)-MOF2**.

The crystal structure of the product was determined through a 3D ED analysis carried out in the same conditions of the previous sample. Four different crystals were analysed and their diffraction data merged with the XDS package,[22] showing the presence of a monoclinic C-centred unit cell, with parameters: a = 26.570 Å, b = 8.330 Å, c = 10.720 Å, β = 106.15 Å. The indexed data were integrated, the crystal structure resolved *ab initio* in

the space group *C*2 and then kinematically refined. The resulting crystal structure is new and exhibits a polymeric network of general formula **{Bi(NTB)}$_n$** identified as **Bi(NTB)MOF-2** (Figure S7.8).

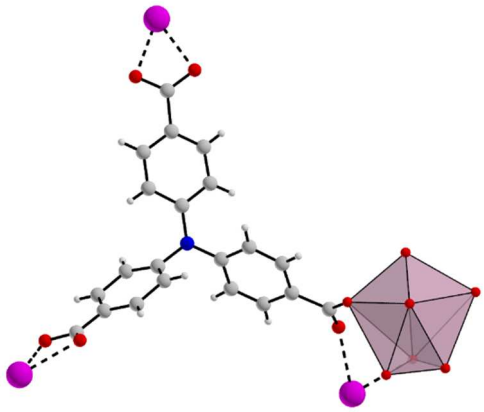

Figure 7.7: Repeating unit of **Bi(NTB)-MOF2.** Bismuth with its coordination environment is represented a magenta polyhedron, while the Bi^{3+} ions coordinating the other arms of the NTB molecule are depicted as magenta spheres connected through dashed bonds. Oxygen, nitrogen, carbon, and hydrogen atoms are reported as red, blue, grey, and white spheres, respectively.

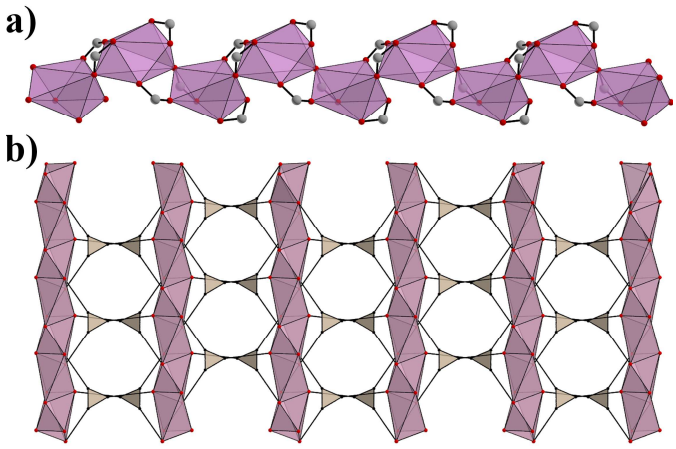

Figure 7.8: (a) Bismuth polyhedra, which share an oxygen atom at their vertices, leading to rod-shaped SBUs. (b) Simplified net of **Bi(NTB)-MOF2** oriented along the *c*-axis, in which the linker molecules are represented as yellow triangle and the bismuth SBUs as magenta rods.

The polymeric network of **Bi(NTB)-MOF2** is composed of fully deprotonated NTB^{3-} molecules coordinated to Bi^{3+} centres, in analogy to **Bi(NTB)-MOF1**. The NTB^{3-} linkers employ two of their benzoic arms as bidentate chelating ligands, while the remaining one acts as bidentate μ_2-bridging ligand (Figure 7.7). The bismuth centres have a coordination number of 7: one of the oxygens (O2B) involved in a chelation on a Bi^{3+} cation also interacts with a neighbouring metal centre. This yields to corrugated Bi-O rods running along the crystallographic *b*-axis, which are composed of bismuth polyhedra linked together by the presence of common vertices.

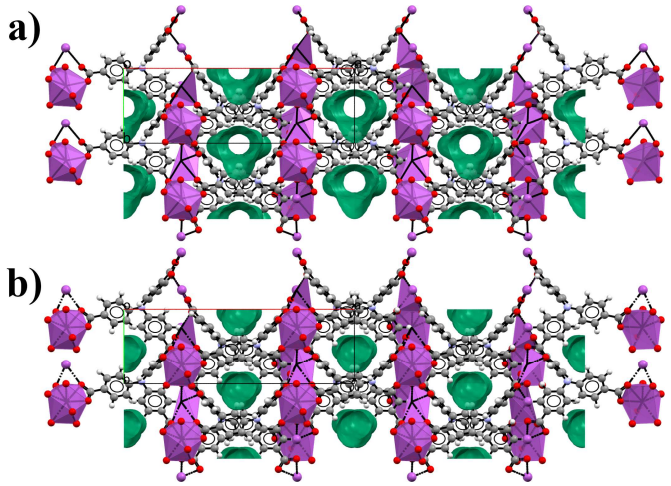

Figure 7.9: Comparison between the **Bi(NTB)-MOF2** structural model from 3D ED analysis (a) and from the Rietveld refinement of PXRD data (b). Both structures have been represented oriented along their crystallographic *c*-axis.

The structural model of **Bi(NTB)-MOF2** displays channels extending along the crystallographic *c*-axis, accounting for the 14% of the unit cell volume (319 $Å^3$, Figure 7.8a). However, from the kinematical refinement performed on the 3D ED data, it was not possible to detect any electron density associated with guest molecules. This result is in line with the removal of guest molecules induced by the high vacuum conditions in which the 3D ED analysis is carried out. In contrast to the structure of **Bi(NTB)-MOF1**,

the empty channel in this crystal structure are no longer parallel to the Bi-O rods. Indeed, a comparison of the structural models of both **Bi(NTB)-MOFs**, oriented along the direction of their Bi-O rods, reveals a difference in the arrangement of these 1D-SBUs (**Figure 7.10**).

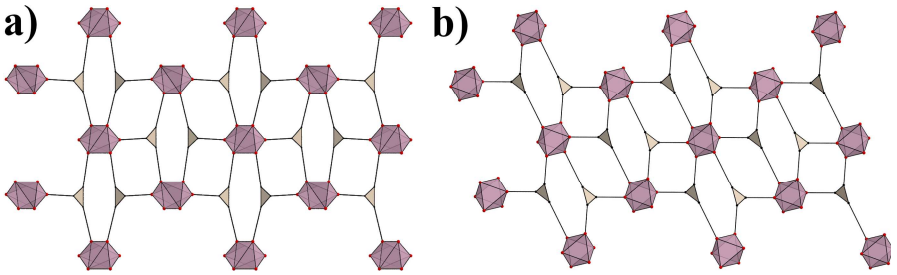

Figure 7.10: Simplified net of **Bi(NTB)-MOF1** (a) and **Bi(NTB)-MOF2** (b) oriented along their *b*-axis and *c*-axis, respectively.

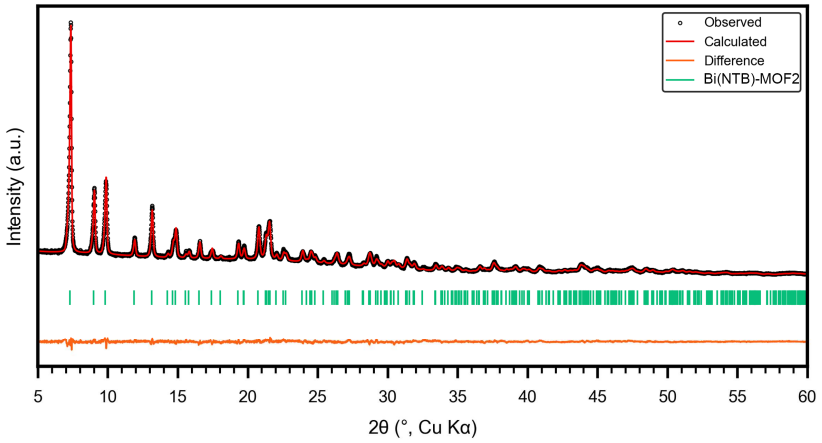

Figure 7.11: Profile fit form Rietveld refinement of **Bi(NTB)-MOF2**. The shown range is limited to 2θ values of 5-70° for clarity, whereas the refinement was carried out in the range 5-90°. The refinement converged to Rp = 3.13 % and wRp = 4.04 %.

The single-crystal structure from the 3D ED analysis was then refined against the PXRD data through the Rietveld approach. (Figure 7.11). The resulting structure is characterized by smaller unit cell parameters (Table 7.2), leading to a more densely packed structure (Figure 7.12). Moreover, the structure obtained from the Rietveld refinement no longer displays channels along the *c*-axis. Instead, it exhibits isolated void regions that occupy 8% of the unit cell volume (159 $Å^3$, Figure 7.9b).

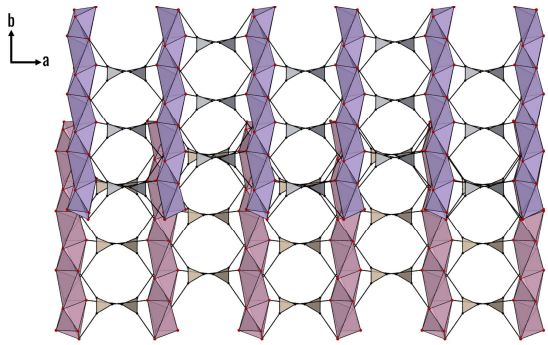

Figure 7.12: Comparison between the simplified net related to the **Bi(NTB)-MOF2** model obtained from 3D ED (*magenta*) and from the Rietveld refinement (*purple*).

Table 7.2: Comparison of the unit cell parameters obtained from the 3D ED analysis and from the Rietveld refinement on PXRD data for the **Bi(NTB)-MOF2** structure.

	3D ED	**PXRD**
a (Å)	26.570(5)	25.2503(7)
b (Å)	8.330(17)	7.8268(3)
c (Å)	10.720(2)	10.2588(2)
α (°)	90	90
β (°)	106.15(3)	106.655(2)
γ (°)	90	90
Vol ($Å^3$)	2279.1(9)	1942.38(10)

Similar to the previous material, **Bi(NTB)-MOF2** has a more densely packed structure under ambient conditions. However, this crystalline phase still exhibits more pronounced void regions compared to **Bi(NTB)-MOF1**, which demonstrates the success of the strategy to synthesise a less densely packed crystal structure.

The simplified net for both MOFs was obtained by identifying their points of contact between organic and inorganic parts, through the point of extension method proposed by Schoedel et.al.[24] The ideal symmetry of their underlying net was determined and a topological analysis was conducted on both networks (calculations performed using Systre and ToposPro software), highlighting the presence of the same 3.3.7.7-c net (**Figure 7.13**). [25,26]

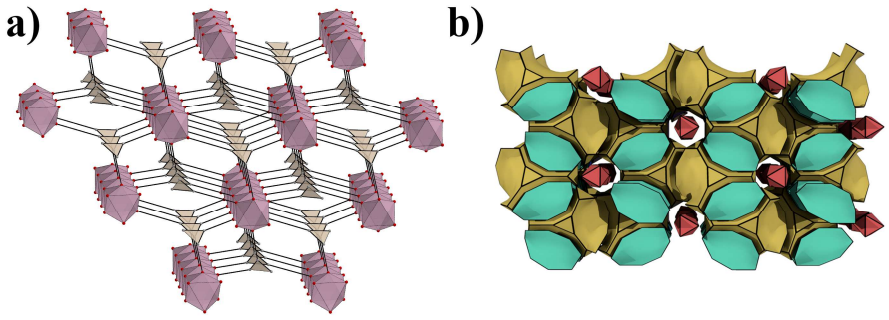

Figure 7.13: (a) Simplified net of both **Bi(NTB)-MOFs**, obtained after the analysis conducted through the Systre software. (b) Visualization of the net's tiling calculated using the 3dt software. [27]

Gas sorption measurements were conducted on both **Bi(NTB)-MOFs**, in collaboration with Prof. Ocean Cheung from Uppsala University. In both cases, the nitrogen adsorption isotherms do not show the presence of an initial Langmuir-like adsorption region (Figure S7.16). These results reflect the presence of micropores which are too narrow to allow the passage of nitrogen, which is in line with their small pore diameter (Table 7.3). However, the gas sorption experiment conducted at 293K revealed that **Bi(NTB)-MOF2** show some porosity towards CO_2 when compared to **Bi(NTB)-MOF1** (Figure 7.14). This confirms the presence of very narrow pores as CO_2 has a lower kinetic diameter than N_2.

Table 7.3: Pore sizes calculated on the **Bi(NTB)-MOFs** crystal structures. PLD = Pore Limiting Diameter, LCD = Largest Cavity Diameter.

	Bi(NTB)-MOF1		**Bi(NTB)-MOF2**	
	3D ED	*PXRD*	*3D ED*	*PXRD*
PLD (Å)	2.04	1.77	2.37	1.76
LCD (Å)	2.89	2.50	3.87	3.15

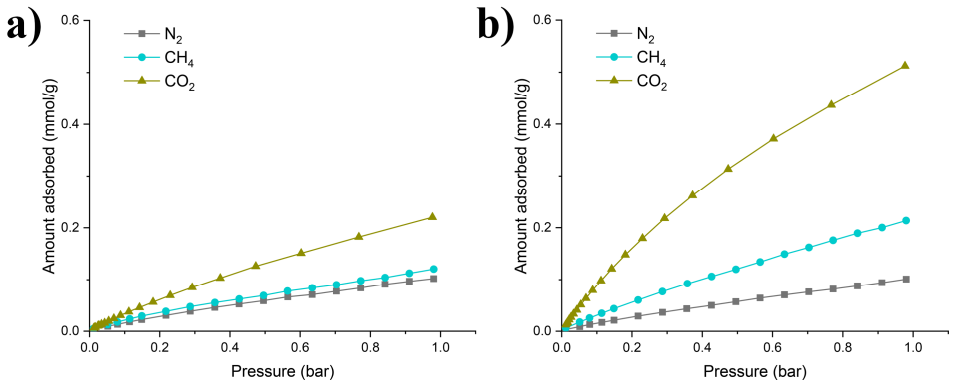

Figure 7.14: N_2, CH_4 and CO_2 gas sorption isotherms at 293 K for **Bi(NTB)-MOF1** (a) and **Bi(NTB)-MOF2** (b).

Furthermore, a CO_2 adsorption isotherm was performed to obtain information on the porosity of this material. The analysis indicated a Langmuir-like uptake of CO_2 in the microporous region of the isotherm (Figure 7.15). The pore size obtained from this experiment stands around 0.375 nm, which is in line with the predicted values (Table 7.3, Figure S7.17). However, the calculated SSA value of 7.0 $m^2 \cdot g^{-1}$, determined using a CO_2-sized probe, is in contrast with the experimental value of 80 m2·g-1. This unexpected increase in the experimental SSA value can be correlated with the presence of interactions between the framework and CO_2, attributable to a dynamic behaviour of the material in such conditions.

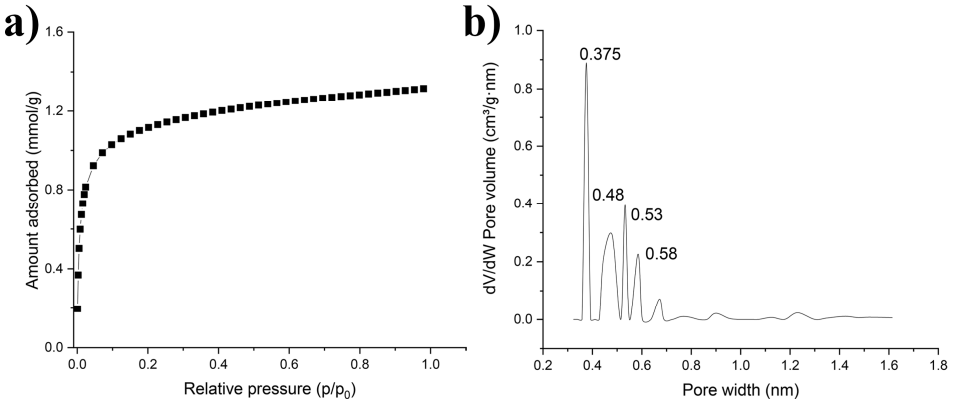

Figure 7.15: CO_2 adsorption isotherm of **Bi(NTB)-MOF2** recorded at 195K (a), and its relative pore size distribution.

7.3 Synthesis and characterization of novel Bismuth Protocatechuate-based reticular materials

Two isoreticular coordination polymers were obtained from the reaction between protocatechuic acid (**H_3PC**) with $Bi(NO_3)_3{\cdot}5H_2O$ in protic solvents such as H_2O or MeOH. The first synthesis was carried out in water at 120°C for 15 minutes under stirring (Scheme 7.5), resulting in a crystalline powder that exhibited the characteristic pattern of a 2D coordination polymer previously identified by the research group (Figure S7.3).

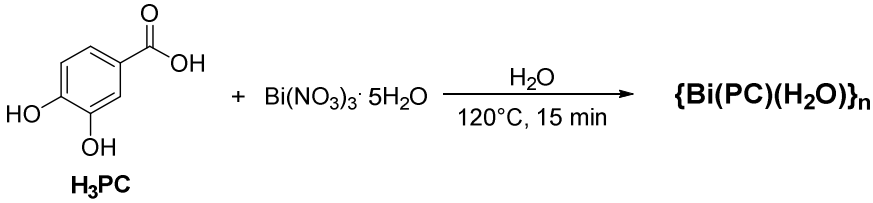

Scheme 7.5: Synthesis of **$\{Bi(PDC)(H_2O)\}_n$**.

The crystal structure was further confirmed using the 3D ED analysis in cRED mode. Subsequently, a kinematical refinement was conducted to improve the structural model and confirm the presence of a polymeric network of general formula **$\{Bi(PDC)(H_2O)\}_n$** (Figure S7.10, Figure 7.16a). This new 2D coordination polymer consists in a network of fully deprotonated PC^{3-} linkers connected to Bi^{3+} centres. The asymmetry unit comprises a PC^{3-} molecule which employs both its carboxylate and catecholate functions to perform a bidentate chelation on two different bismuth cations. The oxygen O3 also acts as a bridging ligand giving rise to a SBU composed of bi-nuclear Bi-O clusters (Figure 7.16b)

The second 2D coordination polymer was then synthesized following the previously described synthetic procedure, but using methanol (MeOH) instead of water as solvent media. The crude product was initially characterized by PXRD analysis, revealing the presence of a crystalline product with a diffraction patter different from the powder diffraction profile of **$\{Bi(PDC)(H_2O)\}_n$** (Figure S7.4). The crystal structure of the obtained

nanocrystalline powder was determined by a 3D ED analysis conducted on eight different crystals. The collected electron diffraction data were indexed individually for each crystal and then merged together through the XSD package. [22] The reciprocal space reconstruction revealed the presence of a monoclinic $P2_1/n$ space group with unit cell parameters in line with those observed in the crystal structure of **{Bi(PDC)(H$_2$O)}$_n$** (Table 7.4). A structural model was then obtained from the integrated reflection data through *ab initio* methods. The resulting kinematically-refined crystal structure consists of a 2D coordination polymer that is isoreticular to the previous one, with formula **{Bi(PDC)(MeOH)}$_n$** (Figure 7.17, Figure S7.11).

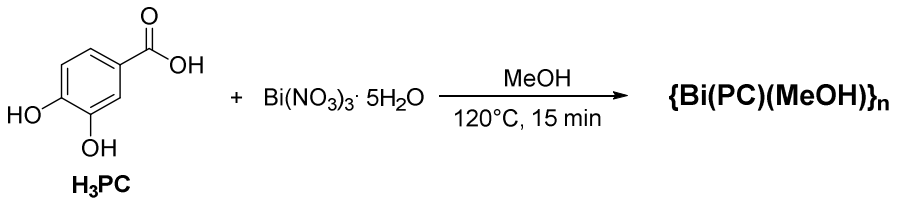

Scheme 7.6: Synthesis of **{Bi(PDC)(MeOH)}$_n$**.

Table 7.4: Comparison of the unit cell parameters for the structures of **{Bi(PC)(H$_2$O)}$_n$** and **{Bi(PC)MeOH}$_n$**.

	{Bi(PC)(H$_2$O)}$_n$	**{Bi(PC)MeOH}$_n$**
a (Å)	9.3751(13)	8.950(5)
b (Å)	9.3487(14)	9.399(5)
c (Å)	9.513(2)	9.685(4)
α (°)	90	90
β (°)	102.899(16)	100.26(4)
γ (°)	90	90
Vol (Å^3)	812.7(2)	801.7(7)

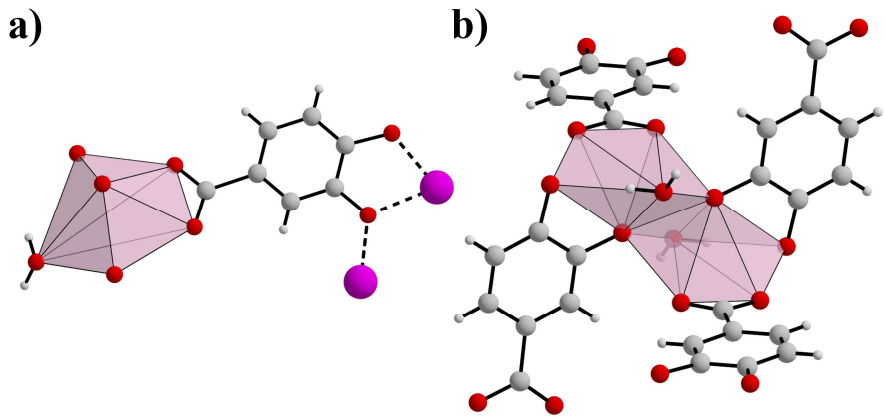

Figure 7.16: (a) Repeating unit of **{Bi(PDC)(H$_2$O)}$_n$** with the bismuth atom surrounded by its coordination sphere highlighted as a magenta polyhedron. Coordination to adjacent cations is shown as dashed bonds. (b) Representation of a bi-nuclear cluster of bismuth. Oxygen, nitrogen, carbon, and hydrogen atoms are reported as red, blue, grey, and white spheres, respectively.

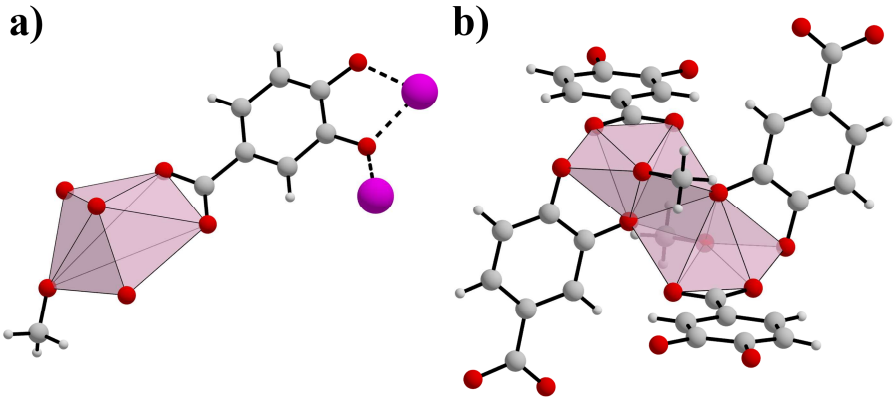

Figure 7.17: (a) Repeating unit of **{Bi(PDC)(MeOH)}$_n$** with the bismuth atom surrounded by its coordination sphere highlighted as a magenta polyhedron. Coordination to adjacent cations is shown as dashed bonds (b) Representation of a bi-nuclear cluster of bismuth. Oxygen, carbon, and hydrogen atoms are reported as red, grey, and white spheres, respectively.

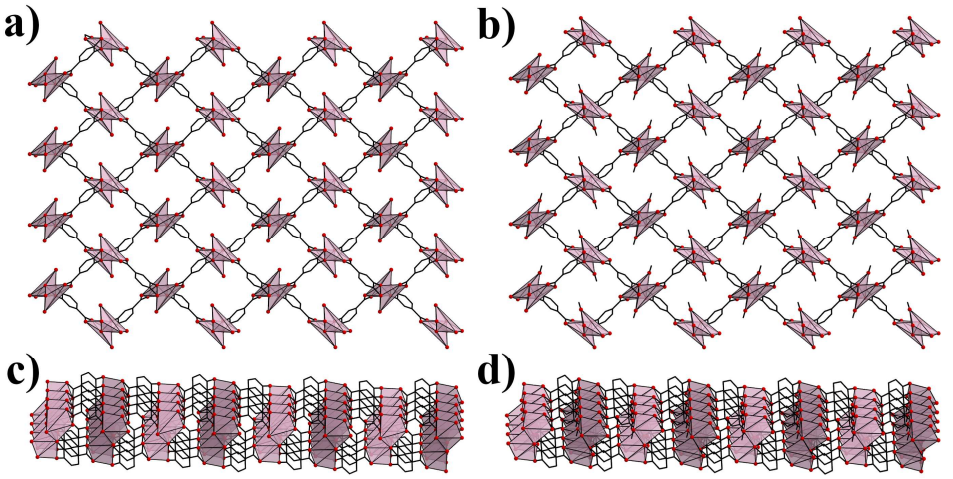

Figure 7.18: Expansions of the 2D polymeric structure of **{Bi(PDC)(H_2O)}$_n$** (a,c) and **{Bi(PDC)(MeOH)}$_n$** (b,d) coordination polymers visualized along their (101) and ($1\bar{1}01$) directions, respectively. Bismuth atoms are represented as magenta polyhedrons, while oxygens are reported as red spheres. Carbon atoms are depicted as black sticks.

The new bismuth-based coordination polymers (CPs) are consisting of sheets disposed along their crystallographic (202) planes (Figure 7.18). Interestingly, in both CPs, these metal-organic layers stacked together through unusual inter-layer Bi···π interactions, leading to a densely packed structure (Figure S7.15). The observed Bi···π contacts involve the aryl groups of the PC^{3-} likers oriented at ~80° towards bismuths centres located at almost 3.3 Å from the centroid (C_g) of the phenyl ring C2-C7. The phenyl rings act as a η^6-ligands, rising the coordination number of bismuth from 7 to 13 (Figure 7.19). Interestingly, a search in the CSD considering the Bi···Cg distance alone, revealed only another similar bismuth··· π contact (Figure S7.14). [28] This prompted us to carry out a further investigation, this time also taking into account the orientation of the fragments involved. Two geometrical parameters were introduced to assess the orientation: i) the C2-Cg-Bi angle and ii) the angle between the mean planes of the phenyl ring and of the Bi complex surface (calculated considering Bi and three of the neighbouring

atoms directly bound to it, see Figure S7.13). The new search in the crystallographic database (Figure 7.20) clearly showed the deviation of the geometrical parameters relative to the new 2D CPs from the values displayed by related systems in other crystal structures.

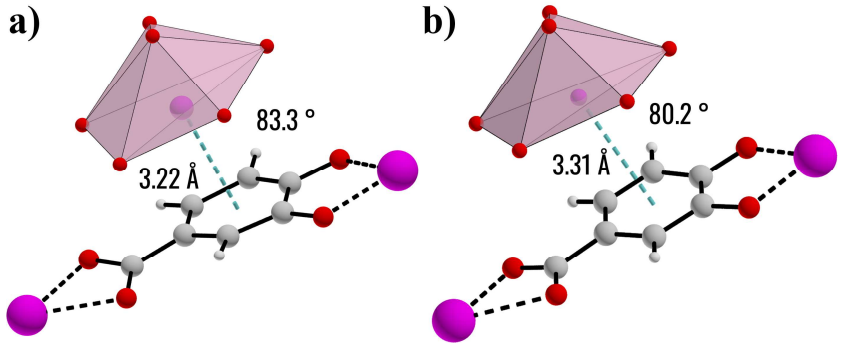

Figure 7.19: Representation of the inter-layer Bi···π contacts in **{Bi(PDC)H$_2$O}$_n$** (a) and **{Bi(PDC)MeOH}$_n$** (b). The centroids C_g of both rings (C2-C7) was defined and the Bi···C_g distance was represented as a turquoise dashed line. The displayed angular value is related to C2-C_g-Bi.

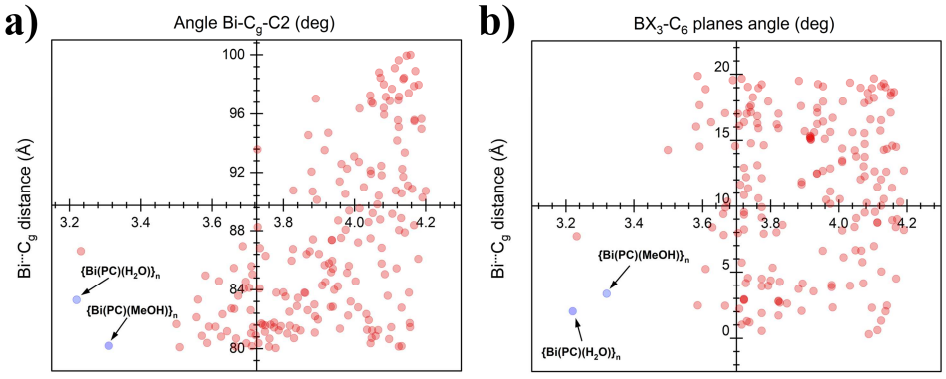

Figure 7.20: Plots of the angular values searched in the CSD. The values relative to **{Bi(PDC)(H$_2$O)}$_n$** and **{Bi(PDC)(MeOH)}$_n$** are shown in blue.

A further synthesis was then carried out with the aim of obtaining a three-dimensional organometallic network comprising Bi^{3+} centres and PC^{3-} linkers. A mixture of MeOH/m-DCB (1:1) was employed as solvent media, while the other reaction parameters were set as in the previously reported synthesis (Scheme 7.7). 1,3-dichlorobenzene (m-DCB) was introduced into the reaction environment with the purpose of attenuating the formation of Bi···π interactions, responsible for the formation of the previously described 2D coordination polymers.

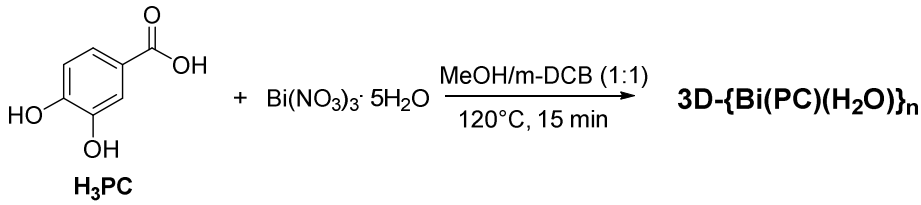

Scheme 7.7: Synthesis of **3D-{Bi(PDC)(H$_2$O)}$_n$**.

These new reaction conditions yielded a novel crystalline phase, which was confirmed by PXRD analysis (Figure S7.6). The microcrystals thus obtained were analysed through 3D ED. The electron diffraction characterization was carried out on three different crystals and their diffraction data merged together to improve the completeness of the data. The indexing process revealed the presence of the monoclinic space group $P2_1/c$, with lattice parameters of $a = 6.2114(7)$ Å, $b = 7.9615(17)$ Å, $c = 14.6898(17)$ Å, and $\beta = 98.775(9)$ °, in contrast to the previously described structures. The crystal structure solved *ab initio* and kinematically refined, revealed the formation of a novel Bi-PC coordination polymer (Figure 7.21).

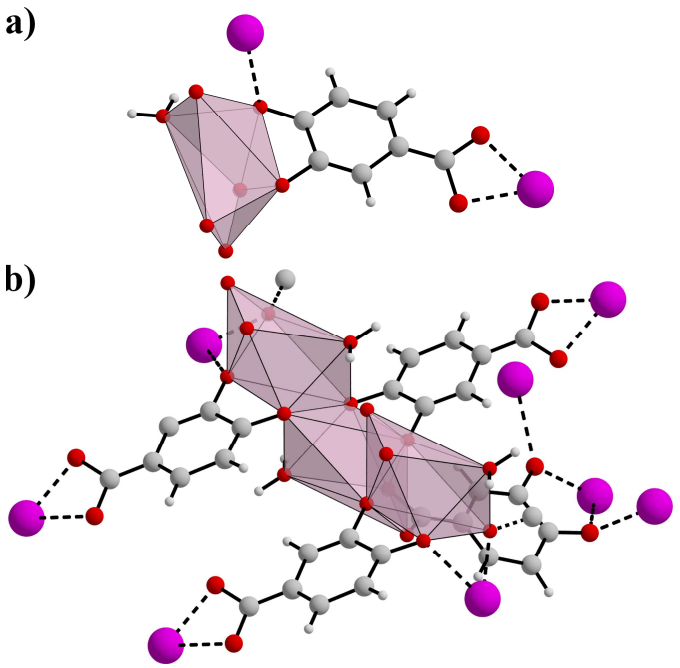

Figure 7.21: Repeating unit of **3D-{Bi(PDC)(H₂O)}ₙ** with the bismuth atom surrounded by its coordination sphere represented as a magenta polyhedron and coordination to adjacent cations shown as dashed bonds. (b) Representation of a Bi-O rod portion. Oxygen, nitrogen, carbon, and hydrogen atoms are reported as red, grey, and white spheres, respectively.

The resulting structural model consists of **{Bi(PDC)(H₂O)}** units connected to each other in a densely packed 3D network (Figure 7.22a). The presence of water molecules may be related to the use of non-dry solvents. The **3D-{Bi(PDC)(H₂O)}ₙ** coordination polymer exhibits Bi^{3+} centres linked by fully deprotonated PC^{3-} ligands. In contrast to the **{Bi(PDC)(H₂O)}ₙ** and **{Bi(PDC)(MeOH)}ₙ** 2D-CPs, this structure displays rod-like SUBs oriented along the crystallographic *a*-axis, in which the bismuth polyhedra share two of their edges (Figure 7.22b). Interestingly, as a result of the introduction of m-DCM into the reaction environment, this new 3D-CP no longer displays the characteristic Bi···π contacts observed in the Bi-PC 2D coordination polymers.

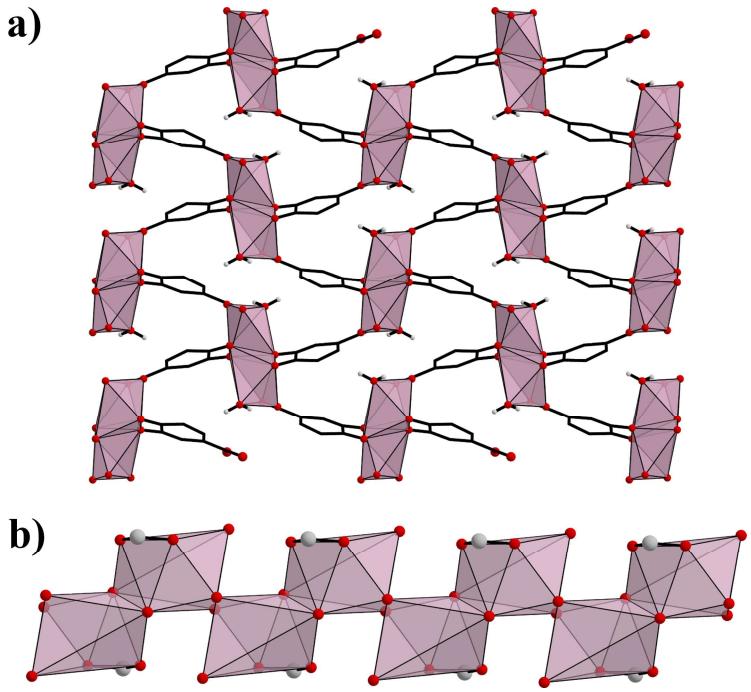

Figure 7.22: (a) Expansions of the **3D-{Bi(PDC)(H$_2$O)}$_n$** structure visualized along its crystallographic *a*-axis. (b) Visualization of a Bi-O rod in which the bismuth polyhedra share their edges, leading to a mono-dimensional SBU. Bismuth atoms are represented as magenta polyhedra, while oxygens are reported as red spheres.

7.4 Conclusions

In the first part of this chapter, two different Bi-NTB MOFs were synthesized and their structure elucidated by combining 3D ED analysis and Rietveld refinement on PXRD data. In both cases, the resulting network exhibited the same topology. Gas sorption measurements were carried out, highlighting an increase in affinity towards the adsorption of CO_2 for **Bi(NTB)MOF2**.

The second part was focused on the synthesis of reticular materials based on bismuth and protocatechuic acid, with the aim to isolate a new metal-organic framework. Two isoreticular 2D coordination polymers were obtained, both exhibiting an uncommon Bi···π interaction. It was also possible to observe how the formation of this contact can be hindered by modifying the reaction parameters to obtain a new 3D coordination polymer based on bismuth and PC^{3-} linkers.

7.5 Supplementary Information

7.5.1 Synthetic Procedures

Bi(NTB)-MOF1 Synthesis

H_3NTB (20.5 mg, 0.0543 mmol), bismuth oxide (12.2 mg, 0.0262 mmol), and 3 mL of a 10% v/v acetic acid solution were added to a 5 mL borosilicate glass tube. The reaction vessel was then sealed though a PTFE screw cap. The tube was then disposed into a pre-heated Al block at 140°. The reaction was left under magnetic stirring (PTFE-coated stir bar) at 140°C for 2 hours. The tube was then removed from the Al block and left to cool down to room temperature. The obtained yellow solid was then removed from the reaction crude through centrifugation. The product was initially washed with acetic acid (20% v/v) and then with methanol. It was left to dry under atmospheric conditions to give a pale-yellow powder. (24.1 mg, yield = 69.0 %) The product was then characterized through PXRD and 3D ED analysis.

Bi(NTB)-MOF2 Synthesis

H_3NTB (40.1 mg, 0.106 mmol), bismuth nitrate pentahydrate (26.3 mg, 0.0542 mmol), and 3 mL of methanol were added to a 5 mL borosilicate glass tube. The reaction vessel was then sealed though a PTFE screw cap. The tube was then disposed into a pre-heated Al block at 120°. The reaction was left under magnetic stirring (PTFE-coated stir bar) at 120°C for 15 minutes. The tube was then removed from the Al block and left to cool down to room temperature. The yellow solid thus obtained was then removed from the reaction crude through centrifugation, washed with methanol and left to dry under ambient condition overnight. (14.2 mg, yield = 22.4 %) The product was then characterized through PXRD and 3D ED analysis.

$\{Bi(PC)H_2O\}_n$ Synthesis

H_3PC (20.9 mg, 0.136 mmol), bismuth nitrate pentahydrate (30.8 mg, 0.0635 mmol), and 3 mL of water were added to a 5 mL borosilicate glass tube. The reaction vessel was then sealed though a PTFE screw cap. The tube was then placed into a pre-heated Al block at 120°. The reaction was left under magnetic stirring (PTFE-coated stir bar) at 120°C for 15 minutes. The tube was then removed from the Al block and left to cool down to room temperature. The obtained pale-yellow solid was then removed from the reaction crude through centrifugation, washed with acetone and left to dry under ambient condition overnight. (6.8 mg, yield = 28 %) The product was then characterized through PXRD and 3D ED analysis.

$\{Bi(PC)MeOH\}_n$ Synthesis

H_3PC (19.7 mg, 0.128 mmol), bismuth nitrate pentahydrate (31.6 mg, 0.0651 mmol), and 3 mL of methanol were added to a 5 mL borosilicate glass tube. The reaction vessel was then sealed though a PTFE screw cap. The tube was then disposed into a pre-heated Al block at 120°. The reaction was left under magnetic stirring (PTFE-coated stir bar) at 120°C for 15 minutes. The tube was then removed from the Al block and left to cool down to room temperature. The obtained yellow solid was then removed from the reaction crude through centrifugation, washed with acetone and left to dry under ambient condition overnight. (8.1 mg, yield = 33 %) The product was then characterized through PXRD and 3D ED analysis.

3D-{Bi(PC)H_2O}$_n$ Synthesis

H_3PC (20.0 mg, 0.128 mmol), bismuth nitrate pentahydrate (31.1 mg, 0.0641 mmol), and 3 mL of a MeOH/m-DCB (1:1) solution were added to a 5 mL borosilicate glass tube. The reaction vessel was then sealed though a PTFE screw cap. The tube was then disposed into a pre-heated Al block at 120°. The reaction was left under magnetic stirring (PTFE-coated stir bar) at 120°C for 15 minutes. The tube was then removed from the Al block and left to cool down to room temperature. The yellow solid thus obtained was then removed from the reaction crude through centrifugation, washed with acetone and left to dry under ambient condition overnight. (11.3 mg, yield = 46.5 %) The product was then characterized through PXRD and 3D ED analysis.

7.5.2 Structural Characterization

Powder X-ray Diffraction (PXRD)

The powder X-ray diffraction data used for Rietveld refinement analysis were collected in a 0.5 mm borosilicate glass capillary, using Cu Kα radiation ($\lambda_{K\alpha1}$ = 1.5406 Å, $\lambda_{K\alpha2}$ = 1.5444 Å) on a Bruker D8 Advance equipped with a Göbel Mirror and a Lynxeye XE-T detector. The Rietveld refinement on powder X-ray diffraction data was conducted with TOPAS-Academic V6.[29]

The PXRD patterns of the remaining samples were collected in Bragg-Brentano geometry, using a Ni-filtered Cu radiation ($\lambda_{K\alpha1}$ = 1.5406 Å, $\lambda_{K\alpha2}$ = 1.5444 Å), on Panalytical X'pert Pro diffractometer. The PXRD data ware acquired loading the sample onto zero-background silicon plates.

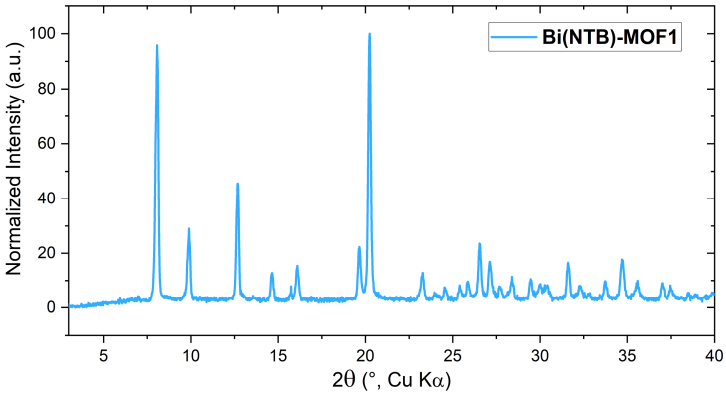

Figure S7.1: PXRD profile of the as-synthesized **Bi(NTB)-MOF1**.

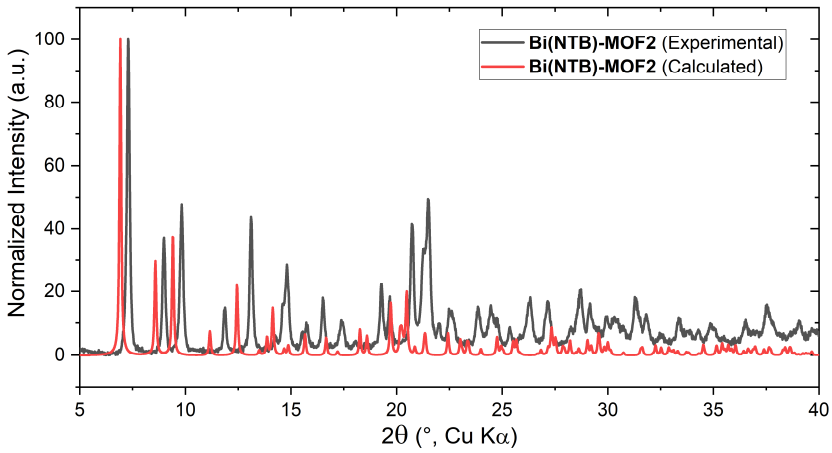

Figure S7.2 Comparison of the PXRD profile between the calculated (from the 3D ED model) and the experimental pattern for **Bi(NTB)-MOF2**. The PXRD data collection was carried out using a variable slits measurement in a Bragg-Brentano geometry.

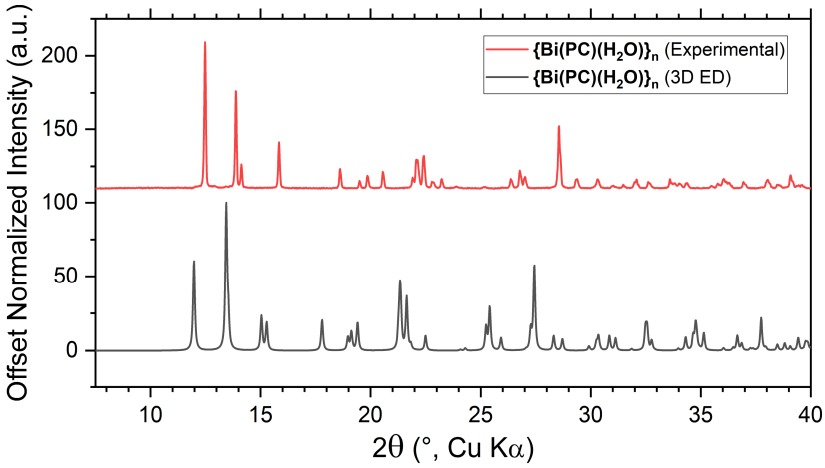

Figure S7.3: Comparison of the PXRD profile between the calculated (from the 3D ED model) and the experimental pattern for **{Bi(PC)(H$_2$O)}$_n$**. The PXRD data collection was carried out using a variable slits measurement in a Bragg-Brentano geometry.

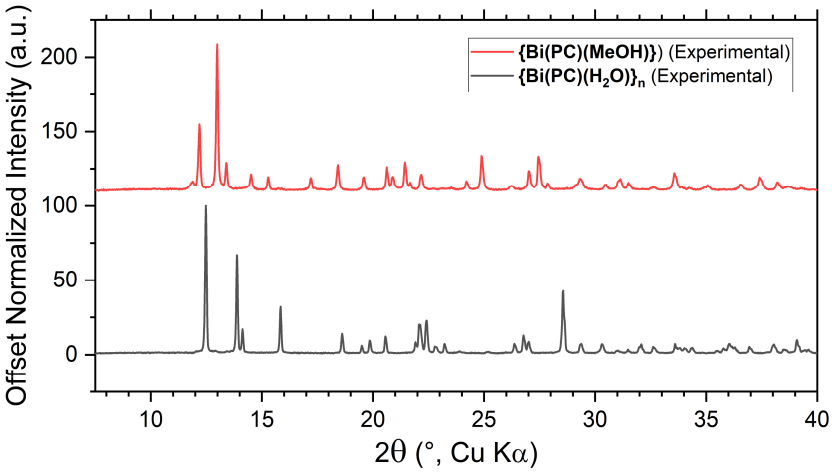

Figure S7.4: Comparison of the PXRD profile between the experimental patterns of **{Bi(PC)(MeOH)}$_n$** and **{Bi(PC)(H$_2$O)}$_n$**. The PXRD data collection was carried out using a variable slits measurement in a Bragg-Brentano geometry.

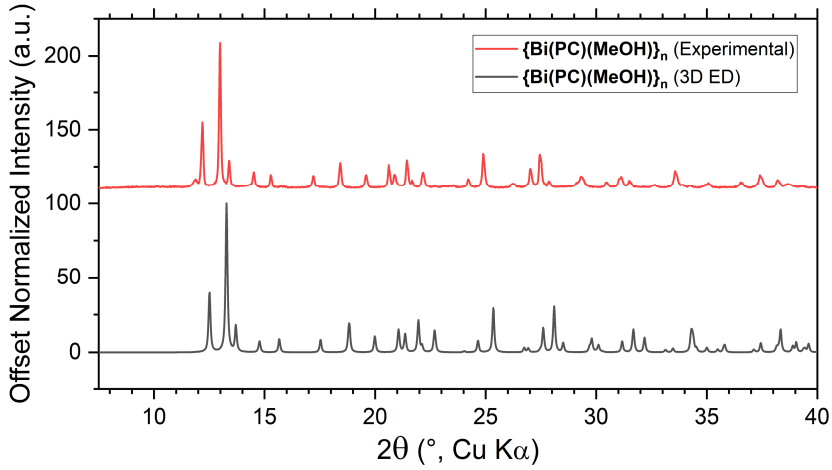

Figure S7.5: Comparison of the PXRD profile between the calculated (from the 3D ED model) and the experimental pattern for **{Bi(PC)(MeOH)}$_n$**. The PXRD data collection was carried out using a variable slits measurement in a Bragg-Brentano geometry.

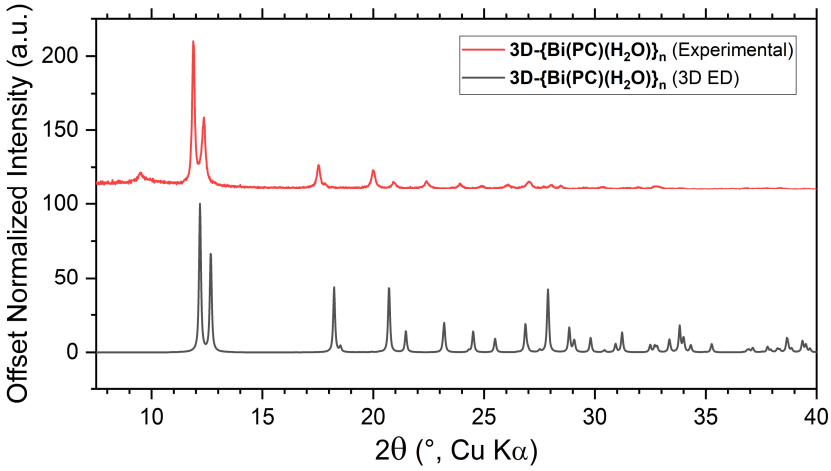

Figure S7.6: Comparison of the PXRD profile between the calculated (from the 3D ED model) and the experimental pattern for the 3D coordination polymer **{Bi(PC)(H₂O)}ₙ**. The PXRD data collection was carried out using a variable slits measurement in a Bragg-Brentano geometry.

3D Electron Diffraction (3D ED) and TEM analysis

3D electron diffraction analysis was carried out on a Zeiss Libra 120 transmission electron microscope, equipped with a LaB_6 thermionic source operating at 200 kV (λ=0.0251 Å) and a Timepix single-electron detector by ASI for collecting diffraction patterns in low dose mode. 3D electron diffraction data were collected on single nanocrystals in SAED mode through a cRED protocol with a rotation speed of 0.45 deg·s^{-1}. The data collection was performed by controlling the TEM using the Instamatic software.[21] The 3D ED data were analysed using the XRD software. Ab-initio structure determinations were performed with the ShelXT package.[30] Data were refined with a fully kinematical approximation, i.e. neglecting dynamical scattering and assuming that I_{hkl} is proportional to $|F_{hkl}|^2$. Least-squares structure refinement was performed with the software SHELXL-2014 [32] interfaced with Olex2 [33].

Table S7.1: Crystallographic information for **Bi(NTB)-MOF1**

Empirical formula	$C_{21}H_{12}BiNO_6$
Formula weight	583.31
Temperature/K	100(2)
Crystal system	orthorhombic
Space group	*Pca*2$_1$
a/Å	19.070
b/Å	15.160
c/Å	7.810
α/°	90
β/°	90
γ/°	90
Volume/Å^3	2257.9
Z	4
ρ_{calc}g/cm^3	1.033
F(000)	276
Radiation	Electrons (λ = 0.02508 Å)
2ϑ range for data collection/°	0.094 to 1.61
Index ranges	-20 ≤ h ≤ 20, -16 ≤ k ≤ 16, -8 ≤ l ≤ 8
Reflections collected	18828
Independent reflections	3239 [R_{int} = 0.2939, R_{sigma} = 0.2158]
Data/restraints/parameters	3239/31/117
Goodness-of-fit on F^2	1.127
Final R indexes [I>=2σ (I)] [a]	R_1 = 0.1536, wR_2 = 0.3626
Final R indexes [all data] [a]	R_1 = 0.1672, wR_2 = 0.3773

[a] $R_1 = \Sigma \| F_o | - | F_c \| / \Sigma | F_o |$, $wR_2 = [\Sigma[w(F_o^2-F_c^2)^2]/\Sigma[w(F_o^2)^2]]^{1/2}$

Table S7.2: Crystallographic information for **Bi(NTB)-MOF2**

Empirical formula	$C_{21}H_{12}BiNO_6$
Formula weight	583.31
Temperature/K	100(2)
Crystal system	monoclinic
Space group	*C*2
a/Å	26.570(5)
b/Å	8.3300(17)
c/Å	10.720(2)
α/°	90
β/°	106.15(3)
γ/°	90
Volume/Å^3	2279.1(9)
Z	4
ρ_{calc}g/cm^3	1.023
F(000)	276
Radiation	Electrons (λ = 0.02508 Å)
2ϑ range for data collection/°	0.112 to 1.62
Index ranges	-29 ≤ h ≤ 28, -9 ≤ k ≤ 9, -12 ≤ l ≤ 12
Reflections collected	19179
Independent reflections	3303 [R_{int} = 0.2604, R_{sigma} = 0.2146]
Data/restraints/parameters	3303/196/263
Goodness-of-fit on F^2	1.305
Final R indexes [I>=2σ (I)] [a]	R_1 = 0.1481, wR_2 = 0.3760
Final R indexes [all data] [a]	R_1 = 0.1638, wR_2 = 0.3934

[a] $R_1 = \Sigma \| F_o | - | F_c \| / \Sigma | F_o |$, $wR_2 = [\Sigma[w(F_o^2-F_c^2)^2]/\Sigma[w(F_o^2)^2]]^{1/2}$

Table S7.3: Crystallographic information for **{Bi(PC)(H$_2$O)}$_n$**

Empirical formula	$C_7H_5BiO_5$
Formula weight	378.9
Temperature/K	100(2)
Crystal system	Monoclinic
Space group	$P2_1/n$
a/Å	9.3751(13)
b/Å	9.3487(14)
c/Å	9.513(2)
α/°	90
β/°	102.899(16)
γ/°	90
Volume/Å^3	812.7(2)
Z	4
ρ_{calc}g/cm^3	1.864
F(000)	170
Radiation	Electrons (λ = 0.02508 Å)
2ϑ range for data collection/°	0.194 to 2.02
Index ranges	-13 ≤ h ≤ 13, -12 ≤ k ≤ 12, -11 ≤ l ≤ 12
Reflections collected	3665
Independent reflections	1579 [R_{int} = 0.1649, R_{sigma} = 0.1983]
Data/restraints/parameters	1579/11/43
Goodness-of-fit on F^2	1.179
Final R indexes [I>=2σ (I)] [a]	R_1 = 0.2216, wR_2 = 0.4726
Final R indexes [all data] [a]	R_1 = 0.2455, wR_2 = 0.4919

[a] $R_1 = \Sigma \| F_o | - | F_c \| / \Sigma | F_o |$, $wR_2 = [\Sigma[w(F_o^2-F_c^2)^2]/\Sigma[w(F_o^2)^2]]^{1/2}$

Table S7.4: Crystallographic information for **{Bi(PC)(MeOH)}$_n$**

Empirical formula	$C_8H_6BiO_5$
Formula weight	391.10
Temperature/K	100(2)
Crystal system	Monoclinic
Space group	$P2_1/n$
a/Å	8.950(5)
b/Å	9.399(5)
c/Å	9.685(4)
α/°	90
β/°	100.26(4)
γ/°	90
Volume/Å^3	801.7(7)
Z	4
ρ_{calc}g/cm^3	1.924
F(000)	177
Radiation	Electrons (λ = 0.02508 Å)
2ϑ range for data collection/°	0.204 to 2.052
Index ranges	$-12 \leq h \leq 11$, $-13 \leq k \leq 13$, $-13 \leq l \leq 13$
Reflections collected	15621
Independent reflections	2160 [R_{int} = 0.3712, R_{sigma} = 0.2128]
Data/restraints/parameters	2160/8/59
Goodness-of-fit on F^2	1.192
Final R indexes [I>=2σ (I)] [a]	R_1 = 0.1994, wR_2 = 0.4639
Final R indexes [all data] [a]	R_1 = 0.2323, wR_2 = 0.4893

[a] $R_1 = \Sigma \| F_o | - | F_c \| / \Sigma | F_o |$, $wR_2 = [\Sigma[w(F_o^2-F_c^2)^2]/\Sigma[w(F_o^2)^2]]^{1/2}$

Table S7.5: Crystallographic information for **3D-{Bi(PC)(H_2O)}$_n$**

Empirical formula	$C_8H_6BiO_5$
Formula weight	378.9
Temperature/K	100(2)
Crystal system	Monoclinic
Space group	$P2_1/c$
a/Å	6.2114(7)
b/Å	7.9615(17)
c/Å	14.6898(17)
α/°	90
β/°	98.775(9)
γ/°	90
Volume/Å^3	717.94(19)
Z	4
ρ_{calc}g/cm^3	2.111
F(000)	170
Radiation	Electrons (λ = 0.02508 Å)
2ϑ range for data collection/°	0.198 to 2.156
Index ranges	$-9 \leq h \leq 9$, $-10 \leq k \leq 10$, $-21 \leq l \leq 22$
Reflections collected	5140
Independent reflections	1741 [R_{int} = 0.1625, R_{sigma} = 0.1647]
Data/restraints/parameters	1741/7/55
Goodness-of-fit on F^2	2.194
Final R indexes [I>=2σ (I)] [a]	R_1 = 0.2439, wR_2 = 0.5852
Final R indexes [all data] [a]	R_1 = 0.2690, wR_2 = 0.6108

[a] $R_1 = \Sigma \| F_o | - | F_c \| / \Sigma | F_o |$, $wR_2 = [\Sigma[w(F_o^2-F_c^2)^2]/\Sigma[w(F_o^2)^2]]^{1/2}$

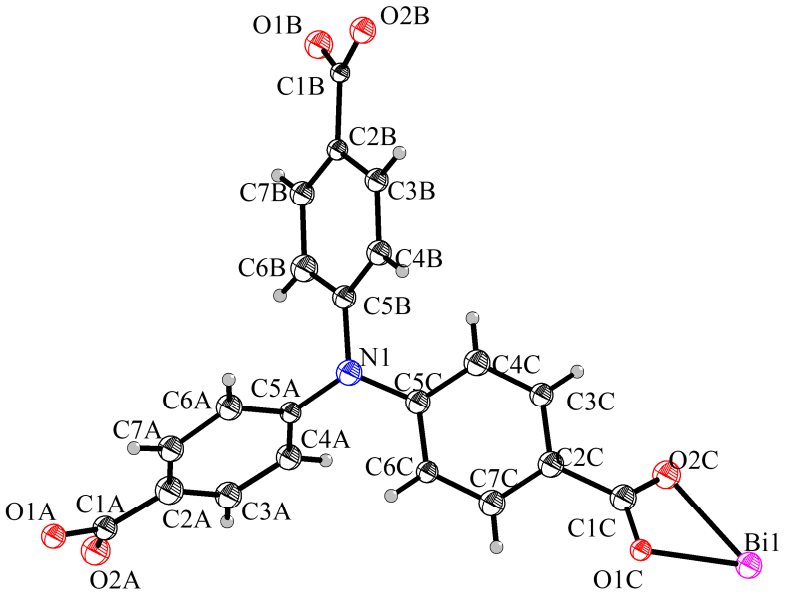

Figure S7.7: Ortep view of the asymmetric unit of **Bi(NTB)-MOF1** (probability level 50%).

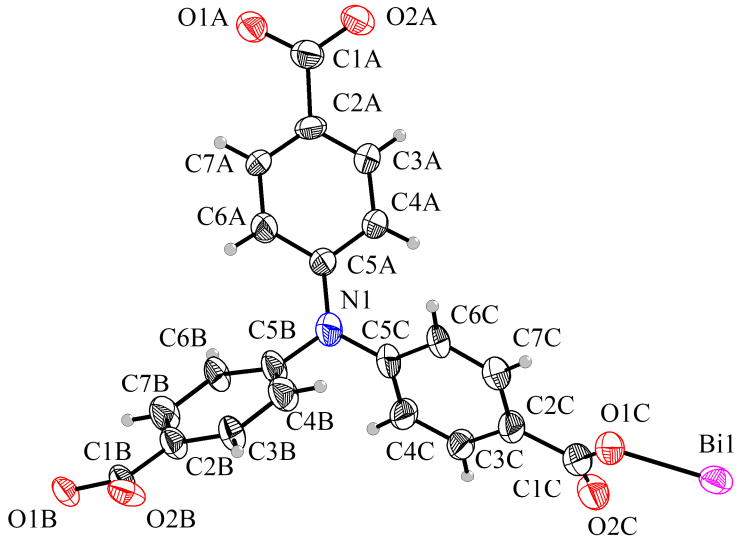

Figure S7.8: Ortep view of the asymmetric unit of **Bi(NTB)-MOF2** (probability level 50%).

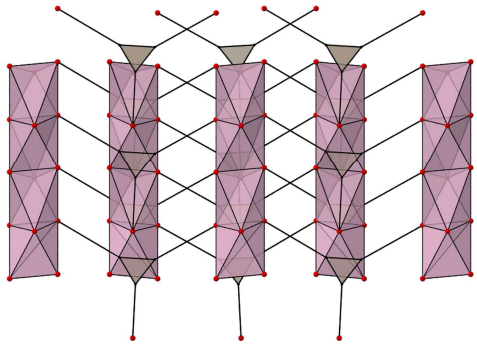

Figure S7.9: Simplified net of **Bi(NTB)-MOF1** oriented along the crystallographic *a*-axis.

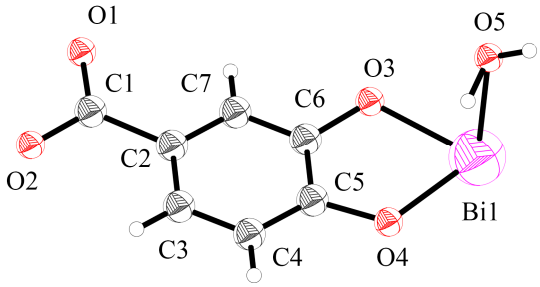

Figure S7.10: Ortep view of the asymmetric unit of **{Bi(PC)(H$_2$O)}$_n$** (probability level 50%).

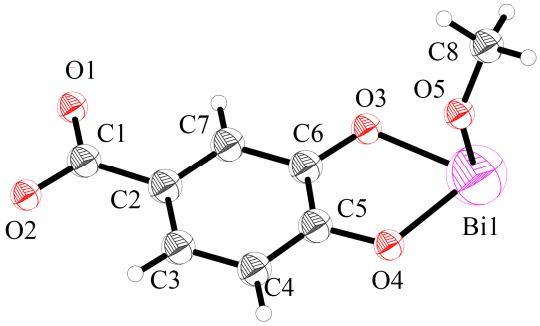

Figure S7.11: Ortep view of the asymmetric unit of **{Bi(PC)(MeOH)}$_n$** (probability level 50%).

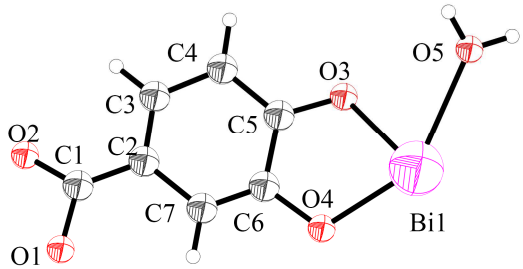

Figure S7.12: Ortep view of the asymmetric unit of the **3D-CP {Bi(PC)(H$_2$O)}$_n$** (probability level 50%).

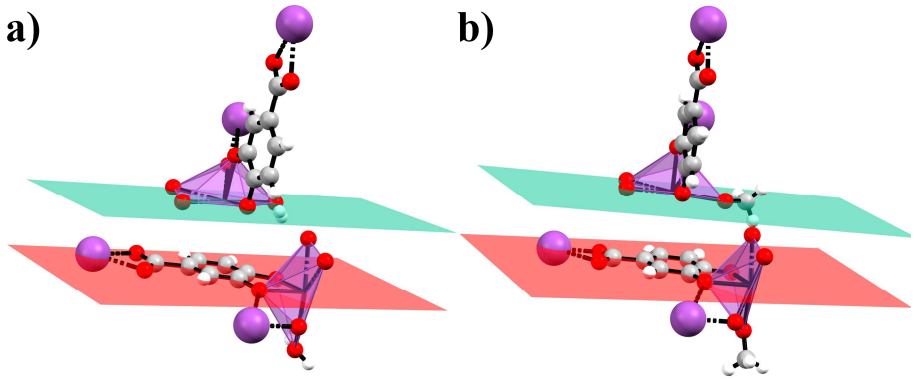

Figure S7.13: Illustration of the mean planes calculated for the aryl group (red plane) and the bismuth complex (green plane): (a) **{Bi(PC)(H$_2$O)}$_n$**, (b) **{Bi(PC)(MeOH)}$_n$**. The angles between these planes are: **θ**(a) = 2.03°, **θ**(b) = 3.35°.

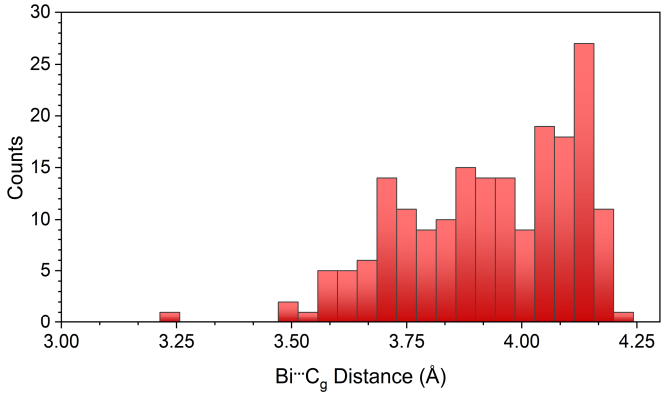

Figure S7.14: Histogram from the data analysis on Bi···π contacts conducted through the CSD. A Bi···Cg distance of 4.3 Å was considered as upper limit threshold.

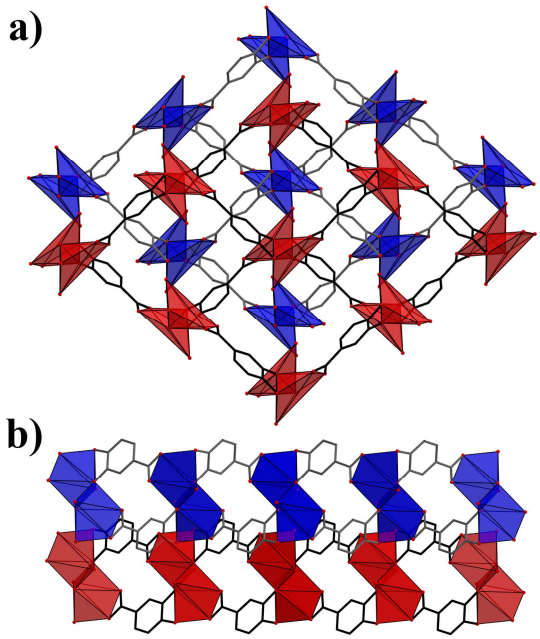

Figure S7.15: Stacked view of two different Bi-PC layers oriented along the crystallographic (101) direction and *b*-axis, respectively.

7.5.3 Gas sorption

The gas sorption measurements were carried out by Prof. Ocean Cheung from Uppsala University on a Micromeritics ASAP202 surface analyser. Before gas sorption measurements, the as-synthesized MOFs were activated under dynamical vacuum.

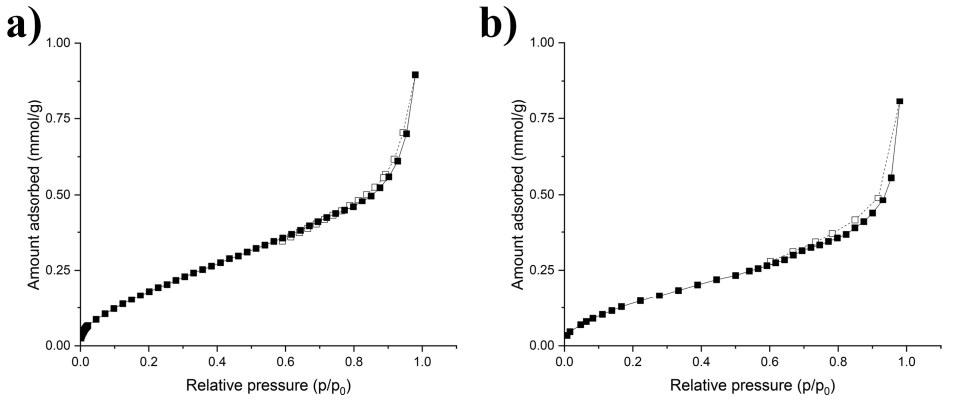

Figure S7.16: Nitrogen adsorption isotherms of **Bi(NTB)-MOF1** (a) and **Bi(NTB)-MOF2** (b), both recorded at liquid N_2 temperature.

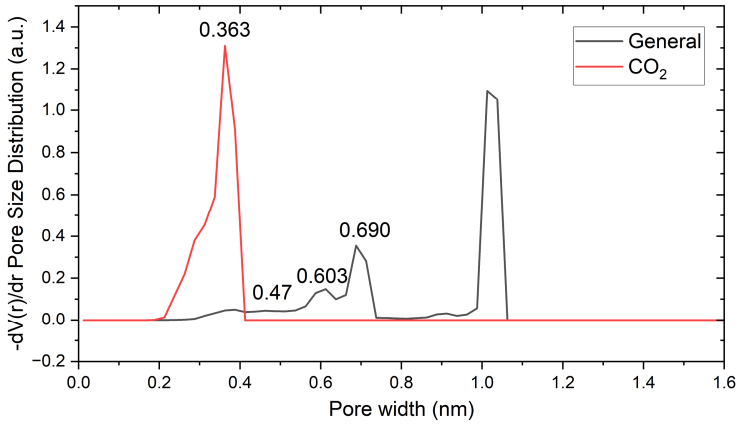

Figure S7.17: Pore size distribution for **Bi(NTB)-MOF2** calculated on the whole porous space (grey line) and on the accessible network for a CO_2 probe (red line). The calculation was carried out using the PoreBlazer software.[35]

Bibliography:

[1] Q.-X. Wang, G. Li, "Bi(III) MOFs: syntheses, structures and applications", *Inorg. Chem. Front.* 8 (2021) 572–589. https://doi.org/10.1039/D0QI01055C.

[2] Z. Wang, Z. Zeng, H. Wang, G. Zeng, P. Xu, R. Xiao, D. Huang, S. Chen, Y. He, C. Zhou, M. Cheng, H. Qin, "Bismuth-based metal–organic frameworks and their derivatives: Opportunities and challenges", Coordination Chem. Rev.s 439 (2021) 213902. https://doi.org/10.1016/j.ccr.2021.213902.

[3] Q.L. Guan, Y.H. Xing, J. Liu, C. Han, C.Y. Hou, F.Y. Bai, "Bismuth-Carboxylate Ligand 1,3,6,8-Tetrakis(*p* -benzoic acid)pyrene Frameworks, Photophysical Properties, Biological Imaging, and Fluorescent Sensor for Biothiols", *J. Phys. Chem. C* 123 (2019) 23287–23296. https://doi.org/10.1021/acs.jpcc.9b02709.

[4] N. Han, P. Ding, L. He, Y. Li, Y. Li, "Promises of Main Group Metal–Based Nanostructured Materials for Electrochemical CO 2 Reduction to Formate", *Adv. Energy Mater.* 10 (2020) 1902338. https://doi.org/10.1002/aenm.201902338.

[5] A. García-Sánchez, M. Gomez-Mendoza, M. Barawi, I.J. Villar-Garcia, M. Liras, F. Gándara, V.A. De La Peña O'Shea, "Fundamental Insights into Photoelectrocatalytic Hydrogen Production with a Hole-Transport Bismuth Metal–Organic Framework", *J. Am. Chem. Soc.* 142 (2020) 318–326. https://doi.org/10.1021/jacs.9b10261.

[6] Y. Xiao, X. Guo, J. Liu, L. Liu, F. Zhang, C. Li, "Development of a bismuth-based metal-organic framework for photocatalytic hydrogen production", *Chinese J. Catal.* 40 (2019) 1339–1344. https://doi.org/10.1016/S1872-2067(19)63329-2.

[7] A.K. Adcock, B. Gibbons, J.D. Einkauf, J.A. Bertke, J.F. Rubinson, D.T. De Lill, K.E. Knope, "Bismuth(III)-thiophenedicarboxylates as host frameworks for lanthanide ions: synthesis, structural characterization, and photoluminescent behavior", *Dalton Trans.* 47 (2018) 13419–13433. https://doi.org/10.1039/C8DT02920B.

[8] C. Orellana-Tavra, M. Köppen, A. Li, N. Stock, D. Fairen-Jimenez, "Biocompatible, Crystalline, and Amorphous Bismuth-Based Metal–Organic Frameworks for Drug Delivery", *ACS Appl. Mater. Interfaces* 12 (2020) 5633–5641. https://doi.org/10.1021/acsami.9b21692.

[9] L. Robison, L. Zhang, R.J. Drout, P. Li, C.R. Haney, A. Brikha, H. Noh, B.L. Mehdi, N.D. Browning, V.P. Dravid, Q. Cui, T. Islamoglu, O.K.

Farha, "A Bismuth Metal–Organic Framework as a Contrast Agent for X-ray Computed Tomography", *ACS Appl. Bio Mater.* 2 (2019) 1197–1203. https://doi.org/10.1021/acsabm.8b00778.

[10] E.S. Grape, J.G. Flores, T. Hidalgo, E. Martínez-Ahumada, A. Gutiérrez-Alejandre, A. Hautier, D.R. Williams, M. O'Keeffe, L. Öhrström, T. Willhammar, P. Horcajada, I.A. Ibarra, A.K. Inge, A Robust and Biocompatible Bismuth Ellagate MOF Synthesized Under Green Ambient Conditions, *J. Am. Chem. Soc.* 142 (2020) 16795–16804. https://doi.org/10.1021/jacs.0c07525.

[11] Y. Yang, R. Ouyang, L. Xu, N. Guo, W. Li, K. Feng, L. Ouyang, Z. Yang, S. Zhou, Y. Miao, "Review: Bismuth complexes: synthesis and applications in biomedicine", *J. Coord. Chem.* 68 (2015) 379–397. https://doi.org/10.1080/00958972.2014.999672.

[12] A.K. Inge, M. Köppen, J. Su, M. Feyand, H. Xu, X. Zou, M. O'Keeffe, N. Stock, "Unprecedented Topological Complexity in a Metal–Organic Framework Constructed from Simple Building Units", *J. Am. Chem. Soc.* 138 (2016) 1970–1976. https://doi.org/10.1021/jacs.5b12484.

[13] M. Feyand, E. Mugnaioli, F. Vermoortele, B. Bueken, J.M. Dieterich, T. Reimer, U. Kolb, D. de Vos, N. Stock, "Automated Diffraction Tomography for the Structure Elucidation of Twinned, Sub-micrometer Crystals of a Highly Porous, Catalytically Active Bismuth Metal–Organic Framework", *Angew. Chem. Int. Ed.* 51 (2012) 10373–10376. https://doi.org/10.1002/anie.201204963.

[14] E.S. Grape, H. Xu, O. Cheung, M. Calmels, J. Zhao, C. Dejoie, D.M. Proserpio, X. Zou, A.K. Inge, "Breathing Metal–Organic Framework Based on Flexible Inorganic Building Units", *Crystal Growth & Design* 20 (2020) 320–329. https://doi.org/10.1021/acs.cgd.9b01266.

[15] Chou, T. H.; Ding, H. Y.; Lin, R. J.; Liang, J. Y.; Liang, C. H. "Inhibition of Melanogenesis and Oxidation by Protocatechuic Acid from Origanum Vulgare (Oregano)". *J. Nat. Prod.* 2010, 73 (11), 1767–1774. https://doi.org/10.1021/np100281g.

[16] S.T.S. Hassan, E. Švajdlenka, K. Berchová-Bímová, "Hibiscus sabdariffa L. and Its Bioactive Constituents Exhibit Antiviral Activity against HSV-2 and Anti-enzymatic Properties against Urease by an ESI-MS Based Assay", *Molecules* 22 (2017) 722. https://doi.org/10.3390/molecules22050722.

[17] J.A. Salvador, S.A. Figueiredo, R.M. Pinto, S.M. Silvestre, "Bismuth compounds in medicinal chemistry", *Future Med. Chem.* 4 (2012) 1495–1523. https://doi.org/10.4155/fmc.12.95.

[18] D. Keogan, D. Griffith, "Current and Potential Applications of Bismuth-Based Drugs", *Molecules* 19 (2014) 15258–15297. https://doi.org/10.3390/molecules190915258.

[19] E. Echenique-Errandonea, S. Rojas, V.K. Abdelkader-Fernández, M. Pérez-Mendoza, R.F. Mendes, P. Barbosa, F. Figueiredo, F. Figueira, F.A. Almeida Paz, J.M. Delgado-López, A. Rodríguez-Diéguez, J.M. Seco, "Adsorptive Capacity, Inhibitory Activity and Processing Techniques for a Copper-MOF Based on the 3,4-Dihydroxybenzoate Ligand", *Molecules* 27 (2022) 8073. https://doi.org/10.3390/molecules27228073.

[20] I. Nederlof, E. Van Genderen, Y.-W. Li, J.P. Abrahams, "A Medipix quantum area detector allows rotation electron diffraction data collection from submicrometre three-dimensional protein crystals", *Acta Crystallogr. D Biol. Crystallogr.* 69 (2013) 1223–1230. https://doi.org/10.1107/S0907444913009700.

[21] M.O. Cichocka, J. Ångström, B. Wang, X. Zou, S. Smeets, "High-throughput continuous rotation electron diffraction data acquisition *via* software automation", *J. Appl. Crystallogr.* 51 (2018) 1652–1661. https://doi.org/10.1107/S1600576718015145.

[22] M.T.B. Clabbers, E. van Genderen, W. Wan, E.L. Wiegers, T. Gruene, J.P. Abrahams, "Protein structure determination by electron diffraction using a single three-dimensional nanocrystal", *Acta Crystallogr. D Struct. Biol.* 73 (2017) 738–748. https://doi.org/10.1107/S2059798317010348.

[23] C.F. Macrae, I. Sovago, S.J. Cottrell, P.T.A. Galek, P. McCabe, E. Pidcock, M. Platings, G.P. Shields, J.S. Stevens, M. Towler, P.A. Wood, "*Mercury 4.0*: from visualization to analysis, design and prediction", *J. Appl. Crystallogr.* 53 (2020) 226–235. https://doi.org/10.1107/S1600576719014092.

[24] A. Schoedel, M. Li, D. Li, M. O'Keeffe, O.M. Yaghi, "Structures of Metal–Organic Frameworks with Rod Secondary Building Units", *Chem. Rev.* 116 (2016) 12466–12535. https://doi.org/10.1021/acs.chemrev.6b00346.

[25] O. Delgado-Friedrichs, M. O'Keeffe, "Identification of and symmetry computation for crystal nets", *Acta Crystallogr. A Found. Crystallogr.* 59 (2003) 351–360. https://doi.org/10.1107/S0108767303012017.

[26] V.A. Blatov, A.P. Shevchenko, D.M. Proserpio, "Applied Topological Analysis of Crystal Structures with the Program Package ToposPro",

Crystal Growth & Design 14 (2014) 3576–3586. https://doi.org/10.1021/cg500498k.

[27] O. Delgado-Friedrichs, "The GAVROG Project", http://www.gavrog.org/.

[28] A. Aykanat, C.G. Jones, E. Cline, R.M. Stolz, Z. Meng, H.M. Nelson, K.A. Mirica, "Conductive Stimuli-Responsive Coordination Network Linked with Bismuth for Chemiresistive Gas Sensing", *ACS Appl. Mater. Interfaces* 13 (2021) 60306–60318. https://doi.org/10.1021/acsami.1c14453.

[29] A.A. Coelho, "*TOPAS* and *TOPAS-Academic*: an optimization program integrating computer algebra and crystallographic objects written in C++", *J. Appl. Crystallogr.* 51 (2018) 210–218. https://doi.org/10.1107/S1600576718000183.

[26] G.M. Sheldrick, "*SHELXT* – Integrated space-group and crystal-structure determination", *Acta Crystallogr. A Found. Adv.* 71 (2015) 3–8. https://doi.org/10.1107/S2053273314026370.

[27] G.M. Sheldrick, "Crystal structure refinement with *SHELXL*", *Acta Crystallogr. C Struct. Chem.* 71 (2015) 3–8. https://doi.org/10.1107/S2053229614024218.

[28] O.V. Dolomanov, L.J. Bourhis, R.J. Gildea, J.A.K. Howard, H. Puschmann, "*OLEX2*: a complete structure solution, refinement and analysis program", *J. Appl. Crystallogr.* 42 (2009) 339–341. https://doi.org/10.1107/S0021889808042726.

[29] L. Sarkisov, R. Bueno-Perez, M. Sutharson, D. Fairen-Jimenez, "Materials Informatics with PoreBlazer v4.0 and the CSD MOF Database", *Chem. Mater.* 32 (2020) 9849–9867. https://doi.org/10.1021/acs.chemmater.0c03575.